Attenuation Correction of Myocardial Perfusion Scintigraphy Images without Transmission Scanning

Sarah Catherine Cade

PhD Thesis

January 2015

I, Sarah Catherine Cade, confirm that the work presented in this thesis is my own. Where information has been derived from other sources, I confirm that this has been indicated in the thesis.

Abstract

Attenuation correction is essential for reliable interpretation of emission tomography; however the use of transmission measurements to generate attenuation maps is limited by availability of equipment and potential mismatches between the transmission and emission measurements. This work investigates the possibility of estimating an attenuation map using measured scatter data without a transmission scan.

A scatter model has been developed that predicts the distribution of photons which have been scattered once. The scatter model has been used as the basis of a maximum likelihood gradient ascent method (SMLGA) to estimate an attenuation map from measured scatter data. The SMLGA algorithm has been combined with an existing algorithm using photopeak data to estimate an attenuation map (MLAA) in order to obtain a more accurate attenuation map than using either algorithm alone. Iterations of the SMLGA-MLAA algorithm are alternated with iterations of the MLEM algorithm to estimate the activity distribution. Initial tests of the algorithm were performed in 2 dimensions using idealised data before extension to 3 dimensions. The basic algorithm has been tested in 3 dimensions using projection data simulated using a Monte Carlo simulator with software phantoms.

All soft tissues within the body have similar attenuation characteristics and so only a small number of different values are normally present. A Level-Set technique to restrict the attenuation map to a piecewise constant function has therefore been investigated as a potential way to improve the quality of the reconstructed attenuation map.

The basic SMLGA-MLAA algorithm contains a number of assumptions; the effect of these has been investigated and the model extended to include the effect of photons which are scattered more than once and scatter correction of the pho-

topeak. The effect of different phantom shapes and activity distributions has been assessed and the final algorithm tested using data acquired using a physical phantom.

Acknowledgements

There are a large number of people without whom I never would have managed to finish this work. I would also like to acknowledge the contribution of the National Institute for Health Research to the funding of this project through their award of a Doctoral Fellowship.

Firstly my thanks must go to my primary supervisor Brian Hutton for his endless help and encouragement as well as the suggestions and discussions which helped to keep the project on the right track. I would also like to thank my secondary supervisors Simon Arridge and Martyn Evans for their contribution to this project and their suggestions of alternative ways of looking at things.

Thank you to all at the Institute of Nuclear Medicine who made me welcome during my time there and particularly to Ben, Kris and Beverly for your help with accessing the INM computers from home and setting simulations running for me. I would also like to thank my colleagues from Medical Physics at the Royal United Hospital who released me from my role there to enable me to pursue a PhD and who have provided so much support and encouragement along the way.

Without my family and friends it would not have been possible for me to start (let alone finish) a PhD so far from home and so I would like to thank all those who provided me with somewhere to stay and company after work. It was an added bonus of my PhD to be able to spend extra time with so many lovely people. Particular thanks go to my Dad and Margaret who allowed me to take over their spare room despite thinking I'd left home years before, and to Linda whose packed lunches were legendary!

I must also thank Mum for taking the time to proof read my thesis for me. You are one of a very select group of people who have actually read my entire thesis and you have done an amazing job.

Finally, a huge thank you to Iain for your belief I can achieve anything I want and your support to help me do it, and to Marcus for creating so many more interesting things to do when I was supposed to be writing up!

Contents

List of Figures

List of Tables

Abbreviations

CAD	Coronary Artery Disease
CT	Computed Tomography
DAM	Differential Attenuation Method
ECG	Electrocardiogram
FCM	Fuzzy C-means
FFT	Fast Fourier Transform
LVEF	Left Ventricular Ejection Fraction
MLAA	Maximum Likelihood based Attenuation estimation Algorithm
MLEM	Maximum Likelihood Expectation Maximisation
MPI	Myocardial Perfusion Imaging
MRI	Magnetic Resonance Imaging
NaI	Sodium Iodide
OS	Ordered Subsets
OSEM	Ordered Subsets Expectation Maximisation
PET	Positron Emission Tomography
PM	Photomultiplier
RMSE	Root Mean Square Error
SDSE	Slab-Derived Scatter Estimation
SMLGA	Scatter based Maximum Likelihood Gradient Ascent algorithm
SPECT	Single Photon Emission Computed Tomography
^{99m}Tc	Technetium-99m
TEW	Triple Energy Window
Tl	Thallium

Nomenclature

$\boldsymbol{A}_0$	the transfer matrix describing the physical characteristics of the imaging system
$\boldsymbol{A_d}$	is the attenuated transfer matrix giving the probability of a photon scattered in voxel k reaching detector element d
$\boldsymbol{A_k}$	is the attenuated transfer matrix giving the probability of a photon emitted from voxel b reaching voxel k
b	point of emission
C	number of fuzzy clusters
c_{bd}	contribution of geometric effects to the probability of a photon from voxel b reaching detector d
$c_{kj'd}$	contribution of geometric effects to the probability of a photon from voxel k, travelling in direction j', reaching detector d.
d	point of detection
E	photon energy
$H(\boldsymbol{\rho})$	the Heaviside function
i	iteration number
J_{FCM}	Fuzzy C-means objective function
k	point of first scatter event
L	log-likelihood of the observed sinogram
m	"fuzzification" parameter
$N_{jj'}$	Klein-Nishina probability of scattering from direction j to j'
$\boldsymbol{n}^*$	measured SPECT projection data
$\boldsymbol{n}^p$	measured SPECT projection data without scatter
$\boldsymbol{n}^s$	measured SPECT scatter projection data
n_{bd}	number of counts emitted from voxel b that are detected at detector element d
p	pixel size

$\boldsymbol{Q}$	emission function and gives the proportion of photons emitted within a solid angle defined by Ω_j
$\boldsymbol{S_b}$	probability of scattering occurring in the same voxel as the emission
$\boldsymbol{S_k}$	probability of a photon scattering in voxel k
$\boldsymbol{s}(\boldsymbol{\mu})$	estimated scatter projection data
U_{ij}	membership grade for voxel j belonging to cluster i
v	number of voxels
w_i	centroid value for cluster i
x_b and x_d	ends of the ray between b and d
$x_{b'ld}$	intersection length of the path from b' to d with voxel l
α_p	step size for the primary photon based attenuation reconstruction
α_s	step size for the scatter based reconstruction
γ_{bd}	attenuation part of the transfer matrix
$\bar{\varepsilon}^2$	normalised mean square error
η	diameter of the reconstruction area
θ_{bk}	direction of photon travel in the $x-y$ plane
$\boldsymbol{\lambda}$	activity distribution
$(\hat{\boldsymbol{\lambda}}^i)_b$	estimate of the activity at voxel b from ith iteration
$\boldsymbol{\mu}$	linear attenuation coefficient
$\boldsymbol{\rho}$	level set function
Φ_d	detector angle
$\boldsymbol{\phi}$	number of photons emitted from each voxel b travelling in each direction j
φ_{bkd}	scattering angle
$\boldsymbol{\chi}$	normalisation factor to prevent over correction in under-sampled regions of the image volume
ψ_{bk}	direction of photon travel relative to the z-axis
Ω	solid angle subtended by scatter voxel to emission voxel
ω_{bk}	fraction of photons emitted in voxel b that are directed towards voxel k
$\frac{\partial \boldsymbol{X}(\boldsymbol{\mu})}{\partial \boldsymbol{\mu}}$	is defined to be the Jacobian of $\boldsymbol{X}$ with respect to $\boldsymbol{\mu}$

1 Introduction

When performing myocardial perfusion imaging (MPI) using single photon emission computed tomography (SPECT), variation in attenuation of different tissue types in the thorax can lead to significant artefacts in the reconstructed image unless a correction for attenuation is performed. Avoiding such artefacts is clearly desirable since these can mimic perfusion defects and hence lead to incorrect diagnosis. Attenuation correction is also essential if quantitative analysis is to be performed, e.g. comparison of images with a normal database.

The use of X-ray Computed Tomography (CT) images and sealed source transmission scans to provide an attenuation map is well established (Zaidi & Hasegawa 2003). However, there are a number of disadvantages to this approach to attenuation correction. Firstly, the use of a transmission scan to provide the attenuation map can result in a mismatch between the activity distribution and the attenuation map as a result of patient movements, including those due to respiration. Secondly, a new generation of gamma cameras for cardiac imaging is now becoming available. These cameras have the possibility to provide more rapid image acquisition but most do not have the hardware required to acquire a transmission scan and addition of such hardware would be technically challenging. The final consideration when using a transmission scan to acquire attenuation data is that of patient dose; the use of both sealed sources and X-ray CT results in an increased radiation dose to the patient which it would be desirable to avoid if a suitable alternative could be found.

The objective of this work is to develop a reconstruction algorithm for SPECT imaging that includes attenuation correction without the use of a separate transmission scan.

1.1 Overview of Thesis

Some existing approaches to attenuation correction in SPECT imaging and the role of SPECT in cardiac imaging are discussed in Chapter 2. Other factors which can affect the accuracy of SPECT image reconstruction are also discussed; in particular the role of scatter correction.

Chapter 3 shows the development of a new model for scatter sinograms in 2 dimensions using the Klein-Nishina model for scattering probability. The model developed is compared to data generated using Monte Carlo simulation for a number of different phantoms.

The scatter model developed is incorporated into a scatter based maximum likelihood gradient ascent (SMLGA) reconstruction algorithm in Chapter 4 which is tested using simulated data and compared to reconstructions with perfect attenuation correction and without attenuation correction. An existing method of attenuation correction using photopeak data (the MLAA technique (Nuyts *et al.*. 1999)) is also investigated and the combination of the MLAA and SMLGA algorithms tested.

Chapter 5 extends the 2-dimensional scatter model to 3 dimensions. The use of an improved model for the estimation of scattering within voxels close to the source voxel, modelling of the collimator resolution and changes to the attenuation and scattering as a result of reduced photon energy and in different tissue types are also considered.

The final scatter model is used for 3-dimensional image reconstruction in Chapter 6. The use of a 'one-step' late approximation to the gradient of the likelihood of the attenuation map is considered in the 3-dimensional case and some possible methods of reducing the time taken to perform the reconstruction are investigated.

In Chapter 7 some techniques for limiting the number of unknown variables in the reconstruction problem are considered. The use of a piecewise constant (level set) method of limiting the variation in the reconstructed attenuation map is investigated. The effect of the choice of attenuation map used to initialise the reconstruction process is also discussed. As an alternative to the level set technique constraints are used to fix the attenuation map in some regions of the reconstruction.

In Chapter 8 the algorithm is validated with data generated using Monte Carlo simulation and data acquired using a physical torso phantom. The effects of photons which are scattered multiple times and detected within the scatter window and of scattered photons within the photopeak window are also considered in this chapter.

Finally, a summary of the findings of each chapter and potential areas for future investigation are outlined in the Conclusions (Chapter 9).

2 Background

2.1 SPECT Imaging

The aim of this project is to improve image quality in nuclear medicine single photon emission computed tomography (SPECT) imaging by developing a reconstruction algorithm which includes attenuation correction without a transmission scan. This has particular relevance to Myocardial Perfusion Imaging (MPI).

SPECT imaging involves the administration to a patient of a pharmaceutical which is labelled with a radioactive isotope; this is known as a radiopharmaceutical. The radiopharmaceutical is taken up by tissues within the body in proportion to the metabolism of the administered compound. The aim of the study is to determine the distribution of the radiopharmaceutical within the body by measuring the emitted radiation outside the body (Fokas *et al.*. 2006). For SPECT studies a series of planar images are acquired at a number of different angles around the body to provide projection views which can be used to reconstruct the distribution of the radioactive tracer in slices through the body (Patton & Turkington 2008). The images obtained give functional information which is complementary to the structural information provided by other modalities such as magnetic resonance imaging (MRI) or X-ray computed tomography (CT).

A common approach to SPECT imaging studies is to use radioactive isotopes which decay primarily via emission of a gamma photon. This is because other radioactive particles are highly attenuated in tissue and are therefore unlikely to travel far enough to be detected; hence, they can not be used for medical imaging. The isotope that is most commonly used is technetium-99m (^{99m}Tc) which decays via isomeric transition with a half-life of approximately 6 hours, producing gamma rays with an energy of 140keV (ICRP 1983). Emitted gamma

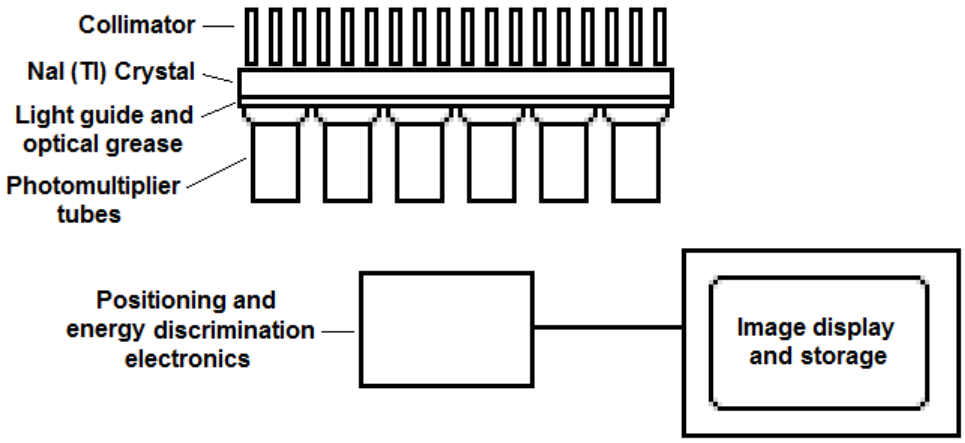

Figure 2.1: Schematic diagram of a conventional gamma camera

photons are detected using a gamma camera when the photon interacts with and deposits its energy at a detector.

2.1.1 Gamma Cameras

In conventional gamma cameras, photon detection occurs using a sodium iodide (NaI) crystal which is doped with thallium (Tl); this is referred to as the scintillation crystal. A schematic diagram of a conventional gamma camera is presented in Figure 2.1. Incident gamma photons deposit their energy in the crystal lattice structure when they interact with electrons, promoting them into the conduction band. As the electrons return to the valence band the consequent change in energy results in the emission of a light photon, with wavelength within the visible range. The light photons are detected by an array of photomultiplier (PM) tubes which converts them into electrons and amplifies the signal. The voltage of the output signal is directly proportional to the energy deposited in the scintillation crystal.

A lead collimator is positioned in front of the camera face in order to provide positional information about the photons incident on the crystal. Only photons which are travelling approximately perpendicular to the camera face are detected, while photons travelling at more oblique angles are absorbed in the collimator. The design of the collimator will affect both the resolution and the sensitivity of the camera; collimators with a small acceptance angle will provide high resolution but a lower sensitivity.

The location where the gamma photon was incident on the camera face is determined by considering the relative amplitudes of the signals from each of the PM tubes. The point within the crystal where the interaction occurred will be within the area defined by the contact area with the PM tube that has the greatest amplitude signal. The precise location is determined by considering the relative amplitudes of different groups of PM tubes with the point of interaction occurring closer to groups with higher amplitude. For example the PM tubes can be divided into two groups ($+X$ and $-X$) depending on the position of the centre of the PM tube along the horizontal axis of the camera face, relative to the centre. If the sum of the amplitudes of the PM tubes in the $+X$ group is greater than in the $+X$ group the interaction can be determine to have occurred in the $+X$ half of the crystal; the exact distance from the central line is given by the relative amplitude of the $+X$ and $-X$ signals. The vertical position can then be determined in a similar way by considering $+Y$ and $-Y$ signals.

2.1.1.1 Dedicated cardiac gamma cameras

Recently a number of gamma cameras optimised for cardiac imaging have become available. These cameras have a smaller field of view, compared to traditional cameras, and often use multiple relatively small solid state detectors. Here, the use of solid state detectors offers an improved sensitivity with the potential of higher spatial and energy resolution. As a result the image acquisition time can be significantly reduced without compromising image quality.

To further reduce imaging times data acquisition can be focussed on a region of interest centred on the heart; known as a region centric acquisition. The region centric acquisition is acquired by either moving each detector or by using a moving pinhole array such that more time is spent with the detectors pointing towards the heart

2.1.2 Factors Affecting Image Accuracy and Quantification

There are a number of factors which can limit the quality of SPECT images unless they are corrected for. One of the most significant of these is that as photons travel though a material there is a finite probability that they will interact with

that material resulting in attenuation of the photon via either absorption or scattering. The probability of attenuation depends on the energy of the photon and the type of material it is travelling through. The effect of attenuation on SPECT images and correction for it is discussed in Section 2.4. When a photon interacts with a material its energy may be totally absorbed by the material in which case the photon is lost. Alternatively the photon may transfer part of its energy to the material and undergo a change of direction in a process known as inelastic or Compton scattering. The effect of scatter, and correction for it, is discussed further in Section 2.5.

The quality of a SPECT image is also affected by the finite resolution of the imaging system. In conventional gamma camera systems the collimators are used to limit the acceptance angle of photons incident on the detector to be approximately perpendicular to the camera face. In an idealised case this means that all photons detected at a given point on the detector originated along a vector normal to that point on the detector. However, in reality collimator holes have a finite size and hence a finite acceptance angle. Photons detected may, therefore, have originated anywhere within a finite solid angle subtended from the point of detection. The resolution of the gamma camera system is defined by the full width at half maximum of the image of a point source. It, therefore, depends on the distance of the source from the collimator. Improved resolution is obtained by positioning the source close to the detector. Since the resolution is defined by the geometry of the collimator holes and the distance of the source from the detector it is possible to model system resolution accurately and hence improve the resolution of the reconstructed images.

The accuracy with which individual voxel values of SPECT images can be determined is affected by the partial volume effect. At the boundaries between different regions two or more organs may be included in the same voxel of the image. As a result the apparent uptake value calculated for the voxel is the average of the different tissues contained within the voxel. This effect is particularly significant for small regions because the proportion of the region that is located close to a boundary is increased; for very small regions the maximum activity within the region may not be accurately recovered as the apparent activity is spread over a volume which is larger than the true region volume. The finite resolution of the gamma camera will also contribute to the partial volume effect as some counts from each voxel are measured in the neighbouring detector bins and hence the

boundaries between different uptake regions become blurred. The use of resolution modelling of the camera system in the reconstruction process can help to reduce the impact of the camera resolution characteristics on the partial volume effect.

Dead-time of the imaging system is caused by the finite time needed by the detectors to respond to each photon that is incident on the detector. If a second photon is incident on the detector a very short time after the previous photon (i.e. during the dead-time) the system is unable to respond and the second photon is lost. The effect of dead-time can reduce the sensitivity of the imaging system, and hence limit the accuracy of quantification, particularly at high count rates. The effect of dead-time can be minimised by the use of small crystal sizes. However at high count-rates the number of photons detected will not increase linearly with the number of photons that are incident on the imaging system and so it is essential to ensure that images are acquired at count-rates within the linear portion of the system response curve if accurate quantification is to be performed.

Patient movement during the image acquisition process can result in artefacts in the reconstructed images. This may occur as a result of physiological motion, such as breathing, or voluntary motion. The effect of movement during the scan disperses the activity from the moving region over a larger volume resulting in reduced image contrast. Furthermore, a mismatch between different phases of the image set (e.g. different frames of a dynamic series or between emission and transmission scans where they are acquired sequentially) may also occur. Mismatches between the emission and transmission scans can result in errors in the attenuation correction process and hence introduce artefacts into the reconstructed activity distribution.

2.1.3 Image Reconstruction

In order to visualise an activity distribution, acquired projection data must be reconstructed to give the activity at each point in the field of view of the detector. The simplest way to do this is to use back projection. In this reconstruction technique the number of counts at each detector point is added to each point within the field of view that is visible at that detector point. This method results in a 'star artefact' around regions of high activity (Figure 2.2); when data from more projections are added the 'star' becomes less prominent, however, the resulting

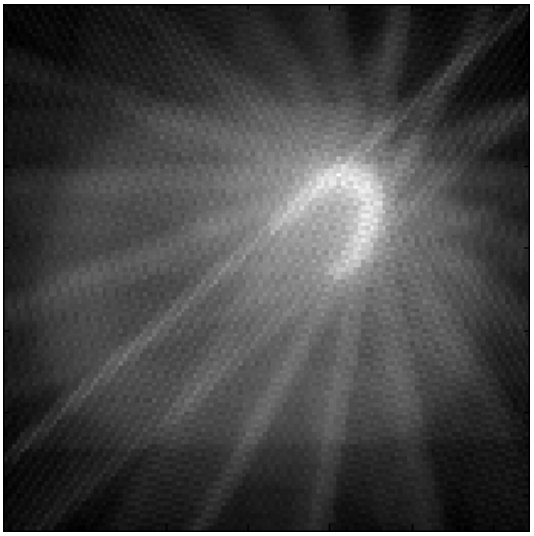

Figure 2.2: Activity distribution reconstructed from 9 projection angles using a back-projection technique showing a 'star artefact'

image is blurred. Blurring can be reduced using a high-pass filter. However this often amplifies noise in the image requiring the use of a low-pass filter to ensure a satisfactory signal to noise ratio. This type of reconstruction is easy to implement but does not take account of the noise characteristics of the data and so is best suited to low noise situations such as X-ray CT acquisitions. SPECT data tends to have much poorer count statistics and so is best reconstructed using an algorithm that accounts for the noise characteristics of the data. Such algorithms are much more complex and are generally used in an iterative process which aims to identify the activity distribution whose calculated projections most closely matched the measured projection data. Iterative image reconstruction is discussed in more detail in Section 2.3.

2.2 Measurement of Cardiac Function

2.2.1 The Structure and Function of the Heart

The primary function of the heart is to pump blood around the body. During the diastole phase of the cardiac cycle the ventricles, shown in Figure 2.3 (*Health Curriculum* 2012), are relaxed and the mitral and tricuspid valves are open. This allows deoxygenated blood from the body to flow from the right atrium to the right ventricle and oxygenated blood to flow from the left atrium to the left

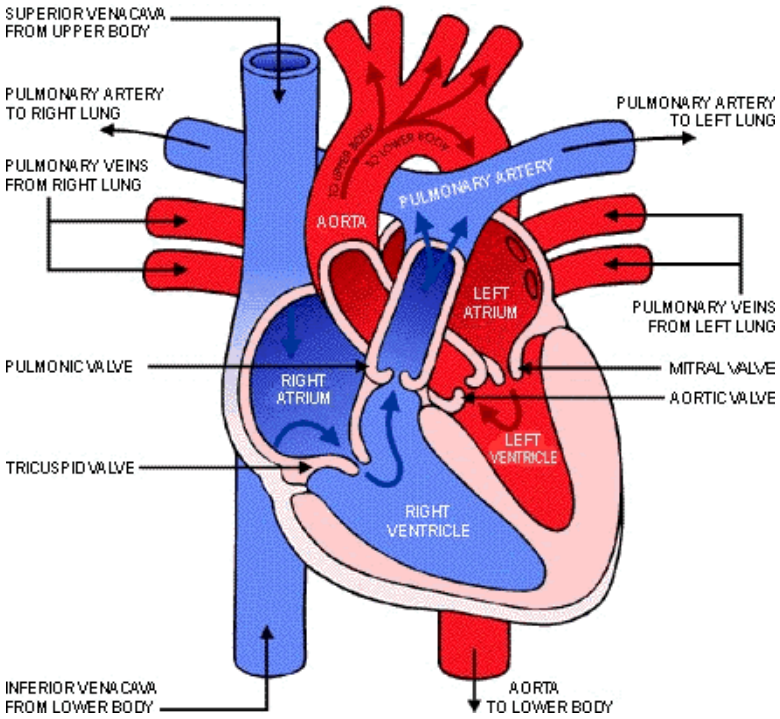

Figure 2.3: The structure of the heart

ventricle. The atria then contract forcing more blood into the ventricles after which the ventricles begin to contract and the mitral and tricuspid values close. Blood is forced from the right ventricle to the lungs and from the left ventricle to the rest of the body (systole). The muscular wall of the left ventricle is the thickest of the four chambers of the heart because, in order to transport blood around the whole body, it contracts with a much greater force than the other chambers.

In order to allow repeated cycles of contraction and relaxation to occur the cardiac muscle is supplied with blood via the coronary arteries. In the presence of Coronary Artery Disease (CAD) arteries supplying the cardiac muscle become narrowed resulting in reduced blood flow to the heart muscle; this is known as ischemia. When there is a severe interruption to blood flow a myocardial infarction (heart attack) can occur resulting in the death of the region of the myocardium which receives its blood supply from the compromised artery. Damage caused by an infarction is irreversible and can compromise the function of the heart. In cases of less severe narrowing of the coronary arteries sufficient blood may be supplied to the myocardium at rest. However, during exercise, when the oxygen demand of the muscles increases, CAD can prevent sufficient blood reaching the heart muscle resulting in pain and shortness of breath. Coronary artery disease is the

single most common cause of death in the European Union and so its diagnosis and treatment is an area of significant interest (Allender *et al.*. 2008).

Determining the most appropriate medical treatment for CAD requires accurate assessment of the presence of ischemia and the viability of the affected heart muscle. The size and location of plaques which cause narrowing of the coronary arteries can be assessed using coronary angiography or cardiac CT. These tests allow the location of plaques to be accurately visualised and are helpful in planning treatments. However, they do not give any indication of the impact the plaque has on perfusion or the viability of the cardiac muscle. Myocardial perfusion imaging (see Section 2.2.2) can be used to assess regions of ischemia which may benefit from revascularisation as well as regions of infarcted and normal tissue where further treatment would not provide any benefit.

2.2.2 Myocardial Perfusion Imaging

Myocardial Perfusion Imaging (MPI) is performed routinely using both Single Photon Emission Computed Tomography (SPECT) and Positron Emission Tomography (PET). Both techniques involve the intravascular injection of a radioactive tracer which is taken up by the myocardium in proportion to the perfusion of the myocardial muscle. Currently, SPECT imaging is more commonly performed than PET imaging because gamma cameras and SPECT tracers are more widely available. MPI studies are normally carried out in two parts; one where the patient is resting in order to show the normal perfusion of the heart and the other where the heart is stressed and hence requiring perfusion.

An ideal tracer for myocardial perfusion imaging would be taken up in the myocardium in linear proportion to blood flow in the area and be retained there during the acquisition process. The two pharmaceuticals that are most commonly used for SPECT myocardial perfusion imaging, sestamibi and tetrofosmin, are both labelled with ^{99m}Tc. However, thallium (^{201}Tl) may also be used.

The sestamibi and tetrofosmin compounds are lipophilic and diffuse from capillaries into the cardiac myocytes where they associate with mitochondria within the cell. The distribution of the tracer is therefore associated with normal mitochondrial function. In areas where the cells are hypoxic as a result of severe ischemia mitochondrial function, and hence the tracer uptake, is reduced. There

is no significant redistribution of either compound from the initial uptake distribution after 3 hours. This lack of redistribution means that imaging does not have to be performed immediately after the stress test; however two separate injections are required to obtain stress and rest images.

Exercise testing is the normal method of stressing the heart. This is performed, using a fixed protocol on a treadmill, or bicycle, in order to raise the patient's heart rate to approximately 80% of the theoretical maximum (220 - age). If this heart rate can not be achieved the test results can not be accurately interpreted as the blood vessels supplying the heart may not be fully dilated. When patients are unable to reach their target heart rate by exercising, e.g. in cases of physical incapacity or uncontrolled hypertension, pharmacological stress agents (e.g. adenosine or dobutamine) are used.

During the image acquisition process an electrocardiogram (ECG) signal can be used to divide the collected counts into a number of bins (normally 8 or 16) which correspond to different parts of the cardiac cycle, a process known as 'gating'. Reconstruction of gated images allows movement of the wall of the left ventricle to be assessed and the ejection fraction ($LVEF$) to be calculated (Equation 2.1).

$$LVEF = \frac{V_D - V_S}{V_D} \tag{2.1}$$

where V_D and V_S are the volumes of the left ventricle at end-diastole and end-systole respectively.

In order to allow visual inspection of the perfusion of the left ventricle acquired data are normally reconstructed into slices along the short, horizontal long and vertical long axes as illustrated in Figure 2.4. Images acquired at rest and at stress can be compared to identify areas of abnormal perfusion (perfusion defects). Perfusion defects which are visualised in both the rest and stress images indicate previous infarctions which have resulted in the death of the myocardial muscle. A perfusion defect present in the stress image but not in the corresponding segment of the rest image indicates a region of ischemia which may benefit from revascularisation, or a stent, to improve blood flow to the region.

In order to perform more quantitative analysis polar plots may be used (Garcia *et al.*. 1985); an example is shown in Figure 2.5. These plots display a representation of the perfusion of the complete left ventricle on a single, circular, image;

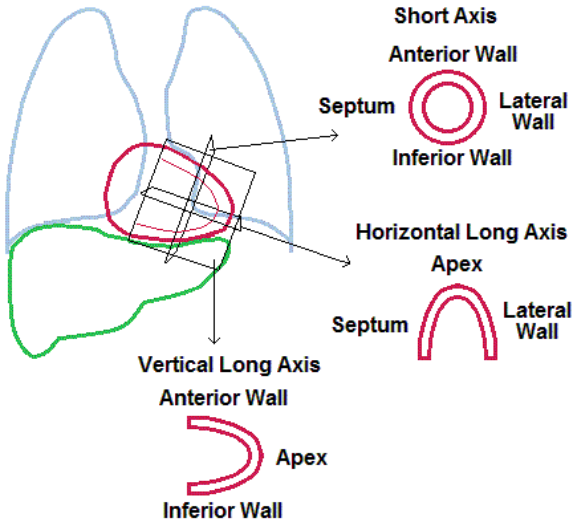

Figure 2.4: Reconstruction planes for myocardial perfusion imaging

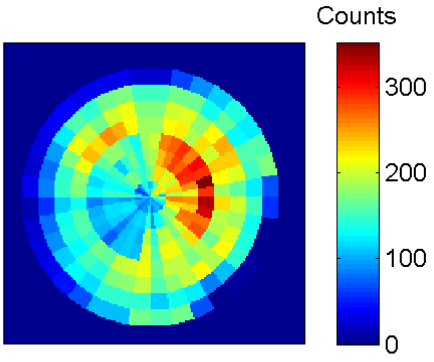

Figure 2.5: Polar plot for normal left ventricle with uniform uptake in all regions.

the apex is located at the centre of the plot with the base at the edge of the plot. The use of polar plots allows images to be compared to a database of images of normal (healthy) hearts to evaluate the extent and severity of any defects quantitatively. However, the use of quantitative analysis is limited by artefacts within the acquired images which can significantly alter the appearance of the tracer distribution. The attenuation and scatter of photons as they pass through the tissue surrounding the heart are significant causes of artefacts in myocardial perfusion images, hence, accurate correction for them is required in order to improve the quality of the reconstructed images.

2.3 Iterative Image Reconstruction

Iterative techniques have a number of advantages over analytical techniques such as filtered back projection. In particular, filtered back projection does not handle noise optimally and lacks flexibility for different scanner configurations. Iterative reconstruction techniques can take account of noise within the measurement process as well as attenuation, scatter and the measurement characteristics of the system resulting in reduced noise in the final reconstructed image.

There are many different iterative reconstruction algorithms but they all have the same basic aim; that is to find an estimated image whose projections match the measured projection data. One of the most commonly used iterative reconstruction algorithms for emission tomography is the maximum likelihood expectation maximisation (MLEM) algorithm derived by Shepp & Vardi (1982) and separately by Lange & Carson (1984). The algorithm is derived using the Poisson nature of the data to calculate the likelihood that the given estimate of the activity distribution matches the true activity distribution, given the measured projection data.

If the measured SPECT projection data is given by $(\boldsymbol{n}^*)_d = \sum_b n_{bd}$, where n_{bd} is the number of counts emitted from voxel b that are detected at detector element d, then the expected number of counts emitted from b that will be detected at d is equal to the activity in voxel b multiplied by element bd of the transfer matrix $\boldsymbol{A}_0$ which describes the physical characteristics of the imaging system and attenuation within the patient. The relationship between activity and detected counts is described by Poisson statistics. Therefore,the probability (or likelihood) of detecting a count (λ_{bd}) in d given activity $\boldsymbol{\lambda}_b$ at b is given by Equation 2.2.

$$P(n_{bd} \mid \lambda_{bd}) = \prod_b \prod_d \frac{\lambda_{bd}^{n_{bd}} \cdot e^{-\lambda_{bd}}}{n_{bd}!} \tag{2.2}$$

$\lambda_{bd} = (\boldsymbol{A}_0)_{bd} \cdot \boldsymbol{\lambda}_b$
$(\boldsymbol{A}_0)_{bd} = c_{bd} \exp\left[-\int_b^d \boldsymbol{\mu}(x)\mathrm{d}x\right]$
c_{bd} gives contribution of geometric effects to the probability of a photon from voxel b reaching detector d.
x is the position along the ray between b and d

The log-likelihood is calculated from Equation 2.2 by taking the natural logarithm

of both sides giving:

$$\ln P\big(n_{bd} \mid \lambda_{bd}\big) = \sum_b \sum_d \Big(n_{bd} \cdot \ln\big(\lambda_{bd}\big) - \lambda_{bd} - \ln\big(n_{bd}!\big) \Big) \tag{2.3}$$

The conditional expectation of the log-likelihood given the measured projection data and the current estimate of the activity distribution, $(\hat{\boldsymbol{\lambda}}^i)_b$ is then given by Equation 2.4.

$$E\Big[\ln P\big(n_{bd} \mid \lambda_{bd}\big) \mid (\boldsymbol{n}^*)_d, (\hat{\boldsymbol{\lambda}}^i)_b\Big] = \sum_b \sum_d \Big(E\big[n_{bd} \mid (\boldsymbol{n}^*)_d, (\hat{\boldsymbol{\lambda}}^i)_b\big] \cdot \ln \lambda_{bd} - \lambda_{bd} - E\big[\ln(n_{bd}!)\big] \Big) \tag{2.4}$$

$E\big[n_{bd} \mid (\boldsymbol{n}^*)_d, (\hat{\boldsymbol{\lambda}}^i)_b\big]$ is the fraction of the counts measured in detector element d that are expected to have originated from voxel b and is defined as:

$$\begin{aligned} E\big[n_{bd} \mid (\boldsymbol{n}^*)_d, (\hat{\boldsymbol{\lambda}}^i)_b\big] &= \frac{(\boldsymbol{A}_0)_{bd} \cdot (\hat{\boldsymbol{\lambda}}^i)_b}{\sum_{b'} (\boldsymbol{A}_0)_{b'd} \cdot (\hat{\boldsymbol{\lambda}}^i)_{b'}} \cdot (\boldsymbol{n}^*)_d \\ &= p_{bd} \end{aligned} \tag{2.5}$$

In order to maximise the conditional expectation of the log-likelihood the partial gradient of the function is found with respect to $\boldsymbol{\lambda}$, as shown in Equation 2.6.

$$\begin{aligned} &\frac{\partial}{\partial(\boldsymbol{\lambda})_b} E\Big[\ln P\big(n_{bd} \mid \lambda_{bd}\big) \mid (\boldsymbol{n}^*)_{bd}, (\hat{\boldsymbol{\lambda}}^i)_b\Big] \\ &\quad = \frac{\partial}{\partial(\boldsymbol{\lambda})_b} \sum_d \Big(p_{bd} \cdot \ln((\boldsymbol{A}_0)_{bd}(\boldsymbol{\lambda})_b - (\boldsymbol{A}_0)_{bd}(\boldsymbol{\lambda})_b - E\big[\ln(n_{bd}!)\big] \Big) \\ &\quad = \sum_d \frac{p_{bd}}{(\boldsymbol{\lambda})_b} - (\boldsymbol{A}_0)_{bd} \end{aligned} \tag{2.6}$$

In order to find the maximum, the gradient of the conditional expectation of the log-likelihood can then be set equal to zero and rearranged to find the next estimate of the activity distribution, $\boldsymbol{\lambda}^{i+1}$, as shown in Equation 2.7. This is the

commonly used MLEM formula derived by Lange (Lange & Carson 1984).

$$
\begin{aligned}
(\boldsymbol{\lambda}^{i+1})_b &= \sum_d \frac{p_{bd}}{(\boldsymbol{A}_0)_{bd}} \\
&= \frac{(\boldsymbol{\lambda}^i)_b}{\sum_d (\boldsymbol{A}_0)_{bd}} \sum_d \frac{(\boldsymbol{A}_0)_{bd} \cdot (\boldsymbol{n}^*)_d}{\sum_{b'} (\boldsymbol{A}_0)_{b'd} (\boldsymbol{\lambda}^i)_{b'}}
\end{aligned}
\tag{2.7}
$$

The MLEM formula above is used as an iterative process for estimating an activity distribution from measured projection data. When increasing numbers of iterations are performed the likelihood that the estimated distribution is equal to the true distribution increases, however the estimates will also appear increasingly noisy and so in clinical practice the reconstruction is often stopped after a small number of iterations in order to produce images which are visually appealing. However, not all regions of the image will converge at the same rate and so this approach can lead to reduced accuracy of the reconstruction. Using a larger number of iterations and then smoothing the resulting image would ensure that all regions of the image have converged and reduce the noisy appearance of the image. The accuracy of the MLEM reconstruction technique depends on the accuracy of the transfer matrix.

One significant limitation of the MLEM algorithm is the time taken to perform a reconstruction. Each iteration of MLEM, which includes a forward and backward projection step, takes approximately twice as long as reconstruction using the filtered back projection method. Since around 20 iterations are commonly performed this leads to reconstruction times which are approximately 40 times longer.

A number of methods for increasing the speed of the reconstruction have been proposed which have facilitated the use of iterative reconstruction techniques in widespread clinical practice (Hutton *et al.*. 1997). The number of iterations that are required in order for iterative reconstructions to converge to a solution can be reduced by the use of preconditioning filters (Clinthorne *et al.*. 1993), or by the inclusion of some prior knowledge about the expected solution in the algorithm (Lange *et al.*. 1987). Alternatively the calculation of the reconstruction can be reduced, the ordered subsets method (Hudson & Larkin 1994) is the most widely used of these techniques. The Ordered Subsets Expectation Maximisation (OSEM) method uses a small subset of the measured projections to perform each

update (sub-iteration) of the activity distribution. A number of sub-iterations are then performed in order to utilise the complete set of measured projections. The projections which are included in each sub-iteration are selected such that the amount of new information that is included is maximised. Provided that the number of projections in each subset is not too small and that the subset order is carefully selected the estimated activity distribution resulting after each sub-iteration of the OSEM algorithm is virtually indistinguishable from the estimate resulting from the same number of full iterations of the MLEM algorithm (Zaidi 2006).

2.3.1 The Transfer Matrix

The transfer matrix $\boldsymbol{A}_0$ describes the physical characteristics of the imaging system. The elements of $\boldsymbol{A}_0$ give the probability that a photon emitted from voxel b, travelling in direction Ω will be detected in detector element d. The quality of the reconstructed image depends on the accuracy of the transfer matrix which can include the effects of attenuation and scatter as well as geometric factors. In order to include the effects of attenuation the transfer matrix is divided into two parts, a geometric part, $\boldsymbol{C}$ with elements c_{bd}, and an attenuation part ($\boldsymbol{\gamma}_{bd}$) as described in Equation 2.8.

$$\boldsymbol{\gamma}_{bd} = \exp\left[-\int_b^d \boldsymbol{\mu}(x)\mathrm{d}x\right] \tag{2.8}$$

$\boldsymbol{\mu}$ is the matrix defining the linear attenuation coefficient at each point in the reconstruction volume
x is the position along the ray between b and d

There are a number of ways to calculate the geometric component, $\boldsymbol{C}$, of the transfer matrix (the radiological path). One method is to pre-compute the relationship between every voxel and every detector element, however, this requires a very large matrix to be stored. Siddon et al. (Siddon 1985) have suggested an efficient method of calculating the radiological path that requires a much smaller matrix to be stored (scaling with $3N$ rather than N^3 for matrix size N). It also has the advantage that the order of the voxels along the radiological path is known, which is important for the calculation of attenuation along the path. This method works by considering the array of voxels to be the intersection vol-

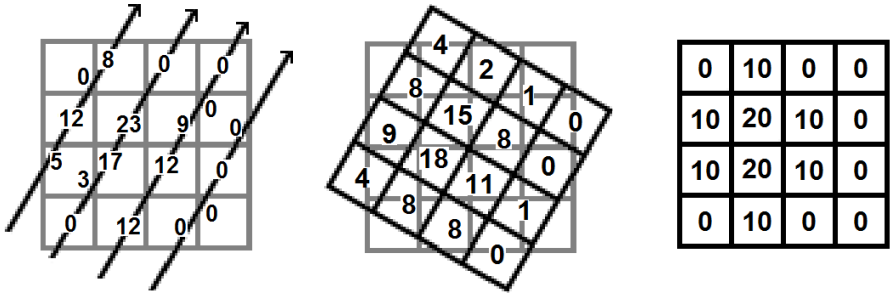

(i) (ii) (iii)

Figure 2.6: Illustration of (i) central ray (Siddon method) and (ii) rotation based projectors; (iii) original matrix

umes of sets of equally spaced parallel planes. The intersection of the radiological path with each set of planes is then calculated. Since, within each set of planes, individual planes are parallel and equally spaced, each intersection point does not need to be calculated individually. Instead the first intersection with each set of planes can be calculated and all the other intersection points generated by recursion. Once the intersection points have been calculated for each set of planes they are sorted into order. This gives the position of each intersection along the radiological path. The intersection length with a given voxel is then the difference between two adjacent intersection points along the radiological path and the voxel index is calculated from the relationship between the starting and end points of the radiological path and the location of the planes that define the image array. Han *et al.*. (1999) proposed a potential improvement to the Siddon ray tracing technique (Siddon 1985) which increments from one point on the ray to the next removing the need for a number of multiplicative steps in the Siddon technique.

A limitation of the Siddon method is that it only considers the central ray of each projection line; the contribution of a pixel to a given ray is considered as the length of the pixel that lies on the central ray, expressed as a fraction of the pixel size. As a result, at oblique angles to the image matrix some pixels may be included in multiple rays and the total contribution from all rays could be greater than one. Improvements to the ray path calculation can be achieved using tubes or volumes in place of central rays (Popescu & Lewitt 2004, Scheins *et al.*. 2006, Schretter 2006). An alternative method of calculation is to used a rotation based projector as illustrated in Figure 2.6. In this case the image matrix is rotated to the required angle in order to calculate which pixels lie along each path. The rotated image is then interpolated to fit a square matrix from which projections are calculated using the sum of the pixels along each

column. This method of projection is limited in accuracy by the accuracy of the interpolation method used; but has the advantage that detector resolution effects may be easily incorporated as the distance of each row of pixels in the interpolated image is a known distance from the detector and can therefore be convolved with an appropriate point spread function to match the response of the detector to sources at that distance from the detector.

2.4 The Effect of Attenuation and Attenuation Correction

As photons travel through any material there is a finite probability that they will interact with it. For photons with energies in the range normally encountered in nuclear medicine (in the keV range) there are two main mechanisms of interaction. Photoelectric interactions occur when the incident photon interacts with an electron and the energy of the photon is totally absorbed. Alternatively, the photon may undergo a scattering interaction in which the photon is removed from the primary beam, resulting in attenuation of the primary beam. After a scattering interaction the scattered photon may go on to interact or be detected elsewhere. The process of scatter and the potential problems associated with it are discussed in Section 2.5.

The transmission of photons through an attenuating material is given by Equation 2.9 (Sorensen & Phelps 1980) and depends on the energy (E) of the incident photons.

$$I(E) = I_o(E) \exp\Big(- \int_0^X \mu(x, E) dx \Big) \tag{2.9}$$

$I_o(E)$ is the incident intensity
I is the transmitted intensity
$\mu(x, E)$ is the linear attenuation coefficient at point x

Since attenuation depends on both the path length through a material and the linear attenuation coefficient of the material, photons which originate further from the detector or in, or behind, a dense material will be attenuated more than those from more superficial regions. The effect of attenuation on image quality can be

significant since the thickness and density of the tissue will vary for different regions of the patient's anatomy. Myocardial imaging is particularly susceptible to attenuation effects given the range of different tissue types that are present in the thorax.

With experience it may be possible to interpret images with attenuation artefacts as knowledge of the most likely attenuation distributions and associated effects can be used by an experienced operator to mentally correct the reconstructed images. However, in order to increase confidence in the interpretation of images and to allow quantitative analysis, correction of attenuation is essential. There are two broad classes of attenuation correction; those which use a separate transmission scan and those which do not.

2.4.1 Transmission Based Attenuation Correction

Currently the most accurate methods of attenuation correction (for both PET and SPECT studies) make use of transmission scans to provide an attenuation map using either radionuclides or X-ray CT.

The use of radionuclides for transmission scanning was proposed in the 1950s (Mayneord 1952) and since then several possible scanning geometries have emerged to use radionuclide transmission scans as a means of providing attenuation correction for SPECT or PET studies (Zaidi & Hasegawa 2003, Bailey 1998). The acquisition of the radionuclide attenuation map may be performed before, after, during or interleaved with the emission study. Sequential imaging is technically easiest; however, this results in increased imaging time and accurate registration of the emission and transmission scans may not be possible due to patient movements. Acquiring the two scans simultaneously removes registration problems and means that any blurring as a result of physiological movements (e.g. breathing) are perfectly matched. One of the main limitations of the accuracy of radionuclide transmission scans for attenuation correction occurs due to cross-talk between the two scans. It is important that cross-talk and spill-over from the emission scan to the transmission scan is minimised(Ficaro *et al.*. 1994). Another source of degraded image quality arising from the use of radionuclide transmission scans occurs due to noise from the transmission scan propagating through to the emission reconstruction. In order to avoid this long scan times can be used to improve the signal to noise ratio of the transmission image. Alternatively,

segmentation of the transmission image can be performed to delineate regions of different tissue types and known attenuation coefficients can then be applied (Meikle *et al.*. 1993, Bettinardi *et al.*. 1999, Xu *et al.*. 1996, Zaidi *et al.*. 2002).

In recent years hybrid SPECT/CT systems, combining traditional gamma camera with an x-ray CT scanner, have largely replaced the use of sealed sources. The use of a CT scan provides patient specific attenuation maps, but, must be converted, from the x-ray energy at which it is acquired, to the primary photon energy of the isotope used for the emission scan (Blankespoor *et al.*. 1996). The use of CT systems for transmission scanning offers an advantage over radionuclide transmission scans as the scan can be used not only for attenuation correction but also for localisation of lesions when the SPECT and CT images are co-registered. However, there are also a number of disadvantages. Firstly, the use of CT scanners can result in much higher patient doses. This increase can be limited through the use of 'low dose' scanning protocols when a diagnostic quality CT scan is not required. When the transmission and emission scans are acquired sequentially, as is always the case with CT attenuation maps, significant artefacts can occur in the reconstruction as a result of mis-registration of the transmission and emission datasets (Goetze & Wahl 2007, Lautamaeki *et al.*. 2008, Martinez-Moeller *et al.*. 2007, McQuaid & Hutton 2008).

2.4.2 Attenuation Correction without Transmission Scanning

The ability to determine an attenuation map without the need for a separate transmission scan is an area of ongoing interest. Such a technique would not be subject to errors arising from the matching of the attenuation map and the emission data. It may also be suitable for the new generation of dedicated cardiac gamma cameras whose physical characteristics make the inclusion of a transmission scanning system difficult or impossible 2.1.1.1.

The simplest method of attenuation correction without a transmission scan is to assume a known body outline, which may be obtained by manually contouring the body outline or using automatic edge detection of the photopeak or scatter data (Zaidi & Hasegawa 2003). Here, a uniform attenuation coefficient can then be assigned to all points within the outline. Chang (1978) proposed a method of implementing such a correction using a known outline and known attenuation

coefficient. The basis of the correction considers each point within the image separately and calculates a correction factor at each point by comparing the filtered back-projection of the measured data with and without the effect of attenuation. When the imaged object is an extended source this method results in the over-correction of some areas and the under-correction of others, depending on the precise source distribution. A secondary correction can be performed to compensate for this by re-projecting the corrected image and subtracting the new projections from the corresponding original projection. An 'error image' can then be formed by filtered back-projection and corrected in the same way as the primary image. The final image is then obtained by adding the corrected 'error image' to the original corrected image. This process can be repeated for a number of iterations in order to further improve the reconstruction but one iteration is normally sufficient for the image to converge. However, the use of a uniform attenuation coefficient within a known outline is not suitable for cardiac studies due to the difference in attenuation between soft tissue and lung.

The use of scatter window measurements to determine a convex body outline has been proposed for the situation where a uniform attenuation coefficient can be used within the body outline (Ben Younes *et al.*. 1988). The extension of this technique, applied to lung imaging where photopeak data can easily be used to identify the lung boundary, has been found to be successful in producing a synthetic attenuation map using assigned attenuation coefficients for the lung and soft tissue regions (Núñez *et al.*. 2009, Bailey *et al.*. 2008). Pan *et al.*. (1997) proposed a further improvement in myocardial SPECT imaging using counts acquired in both the photopeak and scatter windows to semi-automatically identify both the body and lung outlines and then assigning average attenuation coefficients of 0.05 and 0.15 cm^{-1} to the segmented lung and soft-tissue regions respectively. The resulting attenuation map was smoothed using a Gaussian filter. A similar technique, implemented by Toshiba Medical Systems, has been shown to improve sensitivity to coronary artery disease in the left anterior descending artery territory and specificity in the right coronary artery territory (Yamauchi *et al.*. 2014). However, a number of difficulties with the technique were identified. The most significant of these was the difficulty in accurately identifying the lung boundary; particularly in cases with reduced difference in lung and soft tissue uptake and in larger patients where a reduced number of photons were detected. Furthermore, the use of a single value for lung attenuation, rather than a patient specific value (Van Dyk *et al.*. 1982), will increase the error in the estimation.

Bronnikov (1995) proposes an alternative method of estimating the outline of features within the attenuation map from the measured SPECT data. This approach uses a Maclaurin expansion to give a linearised approximation to the relationship between the SPECT data and the attenuation map at opposite detectors, resulting in a first order approximation to the attenuation map. The accuracy of the reconstruction is limited by the presence of large variations in the activity distribution as well as by circularly symmetrical attenuation, which limit the clinical applications for the technique.

The first statistical method to estimate both the activity distribution and attenuation map without the use of a transmission scan was proposed by Censor *et al.*. (1979). A pixel by pixel description of the image space is used to define the number of photons reaching each detector element d using Equation 2.10.

$$\boldsymbol{n}^* = \boldsymbol{A}(\boldsymbol{\mu})\boldsymbol{\lambda} \tag{2.10}$$

$\boldsymbol{n}^*$ is the vector of the number of photons detected in each detector element
$\boldsymbol{A}(\boldsymbol{\mu})$ is the transfer matrix including attenuation
$\boldsymbol{\lambda}$ is the activity distribution

Censor notes that the resulting system of equations for realistic situations is extremely large with $2N$ unknowns (where N is the total number of pixels) and that it is impossible to solve exactly due to effects such as measurement inaccuracy, noise corruption of the data and the discretisation in the model. Instead they propose solving the set of inequalities given by Equation 2.11 to identify values of $\boldsymbol{\lambda}$ and $\boldsymbol{\mu}$ which are 'close enough' to $\boldsymbol{n}^*$ to provide an acceptable solution to the recovery of the true activity distribution.

$$\boldsymbol{n}^* - \boldsymbol{\epsilon} \leq \boldsymbol{A}(\boldsymbol{\mu})\boldsymbol{\lambda} \leq \boldsymbol{n}^* + \boldsymbol{\epsilon} \tag{2.11}$$

$\boldsymbol{\epsilon}$ is a vector of suitable tolerances

This problem is described as a mixed convex-concave feasibility problem. Equation 2.10 can be considered to define a set of hypersurfaces for which $\boldsymbol{\lambda}$ and $\boldsymbol{\mu}$ have values which would result in the measured projection data $\boldsymbol{n}^*$. Each inequality defines a hyperslab which surrounds the corresponding hypersurface and represents an acceptable region in which $\boldsymbol{\lambda}$ and $\boldsymbol{\mu}$ must lie, hence, the intersection of all the hyperslabs defines the final acceptable values of $\boldsymbol{\lambda}$ and $\boldsymbol{\mu}$. A solution is found

using an iterative process which alternately compares the projections, using the current estimates of $\boldsymbol{\lambda}$ and $\boldsymbol{\mu}$, to the concave and convex surfaces of the inequality hyperslabs.Updates are performed to steps towards the inside of the hyperslab depending on the gradient of the difference between the inequality surface and the current projection estimate, using suitable regularisation parameters.

An alternative statistical method for estimating both the activity distribution and attenuation map from just emission measurements was proposed by Nuyts *et al.*. (1999) (see section 4.1.2 for further details). This method is based on the MLEM iterative reconstruction algorithm and an *a-priori* probability distribution using alternating iterations to update the activity distribution and attenuation map. A similar approach was considered by Krol *et al.*. (2001) using maximum likelihood estimation.

Crepaldi & De Pierro (2007) extended the work of Nuyts to try to eliminate the problem of cross talk between the activity and attenuation. They used the standard MLEM as the basis of the activity estimation and a Newton-Raphson method to maximise the attenuation map. The model was further refined by use of a multiplication factor in order to increase the absolute number of observations so that the problem was better determined. An iterative data refinement was used to further enhance the solution. The effect of this improved algorithm was demonstrated to reduce cross-talk between activity and attenuation cardiac phantom simulations. However, the resulting algorithm required large numbers of iterations to converge; of the order of 5 times greater than the original method for use of the multiplicative factor and 250 times higher when both the multiplicative factor and an iterative data refinement step were used.

Defrise *et al.*. (2012) investigated the use of the algorithm developed by Nuyts (Nuyts *et al.*. 1999) in PET imaging where time of flight information was available. This work demonstrated that the addition of the time of flight data significantly improved the quality of the reconstruction and enabled accurate reconstruction of the attenuation map for PET imaging.

Ramlau *et al.*. (2000) and Panin *et al.*. (2001) use approximations to the attenuated Radon transform as the basis of alternating iterative algorithms to simultaneously reconstruct the activity distribution and attenuation map. The approximation used by Ramlau is evaluated from the sum of a linear operator depending on $\boldsymbol{\lambda}$ and a bi-linear operator depending on $\boldsymbol{\lambda}$ and $\boldsymbol{\mu}$. Reconstruction

results were found to be highly dependent on the choice of the attenuation map used to initialise the reconstruction due to the presence of local minima. Cross-talk between the attenuation and activity reconstructions was also found to limit the quality of the reconstruction.

Panin *et al.*. (2001) uses 'Principal Component Analysis' with a knowledge set of existing attenuation maps. The attenuation map to be reconstructed approximated using the expansion of the eigenvectors of the cross-correlation matrix (limited to the largest eigenvalues) with the objective of finding the expansion coefficient for each of the eigenimages. The resulting set of linear equations is solved using a least squares approach with regularisation. The resulting algorithm was initially tested using computer simulations which found that accurate reconstruction was possible where strong constraints were used. However, in the reconstruction of patient studies the reconstruction of the lung regions was found to be poor.

Attempts to avoid cross-talk between the activity and attenuation reconstructions have been made by reconstructing the activity distribution and attenuation map separately. This type of reconstruction can be performed by using consistency conditions relating to the attenuated Radon transform. The method proposed by Natterer (1993) uses an affine distortion of an initial attenuation map using unknown distortion parameters to match the initial map to the required solution. This method showed good results for computer simulations using simple attenuation maps. Madsen & Lee (1999) have considered a method of using consistency conditions to improve an estimate of lung regions obtained from warping a reference image creating by averaging 50 PET transmission datasets. The resulting attenuation map was found to depend on both the initial lung estimates and the activity distribution showing that consistency conditions are not sufficient to accurately optimise an attenuation map where both the organ contours and attenuation are unknown.

In order to reduce the extent of the problem Bronnikov (1999) suggests the use of discrete consistency conditions, using a matrix representation in place of the continuous transform. This reduces the problem to a set of non-linear algebraic equations which can be solved to find $\boldsymbol{\mu}$ without reconstructing the activity distribution. In order to solve the set of non-linear equations an iterative search method is used with non-linear operators to constrain the attenuation coefficients to be greater than zero and to include information about the values of attenuation for

different tissue types. The change in attenuation at each step is determined using Newton methods; Tikhonov regularisation is used to control the size of each Newton step. Results of a reconstruction using computer simulated data indicate that the technique is able to reconstruct a number of regions within a body outline, although some smoothing occurs as a result of the regularisation. The algorithm also appears to be robust to noise in the measured projection data. The algorithm was also tested using real data acquired using a physical torso phantom. The resulting reconstruction provided acceptable accuracy in the reconstruction of the body outline and lung regions. However, a region of high attenuation corresponding to the spine was incorrectly located in the reconstruction, appearing significantly closer to the centre of the body than in the true phantom. The use of discrete consistency conditions has also been extended to three dimensions with similar results (Bronnikov 2000).

2.4.3 Attenuation Correction with Multi-spectral Emission Data

The use of more than one region of the emission spectrum has been investigated for potential methods of reconstructing a more accurate attenuation map without the use of a transmission scan. For SPECT studies that are acquired using radioactive isotopes with multiple energy photon emissions, there is a possibility to estimate an attenuation map using the differential attenuation of the photons. The likelihood of photon attenuation depends on the energy of the photon with low energy photons experiencing preferential attenuation. Since multiple energy isotopes emit photons at more than one discrete energy in a constant ratio, measurements of the relative size of the different photopeaks detected should, theoretically, enable an attenuation map to be recovered. Hansen & Siegel (1992) suggest a method of reconstruction using the high and low energy peaks from the decay of thallium-201 independently in order to allow the low-to-high count ratio, and hence an attenuation correction map, to be calculated. The use of this technique is limited by its high susceptibility to image noise and down scatter to the low energy window. Kaplan et al. (Kaplan *et al.*. 1999a, Kaplan & Haynor 1999, Kaplan *et al.*. 1999b) have developed a penalized weighted least squares iterative algorithm which uses differential attenuation information to simultaneously estimate both the activity distribution and attenuation map (Differential Attenuation Method, DAM). The results show improved accuracy of the

reconstructed images when using DAM as compared to using no attenuation correction or using a uniform attenuation correction. However it has not been tested with data including scatter which would have a significant effect on the accuracy of the reconstruction.

The use of measured scatter data in the reconstruction of an attenuation map has been suggested by Sitek *et al.*. (2007). The method proposed uses measurements of scatter photons made in several separate energy windows, assuming that all photons have only been scattered once. The probability of scatter within each of the windows is modelled using the current estimate of the activity distribution and knowledge of the Compton scattering angles that correspond to the measured photon energies. The algorithm was tested using a physical torso phantom and demonstrated good reconstruction of the phantom outline. The regions of the lung were also distinguished but the boundaries were not well defined.

2.5 The Effect of Scatter and Scatter Correction

As discussed in section 2.4, scatter of photons can contribute to the attenuation of the primary photon beam as scattering can alter the direction of travel of a photon and hence it will not be detected in the same place as it would have been in the absence of scattering. There are two types of scattering which can occur; coherent or Rayleigh and incoherent or Compton scattering. Coherent scattering involves virtually no loss of energy from the incident photon and results in only a very small change in angle. As a result photons which have undergone coherent scattering can often be included as part of the primary beam.

Compton scattering occurs when a photon interacts with an atomic electron. A fraction of the photon's initial energy is transferred to the electron and the direction of travel of the photon is altered. The angle through which the photon is scattered depends on the amount of energy that is transferred to the electron. The probability of scatter is given by the Klein-Nishina equation (Equation 2.12 (Zaidi 2006)) which gives the differential scattering cross section $d\sigma/d\Omega$ as a function of scattering angle, θ.

$$\frac{d\sigma}{d\Omega} = \frac{r_e^2}{2}(1+\cos^2\theta)\left[\frac{1}{1+\alpha(1-\cos\theta}\right]^2\left[1+\frac{\alpha^2(1-\cos\theta)^2}{[1+\alpha(1-\cos\theta)](1+\cos^2\theta)}\right] \quad (2.12)$$

$\alpha = E/m_o c^2$
r_e is the classical radius of the electron
E is the energy of the incident photon
m_o is the rest mass energy of the electron
c is the speed of light in a vacuum

Scatter may occur within the patient volume or outside the patient in the collimators, bed, detector or materials behind the detector. Once a photon has been scattered it may be directed away from the detectors and hence will not have any impact on the image quality other than as a result of attenuation (as discussed in section 2.4). However photons which originate both inside and outside the gamma camera field of view may be scattered such that they are directed toward one of the gamma camera detectors. The detection of scattered photons results in loss of contrast in the reconstructed image and prevents accurate quantitative measurements being made. The reason that scattered photons degrade image quality is because of the change of direction that occurs during the scattering process. This means that, unless scatter correction is performed, the detected scattered photon is assumed to have come from an emission site perpendicular to the point of detection and hence is incorrectly located during the reconstruction. During the image acquisition an energy window, centred on the photopeak, is used to exclude scattered photons which have undergone significant energy loss. The use of an energy window is a simple and effective way to reduce the effect of scatter; however, in myocardial imaging using ^{99m}Tc the ratio of scattered to unscattered counts recorded in the energy window is approximately 0.34 (Zaidi & Koral 2004). Scatter can, therefore, significantly affect image quality and an effective means of scatter correction is very important.

2.5.1 Scatter Correction Methods

In order to perform an accurate scatter correction a method of estimating the number of scattered photons that reach each detector bin is required. Zaidi & Koral (2004) and Hutton *et al.*. (2011) present reviews of scatter correction methods and discuss the technique of modelling scatter. The distribution of scattered photons will depend on both the activity distribution within the object and the attenuation of it. Existing scatter models can be broadly divided into two categories; those which use measurements of scatter (e.g. King *et al.*. 1997, Ogawa

et al.. 1991) and those which use a theoretical model of scatter, normally including a measurement of attenuation.

A relatively simple method of estimating attenuation from known scatter is the slab-derived scatter estimation (SDSE) method (Frey & Tsui 1993) which models the response of line sources embedded in slabs of material. The resulting scatter functions were modelled using a central Gaussian function with exponential tails and the parameters used to describe these functions were fitted as a function of the source depth. The distance from the collimator was also modelled allowing the slab based scatter function for any source depth and source to detector distance to be calculated. The scatter for more complex object shapes can then be approximated to an appropriately sized slab phantom and the scatter response function for that phantom calculated, provided the surface of the true object is convex. Use of the method with complex uniformly attenuating materials was found to significantly increase the accuracy of quantification. The method has also been successfully extended to three-dimensions (Beekman *et al.*. 1997). A further extension to the method has also been proposed (Frey & Tsui 1996) in order to improve the accuracy of the technique with Tl-201 SPECT and for objects with non-uniform attenuation; the effective source scatter estimation (ESSE).

Welch *et al.*. (1995) have proposed a method of modelling scatter which uses a Gaussian function, with factors derived from Monte Carlo simulation, to calculate the probability of a photon scattering through a given angle and still being detected in the photopeak window. The probability of scatter is assumed to be linearly dependent on the measured attenuation coefficient at the point of scatter. The calculated scatter factor is used to calculate the number of photons scattered within a given voxel from the number of photons entering the voxel (the sum of photons passing through the voxel corrected for attenuation). The number of scattered photons which go on to reach the detector is calculated, again correcting for attenuation. They note that the scatter probability is, in theory, a combination of the Klein-Nishina formula, the cross section for Compton scattering and the energy dependent detection probability of the gamma camera. However even if these items are accurately modelled there would still be a component from higher order scatter events and so they use the Gaussian function multiplied by attenuation coefficient rather than attempting a more accurate model of first order scatter. The scatter function is incorporated in a two-dimensional projector-backprojector and used with an MLEM algorithm in

order to reconstruct a scatter corrected activity distribution.

Walrand *et al.*. (1994) also use an approach where a single scatter event is modelled, however they use the Klein-Nishina formula to model scatter at this point and an effective attenuation coefficient prior to the point of scatter to account for photons which are scattered multiple times. This assumes that photons which have been scattered multiple times will not be detected in the photopeak energy window. The technique has been shown to produce accurate results for homogeneous phantoms where the object outline is accurately defined but has not been tested with inhomogeneous attenuation densities.

Meikle *et al.*. (1994) propose a transmission based scatter correction which is based on a convolution subtraction method. In this method the measured emission projection data are corrected (potentially iteratively) using scatter fractions calculated from experimentally derived factors and measured transmission data by performing a two dimensional convolution of the scatter fraction with the geometric mean of each projection pair. The use of the geometric mean of the projection data means that this technique was only applied to data acquired over 360^o. Hutton *et al.*. (1996) extend the convolution subtraction technique to allow it to be used with data that is collected over 180^o.

With the increase in computer capabilities in recent years Beekman *et al.*. (2002) have been able to develop a Monte Carlo based scatter correction technique for estimating scatter as part of an iterative reconstruction. In order to reduce the complexity of the calculation required, a dual matrix reconstruction technique is used, i.e. the transfer matrix used for the forward projection step includes attenuation, scatter and detector blurring while the back projection step includes only the effects of attenuation and detector blurring. Monte Carlo simulation is used for the forward projection step making use of convolution based forced detection, which makes use of an analytic detection model instead of a stochastic one in order to reduce the noise in the simulated projections. The speed of reconstruction is further improved by using variable numbers of photon histories, with fewer photons simulated in the initial iterations where the image detection does not need to be modelled so precisely. Photon histories from the previous iteration are also used in order to reduce the number of histories that need to be calculated at each step. The use of the Monte Carlo reprojection step was found to significantly reduce artefacts in the reconstructed images when compared to reconstruction without scatter correction and those with an scatter correction

using an approximate scatter function. Further methods of accelerating reconstruction using a Monte Carlo based forward projection step have been proposed, resulting in clinically realistic reconstruction times (of the order of a few minutes) (de Wit *et al.*. 2004, Sohlberg *et al.*. 2008).

2.6 Monte Carlo Simulation

When comparing a number of different reconstruction techniques it can be difficult to assess which offers the best overall image quality as the true solution may not be known. The use of software simulations allows image reconstruction algorithms to be tested using data where the correct solution is known and so the error in the reconstructed image can be quantified.

Monte Carlo methods are computer algorithms that use repeated random sampling in order to simulate a given system. In order to perform a Monte Carlo simulation of a system, probability density functions are required for the processes that occur in each part of the system. Provided that the probability density functions are accurately defined a Monte Carlo simulation can be performed by randomly sampling the distributions. The accuracy of the outcome parameters depends on the number of samples that are performed. Monte Carlo simulation allows accurate modelling of the processes within a system to provide realistic results whilst enabling individual parameters to be precisely controlled so that their effect can be examined.

In nuclear medicine imaging systems Monte Carlo simulation can be used to model each photon path. Each photon path begins with the emission of a photon which is calculated from the distribution of activity. From the point of emission the path length to the next point of interaction is calculated based on the energy of the photon and the density and composition of the material it is travelling through. At the interaction point the type of interaction that occurs is assigned to be either photo-electric, Compton scatter, coherent scatter or pair production based relative probabilities defined by the partial attenuation coefficients for each interaction type. For coherent and Compton scatter events the scattering angle is calculated based on the relevant cross-section; for Compton scatter the resulting energy of the photon is also calculated. Subsequent interaction points are calculated from the direction of travel from the first interaction point and the path

length in this direction. Repeated interactions are calculated until the photon reaches the detection system. The detection of a photon by the imaging system can also be modelled to include the effects of collimation, interactions within the scintillation crystal and the use of energy windows.

In this work the SIMIND Monte Carlo program (Ljungberg & Strand 1989), which simulates nuclear medicine medical imaging systems, has been used. The SIMIND code allows the user to choose different materials for the detector and cover and to input a range of different phantoms including direct input of the XCAT phantom (Segars *et al.*. 1999). Photoelectric, incoherent, coherent interactions and pair production are simulated within the phantom and detector parameters such as the energy pulse-height distribution and pulse pile-up due to finite decay time of the scintillation light emission, can be modelled. The energy resolution of the system is simulated by convolving the energy imparted with an energy-dependent Gaussian function. Collimators are also included in the simulation and can be selected from a file containing many clinical collimators or specified in terms of the acceptance solid angle. The maximum number of scatter events that occur and the energy window for detection can also be specified by the user.

3 Development of a Model for Measured Scatter Data

As discussed in Section 2.5 the probability of scatter occurring at a given point in an object is closely related to the linear attenuation at that point. It is therefore proposed that if scattered photons can be accurately modelled and measurements are made of scattered photons at the time of measuring the emission sinogram (i.e. a scatter sinogram is also recorded) then the emission and scatter sinograms can be used to jointly reconstruct both the activity distribution and attenuation map. In this chapter a model for first order scatter, which could be used as the basis of an algorithm to estimate the attenuation map from modelled and measured scatter, has been developed.

3.1 Theory

3.1.1 Basic Scatter Model Theory

The emission and subsequent scatter of photons prior to detection can be considered to be independent Poisson processes (Lewitt & Matej 2003) such that the measured emission sinogram ($\boldsymbol{n}^*$) is the sum of a sinogram without scatter ($\boldsymbol{n}^p$) and a sinogram which contains only scatter events ($\boldsymbol{n}^s$). During the scattering process photons lose energy and so measurements of the emission sinogram using an energy window centred on the photopeak energy normally contain only part of the scatter sinogram. A number of methods have been investigated which aim to estimate the contribution of $\boldsymbol{n}^s$ to the measured photopeak emission sinogram so that the contribution of scatter events can be removed from the measured emission sinogram either before or during image reconstruction. Here we aim

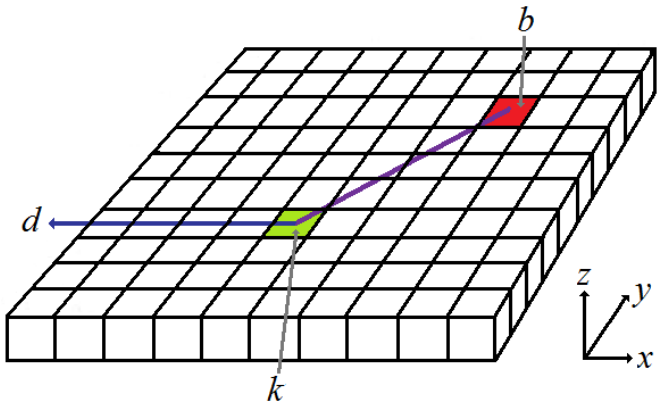

Figure 3.1: Illustration of the path of a scattered photon

to develop a model for scatter which can reproduce the distribution of scattered photons measured both in the photopeak window and in an energy window positioned below the photopeak.

The path of a scattered photons is illustrated in Figure 3.1 and can be considered to consist of 4 parts; the emission of a primary photon, the travel of the primary photon from the point of emission to the point of scatter, the scatter of the photon and the travel of the scattered photon from the point of scatter to the point of detection.

The photon is emitted from voxel b and travels along the path shown to voxel k. The probability of a photon being emitted in voxel b and travelling in the direction of voxel k depends on the activity in voxel b ($(\boldsymbol{\lambda})_b$) and the distance between the two voxels. The path length, R, between the two voxels is calculated from the voxel indices using Pythagoras' theorem. It is assumed that emission occurs at a point source located at the centre of the voxel and that the scatter voxel can be approximated by a sphere with volume equal to the volume of the cubic voxel, i.e. a sphere with radius $r = p/\sqrt[3]{\frac{3}{4\pi}}$, where p is the length of one side of the cubic voxel. The solid angle (Ω) subtended by the scatter voxel to the emission voxel can then be calculated using Equation 3.1a (Serway 1982), as illustrated in Figure 3.2. The fraction of the total number of photons emitted that are directed towards the scattering voxel (ω_{bk}) is found by dividing Ω by the

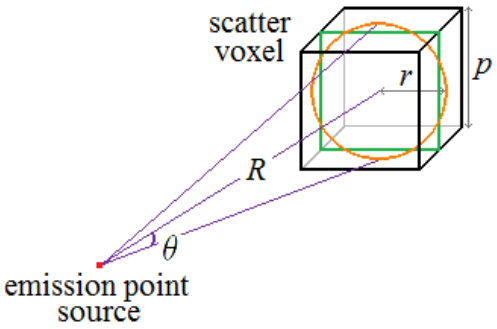

Figure 3.2: Illustration of the solid angle subtended by the scattering voxel to the emission source, approximated by a sphere

total solid angle of a sphere (4π) and is given by Equation 3.1b.

$$\Omega = 2\pi(1 - \cos\theta) \tag{3.1a}$$

$$\omega_{bk} = \frac{1 - \cos\theta}{2} \tag{3.1b}$$

$$\theta = tan^{-1}\left(\frac{r}{R}\right) \tag{3.1c}$$

The number of photons that reach the scattering voxel will also depend on the attenuation between the point of emission and the point of scatter. This can be calculated by using the Siddon method (Siddon 1985) to calculate the path from a given source voxel to all possible points of scatter, i.e. all other voxels within the matrix. The attenuation along the path is then the sum of the attenuation of each voxel along the path multiplied by the proportion of that voxel which the path intersects. In order to calculate the total number of photons reaching each scattering voxel from all sources of emission a sum over all emission voxels must be calculated. The speed of this computation can be improved by only calculating paths for source voxels b where the activity $(\boldsymbol{\lambda})_b$ is greater than zero. An alternative method of performing the same calculation is to rotate the matrices containing the emission and attenuation images to align each source and scatter voxel; however the process of rotating a matrix is slow and so the Siddon method offers a significant time saving.

For the 2-dimensional case (i.e. a single slice of voxels) the total number of photons, from all points of emission, arriving at each scattering voxel is stored with information about the initial direction of travel of the photons. This is done by

storing a set of 360 matrices corresponding to the number of photons arriving at each voxel travelling at each possible angle (rounded to the nearest degree). The probability of the photons arriving at each voxel being scattered towards the detector can be calculated using the Klein-Nishina formula (Equation 3.2 (Klein & Nishina 1929)).

$$\frac{\partial\sigma}{\partial\varepsilon} = \pi r_e^2 \frac{m_e c^2}{E_0}\left[\frac{1}{\varepsilon} + \varepsilon\right]\left[1 - \frac{\varepsilon \sin^2\theta}{1+\varepsilon^2}\right] \tag{3.2}$$

$\frac{\partial\sigma}{\partial\varepsilon}$ is the differential scattering cross-section
r_e^2 is the classical radius of an electron
$m_e c^2$ is the rest mass of an electron
$\varepsilon = \frac{E_1}{E_0}$
E_0 is the initial photon energy
E_1 is the energy of the scattered photon

Where the angle of scatter, θ, is determined by the change in energy of the photons according to the Compton formula (Equation 3.3 (Serway 1982)).

$$\Delta\lambda = \frac{h}{m_e c}(1 - \cos\theta) \tag{3.3}$$

$\Delta\lambda = \frac{hc}{\Delta E}$, is the change in wavelength of the photon
ΔE is the corresponding change in energy
h is Plank's constant
c is the speed of light in a vacuum

Figure 3.3 shows the relative probability of a photon being scattered through a given angle, assuming a wide energy window so that all scattered photons are detected. After the relative probability of scatter through the angle required for the photons to reach the detector has been calculated the total probability of scatter occurring is determined using the the linear attenuation coefficient at the point of scatter. The probability of a photon not being attenuated as it travels through the scattering voxel is given by the Beer-Lambert Law (Equation 3.4a) and so the probability of scattering is given by Equation 3.4b; this assumes that the proportion of photons which are attenuated by processes other than Compton scattering is negligible. This assumption can be justified by considering the Hubbell data (Hubbell 1969) for physiologically relevant compounds at energies corresponding to common gamma emitters. For example the attenuation of water

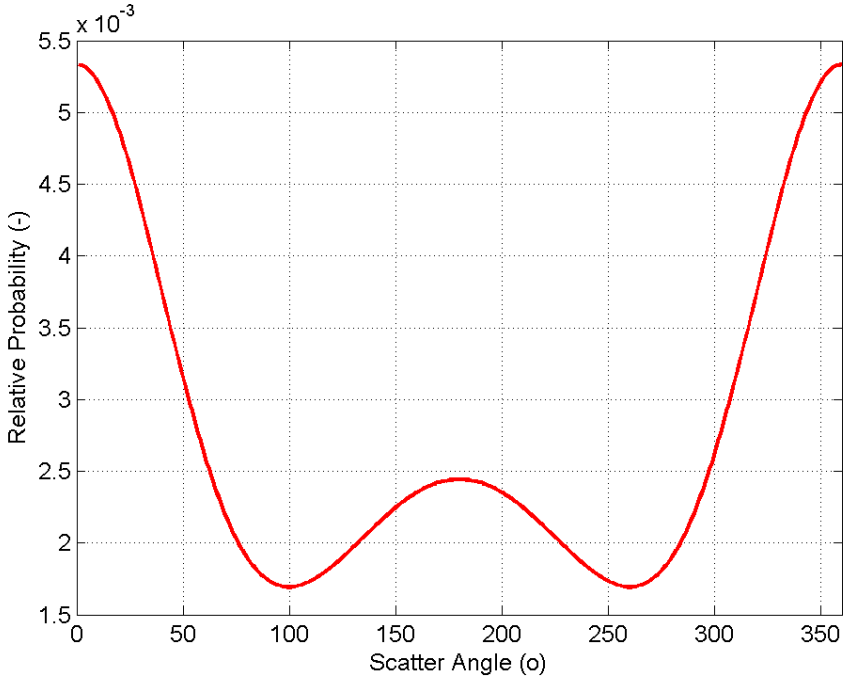

Figure 3.3: Relative Klein-Nishina probability of a photon being scattered through a given angle

at 150keV is 0.151cm^{-1} with attenuation due to Compton scatter of 0.148cm^{-1}.

$$p(survival) = \exp(-(\boldsymbol{\mu})_k x) \tag{3.4a}$$

$$p(scatter) = 1 - \exp(-(\boldsymbol{\mu})_k x) \tag{3.4b}$$

$(\boldsymbol{\mu})_k$ is the linear attenuation coefficient of scattering voxel k
x is the path length through a voxel

The contribution of photons which are scattered in the same voxel as they are emitted (i.e. where $b = k$) must also be considered. In this case the probability of scatter is the same for all directions, since there is an equal probability of emission for all directions. The voxel is again approximated to a sphere with the same volume as the cubic voxel and the point of emission is assumed to be a point source located at the centre of the voxel. The probability of a photon travelling in a direction within the slice of interest can be calculated using Equation 3.5a as the solid angle subtended by the area of a ring around the centre of the voxel at a distance equal to the spherical radius of the voxel which has a height equal to the radius of the equivalent sphere (see Figure 3.4). The total probability of scatter is again found using the Beer-Lambert Law (Equation 3.4b) but in this

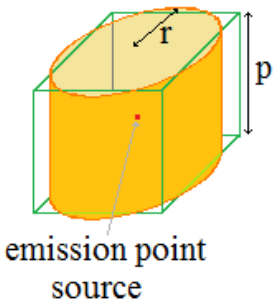

Figure 3.4: Illustration of the solid angle subtended by the surface exiting a voxel within a given slice of voxels where the point of emission is within the scattering voxel which is approximated by a sphere

case the distance travelled by the photon is not equal to the size of the voxel; it is the distance from the point of emission to the edge of the sphere (i.e. the radius of the sphere $= p/\sqrt[3]{\frac{3}{4\pi}}$). The probability of scatter is then multiplied by the number of photons emitted in the voxel and added to the number of scattered photons calculated as described in the preceding paragraphs.

$$\Omega = \frac{A}{r^2} \tag{3.5a}$$

$$\Omega = \frac{2\pi r \cdot r}{r^2} \tag{3.5b}$$

$$\omega = \frac{\Omega}{4\pi} \tag{3.5c}$$

$$\omega = 0.5 \tag{3.5d}$$

The final part of the scatter model is then to calculate the attenuation from the point of scatter to the point of detection for each detector angle, this calculation has been performed using a rotation based projector. After scattering photons have reduced energy and so will experience increased attenuation. This effect has been ignored in the basic scatter model but is considered in Chapter 5.

The complete basic scatter model ($\boldsymbol{s}(\boldsymbol{\mu})$) is given by Equation 3.6.

$$\boldsymbol{s}(\boldsymbol{\mu}) = \boldsymbol{A_d}(\boldsymbol{\mu})\boldsymbol{S_k}(\boldsymbol{\mu})\boldsymbol{A_k}(\boldsymbol{\mu})\boldsymbol{\phi} + \boldsymbol{A_d}(\boldsymbol{\mu})\boldsymbol{S_b}(\boldsymbol{\mu})\boldsymbol{\phi} \tag{3.6}$$

$$\boldsymbol{\phi} = \boldsymbol{Q} \otimes \boldsymbol{\lambda} \tag{3.7a}$$

$$(\boldsymbol{A_k})_{bjk} = \omega_{bk} \exp\left[-\int_b^k \boldsymbol{\mu}(x)\mathrm{d}x\right] \tag{3.7b}$$

$$(\boldsymbol{S_k})_{kjj'} = (1 - e^{(\boldsymbol{\mu})_k})N_{jj'} \tag{3.7c}$$

$$(\boldsymbol{S_b})_{bkjj'} = \begin{cases} 0.5\left(1 - e^{-(\boldsymbol{\mu})_k \sqrt[3]{\frac{3}{4\pi}}}\right), & b = k \\ 0 & b \neq k \end{cases} \tag{3.7d}$$

$$(\boldsymbol{A_d})_{kj'd} = c_{kj'd} \exp\left[-\int_k^d \boldsymbol{\mu}(x)\mathrm{d}x\right] \tag{3.7e}$$

$(\lambda)_b$ gives the activity in voxel b.

$\boldsymbol{Q}$ is the emission function and gives the proportion of photons emitted within a solid angle defined by Ω_j. $\boldsymbol{Q}$ is isotropic and could define an infinite number of directions j.

$\boldsymbol{\phi}$ gives the number of photons emitted from each voxel b travelling in each direction j; this is a block vector with B blocks each of length J.

$\boldsymbol{A_k}$ is the attenuated transfer matrix giving the probability of a photon emitted from voxel b reaching voxel k; this is a block matrix with B by K blocks, each block is a J by J diagonal matrix since the transfer matrix is not associated with a change in direction.

$\boldsymbol{S_k}$ is the probability of a photon scattering in voxel k from direction j (defined by the positions of b and k) to direction j' (defined by the positions of k and d); this is a K by K block diagonal matrix where each block has J by J' elements.

$N_{jj'}$ is the Klein-Nishina probability of scattering from direction j to j'.

$\boldsymbol{S_b}$ is the probability of scattering occurring in the same voxel as the emission; this is a B by K block diagonal matrix where each block has J by J' elements.

$\boldsymbol{A_d}$ is the attenuated transfer matrix giving the probability of a photon scattered in voxel k reaching detector element d; this is a block matrix with K by D blocks, each block is a J' by J' diagonal matrix since the transfer matrix is not associated with a change in direction.

$c_{kj'd}$ gives contribution of geometric effects to the probability of a photon from voxel k, travelling in direction j', reaching detector d.

3.1.2 Effect of Energy Resolution

The Klein-Nishina formula predicts the number of photons that will be scattered through a given angle which can be related to the change in photon energy using the Compton scatter formula. In reality the effect of the energy resolution of the gamma camera is that photons scattered through a given angle are not detected with a single discrete energy but with a spread of energies. The energy resolution of a gamma camera depends on the incident energy of the photons and normally results in the photopeak having a full width at half maximum (FWHM) of approximately 10% at 140keV. The FWHM will vary with incident photon energy, however a simplified model which uses an energy resolution of 10% at all energies has been used in this work.

In order to include this effect in the calculation of the probability of detecting a photon which has been scattered through a given angle, the Klein-Nishina probabilities calculated using Equation 3.2 are converted to energy using the Compton formula (Equation 3.3). Each point on this curve is then blurred using a Gaussian with an area of unity and FWHM equal to the energy resolution of the gamma camera at that point e.g. for a camera with an energy resolution of 10% at 100keV the FWHM will be 10keV, and at 50keV the FWHM will be 5keV. The number of photons that are scattered through a given angle and are detected in the selected energy window is then found by calculating the integral of the blurred curve, for the given angle, with the integration limits set by the selected energy window.

The effect of the energy window on the detection of photons which are scattered in the same voxel as they are emitted must also be considered. In this case the number of scattered photons which are detected in the given energy window is calculated as a fraction of the total number of scattered photons, taking into account the energy resolution as described above. The number of photons which are scattered in the emission voxel can then be calculated as before and multiplied by this detection fraction.

3.2 Method

The accuracy of the scatter model has been tested by comparing sinograms estimated using the model to those generated using the SIMIND Monte Carlo programme (Ljungberg & Strand 1989) for a number of different phantoms. Each phantom included a 2-dimensional activity distribution in order to simplify the calculation of the scatter distribution; the phantoms used are shown in Figure 3.5. The first phantom contains a slab of uniform attenuation and a point source of emission, which is located outside the region of attenuation. The second phantom has a similar attenuation distribution and a point source of emission but in this case the emission source is located just inside the region of attenuation. In the final case the male XCAT phantom (Segars *et al.*. 1999) (formerly known as the NCAT phantom) is used to provide both the activity and attenuation. The XCAT phantom allows the user to generate activity distributions and attenuation maps at different phases of the cardiac and respiratory cycles and with different activities for male and female phantoms; in this work a male XCAT phantom without respiratory or cardiac motion with the arms raised above the head has been used.

In each case activity was present only in the slice of interest but the attenuation extended through the full simulation volume in the Monte Carlo simulations, this was to avoid potential artefacts caused by photons passing along the edge of the single slice of interest. The Monte Carlo simulation used a high detector resolution and the estimated sinograms assumed perfect detector resolution. Measurements were simulated and estimated for four detector positions which were at 90^o to each other as indicated in Figure 3.5. Initially the model was tested for an open energy window so that the effect of the energy resolution of the detector could be ignored. Similar scatter sinograms were then calculated using an energy window of 80keV to 126keV including a detector energy resolution of 10% in both the Monte Carlo simulation and the scatter model. All the estimated and simulated sinograms excluded the contributions of primary photons and of photons which had been scattered more than once.

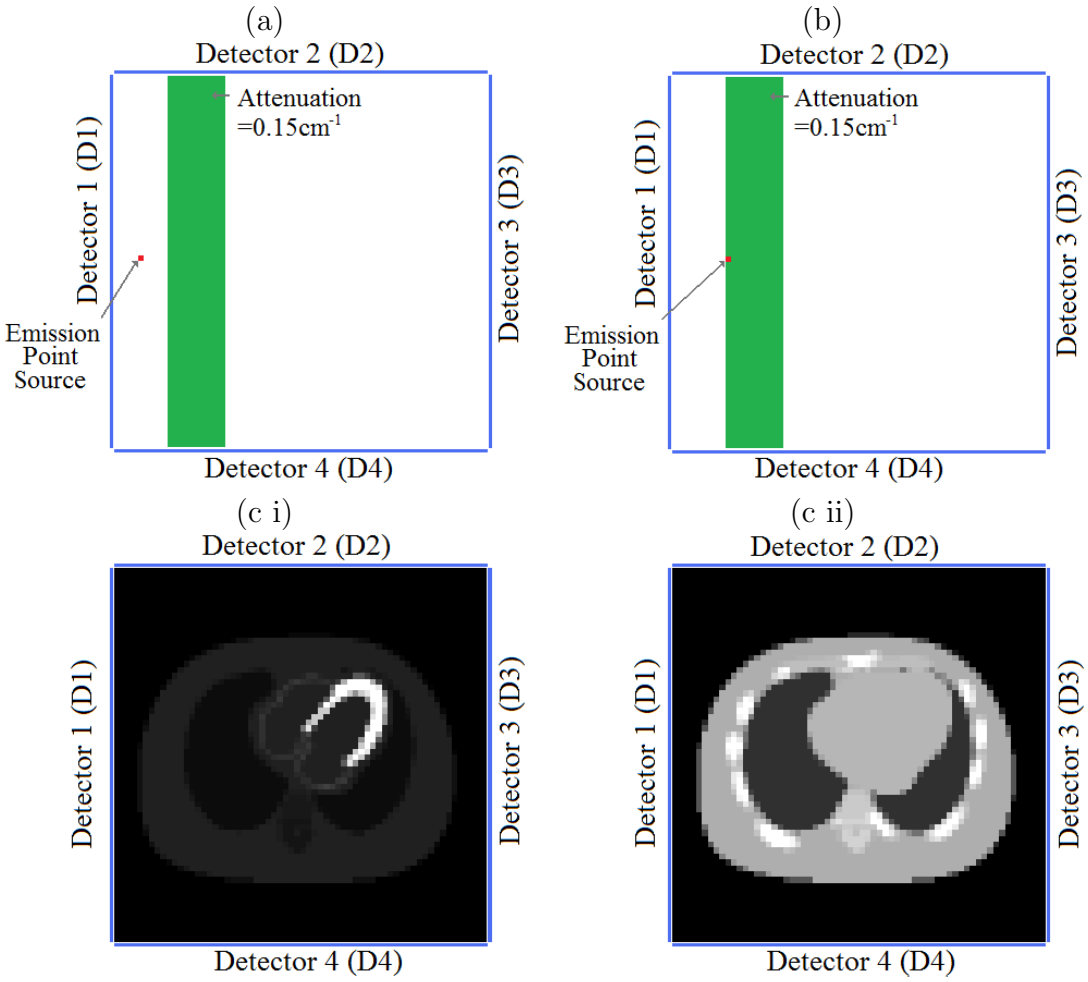

Figure 3.5: Phantoms used to test basic scatter model. (a) Attenuation slab with external point source, (b) attenuation slab with internal point source, (c) XCAT phantom (i) activity and (ii) attenuation

3.3 Results

Figure 3.6 shows the profile of the sinograms generated using the SIMIND programme for each phantom with the sinograms calculated using the scatter model derived in Section 3.1.1. The sinograms calculated using the scatter model have been normalised to have the same mean value as the corresponding Monte Carlo simulation. The result of this is a scaling factor which is required to account for differences in the sensitivity of detection for the scatter model and the Monte Carlo simulations. Table 3.1 shows the scaling factor calculated for each of the simulation set-ups.

Figure 3.7 shows the scattered sinograms calculated and simulated for an energy

(a)

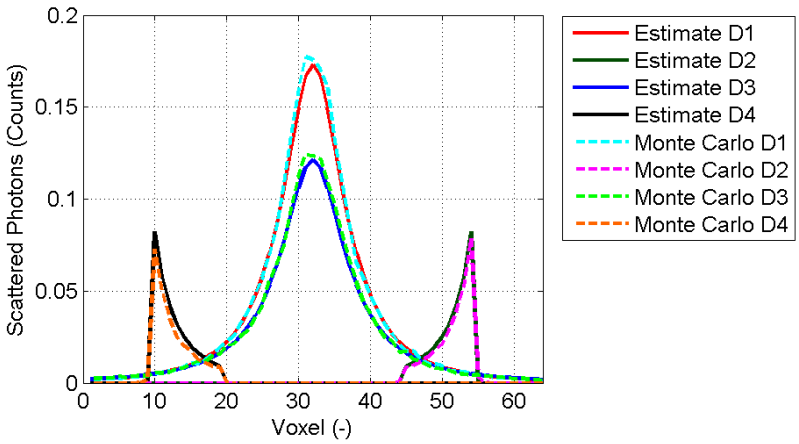

(b)

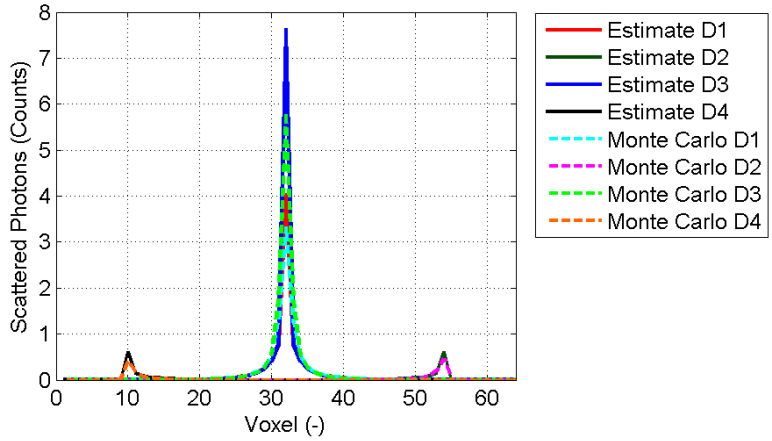

(c)

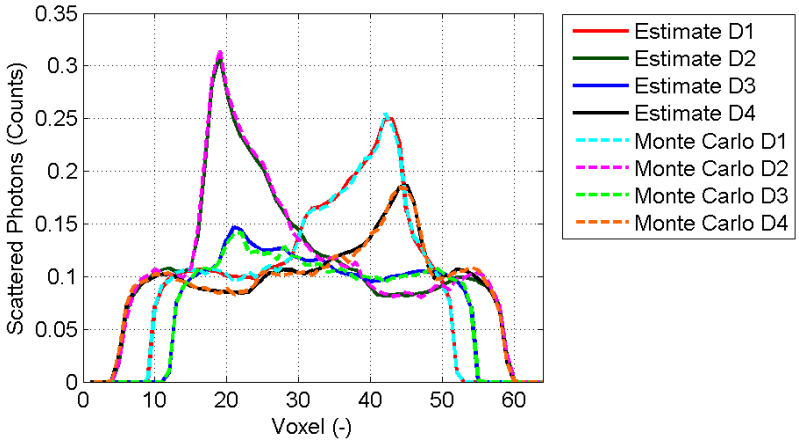

Figure 3.6: Sinograms estimated for an open energy window using the basic scatter model and simulated using the SIMIND Monte Carlo programme for (a) an attenuation slab with external point source, (b) an attenuation slab with internal point source, (c) XCAT phantom activity and attenuation

	Normalisation Factor
Attenuation slab, external point source	1.52
Attenuation slab, internal point source	1.49
NCAT phantom	2.50

Table 3.1: Normalisation factors calculated for calculated sinograms compared to simulated sinograms

Phantom	80-126keV Window	Open Energy Window
Attenuation slab, external point source	0.1568 (0.0875)	0.0574 (0.0846)
Attenuation slab, internal point source	0.0021 (0.0182)	0.0012 (0.0090)
NCAT phantom	0.0033 (0.0897)	0.0022 (0.0493)

Table 3.2: Root mean square error for calculated sinograms compared to simulated sinograms in an open energy window and an 80-126keV energy window including energy resolution effects; the mean value for the simulated sinogram is given in brackets for comparison.

window of 80keV to 126keV, with an energy resolution of $\pm 10\%$ using each of the phantoms illustrated in Figure 3.5. The calculated sinograms have again been normalised to have the same mean value as the corresponding Monte Carlo simulation. The mean and root mean square errors in the estimated projection data are shown in Table 3.2. These results show good agreement between the simulated and calculated results.

3.4 Discussion

The normalised sinograms show that the distribution of scatter events calculated using the scatter model is very similar to the Monte Carlo simulation data in the two dimensional case. However, there is some difference in the number of scatter counts originating within the scattering voxel compare to those originating in a different voxel. The effect of this is that the contribution of scatter events occurring outside the emission voxel is too small compared to the contribution of scatter events occurring in the emission voxel. This can be seen most clearly in the estimation of the sinogram for a point source within a slab of attenuation where the peak is overestimated in all projections compared to Monte Carlo simulation even after the total number of counts has been normalised to the same value in both the simulated and estimated projection data (Figure 3.6b).

(a)

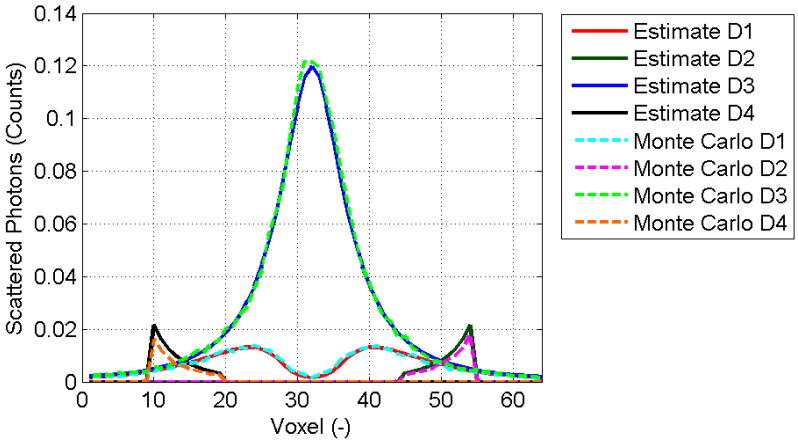

(b)

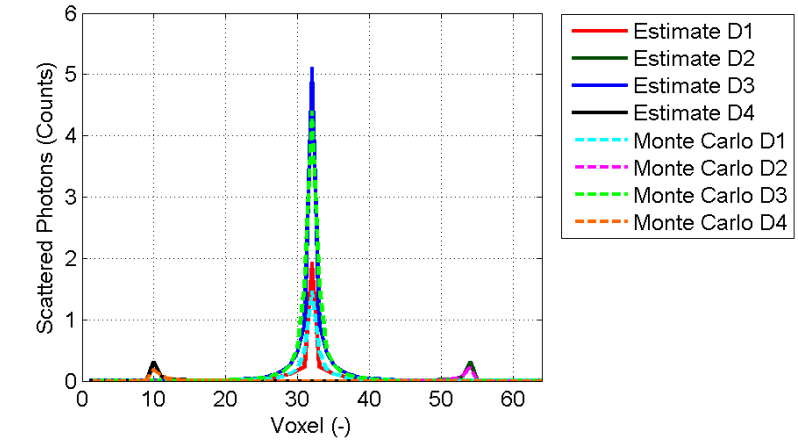

(c)

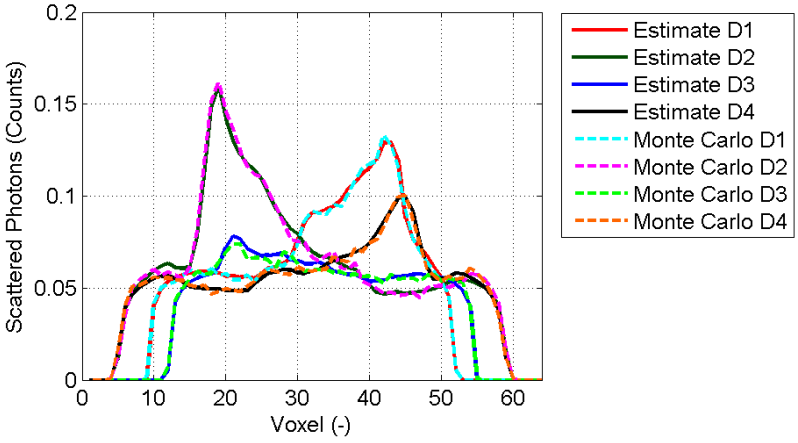

Figure 3.7: Sinograms estimated for a typical scatter energy window including effect of energy resolution, using the basic scatter model and simulated using the SIMIND Monte Carlo programme for (a) an attenuation slab with external point source, (b) an attenuation slab with internal point source, (c) XCAT phantom activity and attenuation

The overall result is that the scaling factor required to match the number of scatter events calculated for the XCAT phantom to the number simulated using Monte Carlo. It has been shown that the effect of camera energy resolution on the measurement of scattered photons within a given energy window can be accurately incorporated into the model of the detection of scatter by blurring the calculated Klein-Nishina scattering probabilities.

The existing model presented here includes a number of approximations which may limit the accuracy of the reconstruction that can be obtained when using the scatter model as the basis of an attenuation reconstruction algorithm. Firstly, the solid angles used to calculate the number of photons that reach each voxel from each possible emission location have been calculated using an assumption that the activity is located at a point at the centre of the emission voxel. It has also been assumed that the voxel where scattering occurs presents a circular area to the emission voxel, such that the volume of the sphere is the same as the volume of the cubic voxel. These approximations can be considered to be accurate for scatter voxels which are far from the point of emission; however for voxels which are close to the emission voxel (particularly the nearest neighbours) the approximations may not be an accurate representation of the true geometry and hence may introduce errors into the scatter model.

An empirically derived scaling factor has been used to normalise the scatter distribution estimated using the model presented here, to the same mean value as the scatter distribution found from the SIMIND Monte Carlo simulation. The primary purpose of this scaling factor is to account for the sensitivity of the gamma camera simulated by the Monte Carlo code. However, it also helps to compensate for inaccuracies in the scatter model.

3.5 Conclusion

An accurate 2-dimensional model for first order scatter has been developed. The accuracy of the model has been shown to be good for different phantoms and energy windows, including the effect of the energy resolution of the gamma camera, when compared to scatter distributions created using Monte Carlo simulation.

Further work is required to extend the model to 3 dimensions and to improve the accuracy of the estimation of scatter from voxels close to the point of emission

compared to the point source approximation used in the model presented here.

4 Estimation of Attenuation from Measured SPECT data

In the work outlined in this chapter a new method of estimating an attenuation map directly from measured SPECT data has been developed. The algorithm uses the model for scatter presented in Chapter 3 to provide an estimate of the expected scatter distribution, based on a current estimate of both the activity distribution and attenuation map, which is compared to the measured scatter distribution. The inclusion of additional information available about the attenuation of the imaged object, from the measured photopeak data, to improve the accuracy of the attenuation map compared to the use of scatter data alone has also been investigated.

4.1 Theory

4.1.1 Reconstruction of Attenuation Map using Scatter Data

If $(\boldsymbol{s}(\boldsymbol{\mu}))_d$ is the expected number of scatter events detected in detector element d, then the log-likelihood (L^s) for the observed scatter sinogram and a given (or estimated) activity distribution can be derived to be that given by Equation 4.1, c.f. derivation of Equation 2.4. The current estimate of $\boldsymbol{\mu}$ can then be updated by maximising the gradient of the likelihood function.

$$L^s(\boldsymbol{\mu}) = \sum_d \left(-(\boldsymbol{s}(\boldsymbol{\mu}))_d + (\boldsymbol{n}^s)_d \cdot \ln(\boldsymbol{s}(\boldsymbol{\mu}))_d\right) \tag{4.1}$$

$\boldsymbol{n}^s$ is the measured scatter projection data

The scatter model developed in Section 3.1.1 can be substituted into the likelihood function and differentiated with respect to $\boldsymbol{\mu}$ in order to maximise the likelihood.

$$\frac{\partial L^s(\boldsymbol{\mu})}{\partial \mu_i} = \sum_d \left(-\frac{\partial (\boldsymbol{s}(\boldsymbol{\mu}))_d}{\partial \mu_i} + \frac{(\boldsymbol{n}^s)_d}{(\boldsymbol{s}(\boldsymbol{\mu}))_d} \cdot \frac{\partial (\boldsymbol{s}(\boldsymbol{\mu}))_d}{\partial \mu_i} \right) \tag{4.2}$$

$$\begin{aligned} \frac{\partial (\boldsymbol{s}(\boldsymbol{\mu}))_d}{\partial \mu_i} = {} & \frac{\partial \boldsymbol{A_d}(\boldsymbol{\mu})}{\partial \mu_i} \boldsymbol{S_k}(\boldsymbol{\mu}) \boldsymbol{A_k}(\boldsymbol{\mu}) \boldsymbol{\phi} + \boldsymbol{A_d}(\boldsymbol{\mu}) \frac{\partial \boldsymbol{S_k}(\boldsymbol{\mu})}{\partial \mu_i} \boldsymbol{A_k}(\boldsymbol{\mu}) \boldsymbol{\phi} \\ & + \boldsymbol{A_d}(\boldsymbol{\mu}) \boldsymbol{S_k}(\boldsymbol{\mu}) \frac{\partial \boldsymbol{A_k}(\boldsymbol{\mu})}{\partial \mu_i} \boldsymbol{\phi} + \frac{\partial \boldsymbol{A_d}(\boldsymbol{\mu})}{\partial \mu_i} \boldsymbol{S_b}(\boldsymbol{\mu}) \boldsymbol{\phi} + \boldsymbol{A_d}(\boldsymbol{\mu}) \frac{\partial \boldsymbol{S_b}(\boldsymbol{\mu})}{\partial \mu_i} \boldsymbol{\phi} \end{aligned} \tag{4.3}$$

In order to simplify the algorithm each scatter path can be considered to have three distinct parts, each of which depend on the attenuation coefficient along that section of the path. The three parts comprise: the portion of the path from the point of emission up to the point of scatter, the point of scatter itself and the portion of the path from the point of scatter to the point of detection. The effect of changing the attenuation coefficients before and after the point of scatter can be assumed to be small compared to the effect of changes to the coefficient at the point of scatter and so they can be assumed to be constant for a given iteration. That is, only the attenuation at the point of scatter is updated by a given iteration although the new attenuation map is then used to calculate the attenuation along each part of the path in the next iteration. This approach leads to a 'one-step late' iteration process which is much simpler to calculate for each iteration and hence results in significantly reduced calculation times. Sitek *et al.*. (2007) use a similar 'one-step late' approach to estimate an attenuation map from measurements of scatter using knowledge of the relationship between Compton scattering angle and the change in energy of the incident photon to predict how many photons are detected in energy windows positioned below the photopeak.

When using the 'one-step late' approach the gradient of expected number of scatter events becomes:

$$\frac{\partial (\boldsymbol{s}(\boldsymbol{\mu}))_d}{\partial \mu_i} \approx \boldsymbol{A_d}(\boldsymbol{\mu}) \frac{\partial \boldsymbol{S_k}(\boldsymbol{\mu})}{\partial \mu_i} \boldsymbol{A_k}(\boldsymbol{\mu}) \boldsymbol{\phi} + \boldsymbol{A_d}(\boldsymbol{\mu}) \frac{\partial \boldsymbol{S_b}(\boldsymbol{\mu})}{\partial \mu_i} \boldsymbol{\phi} \tag{4.4}$$

The differentiation is achieved by calculating a series of partial derivatives for each scatter point k, these are then used to update the current estimate of $\boldsymbol{\mu}$ (Equation 4.5) with a step size α_s which is set manually. This algorithm is referred to as the Scatter based Maximum Likelihood Gradient Ascent (SMLGA) algorithm.

$$(\boldsymbol{\mu}^{i+1})_k = (\boldsymbol{\mu}^i)_k + \alpha_s \cdot \sum_d \left(- \sum_b D'_{bd}(\boldsymbol{\mu}^i, k) + (\boldsymbol{n}^s)_d \cdot \frac{\sum_b D'_{bd}(\boldsymbol{\mu}^i, k)}{(\boldsymbol{s}(\boldsymbol{\mu}))_d} \right) \tag{4.5}$$

$$\begin{aligned} D'_{bd}(\boldsymbol{\mu}^i, k) = \sum_{b \neq k} \Bigg[& (\boldsymbol{\phi})_b \omega_{bjk} \exp\left[- \int_b^k \boldsymbol{\mu}(x) \mathrm{d}x \right] \\ & c_{kj'd} \exp\left[- \int_k^d \boldsymbol{\mu}(x) \mathrm{d}x \right] N_{jj'} e^{-(\boldsymbol{\mu}^i)_k} \Bigg] \\ & + \sqrt[3]{\frac{3}{4\pi}} \frac{(\boldsymbol{\lambda})_{b=k}}{2} c_{kj'd} \exp\left[- \int_k^d \boldsymbol{\mu}(x) \mathrm{d}x \right] e^{-(\boldsymbol{\mu}^i)_{b=k} \sqrt[3]{\frac{3}{4\pi}}} \end{aligned} \tag{4.6}$$

4.1.1.1 Non-uniform imaging geometries

In cases where the measurement system does not sample the image volume uniformly the update to the estimate of the attenuation map at each point will be affected by the extent to which each voxel is under or over-sampled by the measurement system, which can result in instability in the reconstruction. In order to compensate for this, and prevent over correction of under-sampled regions, a normalisation factor ($\boldsymbol{\chi}$) has been introduced. The normalisation factor has been defined to be the number of photons that would be detected at each measurement location in the absence of an effect relating to attenuation at the point of scatter. The normalised scatter update algorithm is given by Equation 4.7.

$$(\boldsymbol{\mu}^{i+1})_k = (\boldsymbol{\mu}^i)_k + \frac{\alpha_s}{(\boldsymbol{\chi})_{kd}} \cdot \sum_d \left(- \sum_b D'_{bd}(\boldsymbol{\mu}^i, k) + (\boldsymbol{n}^s)_d \cdot \frac{\sum_b D'_{bd}(\boldsymbol{\mu}^i, k)}{(\boldsymbol{s})_d} \right) \tag{4.7}$$

$$(\boldsymbol{\chi})_{kd} = \sum_{b \neq k} \Bigg[(\boldsymbol{\phi})_b \omega_{bjk} \exp\left[-\int_b^k \boldsymbol{\mu}(x)\mathrm{d}x \right] \cdot c_{kj'd} \exp\left[-\int_k^d \boldsymbol{\mu}(x)\mathrm{d}x \right] N_{jj'} \Bigg] + \sqrt[3]{\frac{3}{4\pi}} \cdot \frac{(\boldsymbol{\lambda})_{b=k}}{2} \cdot c_{kj'd} \exp\left[-\int_k^d \boldsymbol{\mu}(x)\mathrm{d}x \right] \quad (4.8)$$

4.1.1.2 Joint Reconstruction of Activity and Attenuation

In order to jointly estimate the activity distribution and attenuation map from measurements of primary photons in a photopeak window and scattered photons in a lower energy window iterations of the traditional MLEM algorithm and SMLGA algorithm are alternated as described by Figure 4.1.

4.1.2 Reconstruction of Attenuation Map using Emission Data

As discussed in Section 2.4.2 the photopeak emission sinogram also includes information about the attenuation of the object being imaged. Nuyts *et al.*. (1999) have proposed a maximum likelihood algorithm (MLAA) to simultaneously estimate activity and attenuation distributions from an emission sinogram. In order to reconstruct the activity distribution iterations of the MLEM algorithm (as derived in Section 2.3, Equation 2.7) are used. The attenuation map is updated using a gradient-ascent maximum likelihood algorithm (Equation 4.9) derived by Nuyts. Steps to update the activity distribution and attenuation map are alternated (as in the MLEM-SMLGA algorithm) so that the current estimate of the activity distribution is used in one iteration to update the estimate of the attenuation map which is then itself used in the next iteration to update the activity distribution.

$$(\boldsymbol{\mu}^{i+1})_b = (\boldsymbol{\mu}^{i})_b + \frac{\alpha_p}{\eta \sum_d q_{bd}} \cdot \sum_d q_{bd} \left(1 - \frac{(\boldsymbol{n}^*)_d}{\sum_{b'} (\boldsymbol{A}_0)_{b'd} (\boldsymbol{\lambda})_{b'}} \right) \quad (4.9)$$

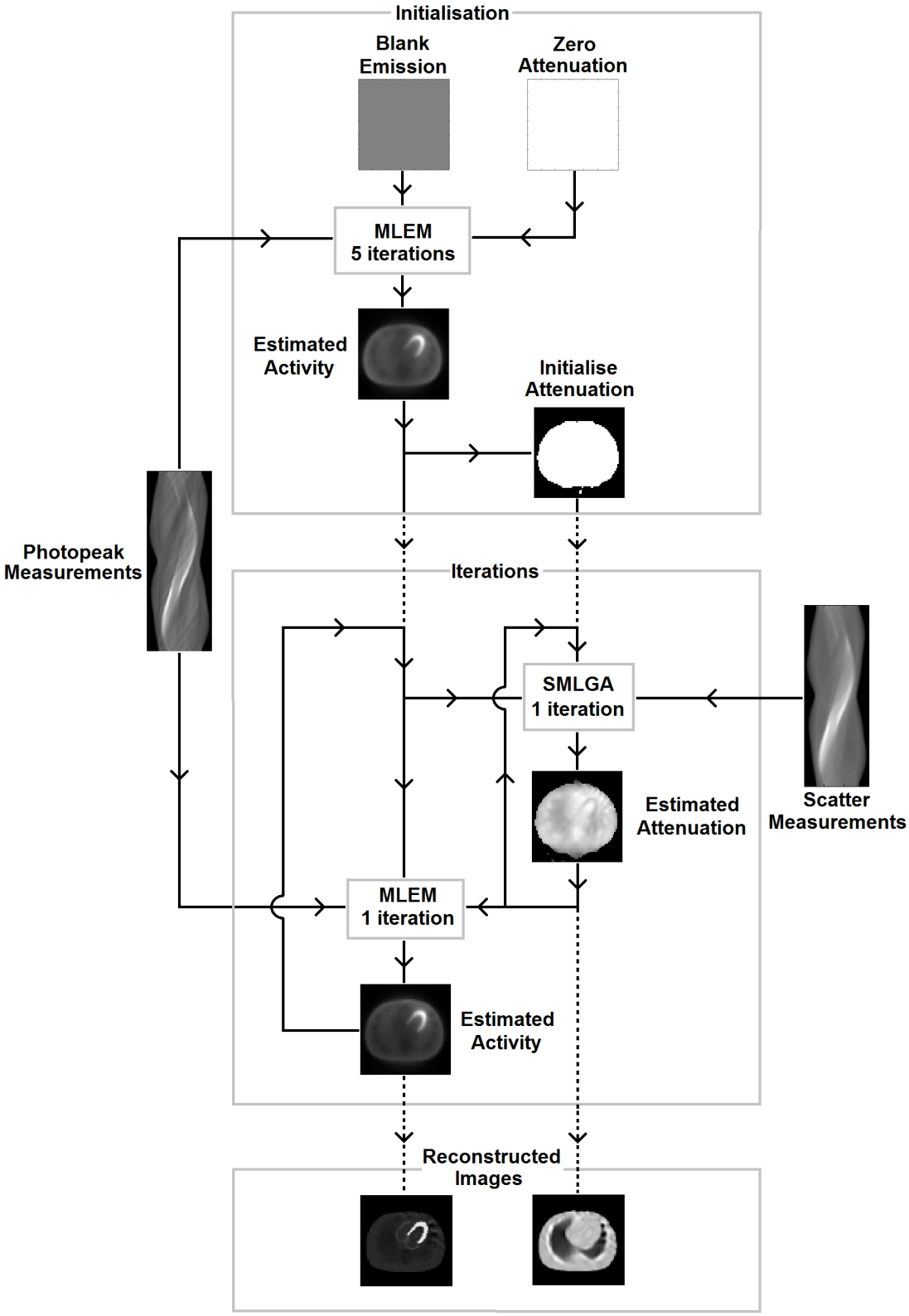

Figure 4.1: Combined MLEM-SMLGA algorithm for the joint estimation of activity and attenuation from measured scatter and photopeak data

$$q_{bd} = \sum_{b'} (\boldsymbol{A}_0)_{b'd} x_{b'ld} (\boldsymbol{\lambda})_{b'} \tag{4.10}$$

α_p is a relaxation parameter
η is the diameter of the reconstruction area
$x_{b'ld}$ is the intersection length of the path from b' to d with voxel l

In order to improve the joint estimation some *a priori* knowledge can also be included in the algorithm. Projection lines which contain no activity can give no information about the attenuation coefficients resulting in missing attenuation data. Nuyts et al. assumed that there is activity uptake within the skin, and that noise can be neglected, and so projection lines with zero activity correspond to regions outside the body and therefore have zero attenuation. A small constant value is, therefore, subtracted from the attenuation coefficients of pixels within these projection lines which has the effect of forcing the attenuation coefficient towards zero outside the region containing most or all of the activity.

A priori information about the attenuation coefficients can be included in the form of a multi-modal probability distribution, thus assuming that only typical values for the attenuation of soft tissue, air, bone and the lungs will be found (Equation 4.11); in the presence of noise a 2D Gibbs distribution can also be used in order to encourage local smoothness ($M_s(\vec{\boldsymbol{\mu}})$; Equation 4.12).

$$\frac{\partial M_a(\boldsymbol{\mu} \mid \bar{\mu}_g, g = 1...G)}{\partial \boldsymbol{\mu}} = \begin{cases} \frac{\boldsymbol{\mu} - t_{g-1}}{\sigma_g^2} & t_{g-1} & < \boldsymbol{\mu} \leq \frac{t_{g-1} + \bar{\mu}_g}{2} \\ \frac{\boldsymbol{\mu} - \bar{\mu}_g}{\sigma_g^2} & \frac{t_{g-1} + \bar{\mu}_g}{2} & < \boldsymbol{\mu} \leq \frac{\bar{\mu}_g + t_g}{2} \\ \frac{\boldsymbol{\mu} - t_g}{\sigma_g^2} & \frac{\bar{\mu}_g + t_g}{2} & < \boldsymbol{\mu} \leq t_g \end{cases} \tag{4.11}$$

$\bar{\mu}_g$ is the mean of the Gaussian function used to define the intensity prior
σ_g is the standard deviation of the Gaussian function
t_g are defined to be the points of intersection between neighbouring Gaussians; it is assumed $t_0 = -\infty$ and $t_G = \infty$

$$M_s(\vec{\boldsymbol{\mu}}) = -\sum_{mn} w_{mn} \Phi_\delta \left((\boldsymbol{\mu})_m - (\boldsymbol{\mu})_n \right) \tag{4.12}$$

$$\Phi_\delta (z) = \frac{(z^2)}{2\delta^2 + z^2} \tag{4.13}$$

$w_{mn} = 0$ if pixels m and n are not nearest neighbours and the Euclidean distance between m and n if they are nearest neighbours

z is the difference between the values at m and n

δ is a constant which represents the tolerance to variation in the pixel values.

The resulting equation for estimating the attenuation distribution is shown in Equation 4.14.

$$(\boldsymbol{\mu}^{i+1})_b = (\boldsymbol{\mu}^i)_b + \frac{\alpha_p}{\eta \sum_d q_{bd} - \alpha_p \partial^2 M(\vec{\boldsymbol{\mu}})/\partial(\boldsymbol{\mu})_b^2} \cdot \left[\sum_d q_{bd} \left(1 - \frac{(\boldsymbol{n}^*)_d}{\sum_{b'} (\boldsymbol{A}_0)_{b'd} (\boldsymbol{\lambda})_{b'}} \right) + \frac{\partial M(\vec{\boldsymbol{\mu}})}{\partial(\boldsymbol{\mu})_b} \right] \quad (4.14)$$

$$M(\vec{\boldsymbol{\mu}}) = \beta_m M_a(\vec{\boldsymbol{\mu}}) + \beta_g M_s(\vec{\boldsymbol{\mu}}) \quad (4.15)$$

β_m and β_g are weighting parameters for the priors.

4.1.3 Reconstruction of Attenuation Map from Emission and Scatter Data

In order to optimise the reconstruction of the attenuation map from measured SPECT data without the need for a separate transmission map it is proposed that information from both the scatter and photopeak energy windows can be used. Since the emission and scatter of photons are independent processes the joint likelihood is the sum of the likelihoods for the measured scatter sinogram and the measured emission sinogram given the current estimates of attenuation and activity and hence each part of the likelihood can be maximised independently. As a result the update for the attenuation map at each step is the sum of the updates calculated for the scatter data and emission data independently (the SMLGA-MLAA algorithm, Equation 4.16).

$$\boldsymbol{\mu}^{i+1} = \boldsymbol{\mu}^i + \alpha_p \Delta \boldsymbol{\mu_p}(b) + \alpha_s \Delta \boldsymbol{\mu_s}(k) \quad (4.16)$$

$$\Delta\boldsymbol{\mu_p}(b) = \frac{1}{\eta \sum_d q_{bd}} \cdot \sum_d q_{bd} \left(1 - \frac{n_d^*}{\sum_{b'} a_{b'd}\lambda_{b'}} \right) \tag{4.17}$$

$$\Delta\boldsymbol{\mu_s}(k) = \frac{1}{(\boldsymbol{\chi})_{kd}} \cdot \sum_d \left(-\sum_b D'_{bd}(\boldsymbol{\mu}^i, k) + (\boldsymbol{n}^s)_d \cdot \frac{\sum_b D'_{bd}(\boldsymbol{\mu}^i, k)}{(\boldsymbol{s})_d} \right) \tag{4.18}$$

α_p is the relaxation parameter for the MLAA reconstruction update
α_s is the relaxation parameter for the SMLGA reconstruction update

4.2 Method

In order to assess the potential of reconstructing both the activity distribution and attenuation map from measured SPECT data, without a separate transmission scan, reconstructions were performed using a 2-dimensional realisation of the male XCAT phantom (Segars *et al.*. 1999) (formerly known as the NCAT phantom). Initially simulated measurements were created using an idealised situation by using the same transfer matrix and scatter model in the reconstruction algorithms as were used to generate the 'measured' data. The photopeak data was free from scatter (i.e. it was assumed to have been perfectly scatter corrected prior to reconstruction) and data in the scatter window contained only photons that had been scattered once (i.e. photons which had been scattered multiple times were excluded as were primary photons falling in this window).

Data were simulated, without noise, for two standard, parallel hole collimator, SPECT geometries with projections every 2^o over 360^o and every 2^o over 180^o. A geometry equivalent to that of a dedicated cardiac scanner was also simulated; this is referred to as a pseudo DSPECT geometry. In order to simulate this imaging geometry a mask was used to extract the projection lines measured by the DSPECT camera from a standard parallel projection sinogram; the full and masked sinograms are shown in Figure 4.2.

For each reconstruction an initial estimate of the activity distribution was made by performing five iterations of the MLEM algorithm, using an assumption of zero attenuation throughout the field of view. One iteration of the estimation of the attenuation map was then performed starting from an initial estimate of the attenuation map with uniform attenuation approximately equal to the attenuation of soft tissue in the region where the initial reconstruction of the activity was

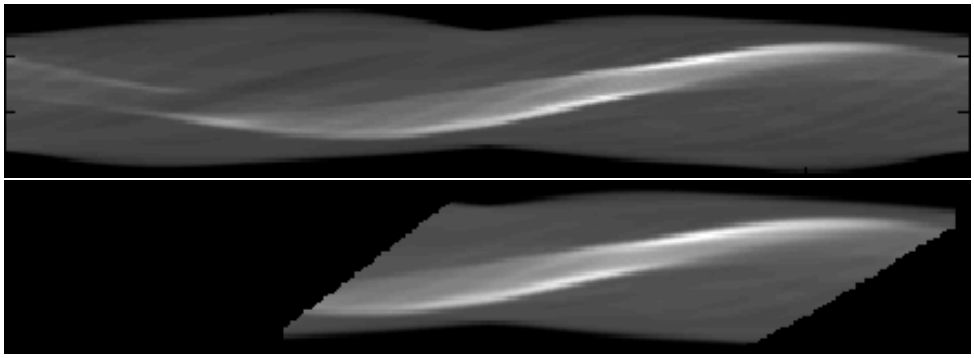

Figure 4.2: Full 360^o sinogram and sinogram masked to produce pseudo-DSPECT geometry

greater than zero. Iterations of the MLEM and attenuation map update algorithms were then applied alternately in order to improve the estimates of both the activity distribution and attenuation map. In order to improve the convergence of the algorithms the attenuation was constrained to be zero outside the body outline where the reconstructed activity per pixel was less than 1. Reconstructions were performed using the SMLGA algorithm, the MLAA algorithm and the combined SMLGA-MLAA algorithm. The results from these reconstructions were compared to reconstructions of the activity distribution without attenuation correction and with perfect attenuation correction.

In order to compare the accuracy of the reconstructions performed using different techniques the difference between the images reconstructed using the technique being tested have been compared to the true activity distribution and attenuation map on a pixel by pixel basis. The overall accuracy (bias) of each technique has been assessed by calculating the mean error for all pixels. However, in order to reduce the effect of artefacts in the reconstructed images the absolute pixel values may not be essential as long as any systematic error is uniform for all pixels. The uniformity of the errors of individual pixels (precision) has been assessed by normalising the estimated image to have the same mean as the true image and then calculating the root mean square error. The root mean square error has been selected to assess the precision of the techniques because the individual pixel errors are not generally normally distributed; an example is shown in Figure 4.3.

When considering the reconstruction of myocardial perfusion images it is not necessarily essential to accurately reconstruct the complete thorax as long as the region of the myocardium is correctly reconstructed. A region of interest was,

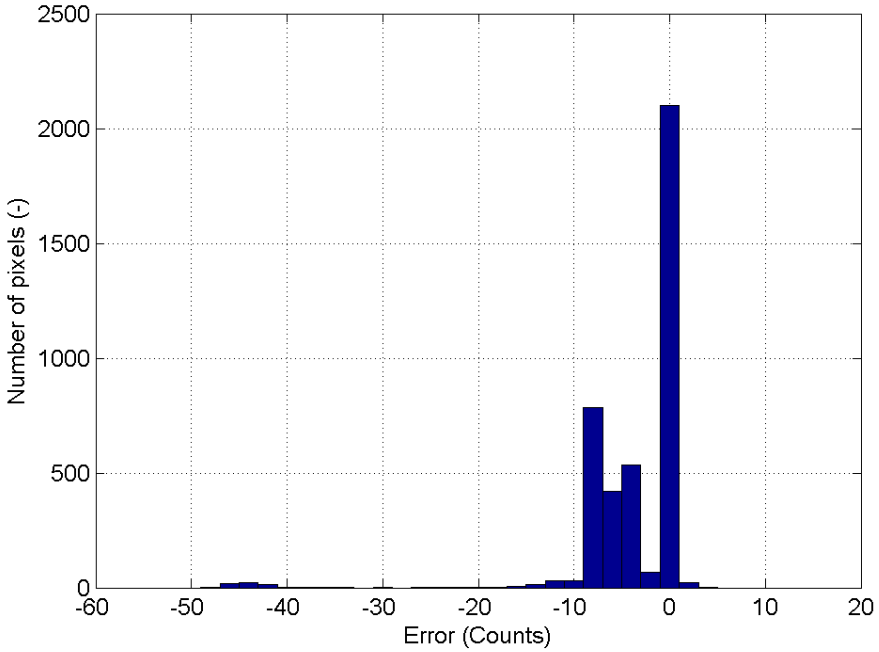

Figure 4.3: Distribution of errors for individual pixels from activity distribution reconstructed using the without attenuation correction compared to the true activity distribution.

therefore, produced around the heart and the mean and root mean square errors inside this region calculated.

4.3 Results

The activity distributions recovered using different methods of estimating the attenuation map are shown in Figures 4.4, 4.8 and 4.12 for the 360^o, 180^o and DSPECT geometries respectively; the differences between the activity distributions and the true activity phantom are shown in Figures 4.5, 4.9 and 4.13. The attenuation maps reconstructed by each technique are shown in Figures 4.6, 4.10 and 4.14 for the 360^o, 180^o and DSPECT geometries respectively and the differences between these and the true attenuation map are shown in Figures 4.7, 4.11 and 4.15.

In each case the results for reconstructions without attenuation correction, and with perfect attenuation correction, are also shown. The mean and root mean square errors (as defined in Section 4.2) for the whole images and for a region of

	Activity Distribution			
	Image		Region	
	Mean	RMSE	Mean	RMSE
SMLGA technique	-0.0044	1.1301	0.0665	1.5998
MLAA technique	-0.3779	2.5243	1.0025	2.3412
SMLGA-MLAA technique	0.0090	0.7187	0.0319	0.9360
Exact attenuation correction	-2.573×10^{-5}	0.4021	0.0088	0.3058
No attenuation correction	-3.7969	4.3377	-6.3789	3.4502

	Attenuation Map			
	Image		Region	
	Mean	RMSE	Mean	RMSE
SMLGA technique	-1.087×10^{-5}	0.0077	0.0005	0.0136
MLAA technique	-2.583×10^{-3}	0.0170	0.0092	0.0246
SMLGA-MLAA technique	6.647×10^{-5}	0.0044	0.0002	0.0075

Table 4.1: Mean error and root mean square error (RMSE) in reconstructions using idealised simulated data with a standard 360^o imaging geometry for the whole image and for a region of interest centred over the heart.

interest centred over the heart are shown in Tables 4.1, 4.2 and 4.3. The results show that the use of data acquired over 360^o and 180^o produce very smilar results. In both cases the SMLGA algorithm shows improved reconstruction compared to the MLAA algorithm and reconstruction without attenuation correction. Further improvement, especially close to the boundaries between different tissue types, is achieved when the SMLGA and MLAA algorithms are combined.

The pseudo-DSPECT geometry also demonstrates accurate reconstruction when using the SMLGA and combined SMLGA-MLAA algorithms in the region at the focus of the acquisition. However, reconstruction of the posterior region of the body (i.e. the area furthest from the camera location) is poor. This is as expected due to under-sampling in this region.

In order to highlight artefacts introduced into the myocardium by the reconstruction progress an enlarged view of the activity distribution in this region is shown in Figures 4.16, 4.17 and 4.18 for the 360^o, 180^o and DSPECT geometries respectively. In each case the errors have been scaled to the mean error in the region of interest over the heart in order to demonstrate the variation in the reconstructed myocardium. These results show that in this region, which is over-sampled by the pseudo-DSPECT imaging geometry, the results for this type of acquisition are as accurate as those obtained using standard SPECT imaging geometries.

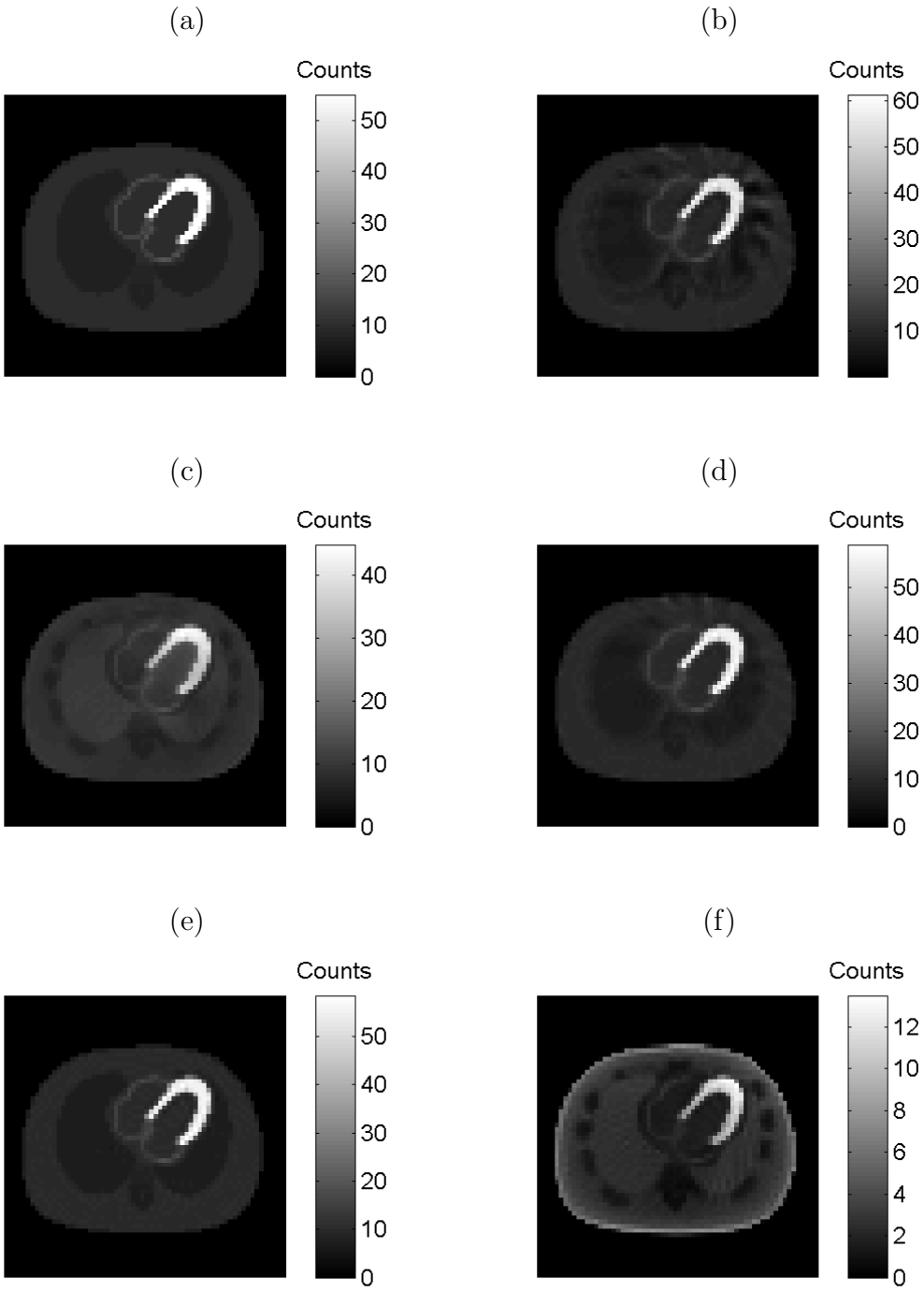

Figure 4.4: Reconstructed activity distributions for a standard 360^o imaging geometry; (a) true phantom activity distribution (b) SMLGA reconstruction, (c) MLAA reconstruction, (d) SMLGA-MLAA reconstruction, (e) using true attenuation map, and (f) without attenuation correction

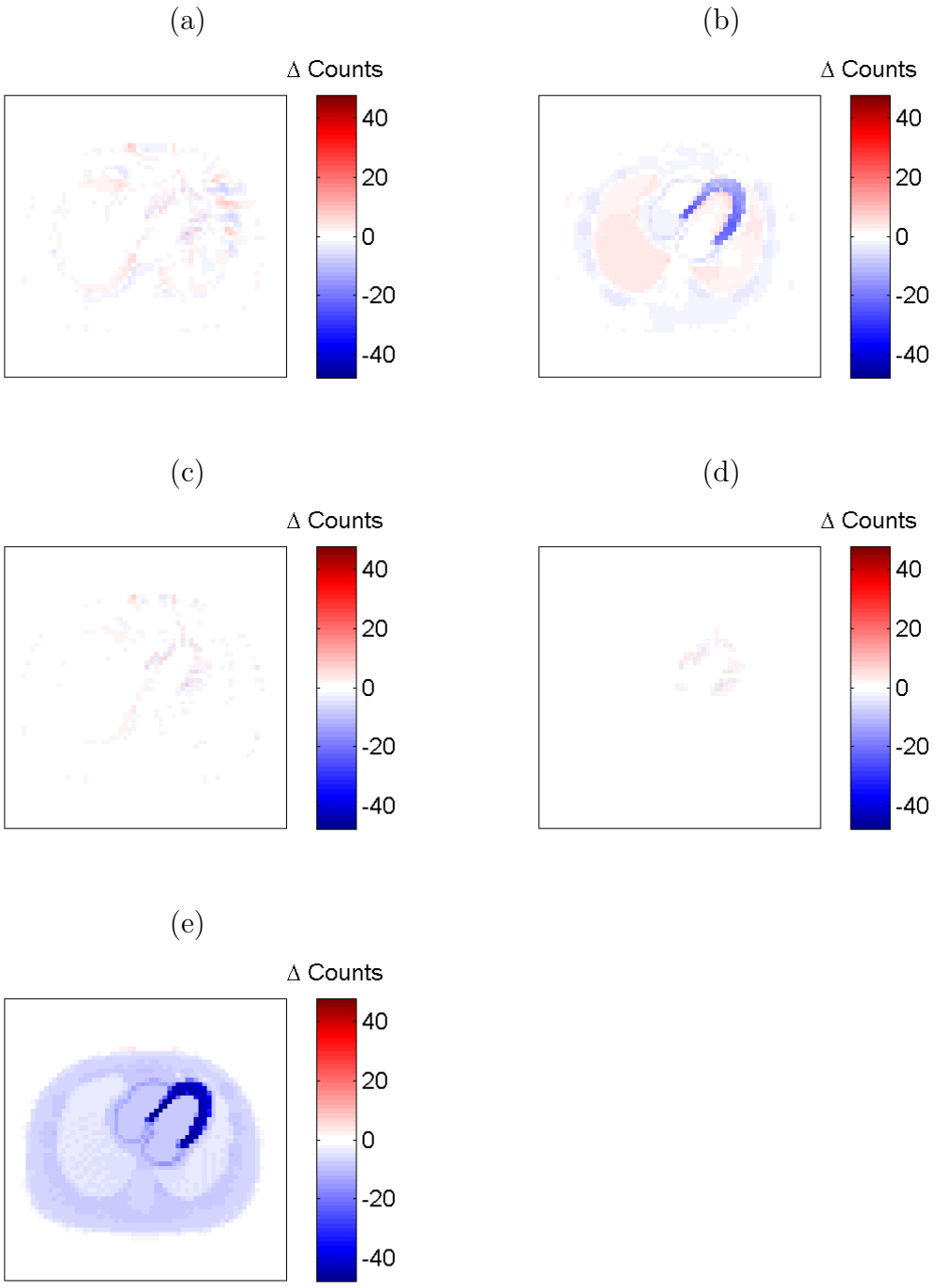

Figure 4.5: Difference between the reconstructed activity distributions and true activity phantom for a 360^o imaging geometry; (a) SMLGA reconstruction, (b) MLAA reconstruction, (c) SMLGA-MLAA reconstruction, (d) using true attenuation map, and (e) without attenuation correction

	Activity Distribution			
	Image		Region	
	Mean	RMSE	Mean	RMSE
SMLGA technique	-0.0133	1.1150	-0.0444	1.2709
MLAA technique	-0.2633	2.5141	1.2720	2.2920
SMLGA-MLAA technique	0.0059	0.7767	0.0491	0.9143
Exact attenuation correction	0.0000	0.4386	0.0075	0.5237
No attenuation correction	-3.7515	3.9364	-6.1370	2.2756

	Attenuation Map			
	Image		Region	
	Mean	RMSE	Mean	RMSE
SMLGA technique	-5.079×10^{-5}	0.0086	-0.0007	0.0177
MLAA technique	-2.263×10^{-3}	0.0193	0.0098	0.0287
SMLGA-MLAA technique	6.252×10^{-5}	0.0055	0.0004	0.0107

Table 4.2: Mean error and root mean square error (RMSE) in reconstructions using idealised simulated data with a standard 180^o imaging geometry for the whole image and for a region of interest centred over the heart.

	Activity Distribution			
	Image		Region	
	Mean	RMSE	Mean	RMSE
SMLGA technique	-0.0213	1.1536	-0.0145	1.2680
MLAA technique	-0.1812	2.6340	1.6097	2.2699
SMLGA-MLAA technique	0.0101	0.7955	0.0684	1.0527
Exact attenuation correction	-0.0025	0.5091	0.0503	0.5884
No attenuation correction	-3.7458	3.7955	-6.0152	2.4581

	Attenuation Map			
	Image		Region	
	Mean	RMSE	Mean	RMSE
SMLGA technique	9.911×10^{-5}	0.0096	0.0006	0.0167
MLAA technique	-9.235×10^{-4}	0.0209	0.0103	0.0283
SMLGA-MLAA technique	2.958×10^{-4}	0.0076	0.0009	0.0128

Table 4.3: Mean error and root mean square error (RMSE) in reconstructions using idealised simulated data with a pseudo-DSPECT imaging geometry for the whole image and for a region of interest centred over the heart.

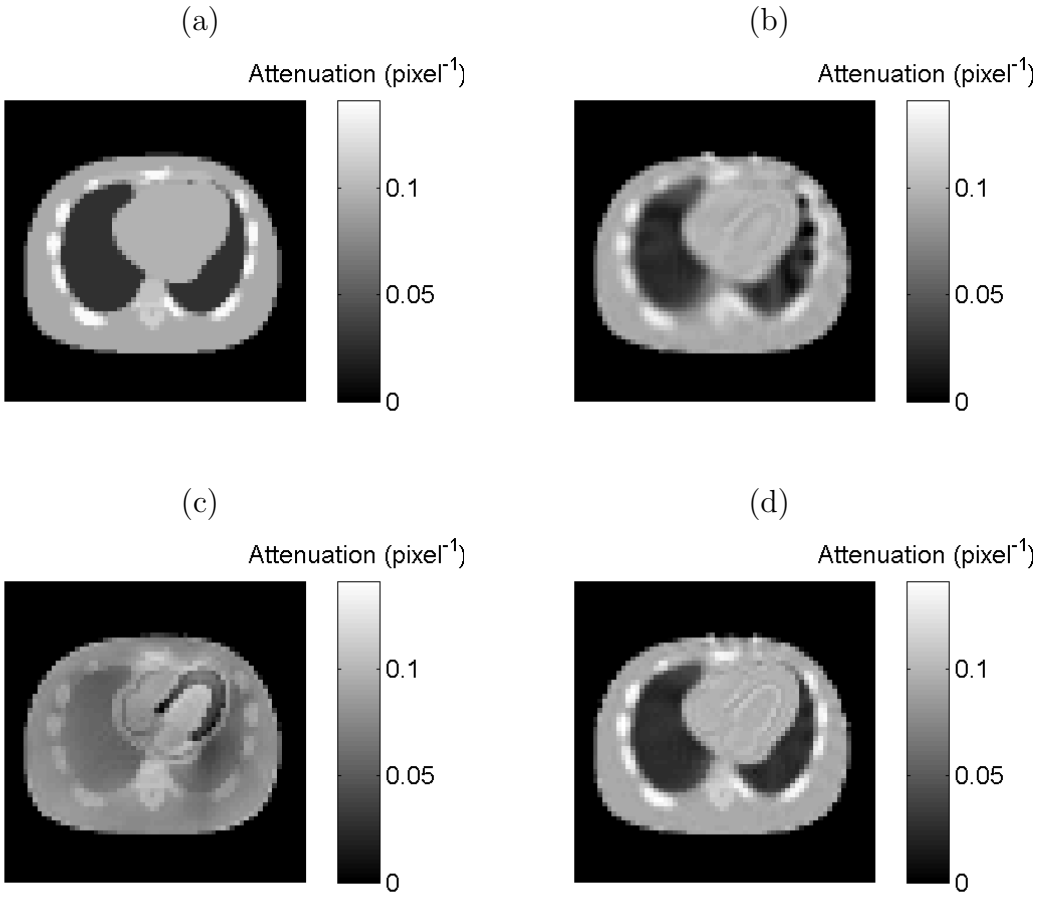

Figure 4.6: Reconstructed attenuation maps for a 360^o imaging geometry; (a) true phantom attenuation map (b) SMLGA reconstruction, (c) MLAA reconstruction, (d) SMLGA-MLAA reconstruction

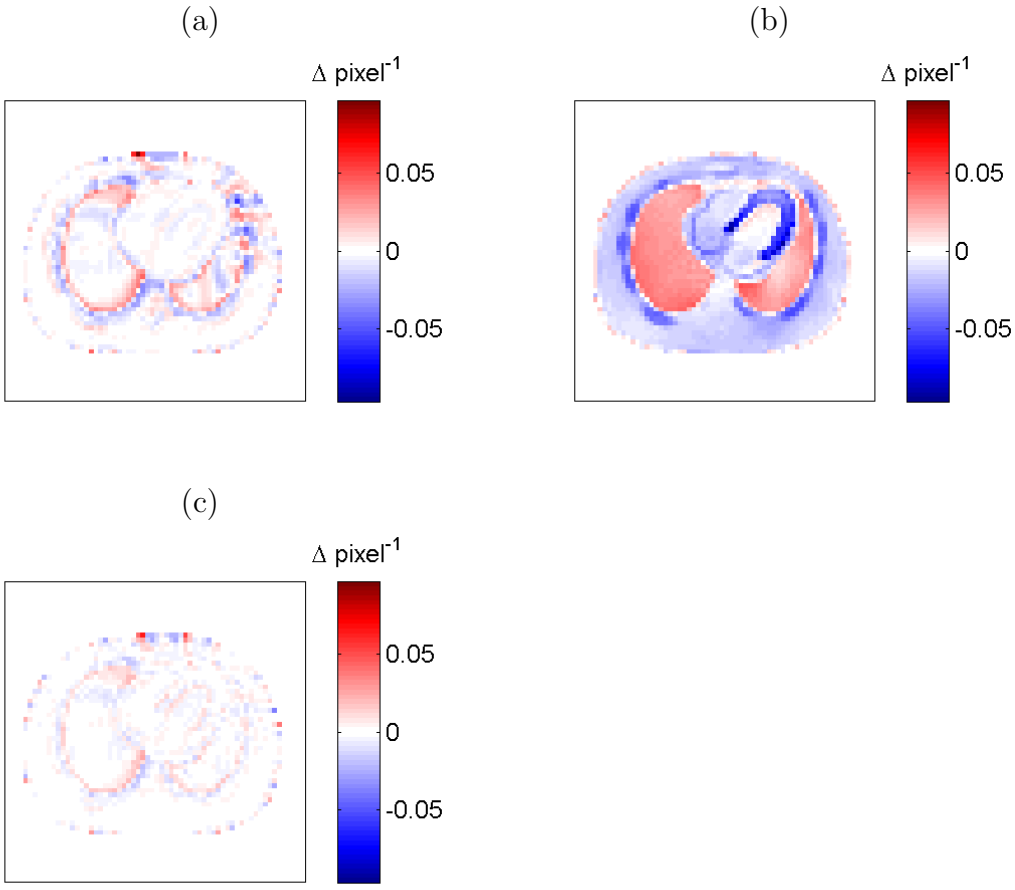

Figure 4.7: Difference between the reconstructed attenuation map and true attenuation phantom for a 360^o imaging geometry; (a) SMLGA reconstruction, (b) MLAA reconstruction, (c) SMLGA-MLAA reconstruction

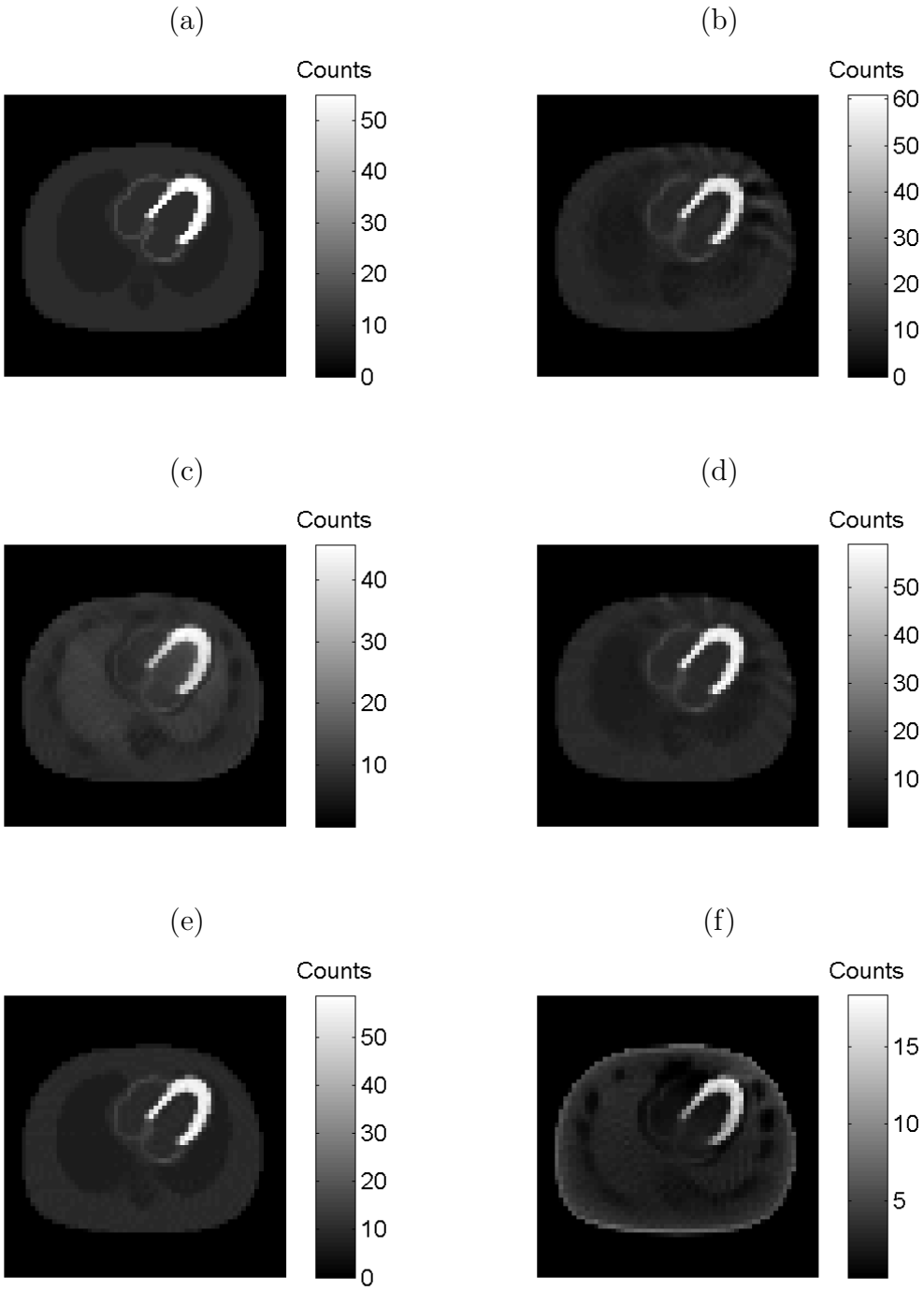

Figure 4.8: Reconstructed activity distributions for an standard 180^o imaging geometry; (a) true phantom activity distribution (b) SMLGA reconstruction, (c) MLAA reconstruction, (d) SMLGA-MLAA reconstruction, (e) using true attenuation map, and (f) without attenuation correction

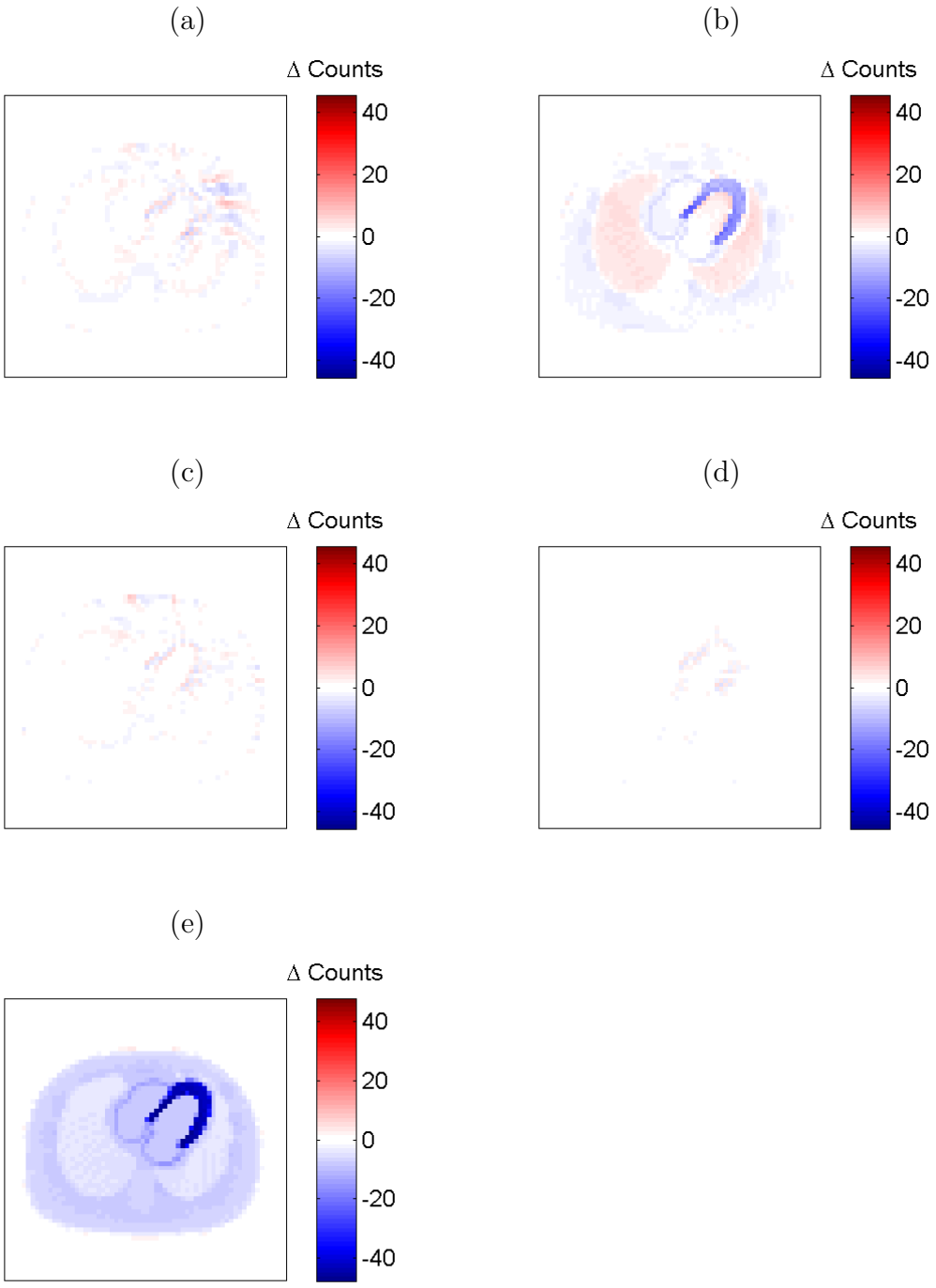

Figure 4.9: Difference between the reconstructed activity distributions and true activity phantom for a 360^o imaging geometry; (a) SMLGA reconstruction, (b) MLAA reconstruction, (c) SMLGA-MLAA reconstruction, (d) using true attenuation map, and (e) without attenuation correction

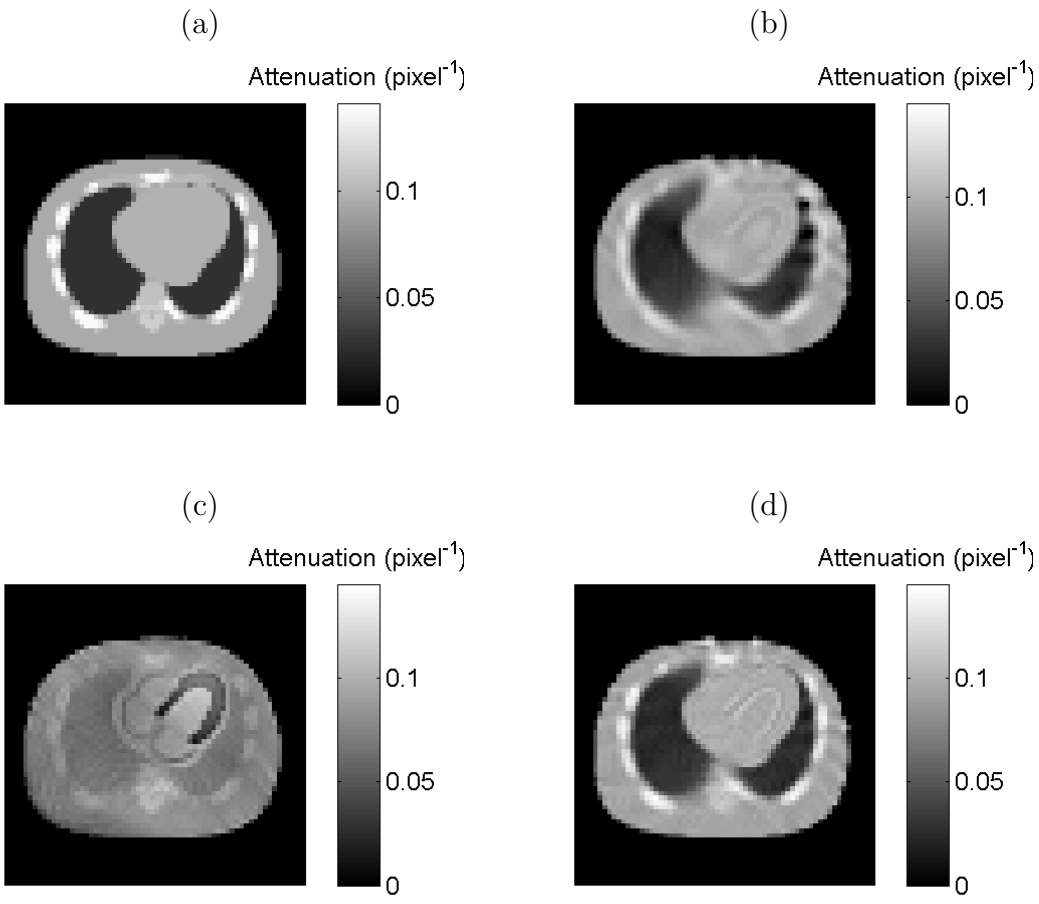

Figure 4.10: Reconstructed attenuation maps for a 180^o imaging geometry; (a) true phantom attenuation map (b) SMLGA reconstruction, (c) MLAA reconstruction, (d) SMLGA-MLAA reconstruction

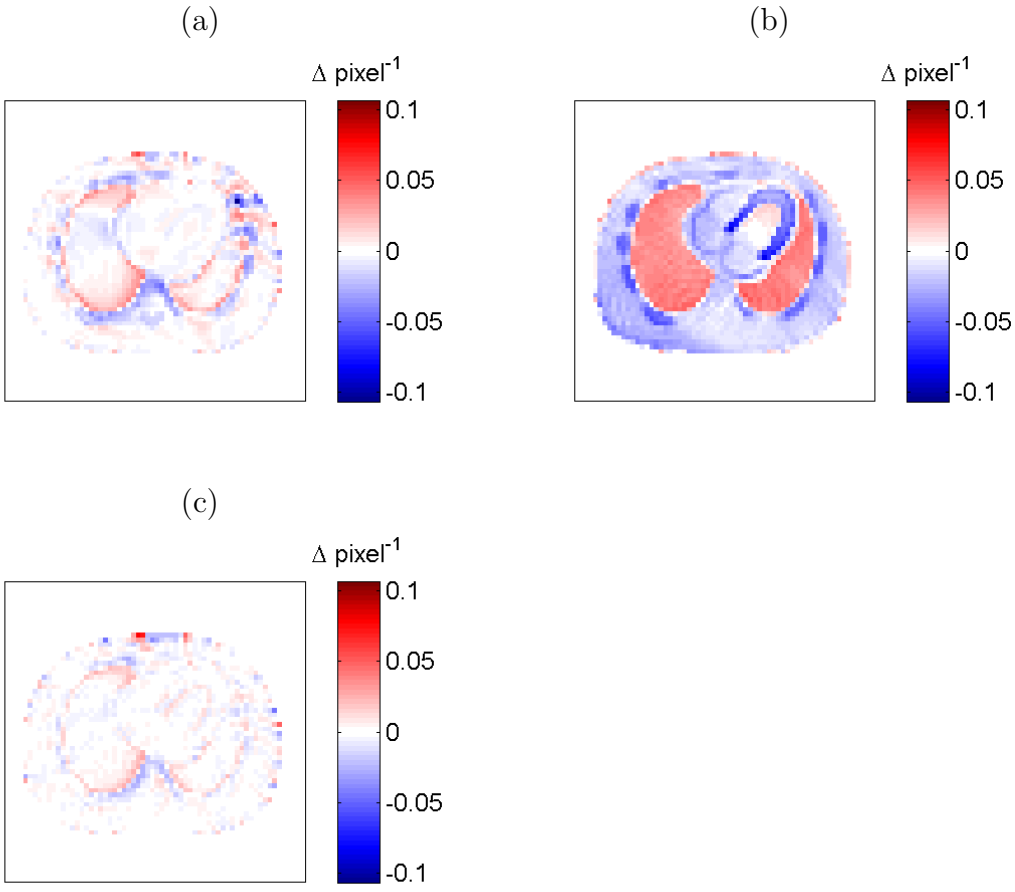

Figure 4.11: Difference between the reconstructed attenuation map and true attenuation phantom for a 180^o imaging geometry; (a) SMLGA reconstruction, (b) MLAA reconstruction, (c) SMLGA-MLAA reconstruction

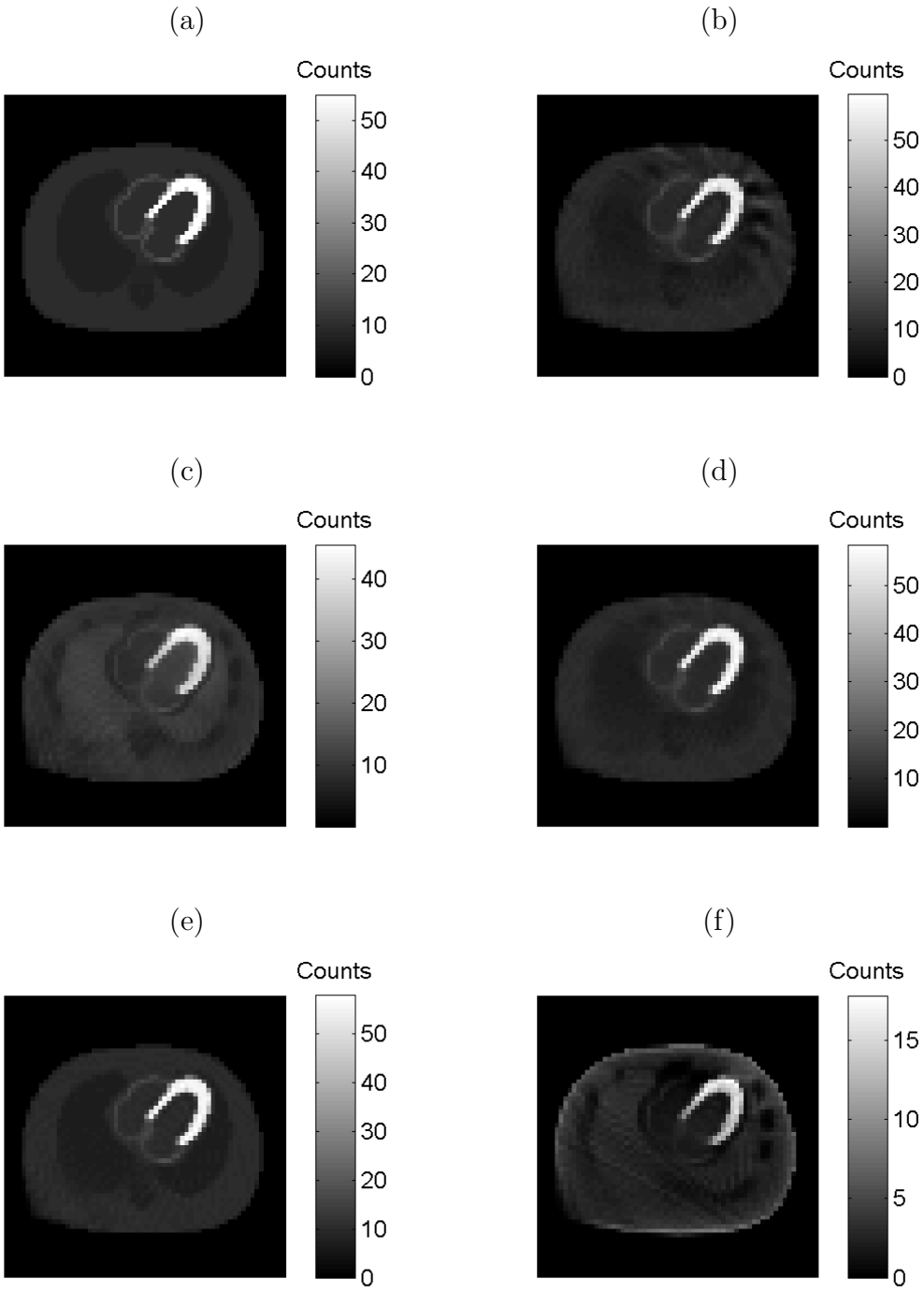

Figure 4.12: Reconstructed activity distributions for a pseudo-DSPECT imaging geometry; (a) true phantom activity distribution (b) SMLGA reconstruction, (c) MLAA reconstruction, (d) SMLGA-MLAA reconstruction, (e) using true attenuation map, and (f) without attenuation correction

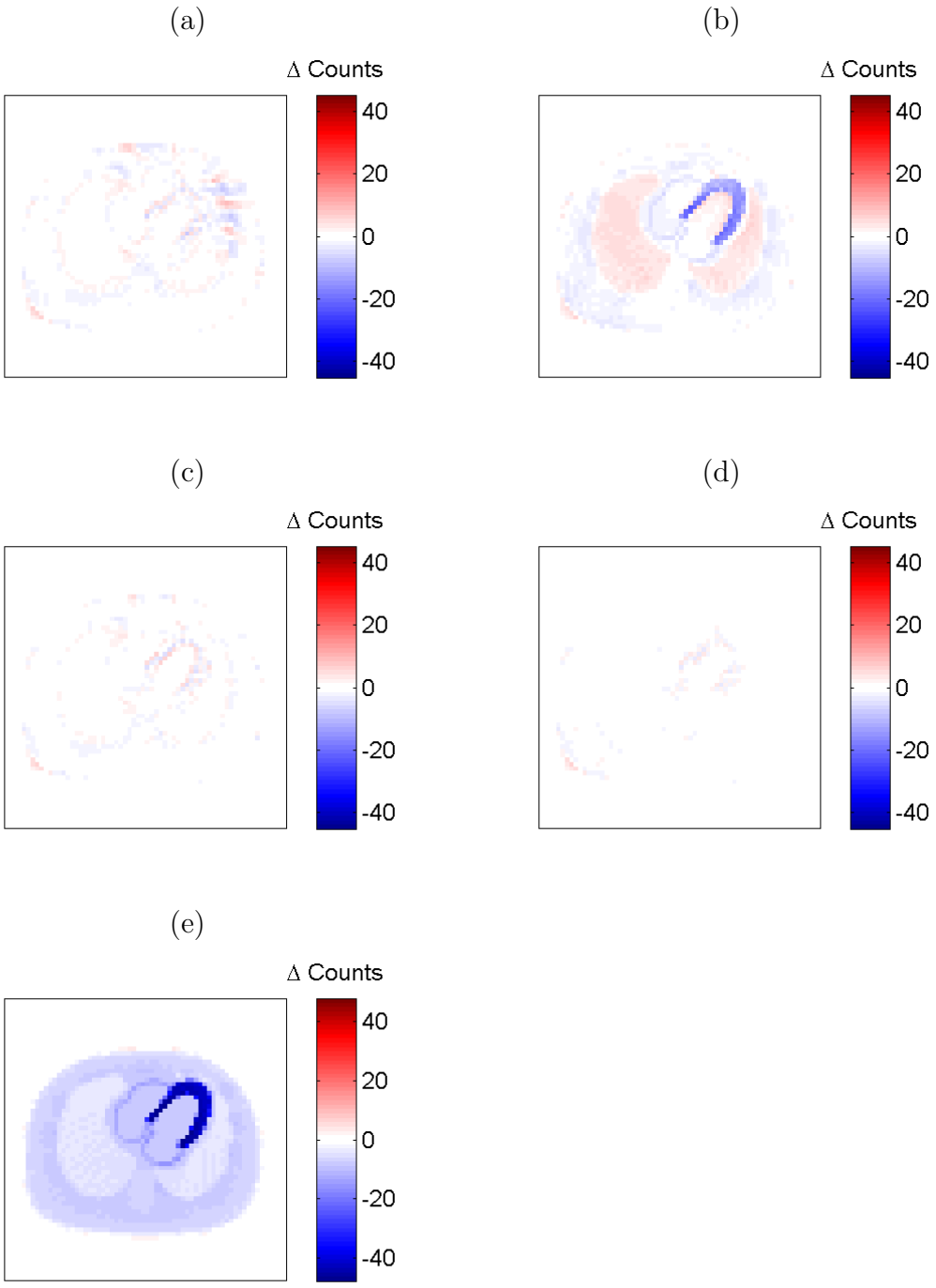

Figure 4.13: Difference between the reconstructed activity distributions and true activity phantom for a pseudo-DSPECT imaging geometry; (a) SMLGA reconstruction, (b) MLAA reconstruction, (c) SMLGA-MLAA reconstruction, (d) using true attenuation map, and (e) without attenuation correction

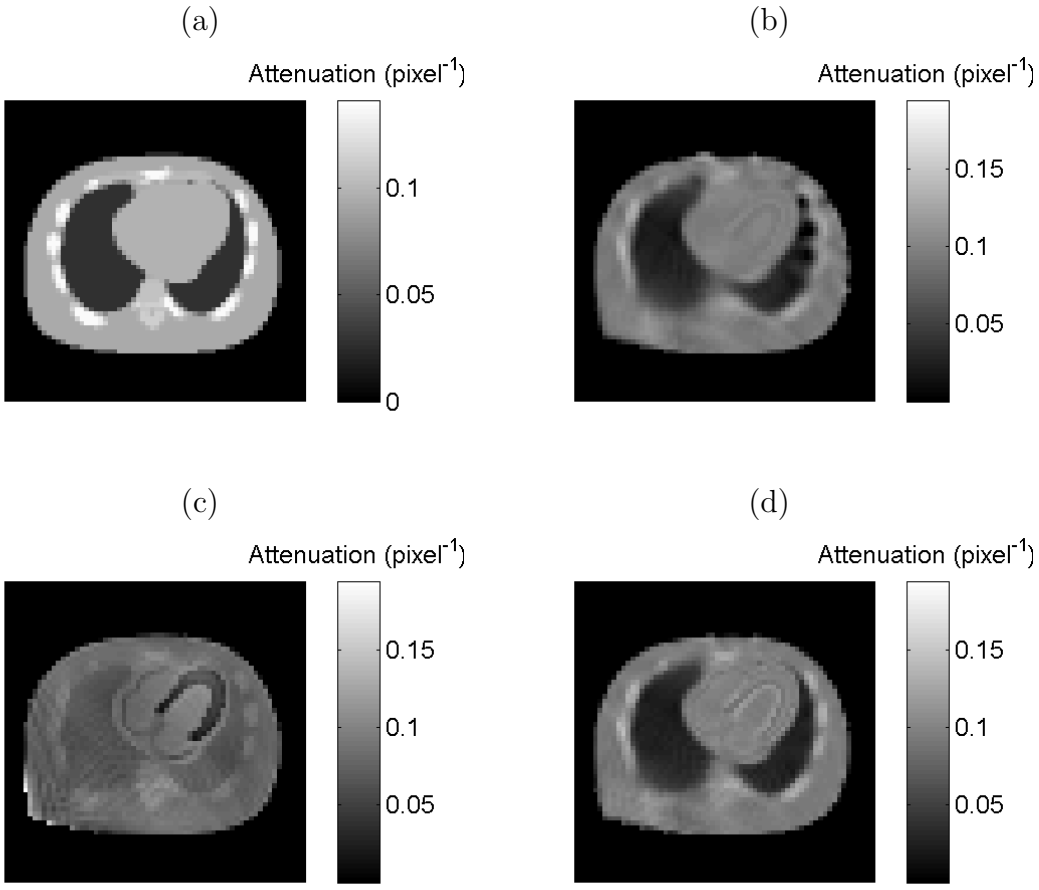

Figure 4.14: Reconstructed attenuation maps for a pseudo-DSPECT imaging geometry; (a) true phantom attenuation map (b) SMLGA reconstruction, (c) MLAA reconstruction, (d) SMLGA-MLAA reconstruction

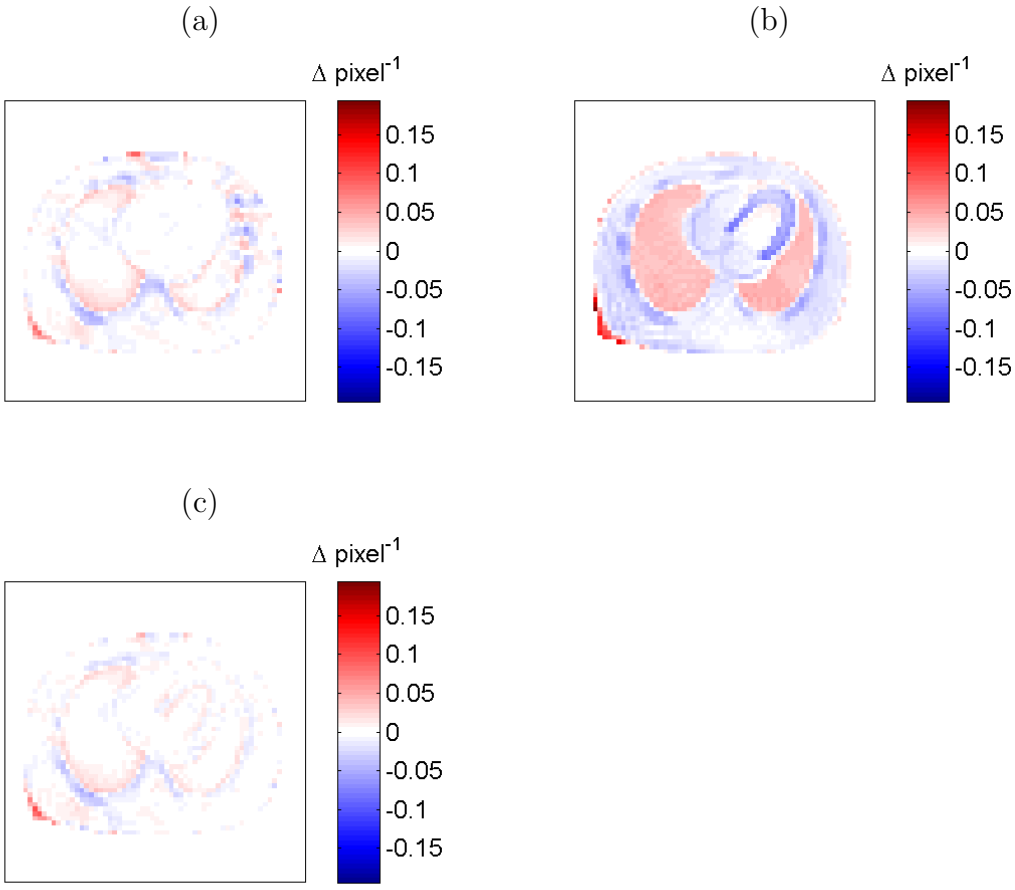

Figure 4.15: Difference between the reconstructed attenuation map and true attenuation phantom for a pseudo-DSPECT imaging geometry; (a) SMLGA reconstruction, (b) MLAA reconstruction, (c) SMLGA-MLAA reconstruction

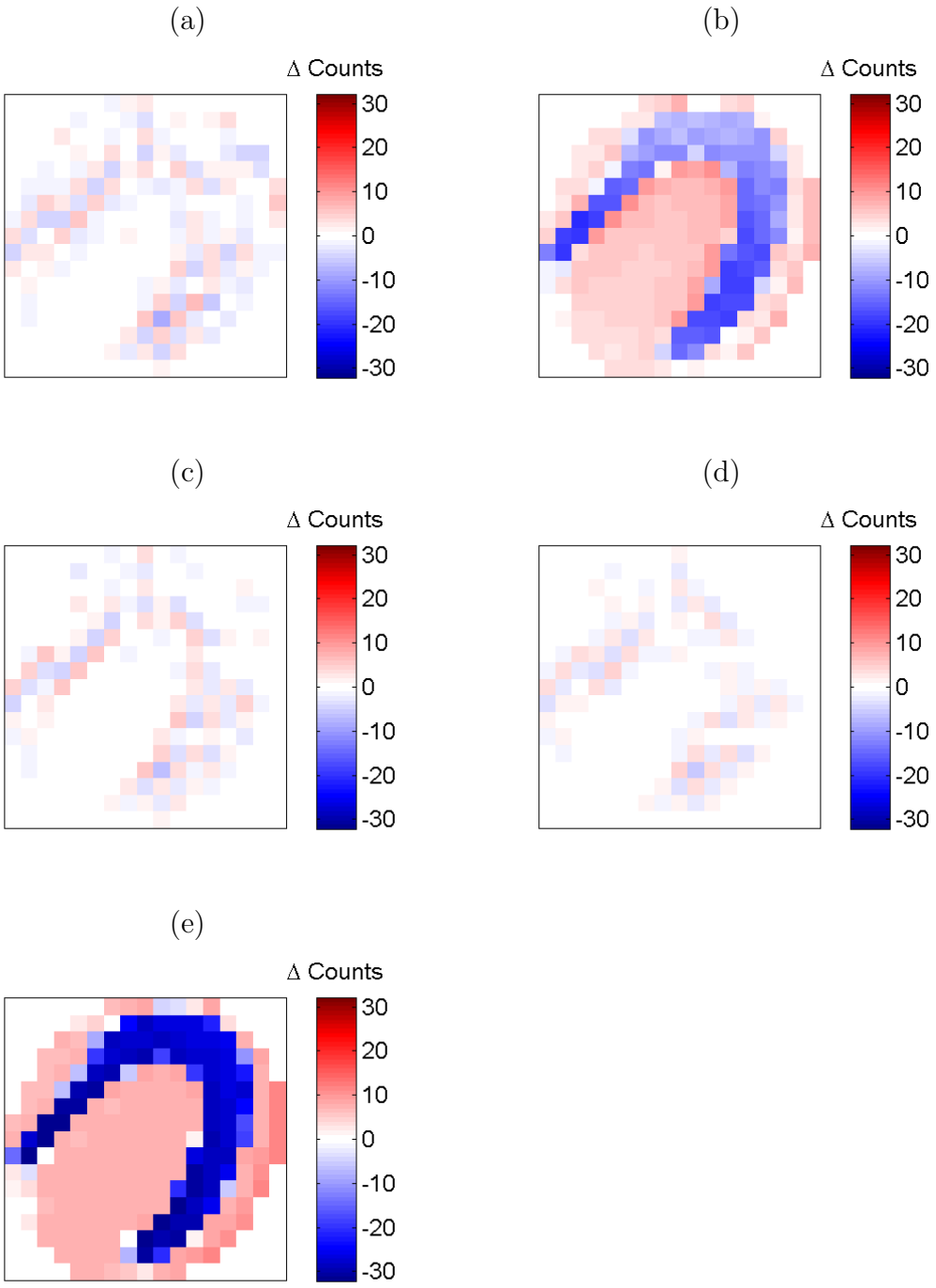

Figure 4.16: Relative errors in the activity distributions reconstructed in the region of the myocardium for a 360^o imaging geometry; (a) SMLGA reconstruction, (b) MLAA reconstruction, (c) SMLGA-MLAA reconstruction, (d) using true attenuation map, and (e) without attenuation correction

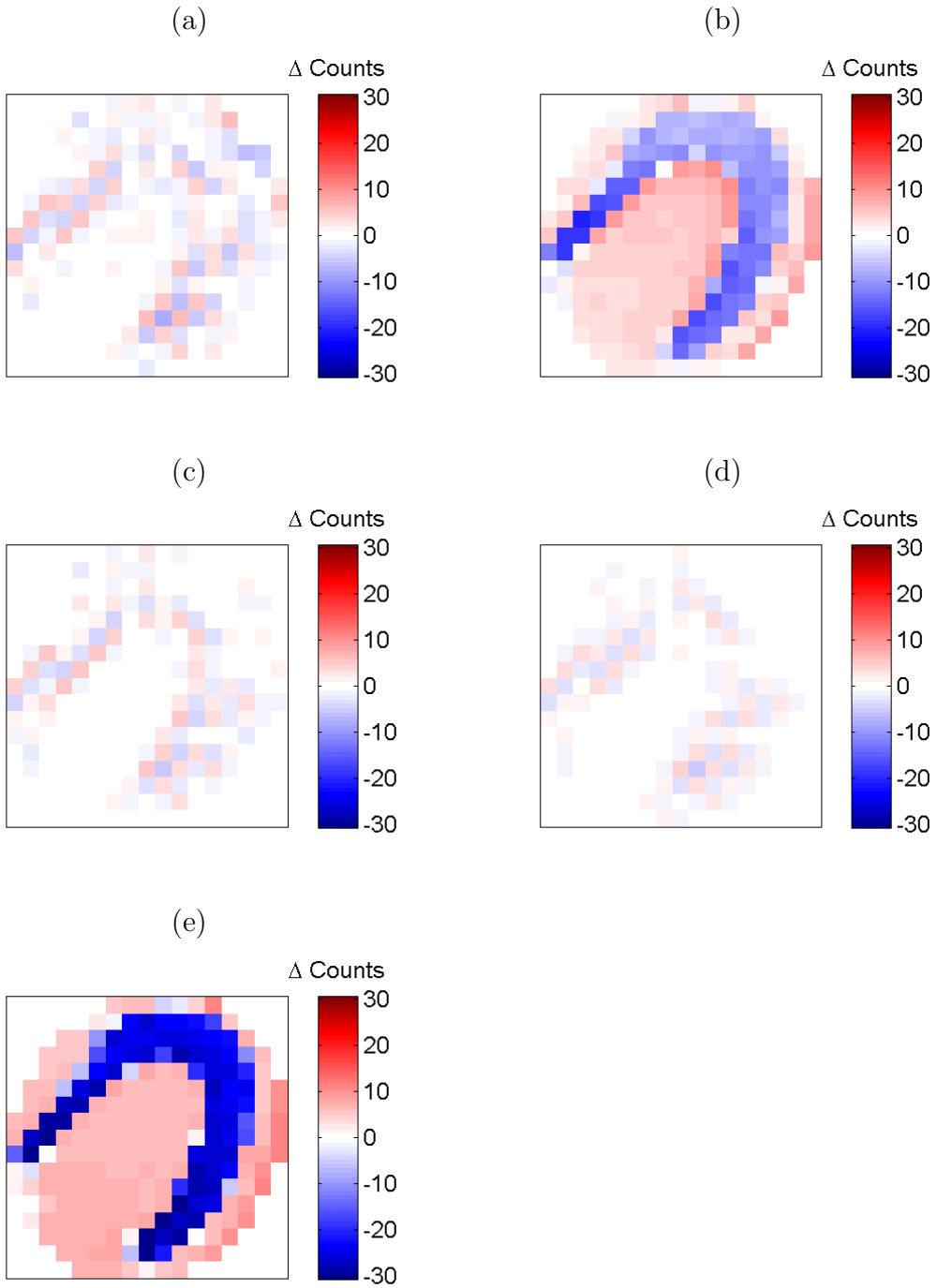

Figure 4.17: Relative errors in the activity distributions reconstructed in the region of the myocardium for a 180^o imaging geometry; (a) SMLGA reconstruction, (b) MLAA reconstruction, (c) SMLGA-MLAA reconstruction, (d) using true attenuation map, and (e) without attenuation correction

4.4 Discussion

The work presented here shows a new method of attenuation correction without the need for a separate transmission scan. The potential for such a method of attenuation correction has wide appeal in SPECT imaging because of the reduction in radiation dose to the patient and removal of potential mismatches between the transmission and emission scans. The ability to perform an attenuation correction without transmission scan would also be applicable to all types of gamma cameras including those, such as a number of dedicated cardiac scanners, where it would be difficult or impossible to add a transmission based scanning system for attenuation correction. This chapter demonstrates a first step towards an accurate method of attenuation correction using scatter data

Results for reconstructions using data simulated over 360^o were found to be similar to reconstructions for data simulated over 180^o for all the algorithms tested. When reconstruction of the emission data was performed using the exact attenuation map only very small differences between the true and estimated activity distribution were found. The differences seen are due to the finite size of the detection matrix. When no attenuation correction is performed the activity estimated towards the centre of the body is significantly reduced compared to the true activity and the activity close to the body boundary is over-estimated. This effect occurs because photons from close to the centre of the body have a higher probability of attenuation and so are less likely to be detected. If attenuation correction is not performed, the attenuated photons are not accounted for and it appears as though there are less photons emitted from regions behind areas of attenuating material resulting in a global underestimation of the activity (i.e. a negative mean error)

As previously demonstrated by other authors (Nuyts *et al.*. 1999, Krol *et al.*. 2001), significant cross-talk was present in the reconstruction of both the activity distribution and attenuation map using just the photopeak data. This results in areas of low attenuation in the region of high activity (e.g. the myocardium) and increased attenuation in regions of low activity (e.g. the lungs). The effect of cross-talk on the activity distribution is to reduce the variation in the activities seen, with regions of high activity reduced and regions of low activity increased compared to the true activity distribution.

The SMLGA reconstruction algorithm developed here shows improved recon-

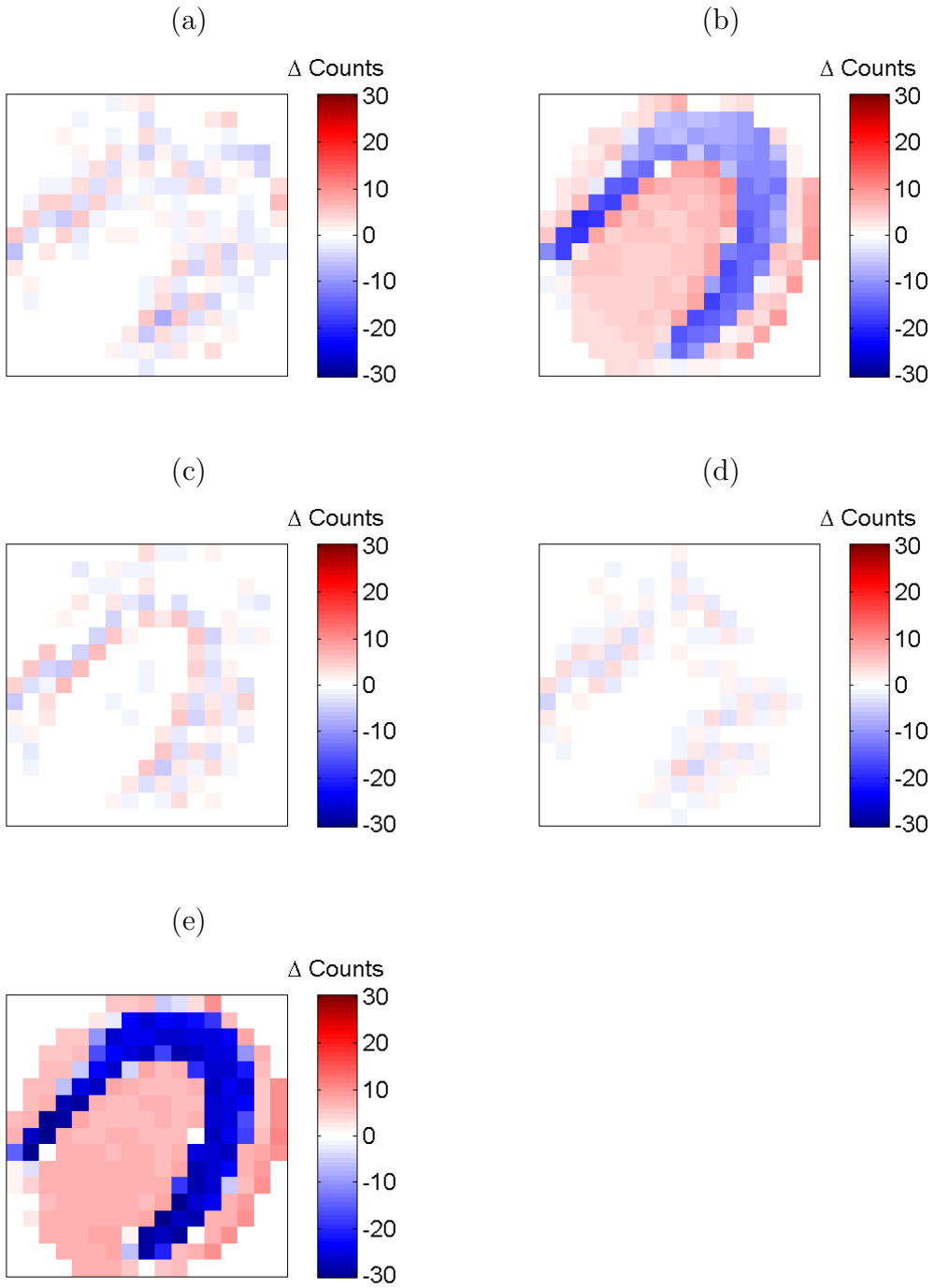

Figure 4.18: Relative errors in the activity distributions reconstructed in the region of the myocardium for a pseudo-DSPECT imaging geometry; (a) SMLGA reconstruction, (b) MLAA reconstruction, (c) SMLGA-MLAA reconstruction, (d) using true attenuation map, and (e) without attenuation correction

struction compared to both reconstruction without attenuation correction and reconstruction using the MLAA method to estimate the attenuation map; this is shown by the reduced bias and spread of errors globally and in the region of interest centred over the heart. The body outline is accurately reconstructed and the lungs are clearly visualised; an increase in attenuation corresponding to the ribs is also seen. However, the reconstruction of the attenuation map close to boundaries of different tissue types is poorer than near to the centre of each region. The effect of this is particularly significant where both lung and rib are present close to the high activity region of the myocardium and results in an underestimation of the attenuation in this area. When the SMLGA algorithm is combined with the MLAA algorithm a more accurate reconstruction of both the activity distribution and attenuation map is possible. This is because the use of scatter data in the SMLGA part of the combined algorithm prevents the cross-talk seen when using the MLAA algorithm alone and the use of the MLAA algorithm with the SMLGA stabilises the reconstruction close to the boundaries between different tissue types.

When considering a pseudo-DSPECT acquisition set-up it is found that the right posterior region of the body is not reconstructed as well as in the standard imaging geometries. This is as expected since this region is under sampled by the pseudo-DSPECT acquisition. Results considering a region of interest centred on the myocardium demonstrate that accurate reconstruction is achieved in this region.

4.5 Conclusion

The use of scatter data has been shown to provide an accurate method of reconstructing an attenuation map, in 2 dimensions, without the use of a transmission scan. The results obtained using the SMLGA algorithm developed here demonstrated improved reconstructions, compared to reconstruction without attenuation correction or using an attenuation map estimated using an MLAA technique, for data acquired using standard SPECT imaging geometries of 360^o or 180^o, or using a pseudo-DSPECT imaging geometry. The results were further improved, particularly close to the boundaries between different tissue types, by combining the SMLGA developed with the MLAA algorithm.

5 An Enhanced Scatter Model in 3 Dimensions

The model for scatter developed in Chapter 3 was shown to represent accurately the distribution of scattered photons in simplified 2-dimensional cases. In the work outlined in this chapter the simple 2D model is first implemented and tested in three dimensions. The three dimensional model is then extended to represent more accurately the real situation by considering the relative effect of voxels close to the scattering voxel compared to more distant voxels and the effect of the resolution of a real collimator (as opposed to perfect parallel projection). The simple scatter model assumed that all attenuation was as a result of Compton scattering and so in the enhanced model the validity of this assumption has been investigated, as has the effect on the probability of detection of the reduction in photon energy after scattering.

5.1 Theory

5.1.1 Implementation of 3D model

The extension of the calculation of the scatter projections in 2-dimensions to 3-dimensions is conceptually quite simple; the emission pixel and scatter pixel may now lie in different planes and so the number of photons from each point of emission travelling to each scatter point is calculated for all pixels in the 3D volume. The initial direction of travel of each photon is now defined by two angles; the direction of travel in the $x-y$ plane (θ_{bk}) and the direction relative to the z-axis (ψ_{bk}). Given the number of possible directions of travel it is not practical to store these directions in 3D and so the angle of scatter required to

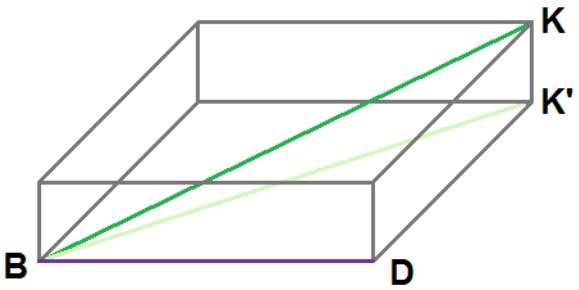

Figure 5.1: Diagram to illustrate combination of angles in 3-dimensions.

reach detector position d is calculated from the angle of the detector (Φ_d) and angles θ_{bk} and ψ_{bk} for each possible pair of points in the image matrix.

In order to calculate the overall angle of scatter (φ_{bkd}) the change in direction in the $x-y$ plane ($\Delta\theta$) and relative to the z-axis ($\Delta\psi$), from the initial direction of travel to the direction of travel required for detection, must be combined. For a standard imaging geometry, assuming perfect detector resolution, the direction of travel required for detection is always parallel to the $x-y$ plane and so $\Delta\psi$ is equal to ψ_{bk}. Figure 5.1 shows the geometry of the 3-dimensional case. The line from B to K is a vector representing the initial direction of travel of the photon, and from B to K' is the projection of this line onto the $x-y$ plane; the line from B to D gives the direction of travel required to reach the detector. In this diagram angle $\Delta\psi$ is equal to the angle defined by points KBK' and $\Delta\theta$ by points K'BD. The overall angle of deflection (φ_{bkd}), defined by points KBD can then be derived using Equation 5.1.

$$\cos(\Delta\theta) = \frac{\text{BD}}{\text{BK'}} \tag{5.1a}$$

$$\cos(\Delta\phi) = \frac{\text{BK'}}{BK} \tag{5.1b}$$

$$\cos(\varphi_{bkd}) = \frac{BD}{BK} \tag{5.1c}$$

$$= \cos(\Delta\theta) \cdot \cos(\Delta\psi) \tag{5.1d}$$

$$\varphi_{bkd} = \cos^{-1}(\cos(\theta_{bk} - \Phi_d) \cdot \cos(\psi_{bk})) \tag{5.1e}$$

5.1.2 Near Neighbour Effects

The original geometric model developed as part of the basic scatter model assumes that each voxel can be considered as a point source in relation to all other voxels. This assumption is valid when voxels are at large distances from each other; however, it is not valid for neighbouring voxels. In voxels close to the emission voxel the exact point of emission within the source voxel and of interaction within the scattering voxel will have a significant effect on both the probability of an interaction occurring and the direction of travel of the photon prior to scattering, and hence on the probability of detecting a scattered photon at a given detector location, within a given energy window. In order to determine the overall probability of detecting photons scattered in voxels close to the point of emission, a series of Monte Carlo simulations have been performed using the SIMIND programme. In each simulation a single scattering location has been defined as a cubic voxel consisting of 8^3 sub-voxels, positioned at the centre of the simulation volume. An emission voxel of the same size has then been defined at a series of locations close to the scattering voxel. All voxels, other than the scattering voxel, were defined to have zero attenuation. For each simulation detectors were placed at 360 angles, equally spaced around the simulation volume, parallel to the z-axis.

From the simulation results the probability of detecting a scattered photon at a given detector angle has been found, for a given source position, with a range of energy windows. These probabilities have been normalised to the probability of detecting a scattered photon at the same detector position when the source voxel is at the same location as the scattering voxel, using an open energy window.

The calculation of the probability of the detection of scattered photons in the scatter model has been modified such that the scatter probability for voxels close to the emission voxel is taken to be the simulated probability instead of the combination of the Klein-Nishina scattering probability and the solid angle. The probability of scatter at distant voxels is calculated from the average angular distribution for distant voxels. These values are scaled according to the solid angle that the scattering voxel subtends to the emission voxel, calculated as in the original scatter model. It is expected that, for scattering voxels which are at a significant distance from the source voxel, the model of solid angle used in the original scatter model will be provide a reasonable approximation. In order

to assess this the total probability of detecting scattered photons at any angle, in an open energy window, in the Monte Carlo simulation has been compared to the solid angle model by scaling the Monte Carlo result at a distant voxel to the theoretical value of solid angle at that voxel and comparing the values at other locations closer to the source voxel.

5.1.3 Resolution Modelling

The effect of blurring on the accuracy of reconstruction has been investigated for many years with early papers considering the combined effect of scatter and collimator response by measuring the system response to point sources positioned at different depths in a tissue equivalent phantom (Miller *et al.*. 1985, Hebert *et al.*. 1993). Alternatively Zeng *et al.*. (1991) have proposed a method for deriving the blurring as a result of the collimator, without the contributions of scatter, septal penetration and intrinsic spread of photons in the detector, from the known geometry of the collimator hole.

In recent years algorithms which include the response of a SPECT system to a point source have become more widespread in clinical use. These algorithms consider the overall geometric response of a SPECT system to a point source, which depends on the distance of the source from the collimator, separately to the effects of scatter. A number of methods of estimating the effect of the distance dependent blurring have been developed in both PET and SPECT imaging (Gilland *et al.*. 1994, Brix *et al.*. 1997, Zeng *et al.*. 1998), many of which use a Gaussian of different widths to approximate the point source response at different source to collimator distances. The simulation of the measured projection can then be calculated as the convolution of the activity distribution at each point with the point source response at that source to detector distance, prior to calculating the ray sum for each detector location. In SPECT the effect of attenuation may be included by multiplying the activity at each voxel by the total attenuation from that point to the detector (Gilland *et al.*. 1994).

The projection of the scattered photons from the point of scatter to the point of detection is the same as that for primary photons and so the same resolution model can be used. Methods of applying the resolution model can be divided into three broad categories; convolution in image space, Fourier transformation followed by multiplication in Fourier-space and, incremental blurring between

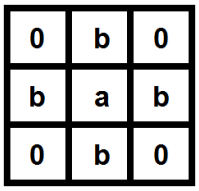

Figure 5.2: Kernel used to approximate collimator response blurring between layers.

layers such as the method proposed by Zeng *et al.*. (1998). Convolution in real space is generally the least efficient technique and so the possible time saving from using Fourier transforms or incremental blurring have been investigated.

In order to apply the resolution model using incremental blurring a measured collimator response function has been used to derive a series of five point blurring kernels where each kernel approximates the blurring from one layer to the next, stepping towards the camera face. Each detector angle is treated separately with the attenuation map and activity distribution (or scattered photon distribution) matrices being rotated to be parallel to the detector. This allows the inter-layer blurring to be applied as the result from the previous layer added to the distribution for the current layer and convolved with the kernel for the current layer. The blurring from the final layer to the detector face is calculated by convolution with a Gaussian with width defined by the collimator response function for the distance of the final layer from the camera face.

The five point blurring kernels are of the form illustrated by Figure 5.2 and are subject to the normalisation constraints

$$b = \frac{1-a}{4} \tag{5.2a}$$

$$0 < a \leq 1. \tag{5.2b}$$

The blurring from each layer l to the detector is approximated by a Gaussian of width σ_l, as given by Equation 5.3.

$$f_l(x,y) = \frac{1}{\sqrt{2\pi\sigma_l^2}} \exp\left(-\frac{x^2+y^2}{2\sigma_l^2}\right) \tag{5.3}$$

Using Equations 5.2a and 5.3 the collimator response for a layer $(l+1)$ adjacent

to layer l can be approximated as

$$f_{l+1}(x,y) \approx a f_l(x,y) + b\left[f_l(x+1,y) + f_l(x-1,y) + f_l(x,y+1) + f_l(x,y-1)\right] \quad (5.4)$$

and hence a new function t_3 defined such that

$$t_3 \approx a t_1 + \frac{1-a}{4} t_2 \quad (5.5)$$

where

$$t_1(x,y) = \exp\left(-\frac{x^2+y^2}{2\sigma_l^2}\right) \quad (5.6a)$$

$$t_2(x,y) = \exp\left(-\frac{(x+1)^2+y^2}{2\sigma_l^2}\right) + \exp\left(-\frac{(x-1)^2+y^2}{2\sigma_l^2}\right) + \exp\left(-\frac{x^2+(y+1)^2}{2\sigma_l^2}\right) + \exp\left(-\frac{x^2+(y-1)^2}{2\sigma_l^2}\right) \quad (5.6b)$$

$$t_3(x,y) = \frac{\sigma_l}{\sigma_{l+1}} \exp\left(-\frac{x^2+y^2}{2\sigma_{l+1}^2}\right) \quad (5.6c)$$

The cost function $F(a)$ given by Equation 5.7 is minimised, using a least squares method, with respect to a. Parameter a can then be calculated using Equation 5.8 for each layer within the image volume (Zeng *et al.*. 1998).

$$F(a) = \sum_x \sum_y \left[a t_1(x,y) + \frac{1-a}{4} t_2(x,y) - t_3(x,y)\right]^2 \quad (5.7)$$

$$a = \frac{\sum_x \sum_y (t_3 - t_2/4)(t_1 - t_2/4)}{(t_1 - t_2/4)^2} \quad (5.8)$$

In order to apply the resolution model in Fourier-space each detector angle is again treated separately with the attenuation map and activity distribution (or scattered photon distribution) matrices being rotated to be parallel to the detector. A fast Fourier transform is performed for each layer of the image and for the corresponding Gaussian blur. The blurring of each layer is then calculated by a point by point multiplication of the two transforms before the inverse Fourier transform is calculated. An advantage of using this technique is that the decon-

volution of the image with the resolution blurring can also be easily calculated by point by point division of the Fourier transform of the blurred image and the transformed blurring Gaussians.

5.1.4 Effect of Increased Attenuation

The Compton scattering process results in reduction of the photon energies as well as a change in direction and so the attenuation experienced by photons after the point of scatter will be increased, as illustrated in Figure 5.3 (Berger *et al.*. 2010). The effect of the increased attenuation after the point of scatter can be included in the scatter model by applying an appropriate scaling factor to the attenuation at each voxel after the point of scatter. The data illustrate that the variation for soft tissue and lung is very similar but that of bone is significantly different. As a result two different sets of scaling factors have been used, one for voxels corresponding to lung and soft tissue and the other for voxels corresponding to bone.

The increase in attenuation will be different for each scattered photon depending on the angle it has scattered through and hence its final energy. In the current implementation of the scatter model it is not practical to calculate the changed attenuation for all photons individually and so the mean photon energy within the selected scatter energy window has been calculated and the scaling factors for this energy have been applied to all scattered photons.

5.1.5 Absorption Effects

The basic scatter model assumes that the contribution of processes other than Compton scattering to the overall attenuation in tissues is negligible at 140keV. In the case of soft tissue and lung this is a reasonable assumption since Compton scatter accounts for 97.75% and 97.53%, respectively, of the total attenuation (Berger *et al.*. 2010). However, for bone the contribution of the photoelectric effect is more significant and so only 90.53% of the attenuation is a result of Compton scattering. The effect of the reduced scattering which occurs compared to that predicted from the linear attenuation coefficient has been incorporated into the scatter model by the use of two scaling factors, applied to the attenuation coefficient at the point of scatter. For voxels with linear attenuation less than or

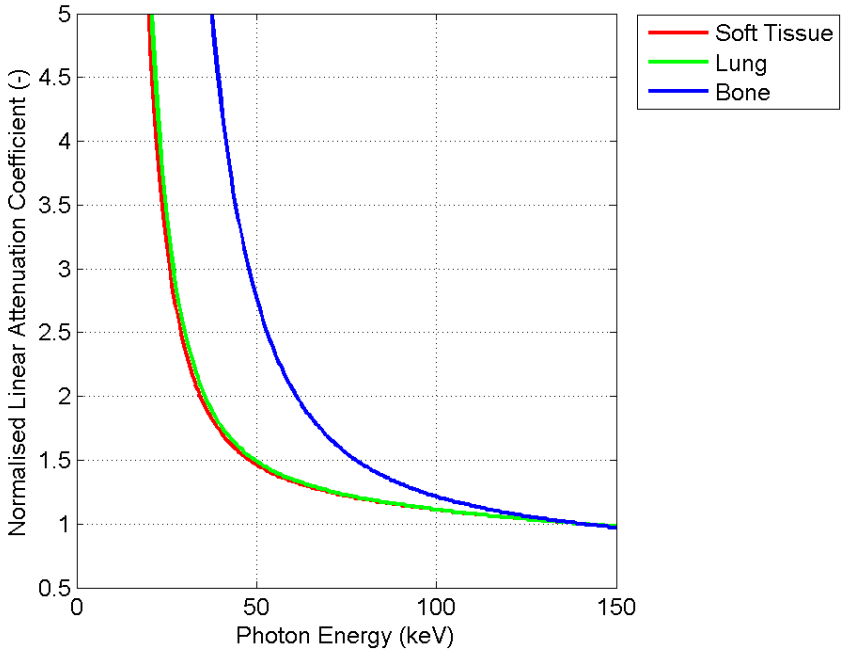

Figure 5.3: Variation in attenuation with photon energy scaled relative to the attenuation at 140keV for soft tissue (red), lung tissue (green) and bone (blue)

equal to 0.16cm^{-1}, i.e. lung and soft tissue, a scaling factor of 0.98 has been used while for those with higher attenuation, i.e. bone, a scaling factor of 0.9 has been used.

5.2 Method

5.2.1 Implementation of 3D model

Although the extension from 2 dimensions to 3 dimensions is conceptually simple it is very computationally expensive as now each voxel is linked to m^3 other voxels rather than m^2. In order to reduce the number of calculations required the effect of calculating the number of photons reaching each scatter point on a reduced matrix has been investigated in 2 dimensions. In order to do this the original 64^2 matrices of attenuation and activity are re-sampled onto 32^2 matrices and the number of photons reaching each scatter point calculated. This matrix of photons reaching each point is then interpolated back to a 64^2 matrix before the contribution of photons scattered at the point of emission is added and the

forward projection to the detector takes place. The scatter sinogram calculated for a single slice of the XCAT phantom has been calculated using this acceleration method and compared to the standard calculation. In the 3-dimensional projector the number of slices is compressed in a similar way.

The accuracy of the single scatter model has been assessed by comparing the results of the model for a 3-dimensional XCAT activity and attenuation distribution with the results of a SIMIND Monte Carlo simulation. In both the model and the simulation the activity extended over 64 slices of the phantom. The Monte Carlo simulation used LEHR collimators and included only single scatter events; the contribution of primary photons in the scatter window was excluded. In order to compare the distribution of the scattered photons both the model and simulation results were scaled to the mean value in the central slice for all projections.

In order to assess the effect of the proposed improvements to the scatter model, each version of the model has been used to calculate the scatter distribution at 8 detector locations, at 45^o to each other, using the XCAT phantom; each version adds the next improvement to the previous version of the model. The error in the number of scatter photons at each detector pixel predicted by each model compared to the Monte Carlo simulation has been calculated by normalising the results from each version of the model to have the same mean value obtained using Monte Carlo simulation. The overall accuracy of each version of the scatter model for each phantom has been determined by considering the square root of the mean of the square of the differences between the normalised model results and the Monte Carlo simulation at each detector pixel.

5.2.2 Resolution Modelling

The first step in any resolution model is to measure the point source response of the collimator to be used. In this work the SIMIND programme has been used to simulate the response of a gamma camera using Low Energy High Resolution (LEHR) collimators. A series of simulations have been performed using point sources at different distances from the camera face, with no attenuation. The number of photons measured at each location on the detector face was then fitted with a Gaussian.

The efficiency of the techniques used to calculate the effect of the collimator

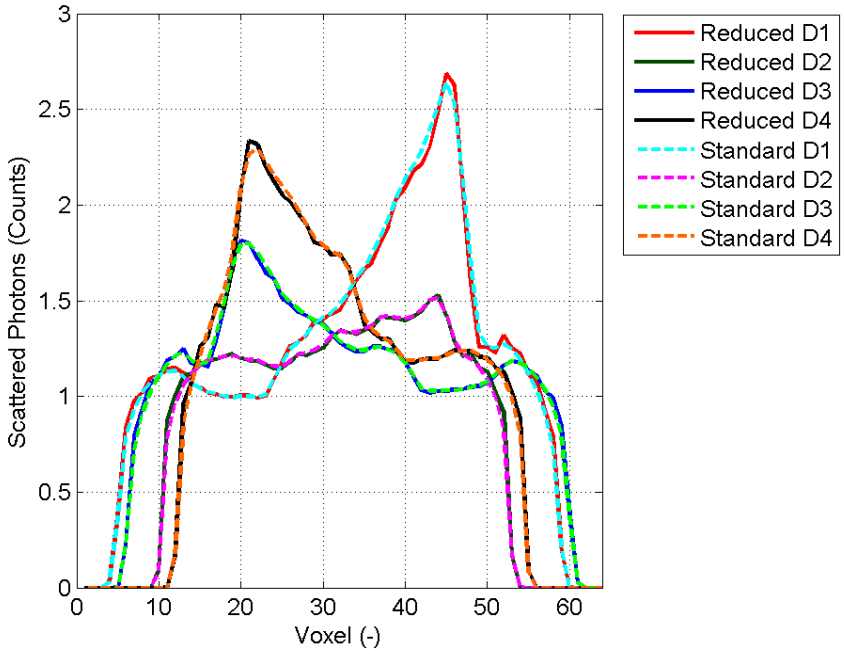

Figure 5.4: Normalised scatter sinograms estimated for a typical scatter energy window using reduced matrix compared to standard calculation in 2 dimensions

response on the measured projections has been assessed by comparing the average time taken to calculate 90 projections for a 64^3 matrix.

5.3 Results

Figure 5.4 shows the scatter sinograms calculated using the XCAT phantom with a reduced matrix size to accelerate the calculation compared to the standard calculation method. The profiles shown correspond to 4 detector positions at 90^o to each other. The maximum absolute percentage difference between the normalised profiles is 0.23%; the mean absolute percentage difference is 0.07%. This demonstrates that a reduced matrix size can be used to calculate the number of photons reaching each scatter point without adversely affecting the accuracy of resulting scatter sinogram.

Figure 5.5 shows a profile through the central slice of the Monte Carlo simulated scatter and model results for 2 projections angles at 90^o to each other. Figure 5.6 shows the difference between the simulated and model results for 8 projections at 45^o to each other. In each case the mean value in the central slice of all projections

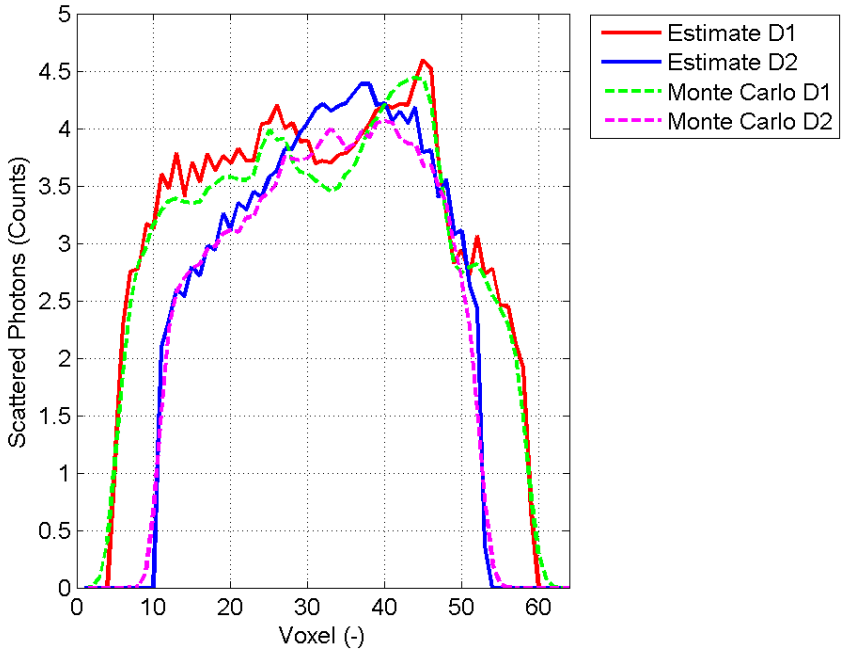

Figure 5.5: Scatter distributions calculated for the central slice of the 3D XCAT phantom using Monte Carlo simulation and the scatter model

has been calculated for the calculated and simulated sinograms and the calculated sinograms scaled such that they have the same mean as the simulation result. The objective here is to identify local variation in the two sets of projection data. A positive value indicates that the scatter model overestimates the activity at that pixel compared to the Monte Carlo simulation. The opposite applies for negative values.

The results indicate that the scatter model is able to broadly recreate the correct shape of distribution, however, it is clear that significant sources of error exist within the original scatter model. In particular it is noted that the number of scattered photons detected is overestimated close to the centre of the body while it is underestimated in more superficial regions.

5.3.1 Near Neighbour Effects

The variation in probability of detecting a photon at a given detector angle with distance between the source and scattering voxels is shown in Figure 5.7; in each case an energy window of 20 to 200keV has been used. The number of

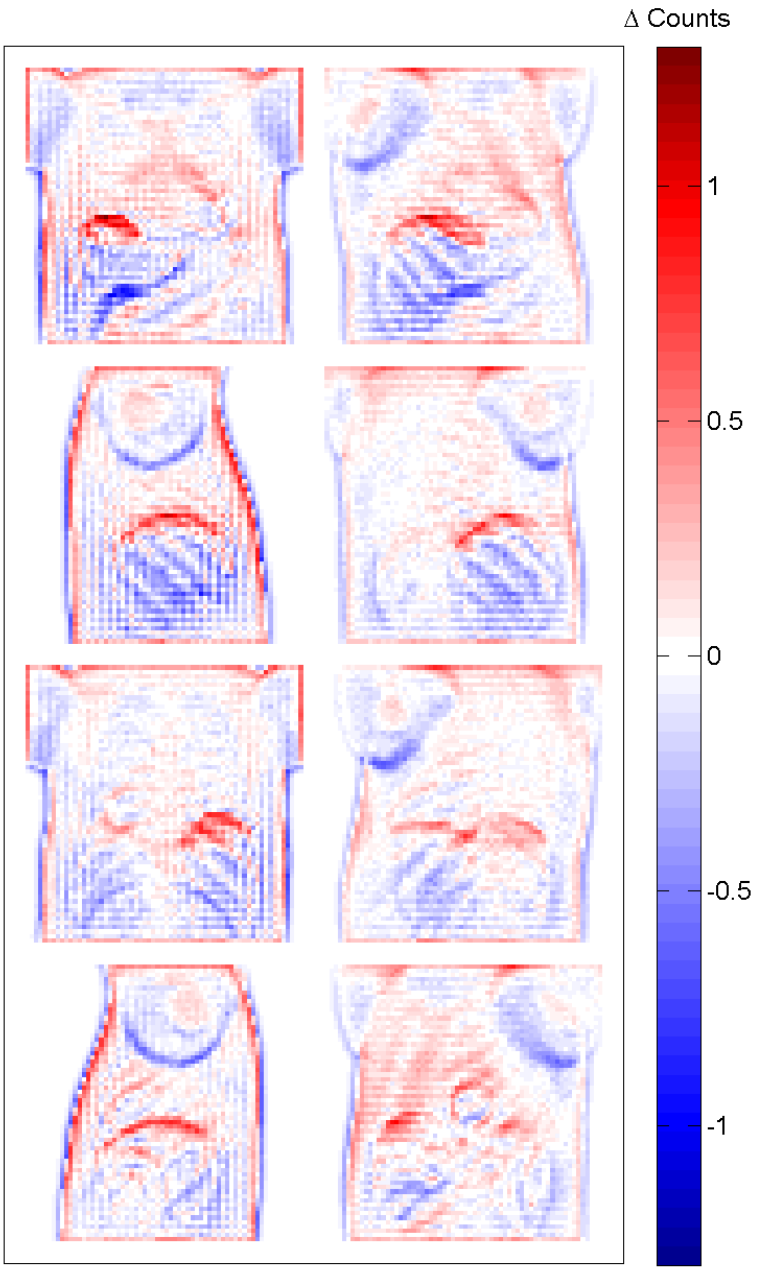

Figure 5.6: Error in scatter distributions calculated for the 3D XCAT phantom using the scatter model compared to Monte Carlo simulation (as shown in Figure 5.5)

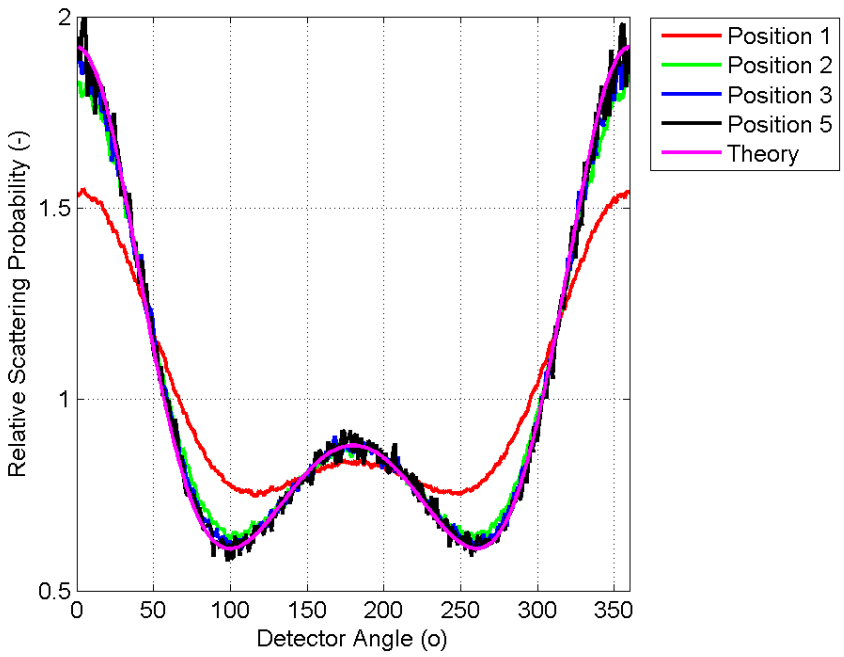

Figure 5.7: The relative detection probabilities for scattered photons at detector positions around a single scattering pixel positioned at (0,0,0). The emission source is located at (1,0,0) position 1, (2,0,0) position 2, (3,0,0) position 3 and (5,0,0) position 5 (each voxel is 0.624cm). The Klein-Nishina probability of scattering through each angle is also shown

photons detected at a given angle has been normalised to the total number of photons detected for the given source location. The Klein-Nishina probability for each angle is also shown for comparison. For scattering voxels close to the point of emission there is much less variation in scatter probability with detector angle than predicted using the Klein-Nishina formula. This is because when the scattering and source voxels are close together photons with a large range of initial directions of travel will interact with the scattering voxel compared to the original model which predicts a single angle based on the location of the centres of the two voxels. For scattering voxels which are at a distance of more than 3 voxels from the source voxel the distribution of scattered photons does not change with distance and is approximately equal to the Klein-Nishina prediction.

Figure 5.8 shows the simulated variation in the total probability of scatter with distance between the scatter and emission voxels compared to the theoretical probability, calculated from the solid angle subtended by one voxel to another. Two or three simulations were performed at each of the distances investigated and the uncertainty in the simulation results has been estimated as the range

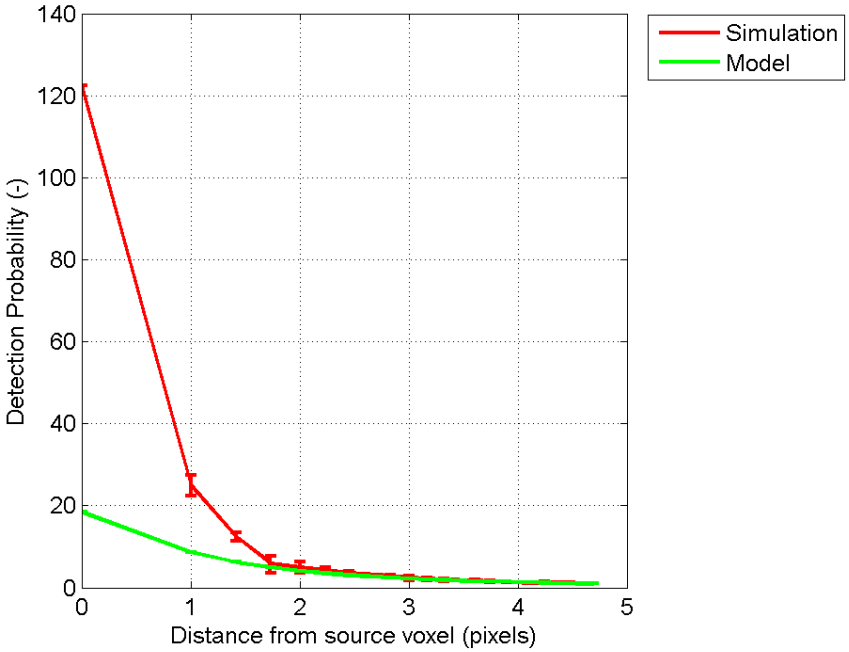

Figure 5.8: The relative probability for detection of scatter events in all detectors at all energies for different source to scatter voxel distances. The Monte Carlo results and calculated solid angle have been normalised to the values at the most distant voxel location.

defined by the different simulation results; these uncertainties are illustrated as error bars on the graph. The results show that, for voxels which are separated from the source pixel by distance of more than 3 pixels, the total probability of scatter occurring is similar to that calculated using the theoretical model of solid angle.

5.3.2 Resolution Modelling

The width of the Gaussian functions which best fitted the response of a gamma camera, with LEHR collimator, to a point source at different distances from the camera face is shown in Figure 5.9. The time taken to perform the resolution blurring calculation using full convolution, Fourier transform and incremental blurring techniques is shown in Table 5.1.

These results show that the use of incremental blurring is approximately three times faster than the use of a fast Fourier transform (FFT) technique where each layer is blurred individually. However, the incremental blurring technique sums

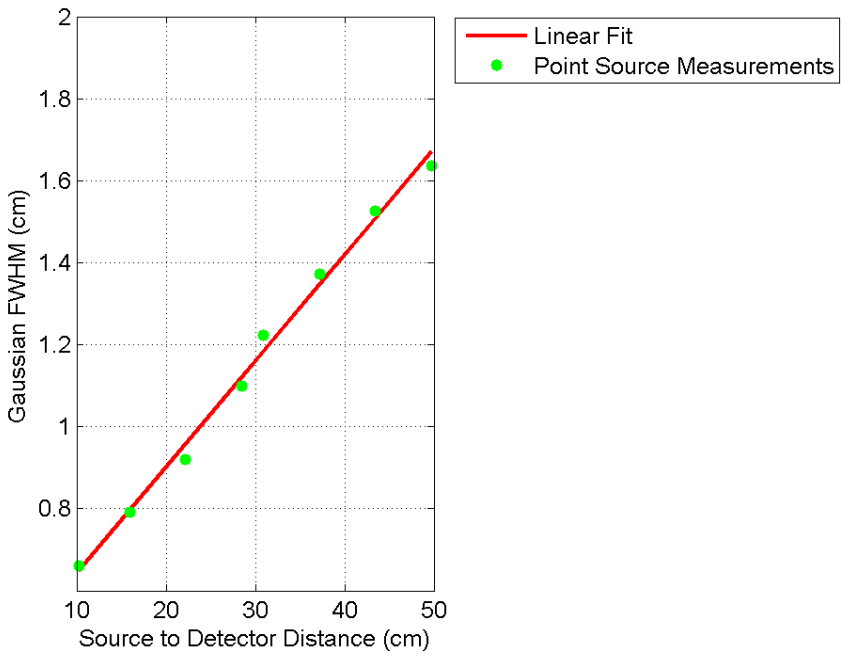

Figure 5.9: Distance dependent blurring of a point source for LEHR collimators

Convolution Technique	Mean time (s)	Standard Deviation
Full Convolution	111.2	0.1
Fourier Transform	5.216	0.012
Incremental Blurring	1.753	0.009

Table 5.1: Times taken to calculate resolution blurring effects using different techniques

the contribution along each path during the calculation while the FFT technique calculates the contribution of each layer separately before summing the contribution of all layers. In the reconstruction algorithm, when calculating the partial derivatives for each point in the image matrix, the contribution from each point to each detector element is required and not just the sum of contributions along each path. As a result the use of incremental blurring would take significantly longer as the process would need to be repeated for each layer individually. The FFT technique has therefore been selected for use in this work.

Figure 5.10 shows the forward projection of primary photons with and without the resolution model compared to the SIMIND simulation of the same XCAT phantom for the central slice of the anterior projection. The root mean square errors in the projection data generated using the model with and without depth

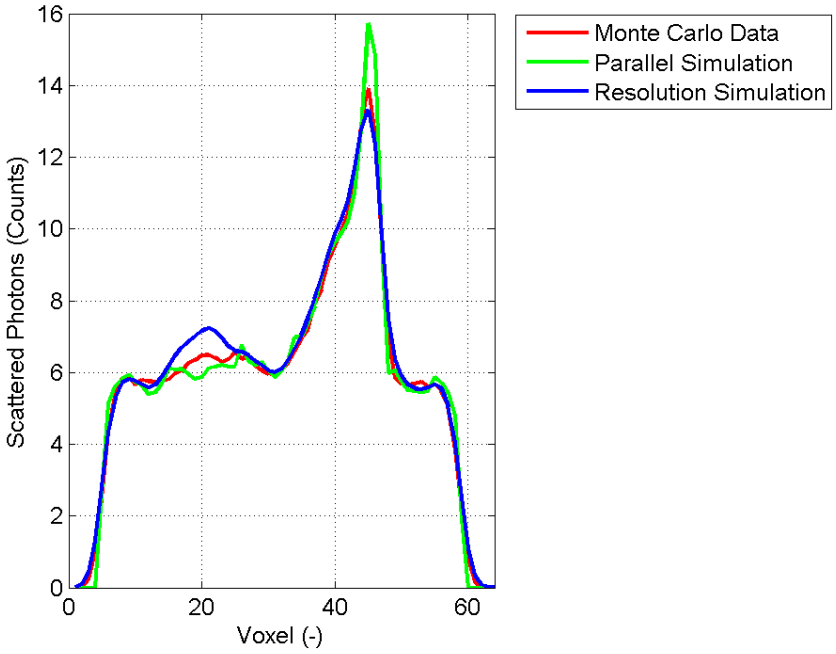

Figure 5.10: Comparison of Monte Carlo simulation of primary photon projection data with forward projection model with and without depth dependent resolution effects.

dependent resolution effects were 0.045 and 0.096 respectively; the distribution of the differences between the model and Monte Carlo projections are shown in Figure 5.11. These results demonstrate a reduction in errors seen at the boundaries between different tissue types.

5.3.3 Comparison to Monte Carlo Data

Table 5.2 shows the root mean square error when comparing the normalised scatter projection data calculated using each version of the scatter model to the Monte Carlo simulation for two energy windows; 80-126keV and 126-154keV. Each version of the scatter model adds the next improvement to the previous version of the model. Figure 5.12 show the differences between the models and the Monte Carlo simulation across the detector in an 80-126keV energy window for two projections positioned at 90^o to each other.

The results show that the use of Monte Carlo simulations to estimate the contribution of the emission voxel's near neighbours to the measured scattered photons, provides a significant improvement to the accuracy of the model. The addition

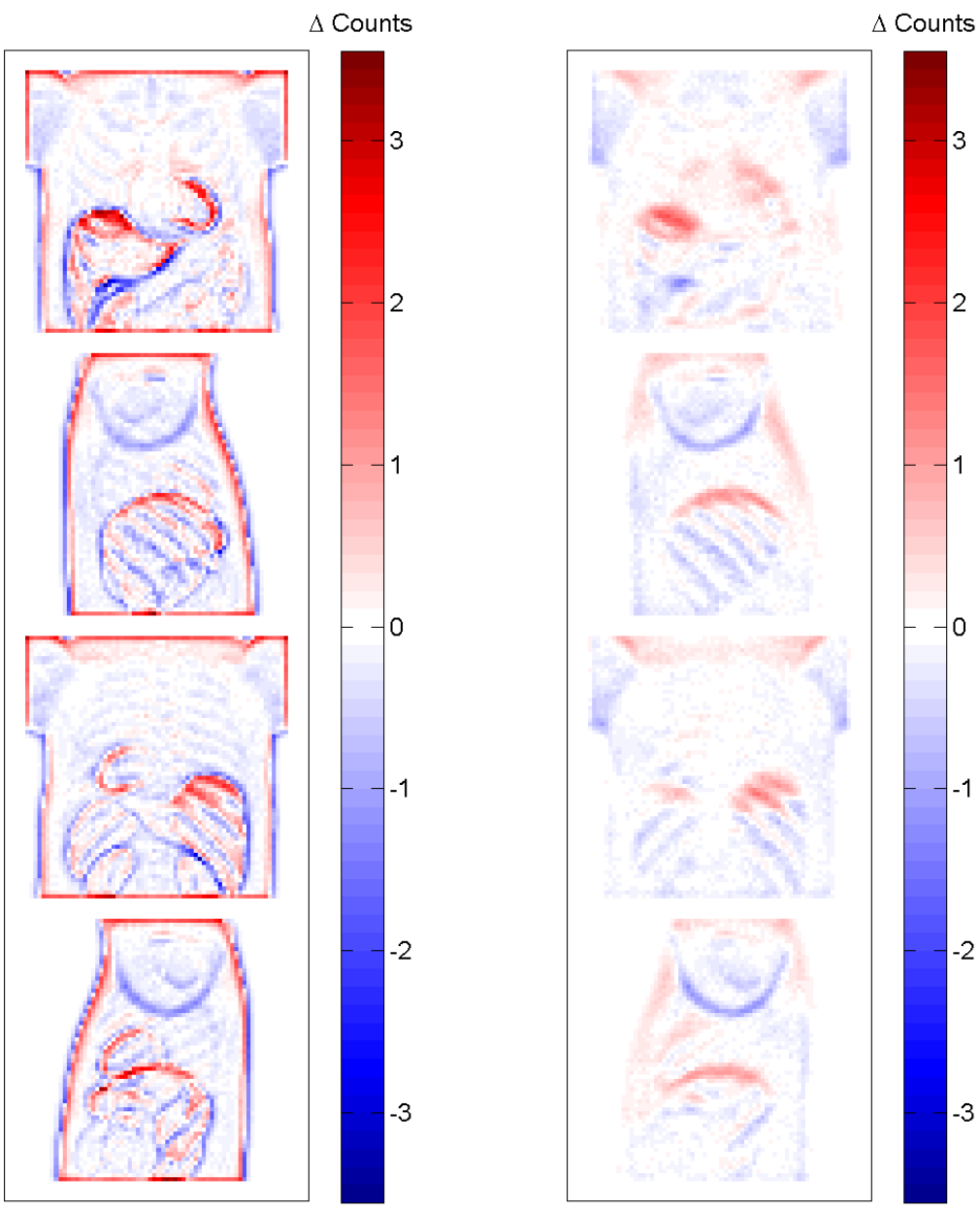

Figure 5.11: Distribution of errors of primary photon projection data (a) with and (b) without depth dependent resolution effects compared to Monte Carlo simulation.

	80-126keV window	126-154keV window
Original Model	0.077	0.075
Near Neighbour	0.073	0.069
Resolution model	0.056	0.050
Increased Attenuation	0.056	0.051
Absorption Effects	0.056	0.050

Table 5.2: Root mean square error for each model compared to Monte Carlo simulation

of modelling of the collimator response to a point source further improves the accuracy. However the inclusion of the effect of increased attenuation after the point of scatter and the difference in the scatter fraction between bone and soft tissue do not provide any additional improvement.

5.4 Discussion

The scatter model has been successfully extended from a single slice to three dimensions. It has been shown that the accuracy can be improved by using data acquired from Monte Carlo simulation to estimate the scatter from voxels close to the source voxel. As expected, the inclusion of depth dependent resolution modelling improves the accuracy of the forward projection at the boundary between regions with different activity levels. This is reflected in the reduction in the number of voxels with large errors compared to the Monte Carlo simulation. As a result the distribution of errors is shown to be closer to the ideal situation (i.e. when the model and simulation produce identical results) and the overall root mean square error is reduced.

Inclusion of the effect of the increase in attenuation of photons after scattering (as a result of the reduction in photon energy) does not affect the results for a window centred over the photopeak. This is because photons detected in this energy window have not experienced significant energy loss. For photons detected in a lower energy window the use of the mean energy window to estimate the effect of increased attenuation for all photons is not sufficiently accurate to predict the difference in attenuation experienced. This is demonstrated by a small increase in the errors calculated when including this effect in the model. A more accurate model of the increase in attenuation with reduced photon energy could be produced by calculating the reduction in energy for each photon path (from

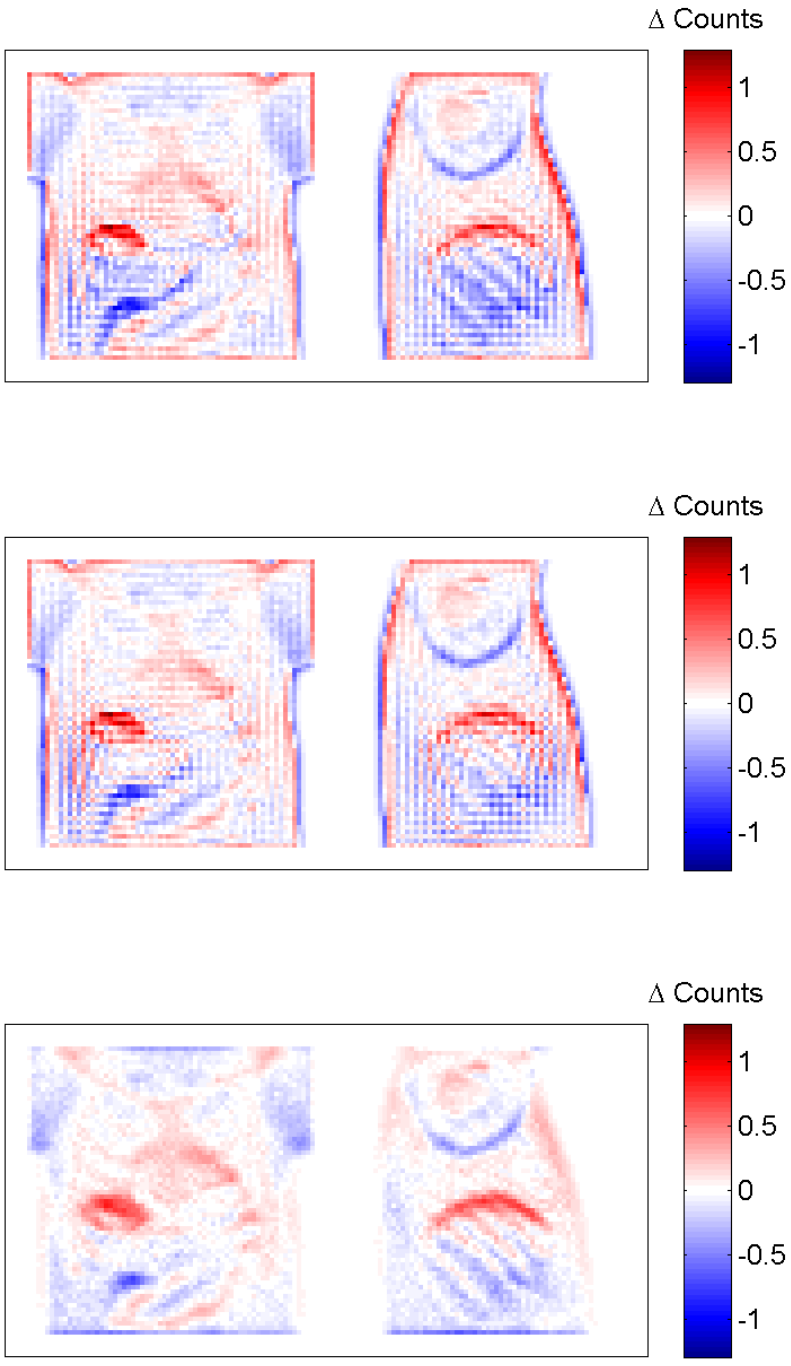

Figure 5.12: Comparison of Monte Carlo simulation with forward projection scatter model. Top line: original model, second line: including near neighbour effects, third line: including resolution model

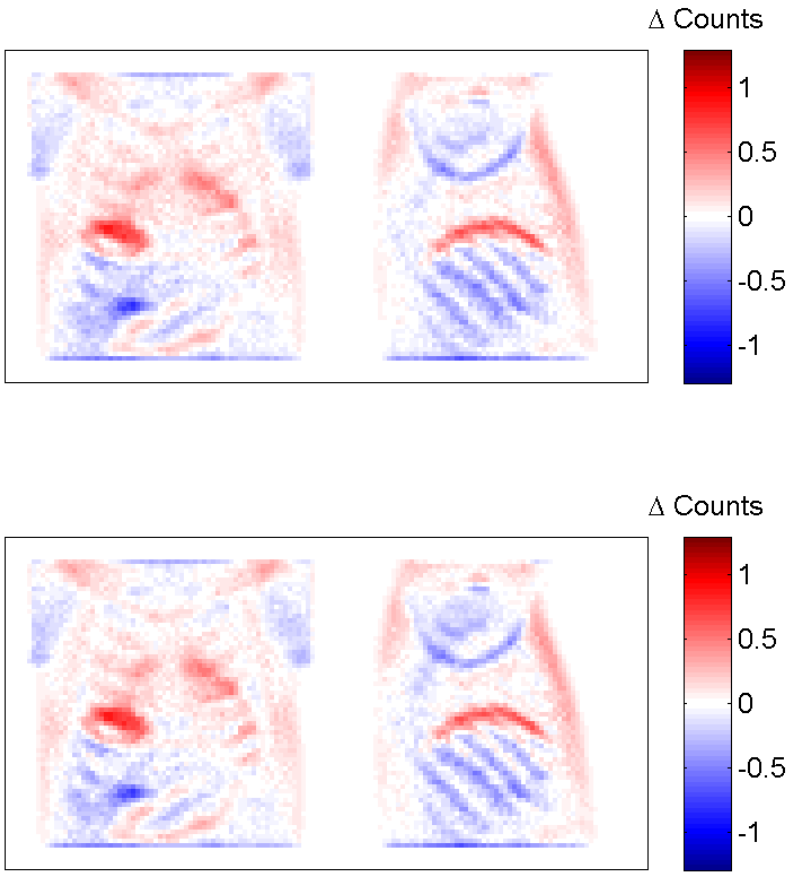

Figure 5.12: Comparison of Monte Carlo simulation with forward projection scatter model (continued). Top line: including reduced attenuation after the point of scatter, second line: including variation in Compton scatter fraction

the scattering angle) and applying the increase in attenuation separately for each path. However, this would require a separate forward projection for each possible scattering angle and hence is not currently feasible to implement in three dimensions.

The results also suggest that the inclusion of differences in the scatter fraction for different materials does not significantly improve the accuracy. This is because the proportion of attenuation that occurs as a result of Compton scattering is similar for all soft tissues and only a small amount of bone is present in the thorax. It is anticipated that if the scatter model were to be used in regions other than the thorax this effect may be more significant.

Given the results presented here, the final scatter model has been defined to

include the effect of differences in scatter pattern for voxels close to the source voxel and the effect of blurring as a result of the distance from the scatter voxel to the detector but the energy effects are not included. The complete model is given by Equation 5.9.

$$\boldsymbol{s}(\boldsymbol{\mu}) = \boldsymbol{A'_d}(\boldsymbol{\mu})\boldsymbol{S'_k}(\boldsymbol{\mu})\boldsymbol{A'_k}(\boldsymbol{\mu})\boldsymbol{\phi} + \boldsymbol{A'_d}(\boldsymbol{\mu})\boldsymbol{S_b}(\boldsymbol{\mu})\boldsymbol{\phi} \tag{5.9}$$

$$\boldsymbol{\phi} = \boldsymbol{Q} \otimes \boldsymbol{\lambda} \tag{5.10a}$$

$$(\boldsymbol{A'_k})_{bjk} = \omega'_{bjk} \exp\left[-\int_b^k \boldsymbol{\mu}(x)\mathrm{d}x\right] \tag{5.10b}$$

$$(\boldsymbol{S'_k})_{kjj'} = (1 - e^{\mu_k})N'_{jj'} \tag{5.10c}$$

$$(\boldsymbol{S_b})_{bkjj'} = \begin{cases} 0.5\left(1 - e^{-\mu_k \sqrt[3]{\frac{3}{4\pi}}}\right), & b = k \\ 0 & b \neq k \end{cases} \tag{5.10d}$$

$$(\boldsymbol{A'_d})_{kj'd} = c'_{kj'd} \exp\left[-\int_k^d \boldsymbol{\mu}(x)\mathrm{d}x\right] \tag{5.10e}$$

$\boldsymbol{\lambda}$ is the activity distribution.

$\boldsymbol{Q}$ is the emission function and gives the proportion of photons emitted within a solid angle defined by Ω_j. $\boldsymbol{Q}$ is isotropic and could define an infinite number of directions j.

$\boldsymbol{\phi}$ gives the number of photons emitted from each voxel b travelling in each direction j; this is a block vector with b blocks each of length j.

$\boldsymbol{A'_k}$ is the attenuated transfer matrix giving the probability of a photon emitted from voxel b reaching voxel k; this is a block matrix with b by k blocks, each block is a j by j diagonal matrix since the transfer matrix is not associated with a change in direction.

ω'_{bjk} is the modified solid angle (as shown in Figure 5.8), i.e. the proportion of photons from voxel b that will pass through voxel k as a result of their relative locations

$\boldsymbol{S'_k}$ is the probability of a photon scattering in voxel k from direction j (defined by the positions of b and k) to direction j' (defined by the positions of k and d); this is a k by k block diagonal matrix where each block has j by j' elements.

$N'_{jj'}$ is the probability of scattering from direction j to j' based on simulation results for near-neighbours (as shown in Figure 5.7) and the Klein-

Nishina probability for distant voxels.

$\boldsymbol{S_b}$ is the probability of scattering occurring in the same voxel as the emission; this is a b by k block diagonal matrix where each block has j by j' elements.

$\boldsymbol{A'_d}$ is the attenuated transfer matrix giving the probability of a photon scattered in voxel k reaching detector element d, including the distance dependent resolution of the detector; this is a block matrix with k by d blocks, each block is a j' by j' diagonal matrix since the transfer matrix is not associated with a change in direction.

$c'_{kj'd}$ gives contribution of geometric effects to the probability of a photon from voxel k, travelling in direction j', reaching detector d including the distance dependent collimator response.

5.5 Conclusion

The 2-dimensional scatter model presented in Chapter 3 has been successfully extended to 3 dimensions. Improvements to the model have been made by modelling the scattering of photons in voxels close to the point of emission using Monte Carlo simulation. The use of resolution modelling has also been investigated and found to improve the accuracy of the estimation of both scattered and primary photons. However, it has been found that including the effects of increased photon attenuation after the point of scatter and increased photon absorption in bone (as compared to soft tissue) does not offer any significant improvement in accuracy of the scatter model compared to Monte Carlo simulation.

6 Reconstruction in 3 Dimensions

In this chapter the improved 3-dimensional scatter model derived in Chapter 5 is used to test the reconstruction algorithm developed in Chapter 4 in 3 dimensions and to investigate the importance of including resolution effects in all parts of the reconstruction algorithm. The use of ordered subsets or a reduced matrix size for the attenuation map reconstruction are considered as possible techniques for reducing the time taken to perform the reconstruction.

6.1 Theory

6.1.1 One Step Late Assumption

In Section 4.1 a one-step late approximation to the gradient of the likelihood function was used in order to improve calculation times. This approximation assumes that the effect of changes to the attenuation before and after the point of scatter can be considered to be small compared to the effect of changes at the point of scatter. The validity of this assumption in 3 dimensions has been tested by calculating the change in likelihood between two attenuation maps (given the true activity distribution) when the attenuation is set to be equal to the correct value for different parts of the sinogram estimation. Three estimated scatter sinograms were calculated, using the estimated value of the attenuation map prior to the point of scatter, at the point of scatter or after the point of scatter, the true attenuation was used at all other points for each sinogram estimation. The relative likelihood of each sinogram was then calculated using Equation 6.1.

$$L(\boldsymbol{\mu}, \boldsymbol{\lambda}) = \frac{\sum_d \left(-(\boldsymbol{s}(\boldsymbol{\mu}))_d + (\boldsymbol{n}^s)_d \cdot \ln(\boldsymbol{s}(\boldsymbol{\mu}))_d\right)}{\sum_d \left(-(\boldsymbol{n}^s)_d + (\boldsymbol{n}^s)_d \cdot \ln(\boldsymbol{n}^s)_d\right)} \tag{6.1}$$

6.2 Method

6.2.1 Simulated Data

For each of the tests presented in this chapter projection data were simulated using a rotation based forward projector (developed in MatLAB) which was perfectly matched to the projectors used in the reconstructions, with resolution modelling equivalent to LEHR collimators. In each case a standard SPECT geometry was used with projections every 4^o over 360^o and 32^3 or 64^3 detector elements per projection. In each case the simulations were performed using a 3D realisation of the male XCAT phantom without respiratory or cardiac motion with the arms raised above the head.

The mean and root mean square error in the reconstructed activity distribution and attenuation map were calculated for each reconstruction in order to compare the results of the different reconstructions.

6.2.2 Use of Polar Plots

The use of polar plots to represent the activity distribution through the myocardium on a single image has been proposed by Garcia *et al.*. (1985). In such a representation slices of the myocardium from the apex to the base are displayed as concentric rings on a polar plot with the apex appearing at the centre of the image and the base as the outermost circle. In this work code has been developed which creates polar plots for a given image by first rotating it such that slices through the volume correspond to the short axis slices and then extracting slices containing part of the myocardium; for reconstructions using the XCAT phantom the rotation angles and slices required were determined from the true XCAT phantom. A mask was then applied to the image so that voxels which did not correspond to part of the myocardium were set to zero; the mask for reconstructions of the XCAT phantom was determined from the true phantom and with the use of a threshold in other cases.

The centre of each short axis slice was determined automatically from the reorientated images such that there was an equal number of counts in each quadrant of the image. Each short axis image was then radially divided into 36 segments and

the total counts in each segment calculated. The ring in the resulting polar plot was also divided into 36 segments with each segment being assigned the value of the total counts in the corresponding short axis slice segment.

In order to compare the relative activity reconstructed by different methods, and hence to aid the identification of perfusion defects, each image set was re-orientated and masked to give the short axis views of the myocardium without extra-cardiac activity. These sets of short axis images were then scaled to have the same mean value as the reference image (e.g. reconstruction with perfect attenuation correction) and a voxel by voxel subtraction performed. The difference image was then used to calculate a polar plot of the scaled differences between the two images in order to identify local variation in the two estimated activity distributions. A positive value indicates that the a technique overestimates the activity in that segment compared to reconstruction with exact attenuation correction. The opposite applies for negative values.

6.2.3 Effect of Resolution Modelling

In Section 5.1.3 the use of resolution modelling to improve the accuracy of estimation of forward projection of photons from the point of emission to the point of detection, and hence to improve the accuracy of the reconstructed activity distribution, was discussed. Since the detection process is the same for primary and scattered photons the same resolution model could be used in the reconstruction of the attenuation map as in the reconstruction of the activity distribution. However, since the attenuation map is unlikely to require the same level of detail as the activity distribution it is possible that the inclusion of the resolution model will not improve the reconstruction of the attenuation map or that the the model may be able to be omitted from either the MLAA or SMLGA steps of the attenuation map reconstruction. This would have the potential to reduce the time taken to perform the attenuation map estimation step of the reconstruction algorithm.

In order to assess whether it is necessary to include a model of the collimator response in the reconstruction of the attenuation map, reconstructions were performed which included the resolution model in the activity distribution reconstruction (MLEM) only, in the activity reconstruction and either the MLAA step or the SMLGA step of the attenuation reconstruction and finally in all parts

of reconstruction. In each case the resolution model was included only in the forward projection part of the reconstruction.

6.2.4 Improving Calculation Time

In order to reduce the total time taken for the solution to converge, two possible techniques for reducing the amount of data used in each iteration have been considered.

6.2.4.1 Ordered Subsets

The use of ordered subset (OS) algorithms has been shown to significantly reduce image reconstruction times for activity distributions (Hudson & Larkin 1994) and transmission tomography (Erdogan & Fessler 1999, Beekman & Kamphuis 2001). Ordered subset methods group the projection data which is to be used to reconstruct the image into blocks (or subsets). Each subset is then used in turn to perform a sub-iteration of the reconstruction in the same way as the full data would be used in a standard iteration. Each subset is used in turn and one full iteration is defined to be a single pass through all the subsets.

The order in which the projections are processed in a ordered subset algorithm may be arbitrary but, as Hudson & Larkin (1994) note, it may be advantageous to select the order of the subsets such that the maximum amount of new information is introduced by each subsequent projection. In the work presented here the projections in each subset have been chosen such that there is maximal angular separation between the projections within each subset; i.e. for s subsets, subset 1 contains projections 1, $(s+1)$, $(2s+1)$, $(3s+1)$..., $(ns+1)$, subset 2 contains projections 2, $(s+2)$, $(2s+2)$, $(3s+2)$..., $(ns+2)$ etc.

The effect of using 2, 5, 10, 15 or 45 subsets has been compared to reconstruction without the use of subsets in order to assess the effect of both the quality of the reconstructed images and the time taken per iteration. The same subsets were used in all parts of each reconstruction.

6.2.4.2 Reduced Matrix size

The attenuation map created during the reconstruction process is used only for attenuation correction (and potentially for scatter estimation) and so fine details within the attenuation do not necessarily need to be recovered by the reconstruction process. Hence, it may be sufficient to reconstruct the attenuation map on a coarser matrix than that which is used for the activity distribution. In order to investigate this a reconstruction which uses the standard 64^3 matrix size for all iterations has been compared to those which use a coarse 32^3 matrix for all iterations or a 32^3 matrix for the initial iterations and a 64^3 matrix for the final 1, 2, 5 or 10 iterations of the attenuation map reconstruction. A 64^3 matrix was used for all iterations of the activity distribution and a total of 10 iterations with 10 subsets were performed in each case.

6.3 Results

6.3.1 One Step Late Assumption

The relative likelihoods of scatter sinograms with estimated attenuation in each part of the estimated sinogram are shown in Table 6.1. These results show that if the scatter is estimated only at locations prior to the point of scatter then the likelihood is very close to the maximum. Hence, changes to the attenuation prior to the point of scatter will not have a significant effect on the likelihood. However, the effect of estimating the attenuation after the point of scatter is similar to estimation at the point of scatter and so this is also important to the calculation of the gradient of the likelihood. The scatter update algorithm has therefore been modified to include the effect of changing the attenuation after the point of scatter as shown in Equation 6.4.

$$\frac{\partial L^s(\boldsymbol{\mu})}{\partial \boldsymbol{\mu}} = \sum_d \left(-\frac{\partial (\boldsymbol{s}(\boldsymbol{\mu}))_d}{\partial \boldsymbol{\mu}} + \frac{(\boldsymbol{n}^s)_d}{(\boldsymbol{s}(\boldsymbol{\mu}))_d} \cdot \frac{\partial (\boldsymbol{s}(\boldsymbol{\mu}))_d}{\partial \boldsymbol{\mu}} \right) \tag{6.2}$$

Location of estimated scatter	Relative Likelihood
Prior to scatter point	0.999
At scatter point	0.816
After scatter point	0.822

Table 6.1: Relative likelihood of scatter sinograms estimated with the true attenuation at different points.

$$\frac{\partial(\boldsymbol{s}(\boldsymbol{\mu}))_d}{\partial \mu_i} \approx \frac{\partial \boldsymbol{A_d}(\boldsymbol{\mu})}{\partial \mu_i}\boldsymbol{S_k}(\boldsymbol{\mu})\boldsymbol{A_k}(\boldsymbol{\mu})\boldsymbol{\phi} + \boldsymbol{A_d}(\boldsymbol{\mu})\frac{\partial \boldsymbol{S_k}(\boldsymbol{\mu})}{\partial \mu_i}\boldsymbol{A_k}(\boldsymbol{\mu})\boldsymbol{\phi} + \boldsymbol{S_b}(\boldsymbol{\mu})\boldsymbol{\phi} + \frac{\partial \boldsymbol{S_b}(\boldsymbol{\mu})}{\partial \mu_i}\boldsymbol{A_d}(\boldsymbol{\mu})\frac{\partial \boldsymbol{A_d}(\boldsymbol{\mu})}{\partial \mu_i}\boldsymbol{\phi} \quad (6.3)$$

$$(\boldsymbol{\mu}^{i+1})_k = (\boldsymbol{\mu}^i)_k + \alpha_s \sum_d \left(-\sum_b D'_{bd}(\boldsymbol{\mu}^i, k) + (\boldsymbol{n}^s)_d \frac{\sum_b D'_{bd}(\boldsymbol{\mu}^i, k)}{(\boldsymbol{s}(\boldsymbol{\mu}))_d} \right) \quad (6.4)$$

$$\begin{aligned} D'_{bd}(\boldsymbol{\mu}^i, k) = \sum_{b \neq k} \Bigg[& (\boldsymbol{\phi})_b \omega_{bjk} \exp\left[-\int_b^k \boldsymbol{\mu}(x)\mathrm{d}x \right] c_{kj'd} \exp\left[-\int_k^d \boldsymbol{\mu}(x)\mathrm{d}x \right] N_{jj'} e^{-(\boldsymbol{\mu}^i)_k} \\ & - (\boldsymbol{\phi})_b \omega_{bjk} \exp\left[-\int_b^k \boldsymbol{\mu}(x)\mathrm{d}x \right] c_{kj'd} \exp\left[-\int_k^d \boldsymbol{\mu}(x)\mathrm{d}x \right] N_{jj'} (1 - e^{-(\boldsymbol{\mu}^i)_k}) \Bigg] \\ & + \sqrt[3]{\frac{3}{4\pi}} \frac{(\boldsymbol{\lambda})_{b=k}}{2} c_{kj'd} \exp\left[-\int_k^d \boldsymbol{\mu}(x)\mathrm{d}x \right] e^{-(\boldsymbol{\mu}^i)_{b=k} \sqrt[3]{\frac{3}{4\pi}}} \\ & - \frac{(\boldsymbol{\lambda})_{b=k}}{2} c_{kj'd} \exp\left[-\int_k^d \boldsymbol{\mu}(x)\mathrm{d}x \right] (1 - e^{-(\boldsymbol{\mu}^i)_{b=k} \sqrt[3]{\frac{3}{4\pi}}}) \end{aligned} \quad (6.5)$$

6.3.2 Effect of Resolution Modelling

The results of the 3-dimensional reconstruction of data generated using the rotation based projector with resolution modelling of LEHR collimators, for the 32^3 male XCAT phantom, are shown in Figure 6.1. The images are from a central slice through the phantom and demonstrate that the inclusion of the resolution model in the MLAA step has the most significant effect on the accuracy of the reconstruction. When the resolution model is included in all parts of the reconstruction the cross-talk between the emission and attenuation is reduced and some contrast can be seen between the lung and soft tissue regions.

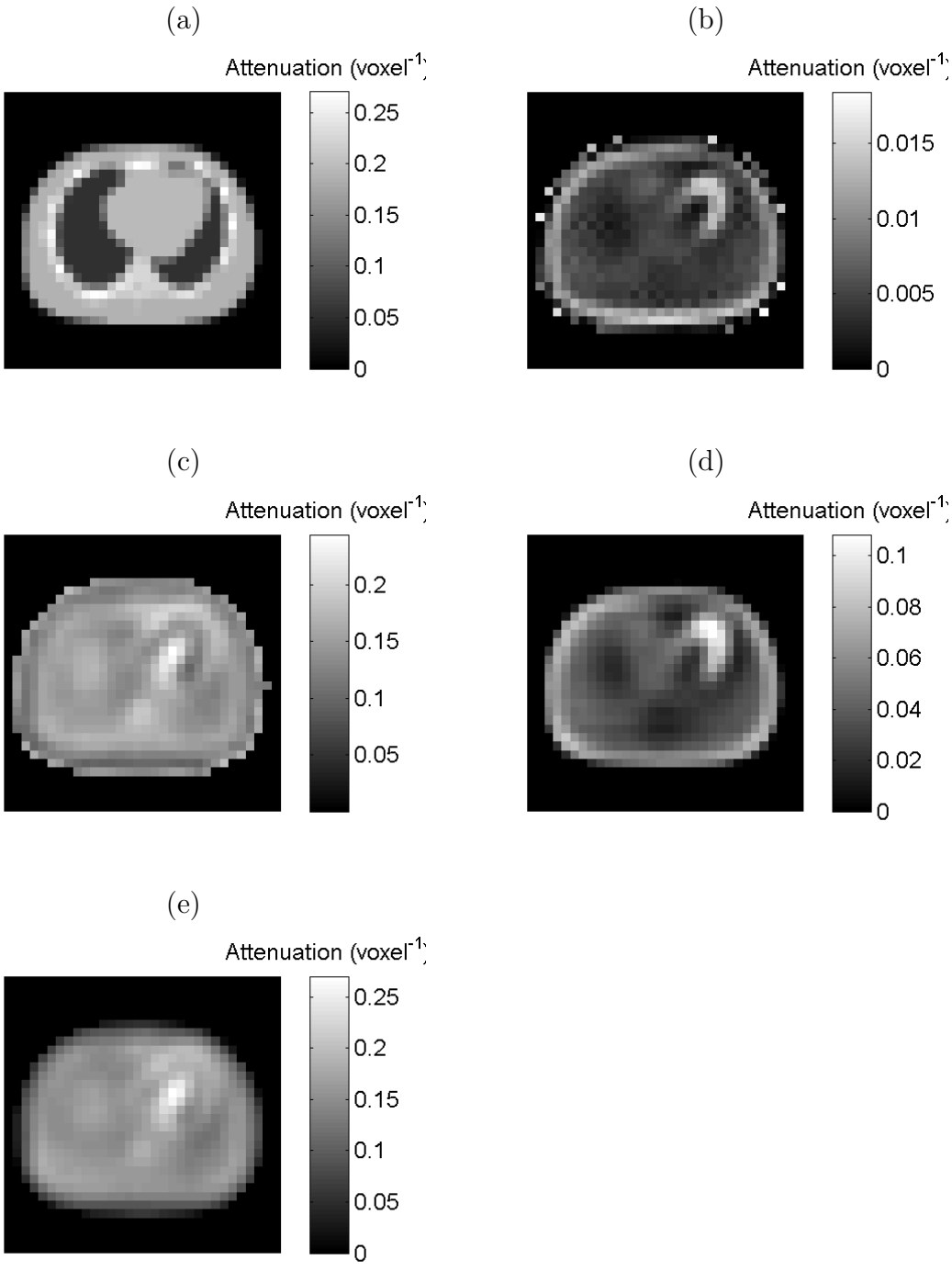

Figure 6.1: Reconstructed attenuation maps for the central slice of a 3D reconstruction using a 360^o imaging geometry; (a) true phantom attenuation map (b) with resolution modelling for emission only, (c) with resolution modelling for emission and MLAA reconstruction steps, (d) with resolution modelling for emission and SMLGA reconstruction steps and, (e) with resolution modelling in all parts on the reconstruction

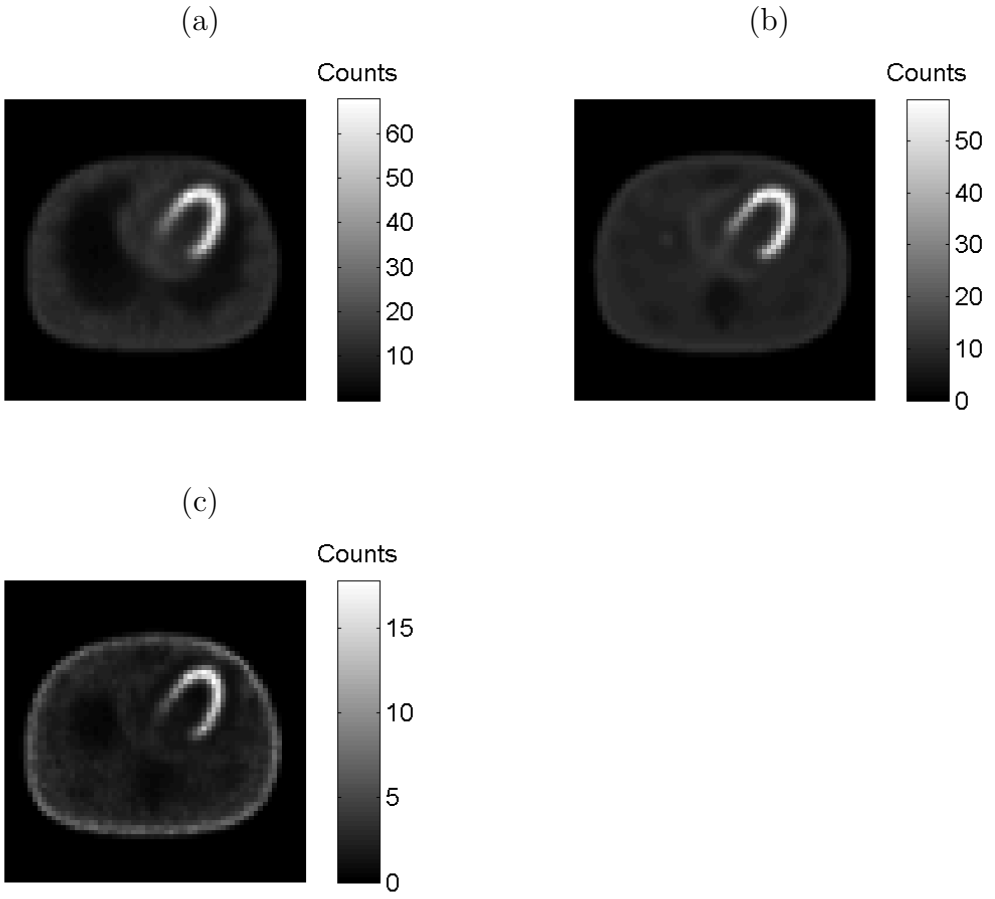

Figure 6.2: Reconstructed activity distribution for the central slice of a 3D reconstruction using a 360^o imaging geometry; (a) exact attenuation correction, (b) scatter based attenuation correction, (c) without attenuation correction

Figure 6.2 shows the results of the reconstruction with scatter based attenuation correction for a central slice through the 64^3 male XCAT phantom compared to reconstruction with perfect attenuation correction and without attenuation correction. Figure 6.3 shows polar plots of the activity distribution in the heart region for each reconstruction technique. The difference between the activity distribution reconstructed in the area of the heart with perfect attenuation correction and that reconstructed using either scatter based attenuation correction or without attenuation correction are shown in Figure 6.4.

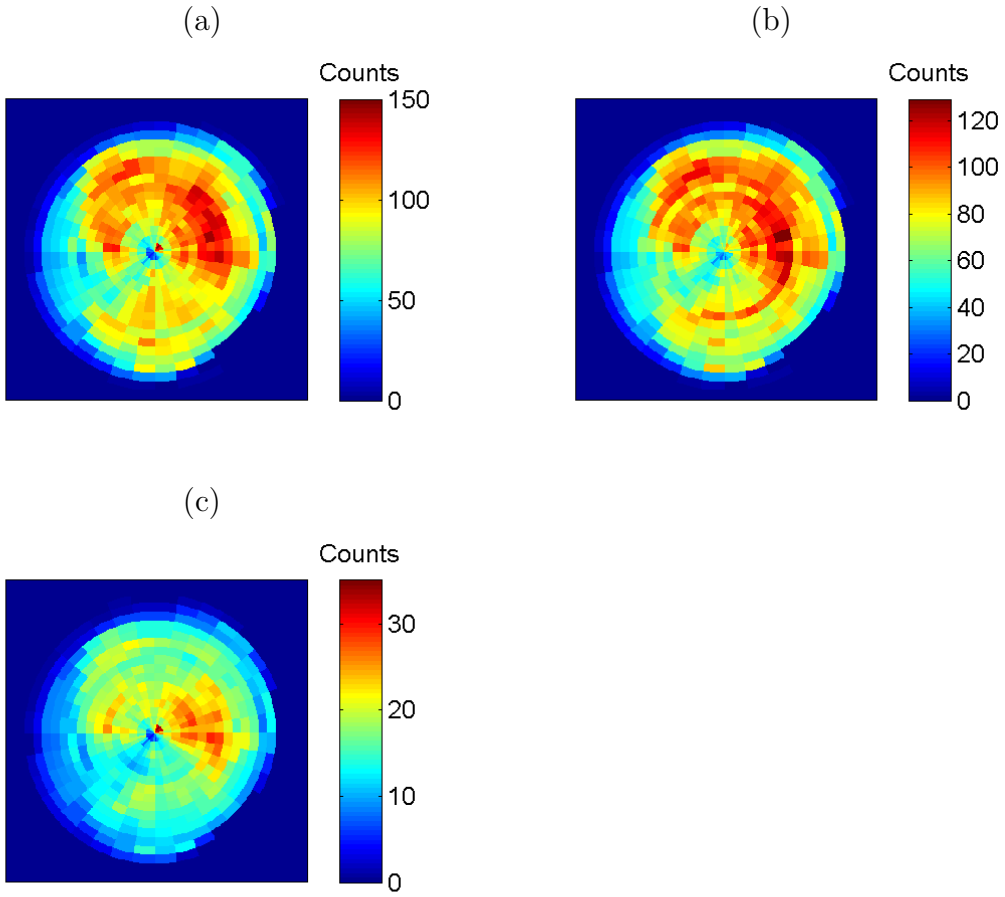

Figure 6.3: Polar plot of reconstructed activity distribution in the region of the heart of a 3D reconstruction using a 360^o imaging geometry; (a) exact attenuation correction, (b) scatter based attenuation correction, (c) without attenuation correction

6.3.3 Improving Calculation Time

6.3.3.1 Ordered Subsets

The time taken to perform each sub-iteration of the reconstruction for different numbers of subsets is shown in Table 6.2. The root mean square errors in the attenuation map and activity distribution after each sub-iteration are shown in Figures 6.5 and 6.6 respectively. The results show that a reduction in calculation time can be achieved when using ordered subsets without compromising reconstruction accuracy, provided that enough projections are included in each subset. When very large numbers of subsets are used there is not enough information included within each subset to enable a good update to the current estimate of

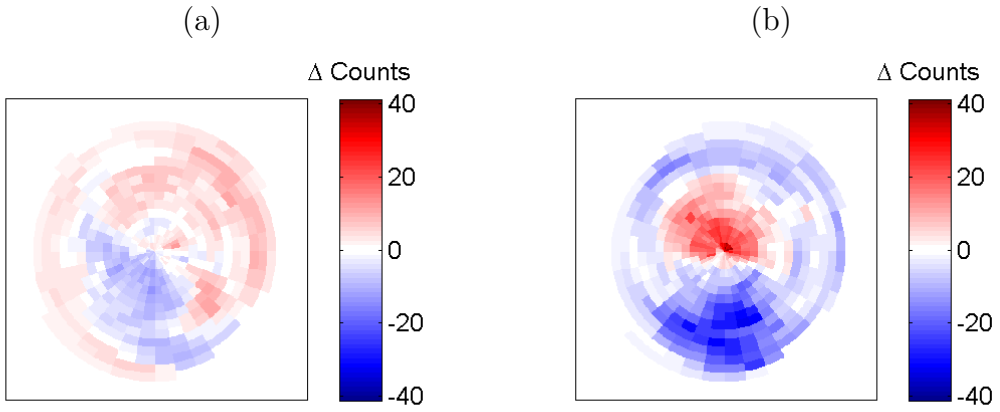

Figure 6.4: Polar plot of error in reconstructed activity distribution in the region of the heart of a 3D reconstruction using a 360^o imaging geometry compared to reconstruction with exact attenuation correction; (a) scatter based attenuation correction and (b) without attenuation correction

Number of Subsets	Time per sub-iteration (min)
1	23
2	19
5	17
10	16
15	15
45	13

Table 6.2: Difference in calculation time when using different numbers of subsets

either the attenuation map or the activity distribution to be made.

6.3.3.2 Reduced Matrix size

The changes in the root mean square error of the reconstructed attenuation map and activity distribution with iteration number are shown in Figures 6.7 and 6.8 respectively, when a reduced matrix size is used for different numbers of iterations. The results show use of the reduced matrix size beyond the very early iterations results in a poorer activity distribution reconstruction than the use of the full 64^3 matrix size. However the use of the reduced matrix size for the first iteration (with 10 subsets) enables the activity distribution to reach a slightly better solution than the use of a 64^3 matrix size throughout. This is likely to be due to improved convergence of the central areas of regions within the attenuation

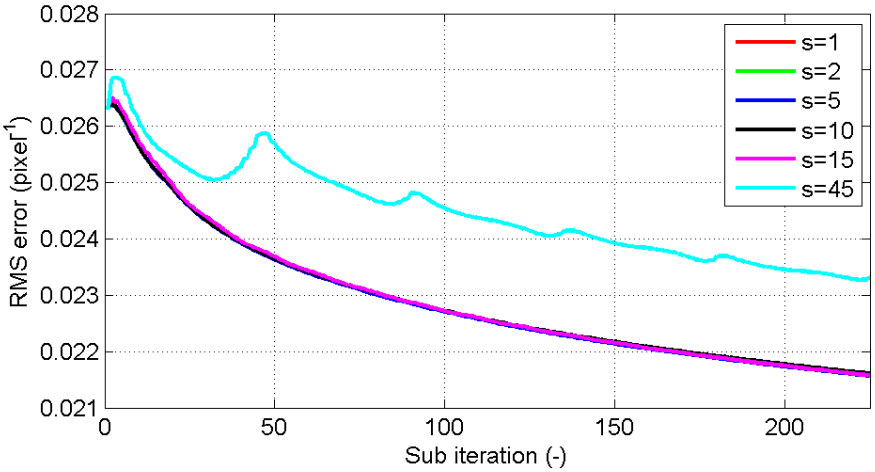

Figure 6.5: Variation in root mean square error, of the reconstructed attenuation map, with sub-iteration number for reconstructions using different numbers of subsets.

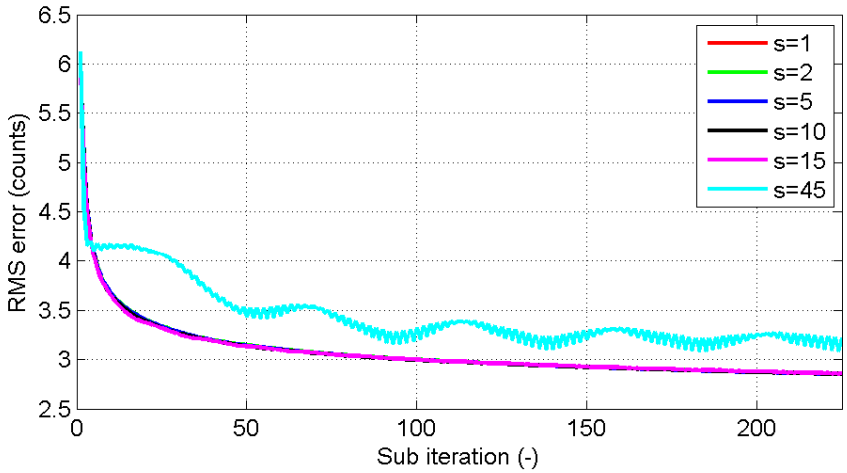

Figure 6.6: Variation in root mean square error, of the reconstructed activity distribution, with sub-iteration number for reconstructions using different numbers of subsets.

map for this early iteration preventing the activity distribution tending towards a less accurate local minima.

6.4 Discussion

The suitability of the one-step late approximation, which was used in the 2-dimensional SMLGA algorithm (Chapter 3), in the 3-dimensional situation was

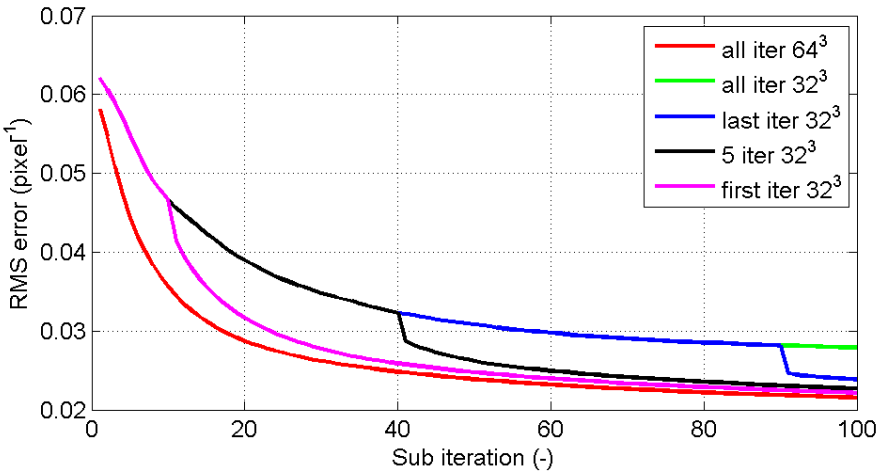

Figure 6.7: Variation in root mean square error, of the reconstructed attenuation map, with sub-iteration number for reconstructions using a coarse (32^3) matrix for different numbers of iterations.

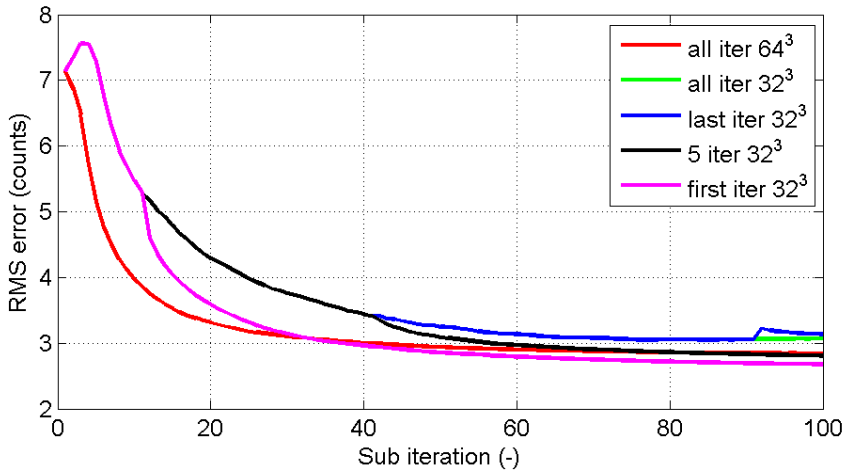

Figure 6.8: Variation in root mean square error, of the reconstructed activity distribution, with sub-iteration number for reconstructions using a coarse (32^3) matrix for different numbers of iterations.

assessed by considering the likelihood of the estimated scatter projection data where exact and approximate attenuation maps were used in different parts of the scatter projection data estimation. It has been found that the use of an approximate attenuation map prior to the point of scatter, in the scatter estimation, does not significantly affect the likelihood of the resulting scatter projection data when compared to the use of the exact attenuation map. However, the use of an approximate attenuation map at either the point of scatter or after the point of scatter does significantly affect the likelihood of the estimated scatter projection

data. As a result the one step late approximation is not appropriate in 3 dimensions and the effect of changes to the attenuation after the point of scatter must be included in the calculation of the gradient (Equation 6.3). This 'half step' late approach has been used in all subsequent reconstructions.

The inclusion of the detector characteristics (resolution modelling) in the reconstruction of activity distributions has been shown to significantly improve the resolution of the resulting images (Zeng & GuIlberg 1992, Brix *et al.*. 1997). However, the use of similar characteristics in the reconstruction of an attenuation map, used only for attenuation correction, has not been presented in the literature. In this chapter the use of resolution modelling in both the MLAA and SMLGA parts of the attenuation step of the reconstruction has been considered. The results demonstrate that, unless the detector characteristics used in the MLAA step are well matched to the measured projection data, the reconstruction of the attenuation map reproduces the prominent features seen in the activity distribution rather than the true attenuation map. The inclusion of the resolution model in the SMLGA part of the algorithm appears to be less critical to the reconstruction, however, it does allow the cross-talk between the activity and attenuation reconstructions to be reduced. The resolution model has, therefore been included in all parts of the reconstruction algorithm for all subsequent tests.

Comparison of reconstructions using the scatter based technique for estimating the attenuation map with reconstructions without attenuation correction and with perfect attenuation correction demonstrate that this method of attenuation correction offers an improvement over reconstruction without attenuation correction. However, the large number of unknown parameters mean that there are many possible solutions and so the likelihood of the reconstruction converges to a local minima rather than finding the global minimum. Further work is required to investigate methods of reducing the sensitivity of the algorithm to local minima. Chapter 7 considers the use of constraints to limit the number of possible solutions and hence aims to reduce the number of possible local minima.

The use of ordered subsets was found to reduce calculation times without compromising the quality of the reconstructed images. However, it is noted that the reduction in calculation time is much smaller than that seen in conventional OS algorithms. This is because in the scatter estimation the majority of the calculation time is taken to calculate the number of photons reaching each scatter point.

This part of the calculation does not depend on the number of measurement positions and hence is not affected by the use of ordered subsets.

As Hudson & Larkin (1994) reported s iterations of the standard algorithm provide similar results to one iteration of the OS algorithm with s subsets. They also noted that with only 2 projections per subset slightly worse results were found than when larger numbers of subsets were retained in each subset. Here we have found that the results obtained when using just 2 projections were significantly worse than when using larger numbers of projections. The solution appears to oscillate between a number of different images after each sub-iteration and hence is much slower to converge towards the optimal solution. Hudson & Larkin (1994) observed a similar effect and suggest that in all cases the algorithm appears to cycle between different limit images but that these images are similar and when larger numbers of projections are included in each subset they become indistinguishable.

When estimating an attenuation map that is to be used for attenuation correction only, it is not necessarily essential to recreate all the details of the distribution. The use of a coarser matrix size for the estimation of the attenuation map was, therefore, considered. The results showed that the use of a coarse matrix resulted in a poorer quality activity distribution reconstruction when used for more than a few initial iterations.

6.5 Conclusion

The use of the SMLGA-MLAA algorithm to estimate an attenuation map without measured transmission data has been found to improve the quality of reconstruction of an activity distribution compared to reconstruction without attenuation correction. Further work is required to consider possible methods for improving the estimation of the attenuation map and hence the quality of the activity distribution reconstruction.

It has been demonstrated that the total reconstruction time can be reduced, without compromising image quality, by using ordered subsets for both the activity and attenuation map reconstruction and by using a coarse matrix for the initial iterations of the attenuation map reconstruction.

7 Use of Constraints for Improved Attenuation Map Reconstruction

In this chapter the use of a piecewise constant model for the attenuation map is considered, in place of the initial voxel by voxel reconstruction, as a possible method of enabling a more accurate and stable reconstruction of the attenuation map and activity distribution. The effect of the choice of attenuation map used to initialise the reconstruction is also investigated.

Alternative constraints to limit the values in some regions of the voxel by voxel reconstruction method are also considered in this chapter.

7.1 Theory

7.1.1 Piecewise Constant Reconstruction

The problem of reconstructing an attenuation map can be considered as the recovery of a piecewise constant function. The function may be considered to have four levels, corresponding to air, soft tissue, lung tissue and bone. The attenuation coefficients for air and soft tissue are well defined and so do not need to be estimated. For improved accuracy, however, the values for the lung and bone regions should be recovered in the reconstruction. The use of level sets offers a possible method of recovering the attenuation map as a piecewise linear function. The use of level sets to recover piecewise linear functions was originally proposed by Osher & Sethian (1988) for tracing interfaces between fluid flow

phases but has also been used to identify the location of discontinuities in digital image functions (Berger 2001, Dorn *et al.*. 2000, Dorn & Lesselier 2006, Litman *et al.*. 1998, Vese & Chan 2002).

In the simplest case the image to be recovered can be considered to comprise two regions with attenuation coefficients μ_0 and μ_1. The level set function $\boldsymbol{\rho}$ is defined to be positive inside the region and negative outside such that the attenuation ($\boldsymbol{\mu}$) is given by Equation 7.1 (van den Doel *et al.*. 2010).

$$\boldsymbol{\mu}(\boldsymbol{\rho}) = \mu_0(1 - H(\boldsymbol{\rho})) + \mu_1 H(\boldsymbol{\rho}) \tag{7.1}$$

$H(\boldsymbol{\rho})$ is the Heaviside function defined by Equation 7.2

$$H(\boldsymbol{\rho}) = \begin{cases} 1, & \boldsymbol{\rho} > 0 \\ 0, & \boldsymbol{\rho} \leq 0 \end{cases} \tag{7.2}$$

If a larger number of regions are required more level set functions can be defined; n level set functions will allow up to 2^n regions. In the case of the attenuation map reconstruction, 4 regions are required and so two level set functions ($\boldsymbol{\rho}_1$ and $\boldsymbol{\rho}_2$) are required; the attenuation is then given by Equation 7.3 (Chan & Tai 2003).

$$\begin{aligned} \boldsymbol{\mu} = \mu_0(1 - H(\boldsymbol{\rho}_1))(1 - H(\boldsymbol{\rho}_2)) + \mu_1 H(\boldsymbol{\rho}_1)H(\boldsymbol{\rho}_2) \\ + \mu_2 H(\boldsymbol{\rho}_1)(1 - H(\boldsymbol{\rho}_2)) + \mu_3(1 - H(\boldsymbol{\rho}_1))H(\boldsymbol{\rho}_2) \end{aligned} \tag{7.3}$$

In the case of the attenuation map the region where $\boldsymbol{\mu} = \mu_0$ is known to be air. Hence, μ_0 can be set equal to zero and the calculation of $\boldsymbol{\mu}$ simplifies to Equation 7.4.

$$\boldsymbol{\mu} = \mu_1 H(\boldsymbol{\rho}_1)H(\boldsymbol{\rho}_2) + \mu_2 H(\boldsymbol{\rho}_1)(1 - H(\boldsymbol{\rho}_2)) + \mu_3(1 - H(\boldsymbol{\rho}_1))H(\boldsymbol{\rho}_2) \tag{7.4}$$

The level set definition of $\boldsymbol{\mu}$ can then be substituted into the calculation of the scatter and emission models ($\boldsymbol{s}(\boldsymbol{\mu})$ and $\boldsymbol{n}^*(\boldsymbol{\mu})$ respectively) and the likelihood of $\boldsymbol{\mu}(\boldsymbol{\rho}_n)$ given the current estimate of the activity distribution is given by Equation 7.5.

$$L[\boldsymbol{\mu}(\boldsymbol{\rho}_n)] = L_S[\boldsymbol{\mu}(\boldsymbol{\rho}_n)] + L_N[\boldsymbol{\mu}(\boldsymbol{\rho}_n)] \tag{7.5}$$

Since the Heaviside function is discontinuous a continuous approximation must be used in order to define the derivative. In this work the approximation given by

Equation 7.6 has been used. The likelihood can then be minimised with respect to the level set functions as shown in Equation 7.7 where the derivatives of L_N and L_s are calculated exactly as in Chapters 4 and 6 respectively.

$$\tilde{H} = \frac{1}{1 + e^{-k\rho}} \tag{7.6}$$

k defines how sharp the transition a $\rho = 0$ is.

$$\frac{\partial L(\boldsymbol{\mu})}{\partial \boldsymbol{\rho}_n} = \frac{\partial L_S(\boldsymbol{\mu})}{\partial \boldsymbol{\mu}} \cdot \frac{\partial \boldsymbol{\mu}}{\partial \boldsymbol{\rho}_n} + \frac{\partial L_N(\boldsymbol{\mu})}{\partial \boldsymbol{\mu}} \cdot \frac{\partial \boldsymbol{\mu}}{\partial \boldsymbol{\rho}_n} \tag{7.7}$$

The partial derivatives of μ with respect to $\boldsymbol{\rho}_n$ are given by Equation 7.8.

$$\frac{\partial \mu}{\partial \boldsymbol{\rho}_1} = \frac{k e^{-k\boldsymbol{\rho}_1}}{(1 + e^{-k\boldsymbol{\rho}_1})} \left(\mu_1 \tilde{H}(\boldsymbol{\rho}_2) + \mu_2 (1 - \tilde{H}(\boldsymbol{\rho}_2)) - \mu_3 \tilde{H}(\boldsymbol{\rho}_2) \right) \tag{7.8a}$$

$$\frac{\partial \mu}{\partial \boldsymbol{\rho}_2} = \frac{k e^{-k\boldsymbol{\rho}_2}}{(1 + e^{-k\boldsymbol{\rho}_2})} \left(\mu_1 \tilde{H}(\boldsymbol{\rho}_1) - \mu_2 \tilde{H}(\boldsymbol{\rho}_1) + \mu_3 (1 - \tilde{H}(\boldsymbol{\rho}_1)) \right) \tag{7.8b}$$

If any of the values μ_n are not known *a-priori*, as in the case of lung tissue, they can be estimated by minimising with respect to μ_n (van den Doel *et al.*. 2010) (Equation 7.9); the value of μ_n for the soft tissue region can be fixed since is constant in all subjects.

$$\frac{\partial L(\boldsymbol{\mu})}{\partial \mu_n} = \frac{\partial L_S(\boldsymbol{\mu})}{\partial \boldsymbol{\mu}} \cdot \frac{\partial \boldsymbol{\mu}}{\partial \mu_n} + \frac{\partial L_N(\boldsymbol{\mu})}{\partial \boldsymbol{\mu}} \cdot \frac{\partial \boldsymbol{\mu}}{\partial \mu_n} \tag{7.9}$$

$$\frac{\partial \boldsymbol{\mu}}{\partial \mu_1} = \tilde{H}(\boldsymbol{\rho}_1)\tilde{H}(\boldsymbol{\rho}_2) \tag{7.10}$$

$$\frac{\partial \boldsymbol{\mu}}{\partial \mu_2} = \tilde{H}(\boldsymbol{\rho}_1) \left(1 - \tilde{H}(\boldsymbol{\rho}_2) \right) \tag{7.11}$$

$$\frac{\partial \boldsymbol{\mu}}{\partial \mu_3} = \left(1 - \tilde{H}(\boldsymbol{\rho}_1) \right) \tilde{H}(\boldsymbol{\rho}_2) \tag{7.12}$$

7.1.2 Fuzzy Cluster Segmentation

When using gradient ascent based iterative reconstruction algorithms it is possible for the solution to converge towards a local minimum rather than the true global minimum. As a result the solution obtained can depend on the initialisation of

the reconstruction, with reconstructions that are initialised with images closer to the true solution being more likely to converge to the true solution. In the case of a joint activity distribution and attenuation map reconstruction algorithm the activity distribution obtained by the first step of the reconstruction could be used to provide information which enables a more accurate initialisation by performing an automatic segmentation of the activity distribution to identify different regions.

The use of a fuzzy cluster segmentation algorithm has been investigated for this purpose. The use of fuzzy clusters has previously been used in Nuclear Medicine imaging for segmentation of dynamic neuroreceptor imaging (Acton *et al.*. 1999) and to improve the accuracy of attenuation correction in PET imaging with noisy transmission scans (Zaidi *et al.*. 2002) and produces good results when used as an automated tool for robustly segmenting noisy images. Fuzzy cluster segmentation is an iterative process in which every voxel is assigned a membership probability for each cluster, depending on the cluster's central value. Such a technique is well suited to the segmentation of nuclear medicine images because it allows for uncertainty in voxel values as a result of image non-uniformities, noise and partial volume effects.

A number of different fuzzy cluster algorithms have been developed which are optimised for different problems including that of highly noisy data. The problem presented here will include noise but not at very high levels and so the fuzzy C-means (FCM) used by Zaidi *et al.*. (2002) has been used; this algorithm requires the number of clusters to be set as an input parameter.

The FCM algorithm iteratively minimises the mean square Euclidean distance between each data point (i.e. each voxel value within the image) and the centroid values of the clusters in order to minimise the objective function J_{FCM} given by Equation 7.13 (Acton *et al.*. 1999) by determining the centroids of each cluster and the membership grade for each voxel for each cluster. As the number of clusters increases, the minimum of the objective function will be reduced up to the limit where every voxel is assigned to a unique cluster. The "fuzzification" parameter m $(1 < m < \infty)$ defines how the system responds to noise and also the certainty of the assignment for each voxel to a cluster.

$$J_{FCM} = \frac{1}{2} \sum_{i=1}^{C} \sum_{j=1}^{v} U_{ij}^{m} \|\lambda_j - w_i\|^2 \tag{7.13}$$

C is the number of clusters
v is the number of voxels in the image to be segmented
U_{ij} is the membership grade for voxel j belonging to cluster i
m is the "fuzzification" parameter
λ_j is the activity in voxel j
w_i is the centroid value for cluster i

Initially the cluster centroid values are set to random values and the membership grade matrix ($\boldsymbol{U}$) is calculated for these starting values using Equation 7.14.

$$U_{ij} = \frac{(\frac{1}{d_{ij}^2})^{1/(m-1)}}{\sum_{i=1}^{C}(\frac{1}{d_{ij}^2})^{1/(m-1)}} \tag{7.14}$$

$$d_{ij} = \sqrt{(\lambda_j - w_i)^2} \tag{7.15}$$

The membership grade matrix is then used to determine the updated cluster centroid values using Equation 7.16.

$$w_i = \frac{\sum_{j=1}^{v}(U_{ij})^m \lambda_j}{\sum_{j=1}^{v}(U_{ij})^m} \tag{7.16}$$

The iterative process is stopped once the maximum change in the membership grades U_{ij} between consecutive iterations is less than the iteration tolerance δ. The final membership probability for each voxel to each cluster is then calculated. A threshold for cluster membership p_c is then applied (i.e. the probability of a voxel belonging to a cluster is lower than the required certainty) and each voxel is assigned to the cluster for which it has the highest membership probability. Using a value of zero for p_c will ensure that all voxels are assigned to a cluster even if they are outliers while as the value of p_c increases the number of voxels which are not assigned to any cluster will increase.

7.2 Method

For each of the tests presented in the this chapter the projection data were simulated using a rotation based forward projector as described in Section 6.2.1. A 32^3 matrix size was used for the tests to investigate the use of Level Sets and for the voxel by voxel reconstructions that were compared to the Level Set recon-

structions. The use of constraints within the voxel by voxel reconstruction was tested using the standard 64^3 matrix size.

7.2.1 Piecewise Constant Reconstruction

The use of level-sets to improve the accuracy of the reconstruction of the attenuation map was initially tested with just soft tissue and lung regions (since the amount of bone in the thorax is small). The values of attenuation of soft tissue and lung were fixed at the known values for the XCAT phantom used. In order to ensure that the resolution of the attenuation map was matched to the resolution of the activity distribution a value of $k = 30$ was used in the approximation of the Heaviside function (Equation 7.6). The use of this value of k also ensured that the transitions in the attenuation map were smooth enough to be observed within one or more voxels of the attenuation map (and not between voxels) as this allowed the algorithm to detect (and hence modify) the transitions between regions more easily.

The effect of the choice of attenuation map used to initialise the reconstruction procedure has been tested for four different attenuation maps. The simplest initialisation was the same for every slice in the image volume with a uniform cylinder defining the body outline containing two cylinders to approximate the lungs. The most accurate initialisation determined the body and lung boundaries from the true attenuation map and so exactly defined the lung and body regions. Two initialisations using the fuzzy cluster segmentation technique described in Section 7.1.2 were then tested. The central slice of the resulting attenuation maps are shown in Figure 7.1.

The first fuzzy cluster segmentation was carried out using an initial reconstruction of the activity distribution estimated from five iterations of the MLEM algorithm with an assumption of zero attenuation. The segmentation was performed setting the "fuzzification" parameter to 3 and the iteration tolerance to 0.001 with 6 clusters; the membership probability for each cluster was set to 0. The two clusters with the lowest centroid value were deemed to be the background region and the low activity region at the boundary of the body outline and so both were set to the background region of the attenuation map while all other clusters were defined to fall within the body outline. The contrast between the lung and soft tissue in the reconstruction of the activity distribution was not sufficient to allow

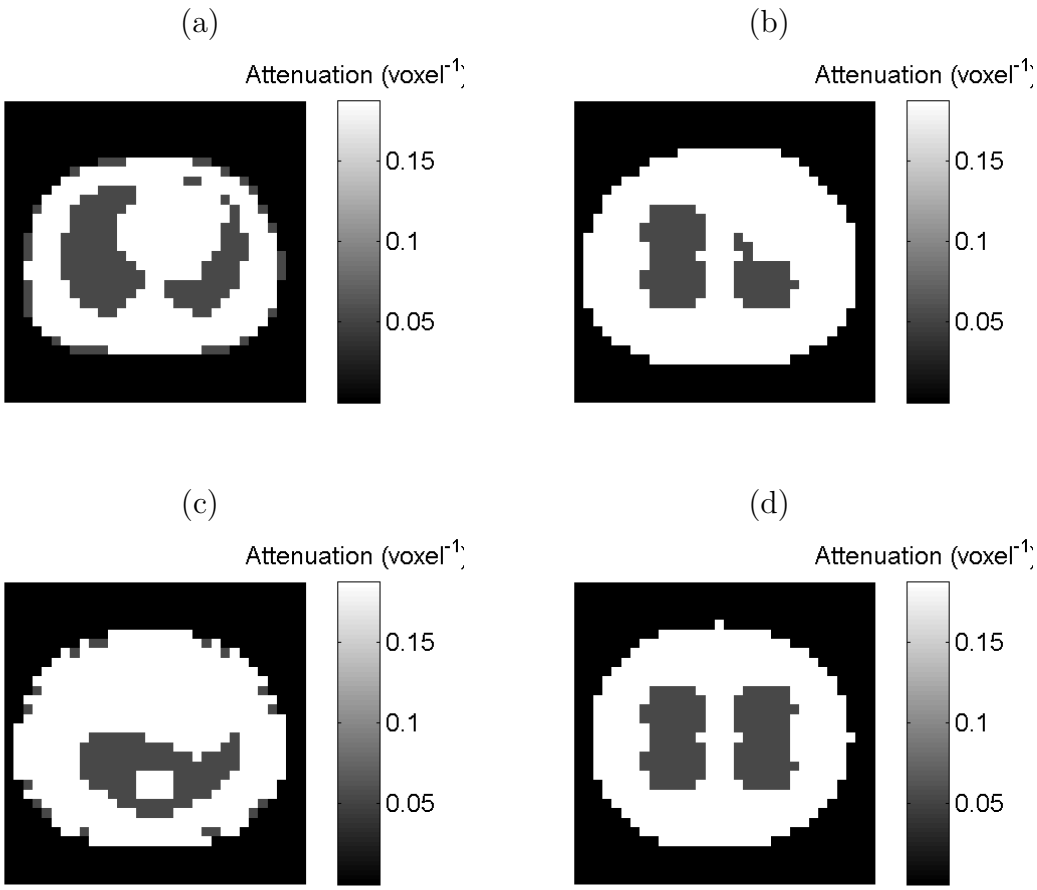

Figure 7.1: Attenuation maps used to initialise reconstruction algorithm; (a) exact segmentation of attenuation map, (b) estimated from segmentation of activity reconstruction, (c) estimated from segmentation of scatter reconstruction and,(d) unguided estimate

direct segmentation of the lungs and so the lungs were initially estimated as two uniform cylinders positioned either side of the midline. However, regions of high activity are not expected within the lungs in myocardial perfusion imaging and so the lung outline was improved by removing voxels which had been assigned to high activity clusters from the lung region. An improved segmentation was performed using a reconstruction of the scatter sinogram after five iterations of the MLEM algorithm. The image was segmented with the "fuzzification" parameter set to 3 and the iteration tolerance to 0.001 with 10 clusters; the membership probability for each cluster was set to 0. Each cluster was manually assigned to be soft tissue, lung or background.

The Level Sets algorithm was then tested with different number of degrees of free-

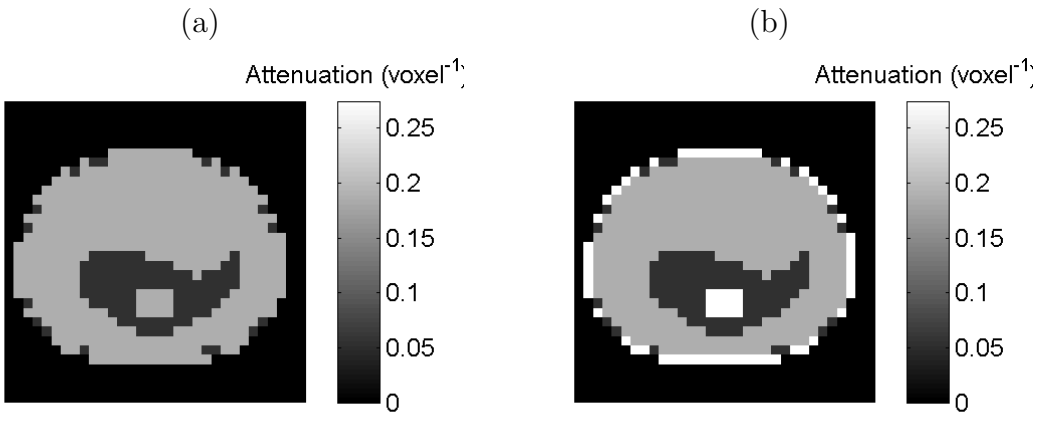

Figure 7.2: Attenuation maps used to initialise reconstruction algorithm; (a) regions of lung and soft tissue only and (b) with lung, soft tissue and bone regions.

dom compared to estimation with just soft tissue and lung regions with known attenuation coefficients. Firstly the value of attenuation in lung was estimated using a starting value of $0.05 voxel^{-1}$ (compared to the true value of $0.054 voxel^{-1}$). A region corresponding to bone was then added to the reconstruction, first with fixed attenuation in all regions ($0.27 voxel^{-1}$ in bone) and then estimating the attenuation in lung and bone (starting values $0.05 voxel^{-1}$ and $0.26 voxel^{-1}$, respectively). The attenuation maps used to initialise the reconstructions with and without regions of bone are shown in Figure 7.2.

7.2.2 Constrained Voxel by Voxel Reconstruction

In Chapter 4 it is shown that when considering a single two dimensional slice of a phantom it is possible to accurately reconstruct an attenuation map, and hence the activity distribution, using the SMLGA-MLAA technique. However, in Chapter 6 it was found that in 3-dimensions the reconstruction of the attenuation map is much poorer with some cross-talk between the lung and soft tissue regions. These results suggest that if the estimation of the attenuation map could be restricted to a smaller volume it may be possible to produce a more accurate reconstruction. In order to do this the attenuation in some regions of the reconstruction has been fixed to a value which can be assumed with a high degree of confidence.

The first region considered is the abdomen. It is known that the apex of the

heart is contiguous with the diaphragm. A reconstruction has, therefore, been performed with all attenuation below the level of the heart and within in the body outline fixed at the value of soft tissue. This is a reasonable assumption since the only bone within the abdomen is the spine which is distant from the region of the heart and therefore unlikely to significantly affect the reconstruction in the cardiac region. In each iteration of the algorithm an update to the attenuation in the abdominal region is calculated in order to allow the body outline to be modified.

A second reconstruction was performed which not only fixed the attenuation in the abdominal region but also aimed to reduce the effect of cross-talk between the attenuation and activity reconstructions in the cardiac region by fixing the attenuation in regions of high activity equal to soft tissue. This is a reasonable assumption since the nature of the pharmaceuticals used in myocardial perfusion imaging is that they are only taken up in soft tissues. Regions of high activity were defined to be those with activity above 55% of the maximum value in the reconstructed activity distribution.

7.3 Results

7.3.1 Piecewise Constant Reconstruction

7.3.1.1 Effect of Attenuation Map Initialisation

The central slice of the attenuation maps reconstructed after initialisation with the maps shown in Figure 7.1 are shown in Figure 7.3. The resulting errors in the region of the heart (as compared to reconstruction with exact attenuation correction) are demonstrated by the polar plots in Figure 7.4. The mean and root mean square errors for each reconstruction compared to reconstruction with exact attenuation correction are shown in Table 7.1.

The results show that, as expected, using an exact segmentation to initialise the attenuation map reconstruction enables a significant improvement in the accuracy of the final reconstructed image. The use of an attenuation map initialised from a fuzzy cluster segmentation of the initial activity distribution reconstruction improves the accuracy of the reconstruction of both the activity distribution

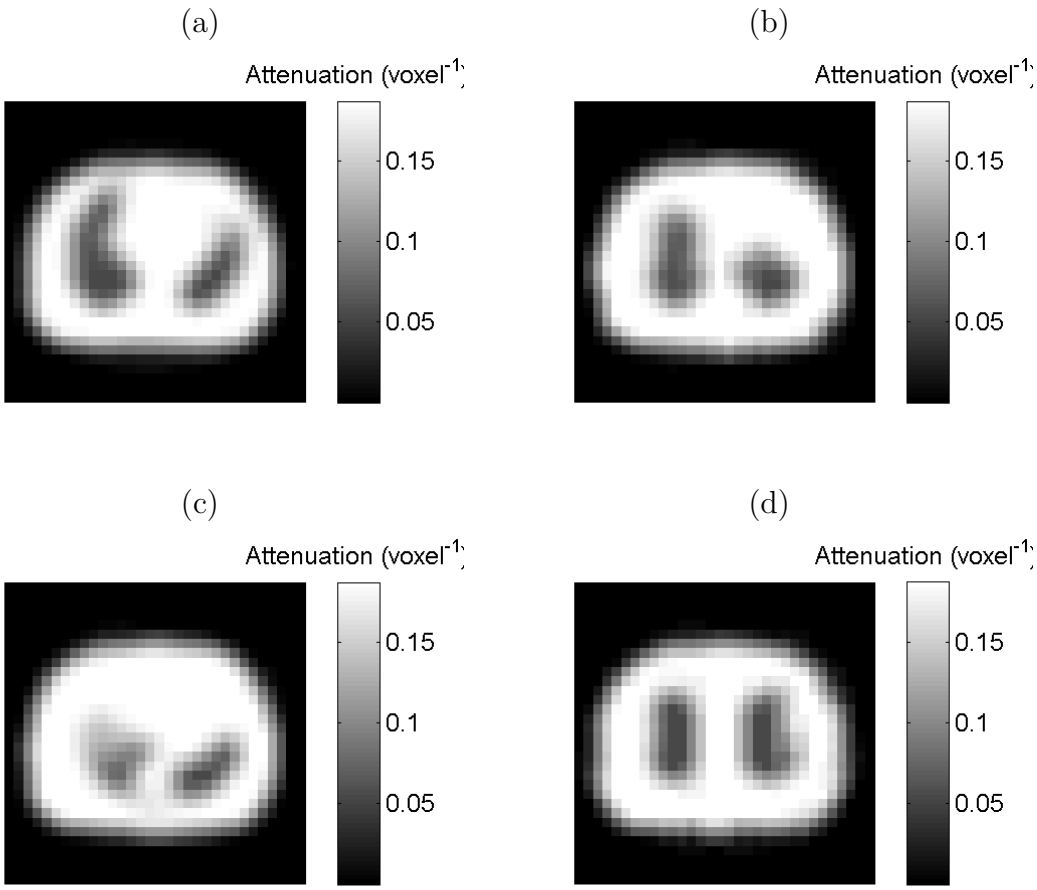

Figure 7.3: Attenuation maps reconstructed after initialisation with (a) exact segmentation of attenuation map, (b) estimated from segmentation of activity reconstruction, (c) estimated from segmentation of scatter reconstruction and, (d) unguided estimate

and attenuation map in the region of the myocardium. This results in a reduction in the artefact seen in the infero-lateral region of the reconstruction of the myocardium after initialisation with the unguided estimate of the attenuation map. The results are further improved by use of an improved segmentation based on the reconstruction of acquired scatter data.

The choice of attenuation map used to initialise the reconstruction has a large effect on the resulting reconstruction which indicates that the algorithm is not always able to find the global maximum for the likelihood. The joint likelihood of the activity distribution and attenuation map for each reconstruction has been calculated, relative to the maximum likelihood, using Equation 7.17 and compared to the likelihood of each starting condition. The results are shown in Table

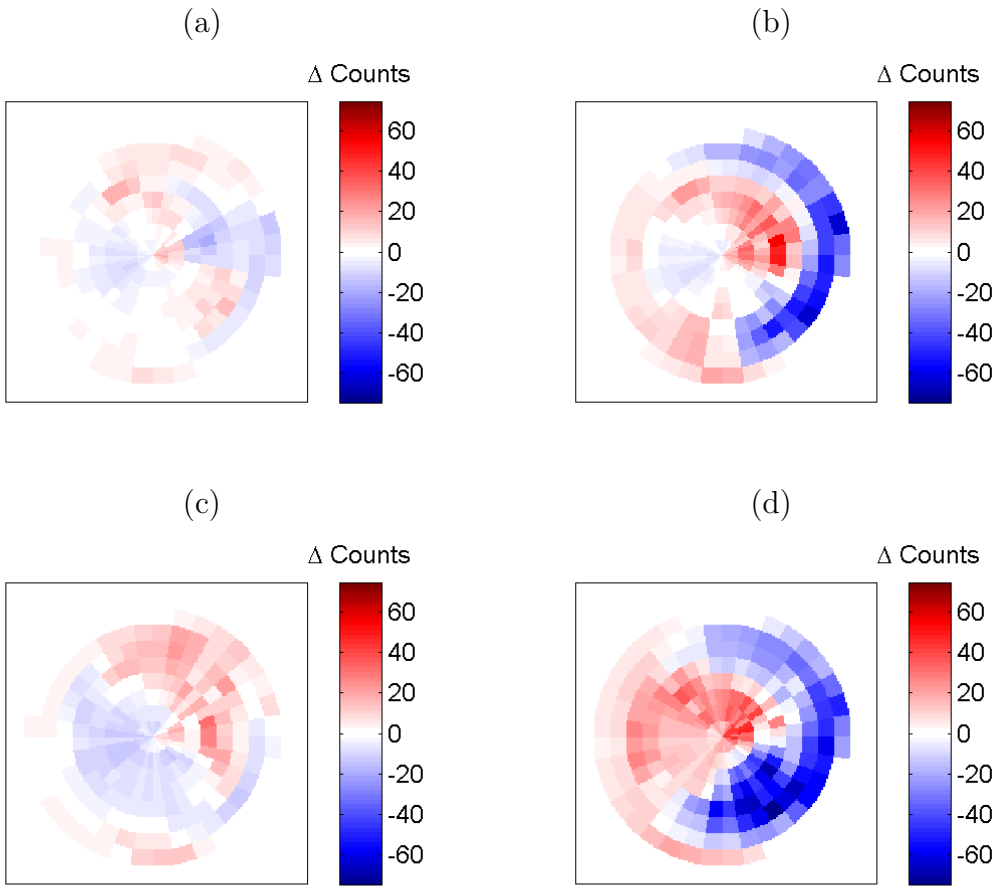

Figure 7.4: Polar plots showing the relative difference between the reconstructed activity distributions for different estimated attenuation compared to exact attenuation correction after initialisation with (a) exact segmentation of attenuation map, (b) estimated from segmentation of activity reconstruction, (c) estimated from segmentation of scatter reconstruction and, (d) unguided estimate

7.2. These results show that the gradient of the likelihood is very shallow with multiple combinations of attenuation map and activity distribution having very similar likelihood. This suggests that a likelihood based algorithm may not be able to find the true solution without the addition of some extra constraints.

$$L(\boldsymbol{\mu},\boldsymbol{\lambda}) = \frac{\sum_d \left(-(\boldsymbol{n}(\boldsymbol{\lambda}))_d + (\boldsymbol{n}^p)_d \cdot \ln(\boldsymbol{n}(\boldsymbol{\lambda}))_d\right) + \sum_d \left(-(\boldsymbol{s}(\boldsymbol{\mu}))_d + (\boldsymbol{n}^s)_d \cdot \ln(\boldsymbol{s}(\boldsymbol{\mu}))_d\right)}{\sum_d \left(-(\boldsymbol{n}^p))_d + (\boldsymbol{n}^p)_d \cdot \ln(\boldsymbol{n}^p)_d\right) + \sum_d \left(-(\boldsymbol{n}^s)_d + (\boldsymbol{n}^s)_d \cdot \ln(\boldsymbol{n}^s)_d\right)} \tag{7.17}$$

	Activity Distribution			
	Image		Region	
	Mean	RMSE	Mean	RMSE
Exact Segmentation	-4.6209	11.2708	-3.1827	4.8391
Activity Segmentation	-4.5789	12.5074	-3.3074	10.9809
Scatter Segmentation	-3.7804	13.8291	-0.5748	6.9910
Unguided Estimate	-7.8281	21.9468	-10.9827	17.3257

	Attenuation Map			
	Image		Region	
	Mean	RMSE	Mean	RMSE
Exact Segmentation	-0.0066	0.0321	-0.0026	0.0065
Activity Segmentation	-0.0076	0.0364	-0.0055	0.0178
Scatter Segmentation	-0.0052	0.0387	-0.0010	0.0060
Unguided Estimate	-0.0105	0.0441	-0.0160	0.0355

Table 7.1: Mean error and root mean square error (RMSE) in reconstructions using different attenuation map initialisations compared to reconstruction with exact attenuation correction, for the whole image volume and for a region of interest centred over the heart.

	Relative Likelihood	
	Initial	Final
Exact Segmentation	0.90345	0.99894
Activity Segmentation	0.94512	0.99894
Scatter Segmentation	0.91665	0.99894
Unguided Estimate	0.90778	0.99894

Table 7.2: Relative likelihood of activity distribution and attenuation maps for each attenuation map initialisation at initialisation and after reconstruction.

7.3.1.2 Effect of Number of Degrees of Freedom

Figure 7.5 shows the central slice of the attenuation maps reconstructed using a level set piecewise constant technique with different degrees of freedom; the attenuation values in each region are shown in Table 7.3. The results demonstrate that the estimation of the attenuation coefficient in each region as well as the region boundaries does not significantly affect the reconstructed attenuation maps. However the inclusion of a region corresponding to bone, in addition to the lung and soft tissue regions, does not enable recovery of the bone regions and is unstable in these areas. The best level set method for determining the different regions of the attenuation map, therefore, has been determined to be that which estimates the attenuation coefficient in lung and which includes only lung and

	Attenuation Coefficient (voxel^{-1})		
	Soft Tissue	Lung	Bone
True Attenuation Map	0.187	0.054	0.27
All values fixed (no bone)	0.187 (f)	0.054 (f)	0 (f)
All values fixed (with bone)	0.187 (f)	0.054 (f)	0.27 (f)
Estimated lung only	0.187 (f)	0.053 (e)	0 (f)
Estimated lung, fixed bone	0.187 (f)	0.057 (e)	0.27 (f)
Estimated lung and bone	0.187 (f)	0.056 (e)	0.026 (e)

Table 7.3: Attenuation coefficients used and estimated during Level Sets reconstruction. Values which are fixed prior to reconstruction are indicated (f) and those estimated during the reconstruction process are indicated (e).

soft tissue regions.

7.3.1.3 Comparison of Piecewise Constant Reconstruction to Voxel by Voxel Reconstruction

The mean and root mean square errors of reconstructions performed using the voxel by voxel and level set piecewise constant methods of estimating the attenuation map, compared to reconstruction using the exact attenuation map (as defined in section 4.2), are shown in Table 7.4 for the whole images and for a region of interest centred over the heart. The mean and root mean square errors of the estimation of the attenuation map using the level set technique are found to be higher when considering the full image volume but are reduced in the region of interest centred over the heart.

The central transaxial slice through the heart activity distributions recovered using the voxel by voxel and level set piecewise constant methods of estimating the attenuation map are shown in Figure 7.6, compared to reconstruction with exact attenuation correction and without attenuation correction. The differences between this slice of the activity distributions reconstructed with each estimated attenuation map compared to using exact attenuation correction are shown in Figures 7.7. The same slice of the attenuation maps reconstructed by each technique are shown in Figure 7.8 and the differences between these and the true attenuation map are shown in Figure 7.9. The accuracy of the reconstructed activity distribution through the whole myocardium is shown using polar plots of

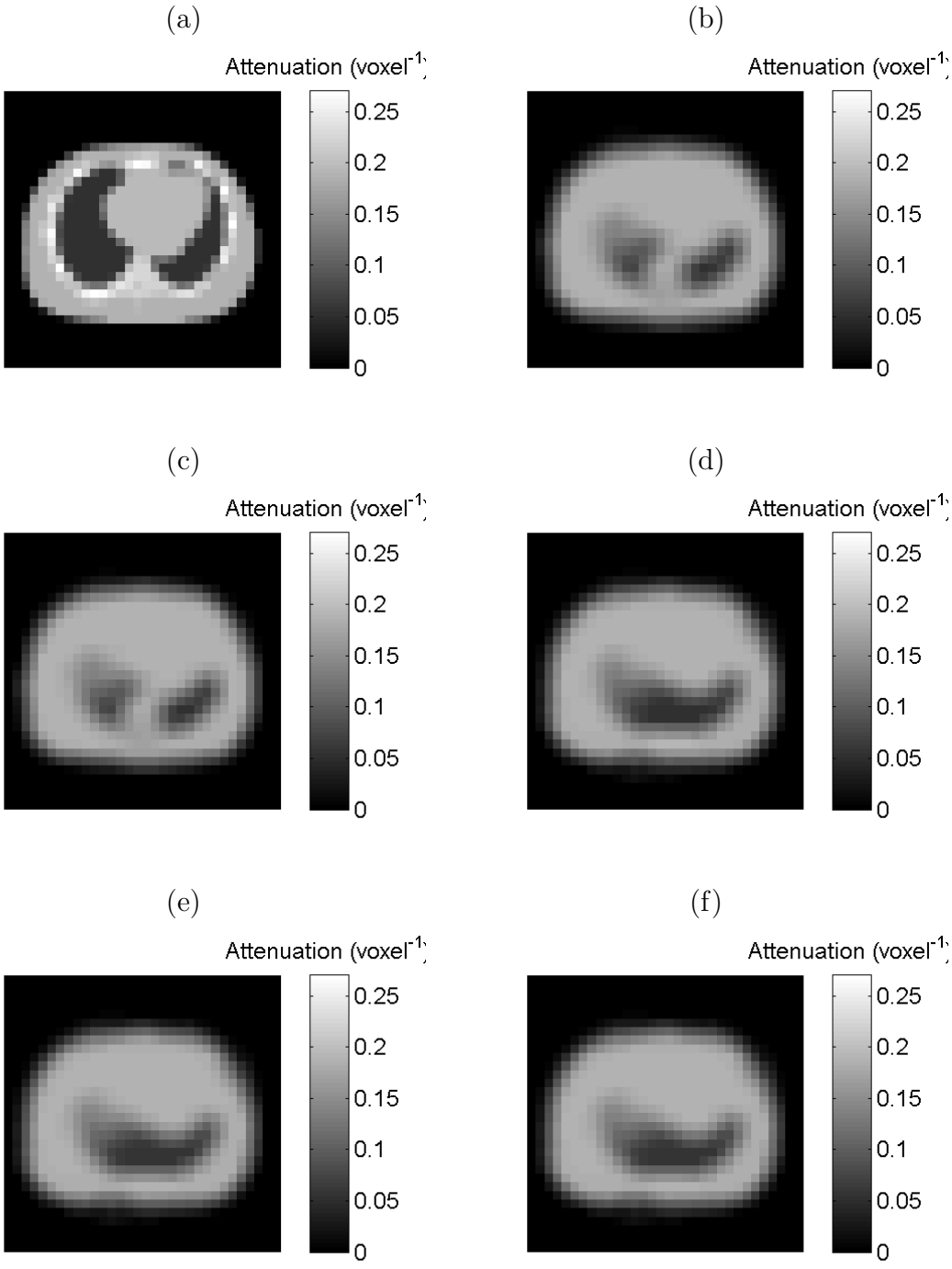

Figure 7.5: Attenuation maps reconstructed using Level Sets piecewise constant technique for the central slice of a 3D reconstruction using a 360^o imaging geometry; (a) true phantom attenuation map (b) with fixed lung attenuation coefficient and no bone, (c) with estimated lung attenuation coefficient and no bone, (d) with fixed lung and bone attenuation coefficient, (e) with estimated lung and fixed bone attenuation coefficient, (e) with estimated lung and bone attenuation coefficients.

	Activity Distribution			
	Image		Region	
	Mean	RMSE	Mean	RMSE
Voxel by Voxel reconstruction	-3.9287	15.4861	-2.5544	8.1414
Level Set reconstruction	-3.7776	13.8277	-0.5809	6.9836
No attenuation correction	-34.3016	38.4769	-41.1806	17.3907

	Attenuation Map			
	Image		Region	
	Mean	RMSE	Mean	RMSE
Voxel by Voxel reconstruction	-0.0044	0.0381	-0.0027	0.0104
Level Set reconstruction	-0.0052	0.0387	-0.0010	0.0060

Table 7.4: Mean error and root mean square error (RMSE) in reconstructions using simulated data with a standard 360^o imaging geometry with estimated attenuation correction compared to reconstruction with exact attenuation correction, for the whole image volume and for a region of interest centred over the heart.

the myocardial region (created as described in Section 6.2.2) for reconstructions using voxel by voxel and level set reconstruction techniques, Figure 7.10. The results for reconstructions using exact attenuation correction and without attenuation correction are also shown. The error in each region of the myocardium is shown in Figure 7.11 for each reconstruction technique compared to reconstruction with exact attenuation correction.

These results demonstrate that in the region of the heart the use of the level set technique to limit the range of possible attenuation values allows the contrast between the lung and soft tissue attenuation to be recovered and prevents the over-estimation of the attenuation seen close to the centre of the heart in the voxel by voxel reconstruction. As a result the reconstructed activity distribution has reduced errors, particularly in the regions of the inferior and infero-lateral walls.

Figures 7.12 and 7.13 show the true and reconstructed attenuation distributions close to the bottom and the top of the reconstructed volume respectively. The results show that both the voxel by voxel and level set estimations correctly identify the body outline in the regions where it is convex and show some reduction in attenuation in the region of bowel gas; in the case of the level set algorithm this has been assigned as lung tissue. Close to the top of the reconstructed volume the body outline becomes convex around the shoulders. The voxel by voxel esti-

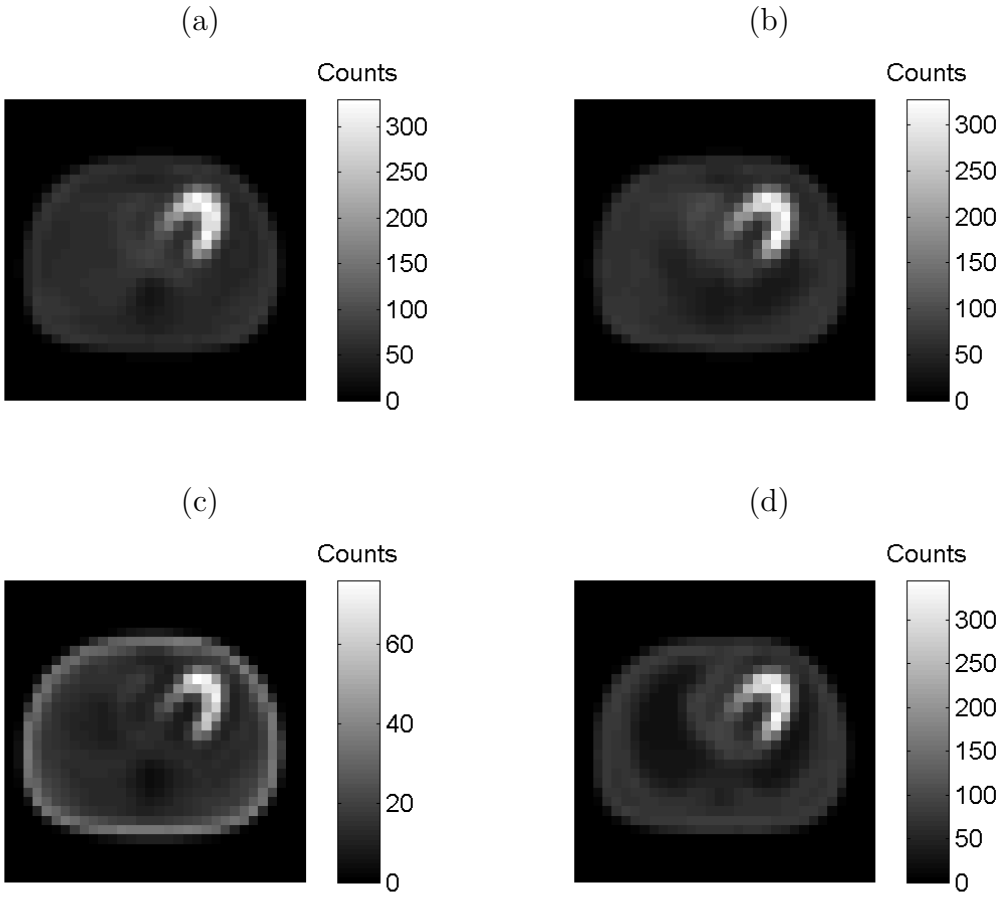

Figure 7.6: Central transaxial slice through reconstructed activity distributions for a standard 360^o imaging geometry; (a) voxel by voxel reconstruction, (b) Level-Set reconstruction, (c) without attenuation correction, (d) exact attenuation correction

mation fails to reconstruct the correct outline in this area and instead produces a larger area of low attenuation to blur the convex surface. The Level Set algorithm is able to partially recreate the convex surface but the sharpest internal corners remain blurred.

7.3.2 Constrained Voxel by Voxel Reconstruction

Figure 7.14 shows the activity distributions reconstructed using the unconstrained SMLGA-MLAA voxel by voxel reconstruction and for two constrained reconstructions, with fixed attenuation in the abdomen and with fixed attenuation in the abdomen and in regions of high activity. The corresponding attenuation maps are

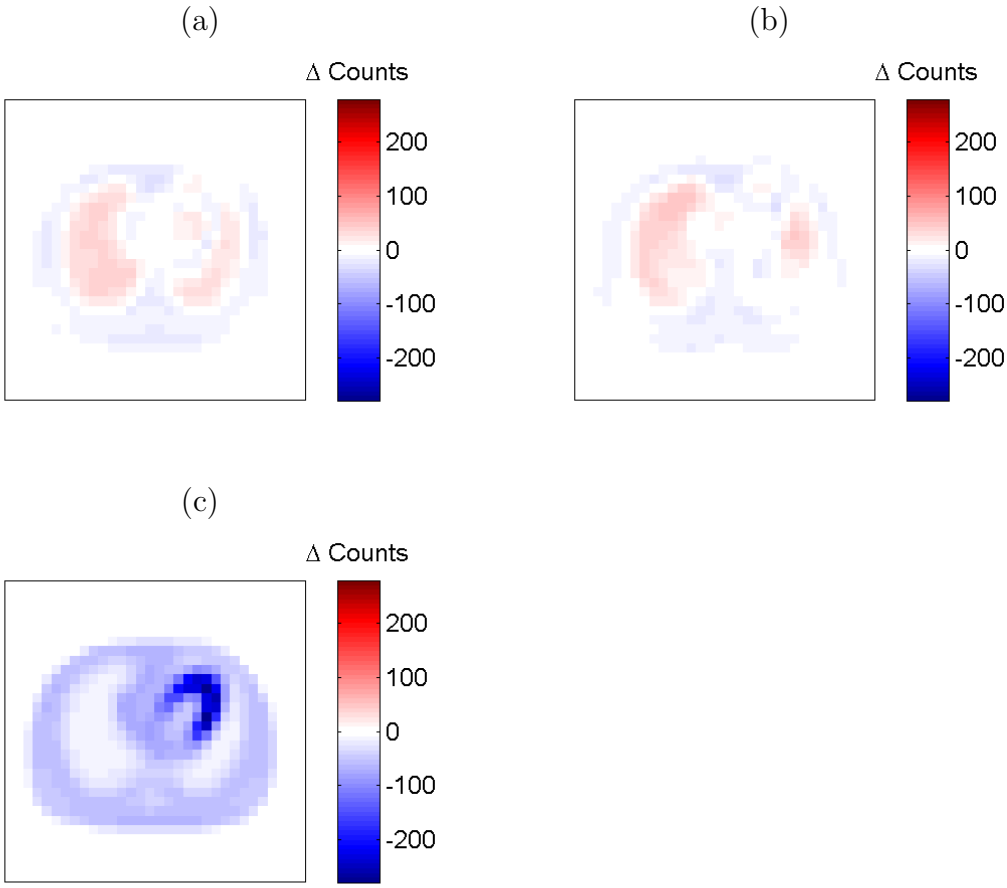

Figure 7.7: Difference between the reconstructed activity distributions for different estimated attenuation compared to exact attenuation correction for a 360^o imaging geometry for the central transaxial slice; (a) voxel by voxel reconstruction, (b) Level-Set reconstruction, (c) without attenuation correction

shown in Figure 7.16 and the errors in the activity distributions and attenuation maps, compared to reconstruction with perfect attenuation correction, are shown in Figures 7.15 and 7.17 respectively. Polar plots of the activity distributions and the relative error in the activity distribution for each reconstruction method are shown in Figures 7.18 and 7.19. Table 7.5 shows the mean and root mean square error for each reconstruction technique in the whole image and in a region of interest centred over the heart.

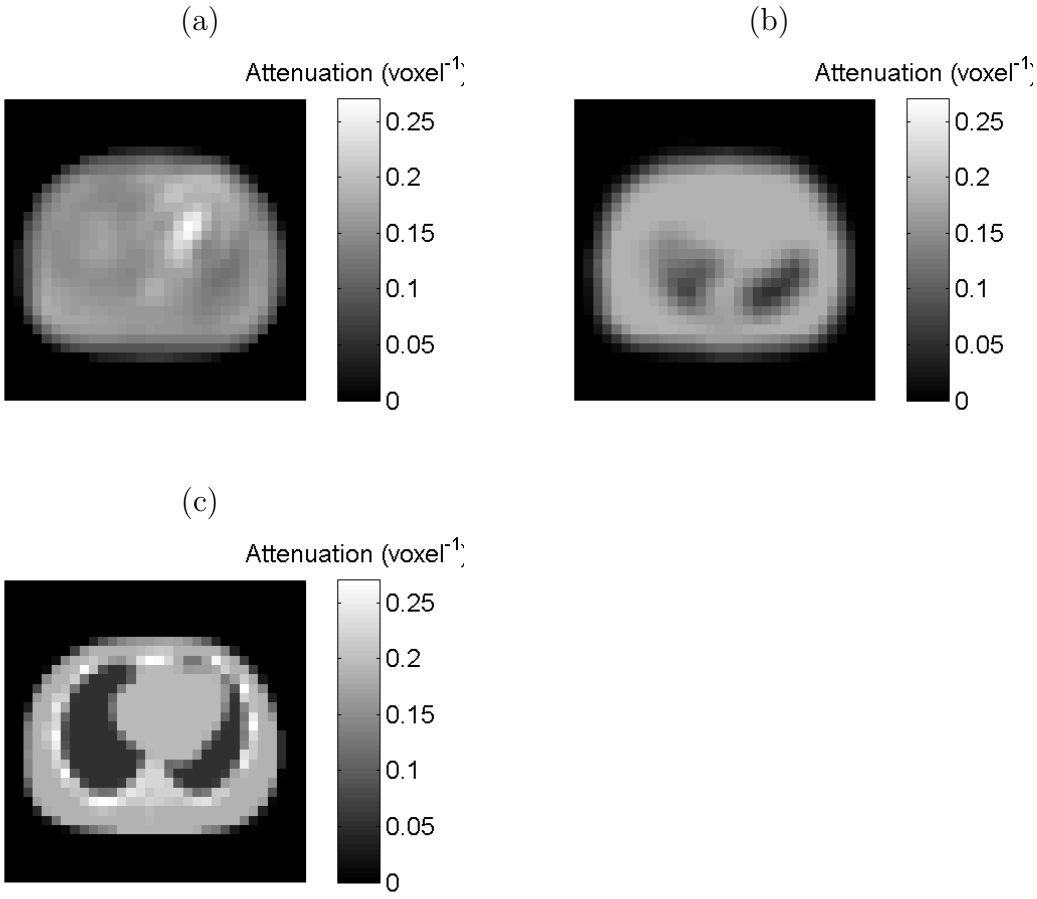

Figure 7.8: Central transaxial slice from reconstructed attenuation maps for a 360^o imaging geometry; (b) voxel by voxel reconstruction, (c) Level-Set reconstruction, (c) true phantom attenuation map

7.4 Discussion

The different tissues within the human body are known to have only a limited number of different attenuation values (namely soft tissue, lung and bone) with only small variations in attenuation between different regions of similar type. The attenuation map used for attenuation correction, therefore, does not need to estimate the attenuation at every point within the body but only to assign each point to the correct type and to estimate the attenuation of each tissue type. In the work presented here a level sets technique has been used to produce this type of piecewise constant reconstruction and to investigate the number of regions that are required for reconstruction of a sufficiently accurate attenuation map of the thorax for attenuation correction purposes. It has been shown that the use of

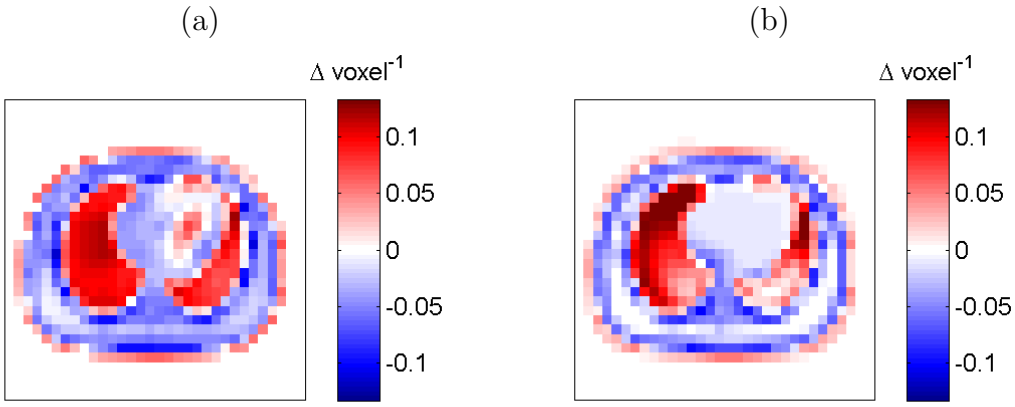

Figure 7.9: Difference between the reconstructed attenuation map and true attenuation phantom for a 360^o imaging geometry for the central transaxial slice; (a) voxel by voxel reconstruction, (b) Level-Set reconstruction

	Activity Distribution			
	Image		Region	
	Mean	RMSE	Mean	RMSE
Unconstrained Reconstruction	0.4125	1.8046	0.6502	1.8542
Fixed Abdominal Attenuation	0.2482	1.6850	-0.2302	1.3417
Fixed High Activity Attenuation	0.2794	1.6698	-0.1218	1.0040

	Attenuation Map			
	Image		Region	
	Mean	RMSE	Mean	RMSE
Unconstrained Reconstruction	0.0037	0.0248	-0.0023	0.0060
Fixed Abdominal Attenuation	0.0018	0.0206	-0.0016	0.0061
Fixed High Activity Attenuation	0.0020	0.0206	-0.0014	0.0054

Table 7.5: Mean error and root mean square error (RMSE) in reconstructions using attenuation maps estimated on a voxel by voxel basis without constraints, with fixed attenuation in the abdominal region, and with fixed attenuation in the abdominal region and regions of high activity.

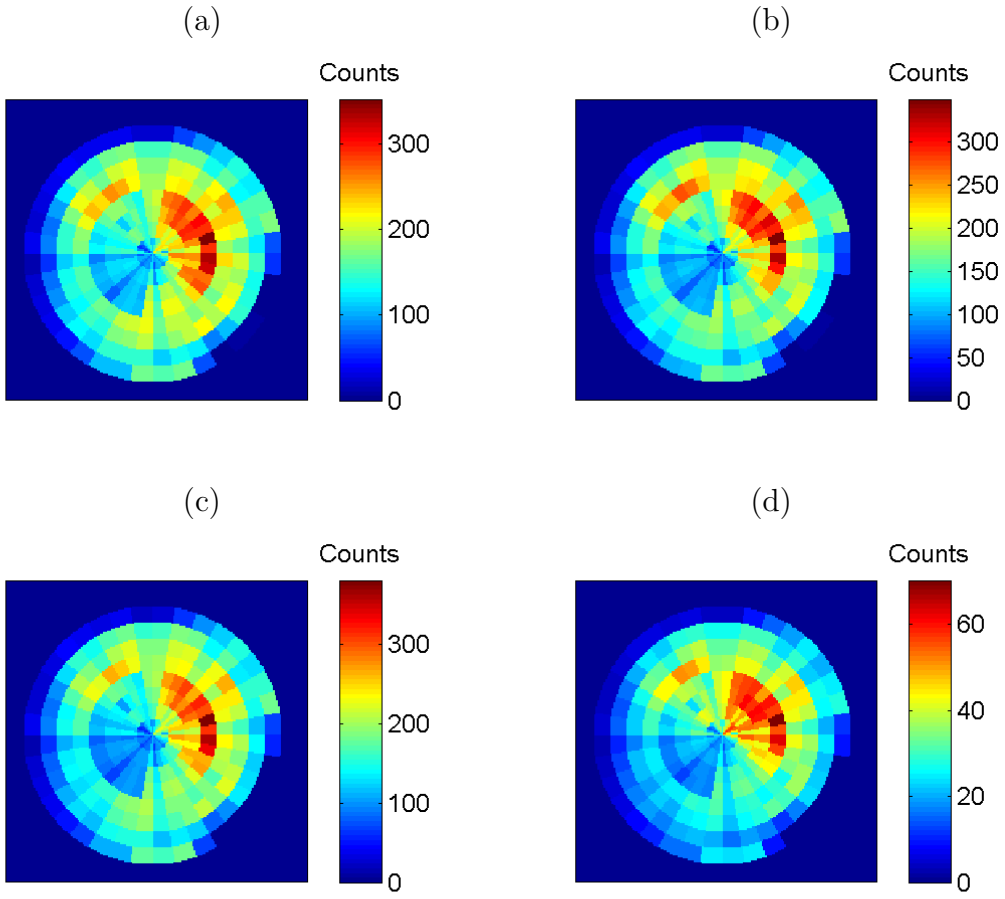

Figure 7.10: Polar plots of reconstructed activity distributions in the myocardium; (a) exact attenuation correction (b) voxel by voxel reconstruction, (c) Level-Set reconstruction, (d) without attenuation correction

the level sets technique is most reliable when only regions of soft tissue and lung are included. When a region corresponding to bone is allowed the reconstruction appears to become unstable in areas which correspond to bone and in some cases these areas are assigned to lung tissue; they are assigned to soft tissue when a bone region is not permitted. In the case where there is no bone but the value of lung attenuation is estimated it has been found that the value of lung attenuation can be recovered by the algorithm with reasonable accuracy.

The use of the level sets technique to produce a piecewise constant attenuation map was found to result, globally, in larger errors than, the voxel by voxel reconstruction, due to the fact that some regions within the reconstructed attenuation map were assigned to the wrong tissue type. However, the errors in the region of the myocardium were reduced. This is because the limited number of possi-

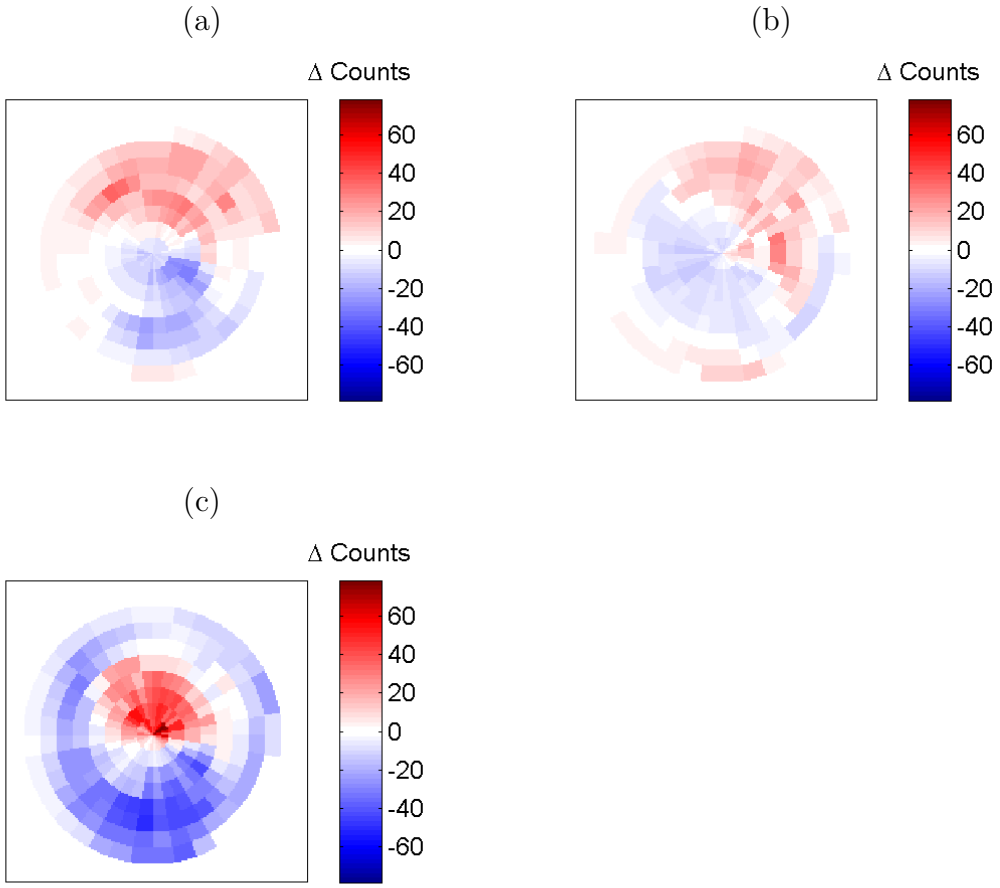

Figure 7.11: Polar plots showing the relative difference between the reconstructed activity distributions for different estimated attenuation compared to exact attenuation correction; (a) voxel by voxel reconstruction, (b) Level-Set reconstruction, (c) without attenuation correction

ble attenuation values enabled the algorithm to correctly recreate the contrast between the soft tissue and lung, and also prevented the overestimation of the attenuation that was observed close to the centre of the myocardium in the voxel by voxel reconstruction. The level set algorithm was also able to more accurately recreate the concave surfaces of the body close to the top of the reconstructed volume.

However, when using a level sets technique the choice of attenuation map used to initialise the reconstruction has been shown to be critical to the final solution. This is due to the large number of variables that the reconstruction aims to recover which means that a large number of attenuation map and activity distribution combinations have very similar likelihood. The level sets version of

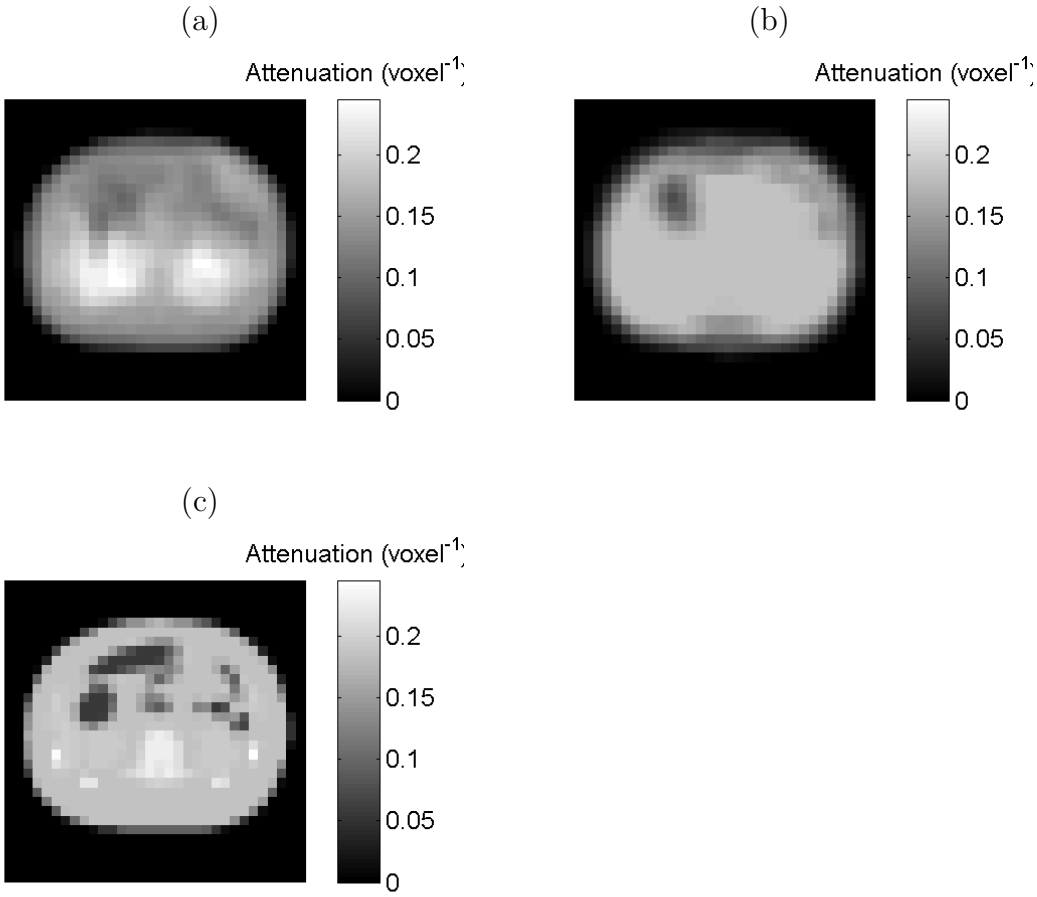

Figure 7.12: Transaxial slice from close to the base of the reconstructed attenuation maps for a 360^o imaging geometry; (b) voxel by voxel reconstruction, (c) Level-Set reconstruction, (c) true phantom attenuation map

the reconstruction algorithm only modifies the boundaries between the different regions and so is very slow to change regions which are distant to the boundaries in the initialisation image. As a result the reconstruction of the activity distribution in these areas tends to converge towards a solution which best matches the initial attenuation value. The maximum likelihood gradient ascent algorithm, therefore, is not able to distinguish between this and the global maximum in the likelihood and hence determine the best solution.

In order to reduce the dependence of the solution on the initialisation of the attenuation map an alternative approach has been considered using a voxel by voxel estimation of the attenuation map whilst limiting the possible values of the attenuation in some regions.

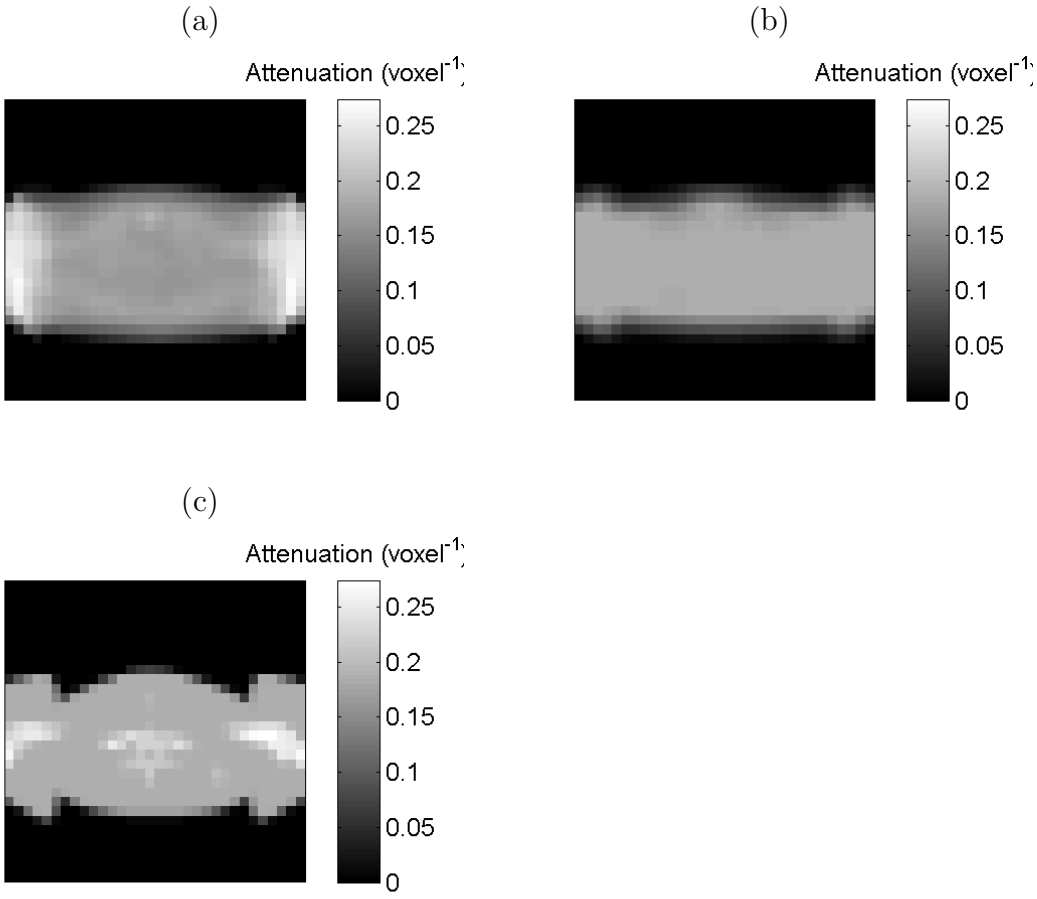

Figure 7.13: Transaxial slice from close to the top of the reconstructed attenuation maps for a 360^o imaging geometry; (b) voxel by voxel reconstruction, (c) Level-Set reconstruction, (c) true phantom attenuation map

When the reconstruction is performed without the use of additional constraints the resulting attenuation map shows very little contrast between the different regions of the phantom. This causes the attenuation in the lung to be over-estimated and hence the activity distribution in the region of the heart is generally over-estimated. When the attenuation in the region of the abdomen is fixed equal to that of soft tissue the quality of the reconstruction of the attenuation map is significantly improved with a clear difference in attenuation between the lungs and soft tissue being observed. However, the attenuation in the region of the high activity of the myocardium is under-estimated as a result of cross-talk between the activity and attenuation map reconstructions. This is similar to the effect demonstrated by Nuyts *et al.*. (1999) and Krol *et al.*. (2001) when using photopeak data alone to perform a joint reconstruction of the attenuation map and activity

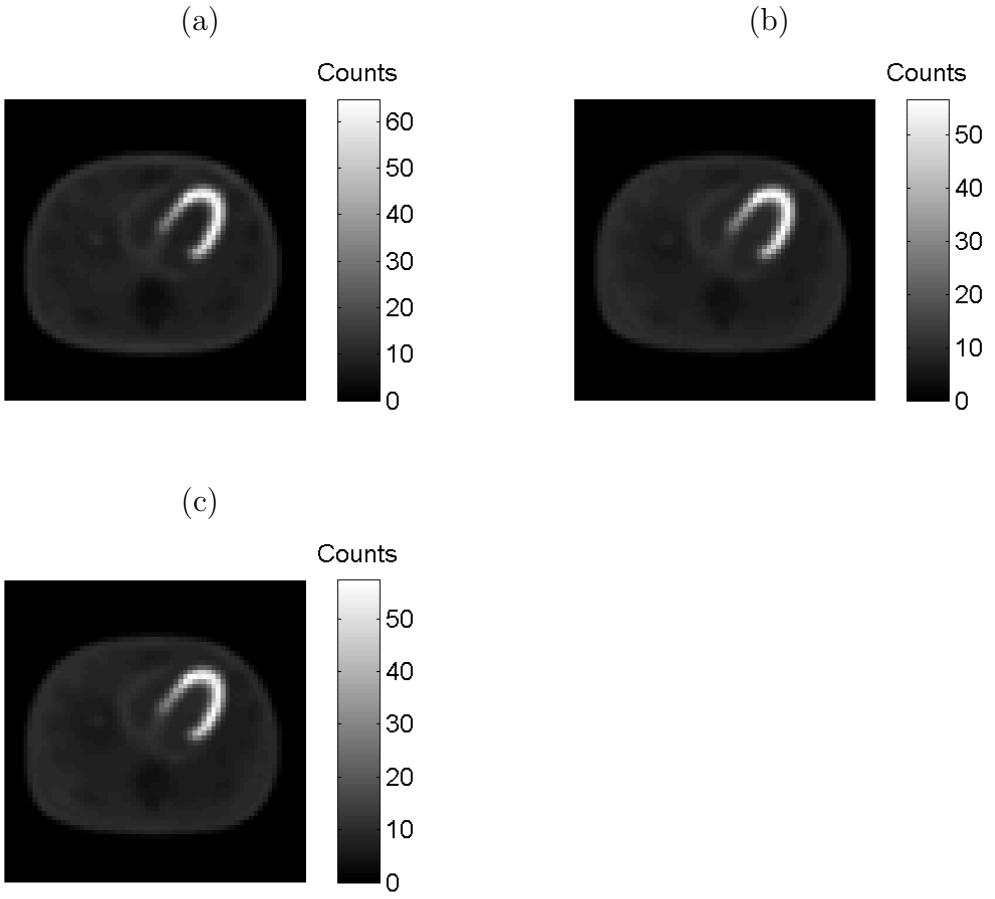

Figure 7.14: Central transaxial slice through reconstructed activity distributions for a standard 360^o imaging geometry; (a) without constraint, (b) fixed abdominal attenuation, (c) fixed abdominal and high activity attenuation.

distribution of SPECT studies. The effect of this cross-talk has been reduced by fixing the attenuation in regions of high activity to be equal to that of soft tissue. In this case the reconstructed attenuation map demonstrates good reconstruction of the body boundary and reasonable recovery of the contrast between the lungs and soft tissue; however, the attenuation in the region of the mediastinum which corresponds to the chamber the left ventricle of the heart is over-estimated.

The effect of the inaccuracies in the attenuation map is to over-estimate the activity of the anterior wall, relative to the rest of the left ventricle, as this is the region which is most affected by the overestimation of the lung attenuation. The overestimation of the attenuation in the chamber of the heart would be expected to have most effect on the septal and lateral walls of the heart, since the photons detected from these areas will pass through the chamber of the heart on

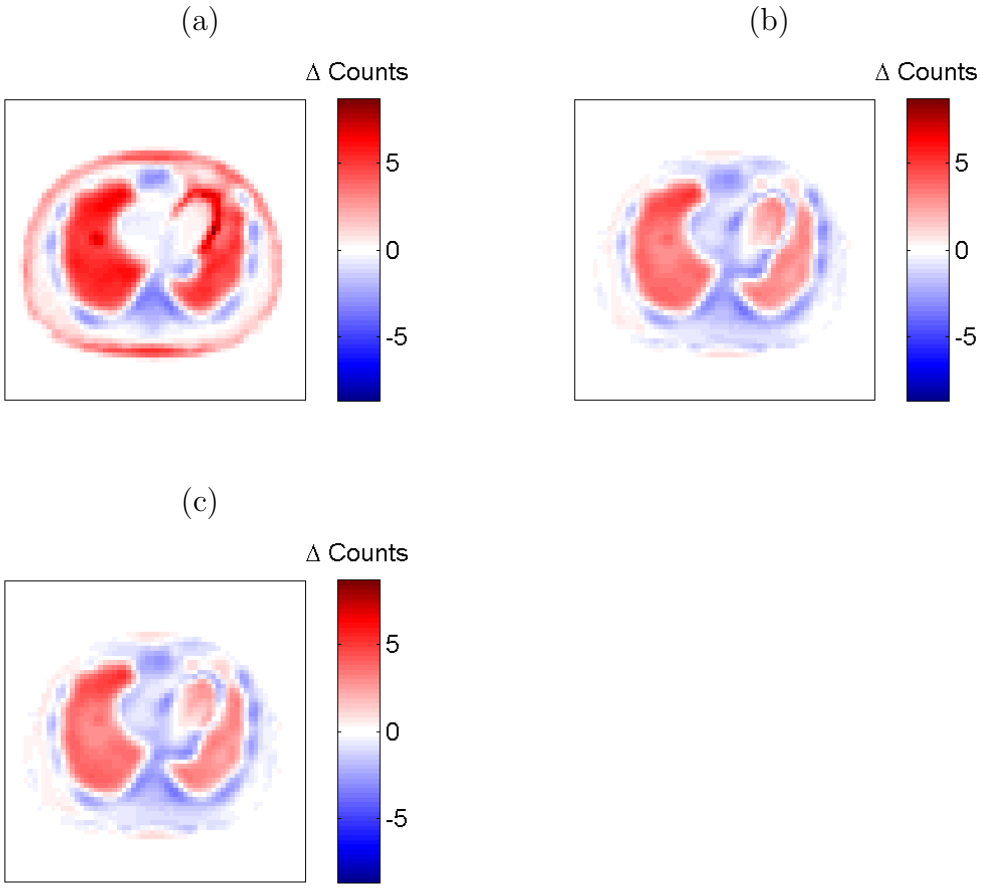

Figure 7.15: Difference between the reconstructed activity distributions for different attenuation map estimation compared to exact attenuation correction for a 360^o imaging geometry for the central transaxial slice; (a) without constraint, (b) fixed abdominal attenuation, (c) fixed abdominal and high activity attenuation.

some of the sinogram projections. However the polar plots of the errors in these walls suggest that the effect is not significant compared to the over-estimation of attenuation in the lung regions.

7.5 Conclusion

The use of a level sets technique to limit the attenuation map to be piecewise constant shows improved results in the region of the myocardium compared to estimation on a voxel by voxel basis. The algorithm achieved the best results when limited to regions of soft tissue and lung, and in this case was able to

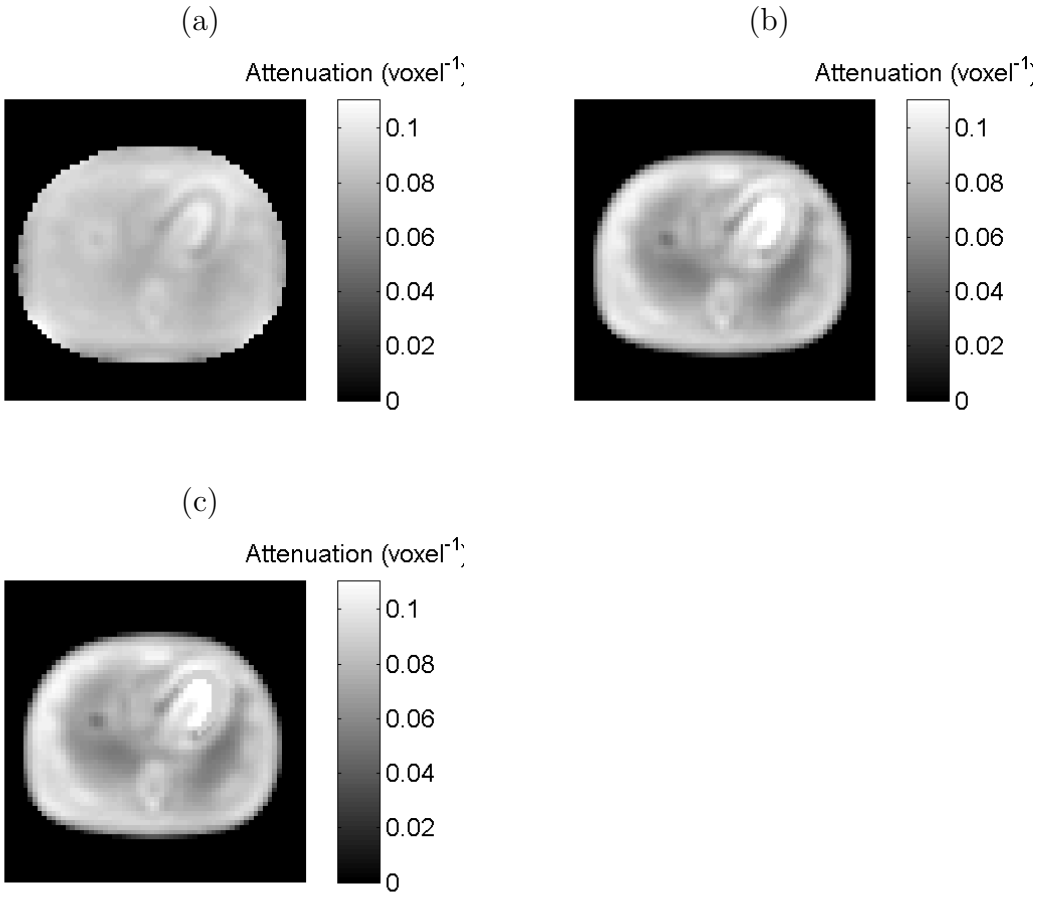

Figure 7.16: Central transaxial slice through reconstructed attenuation map for a standard 360^o imaging geometry; (a) without constraint, (b) fixed abdominal attenuation, (c) fixed abdominal and high activity attenuation.

accurately recover the value of attenuation in lung. However, a large number of attenuation map and activity distribution combinations were found to have a similar likelihood and so the reconstruction produced by the gradient ascent algorithm was found to be highly dependent on the attenuation map used to initialise the algorithm when using level sets.

An improved reconstruction was achieved when using a voxel by voxel reconstruction technique with additional constraints. It has been shown that, by fixing the attenuation in the abdomen and the region of the heart to be equal to that of soft tissue, the regions of the lung can be clearly distinguished from soft tissue within the attenuation map and hence a more accurate activity distribution can be recovered.

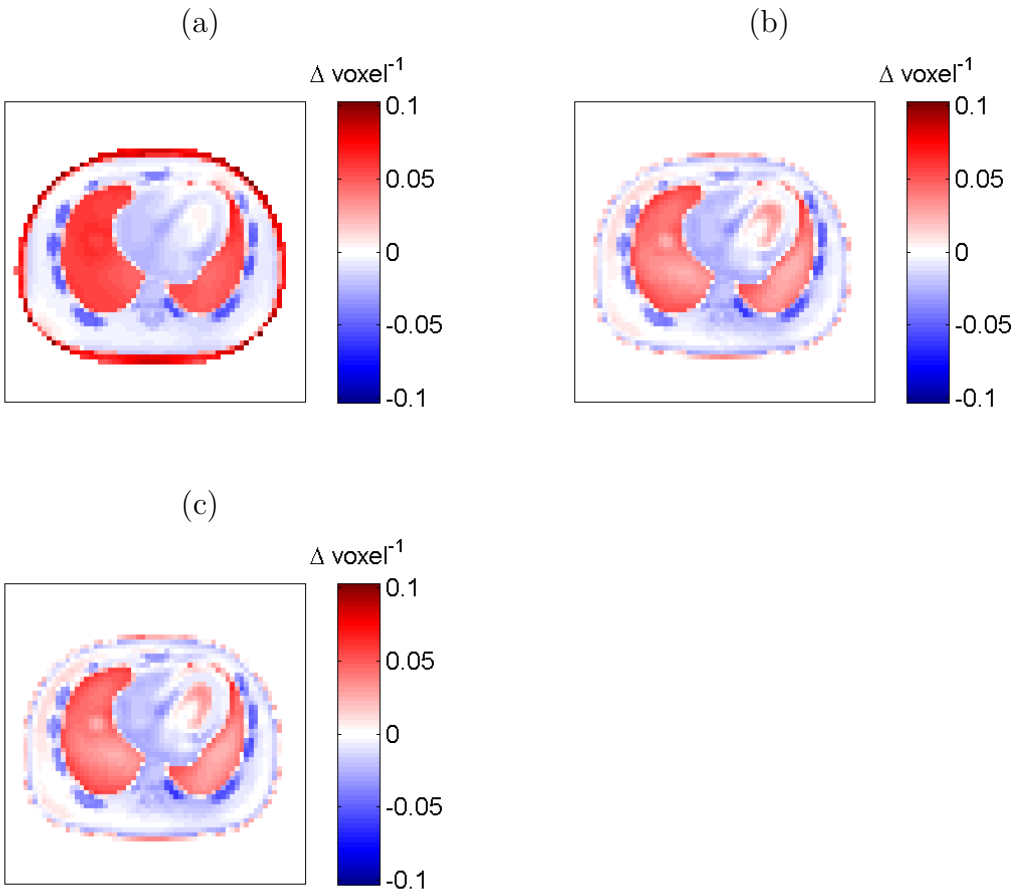

Figure 7.17: Difference between the reconstructed attenuation map and true attenuation map for a 360^o imaging geometry for the central transaxial slice; (a) without constraint, (b) fixed abdominal attenuation, (c) fixed abdominal and high activity attenuation.

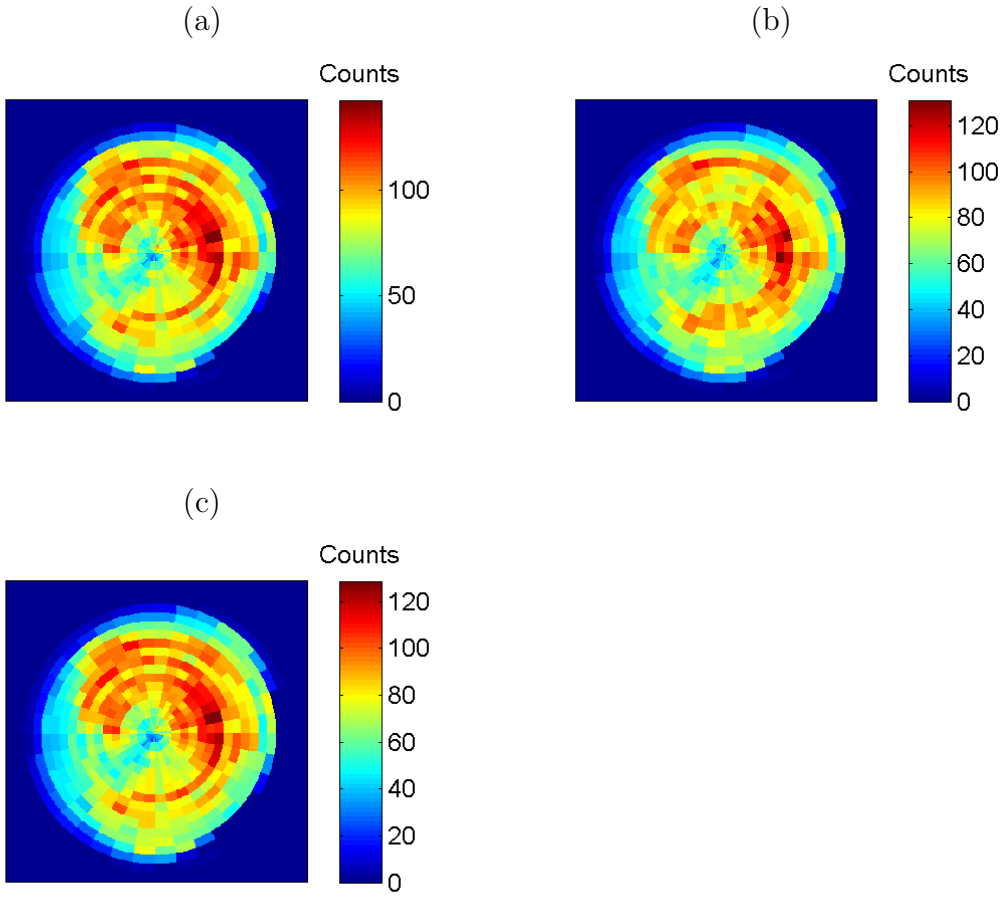

Figure 7.18: Polar plots of reconstructed activity distributions in the myocardium; (a) without constraint, (b) fixed abdominal attenuation, (c) fixed abdominal and high activity attenuation.

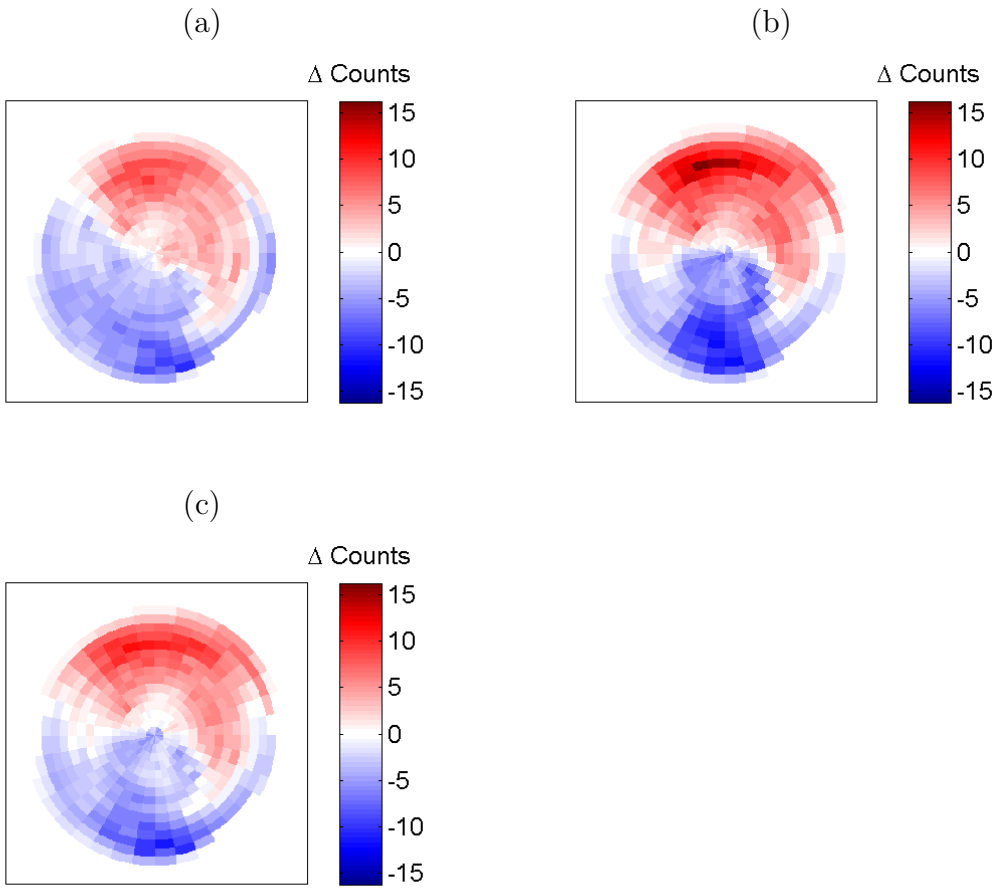

Figure 7.19: Polar plots showing the relative difference between the reconstructed activity distributions for different estimated attenuation compared to exact attenuation correction; (a) without constraint, (b) fixed abdominal attenuation, (c) fixed abdominal and high activity attenuation.

8 Validation and Limitations

8.1 Method

8.1.1 Effect of Phantom on Reconstruction Accuracy

In order to test the robustness of the reconstruction algorithm developed in the preceding chapters it has been tested with three variations of the XCAT phantom (Segars *et al.*. 1999). The first phantom was a typical male phantom without respiratory or cardiac motion (as used in the preceding chapter). The second was a female phantom with the same activity in each region as the male phantom. The final phantom was a male phantom with increased activity in the lung region in order to simulate reduced contrast in the activity between these two regions. Both the female phantom and the phantom with increased lung activity included respiratory and cardiac motion which results in blurred boundaries between different tissue regions. The activity in each region of each phantom is shown in Table 8.1 and the central slice of each phantom's activity distribution and attenuation map are shown in Figures 8.1 and 8.2 respectively.

Region	Male	Female	Low Contrast
Left ventricle myocardium	55	55	55
Other myocardium	30	30	30
Lung	4	4	8
Soft Tissue	10	10	10
Blood	10	10	10
Liver	55	55	55

Table 8.1: Activity assigned to each region of the variations of the XCAT phantom.

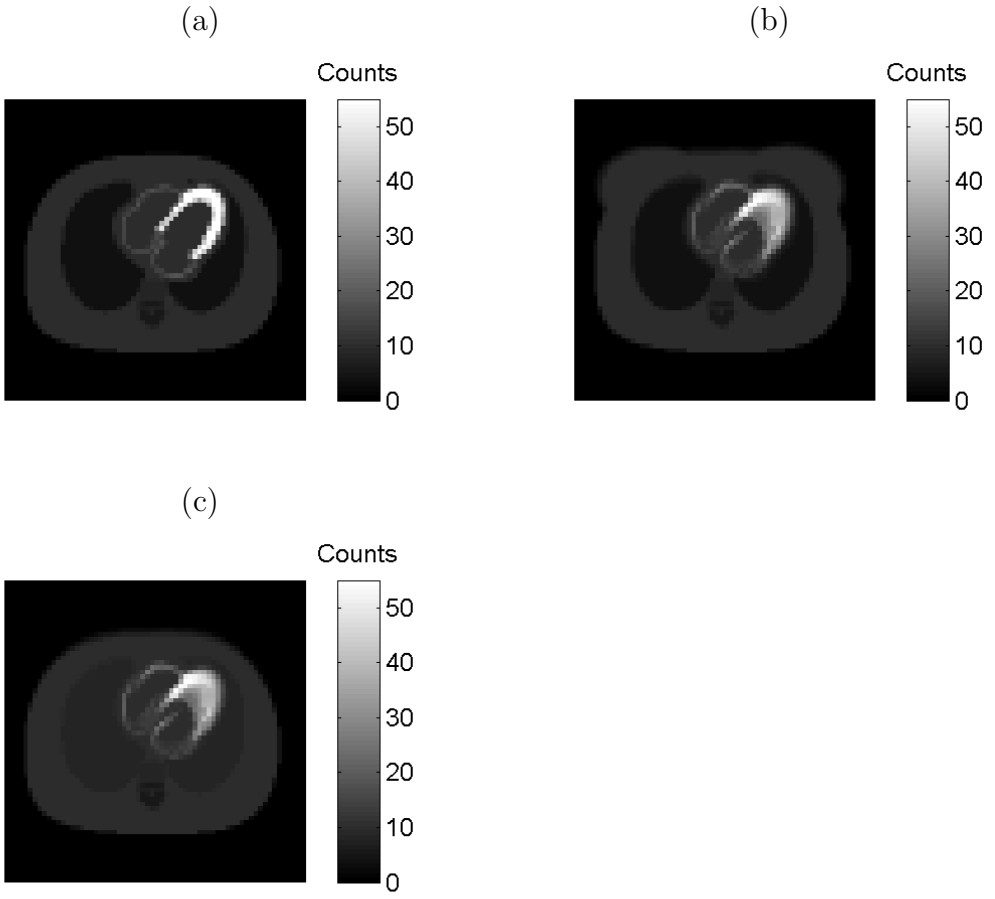

Figure 8.1: Activity distribution for the central slice of the XCAT phantom (a)male phantom, (b) female phantom and (c) male phantom with increased lung activity

Projection data were generated for each phantom using the rotation based projector developed in this work for primary photons and for photons scattered once and detected in an energy widow of 80-126keV. Resolution effects were simulated using the convolution technique described in Section 5.1.3 for a low energy high resolution collimator. Perfect rejection of scattered photons from the photopeak data was included and the scatter data contained only photons which had been scattered once.

Each data set was reconstructed using the SMLGA-MLAA algorithm developed in this work, estimating the attenuation map on a voxel by voxel basis. A initial estimate of the activity distribution was made by performing five iterations of the MLEM algorithm without attenuation correction. An initial estimate of the attenuation map was determined by segmentation of the initial activity distribu-

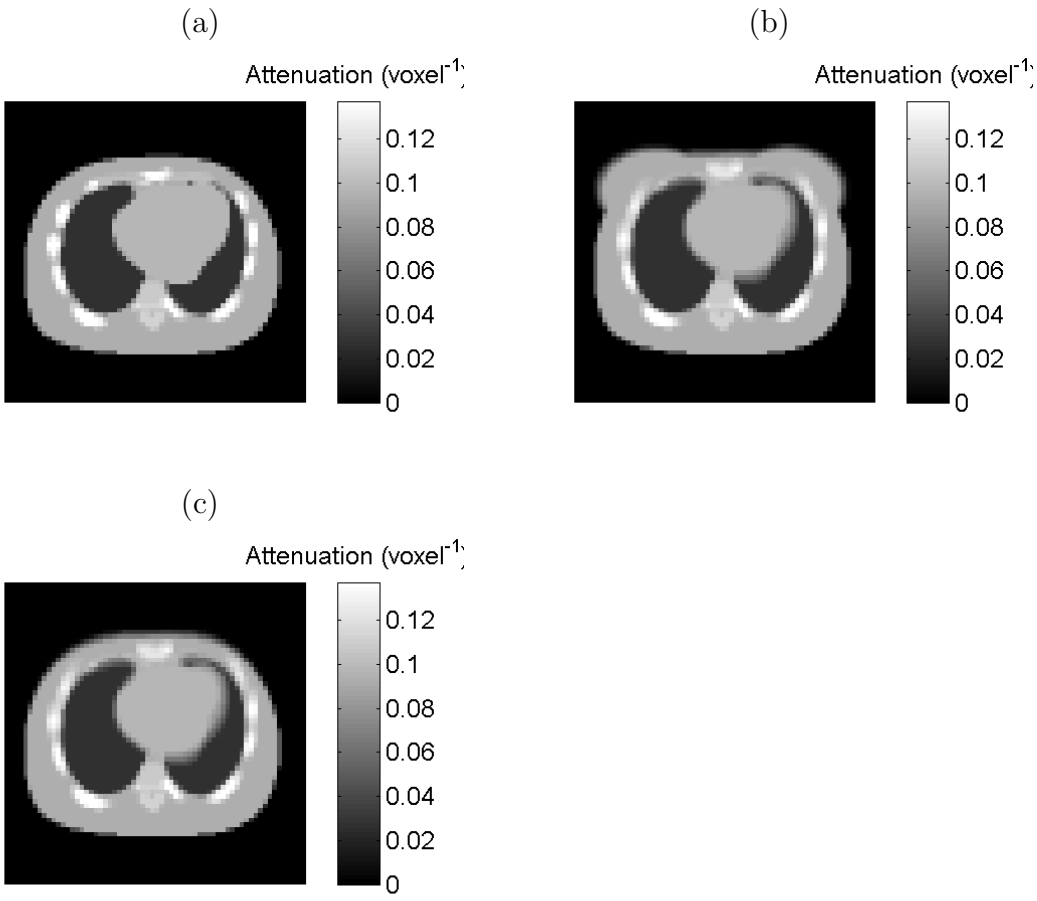

Figure 8.2: Attenuation map for the central slice of the XCAT phantom (a)male phantom, (b) female phantom and (c) male phantom with increased lung activity

tion (using a fuzzy cluster technique) to find the body outline; points within the body outline were assigned the attenuation of soft tissue (0.15cm^{-1}) and points outside the body were assigned zero attenuation. Sub-iterations of the MLEM algorithm (to estimate the activity distribution with fixed attenuation) were then alternated with sub-iterations of the SMLGA-MLAA algorithm (to estimate the attenuation map with fixed activity). 10 iterations were performed, each with 10 subsets. The first iteration used a reduced matrix size (32^3) for the estimation of the attenuation map for all subsets; in all other iterations a matrix size of 64^3 was used for both the activity and attenuation estimations. After each sub-iteration of the attenuation map reconstruction, constraints were applied to limit the attenuation in the abdominal region to be that of soft tissue inside the body outline and zero outside it and to fix the attenuation in regions of high activity (greater than 55% of the maximum counts per pixel) to be that of soft tissue.

8.1.2 Estimation of Higher Order Scatter Events

In order for reconstruction of real data sets to be possible it is necessary to include correction for photons that are scattered more than once ('higher order' scatter events) and for primary photons that are detected in the scatter window. The contribution of higher order scatter events will depend on the attenuation of the object which the photons travel through and the energy of each photon after the first scatter event. As a result the calculation of the exact distribution would be extremely complex. Instead, a simple estimate of the higher order scatter, using a blurred version of the first order scatter sinogram, which ignores the influence of the attenuation map on the higher order scatter event distribution, has been investigated. This is similar to the method proposed by Ollinger (1996) for PET scatter correction. The complete scatter sinogram ($\boldsymbol{s}^*(\boldsymbol{\mu})$) is then the sum of the first order scatter sinogram ($\boldsymbol{s}(\boldsymbol{\mu})$), the higher order scatter events ($\boldsymbol{h}$) and the primary photon sinogram multiplied by an appropriate scaling factor (w_p) depending on the number of primary photons detected in the given energy window; Equation 8.1.

$$\boldsymbol{s}^*(\boldsymbol{\mu}) = \boldsymbol{s}(\boldsymbol{\mu}) + \boldsymbol{h} + w_p \boldsymbol{n}^p \tag{8.1}$$

$$\boldsymbol{h} \approx w_h \left(B \otimes \boldsymbol{s}(\boldsymbol{\mu})\right) \tag{8.2}$$

B is a smoothing function

Four different approximations (given by Equations 8.3) to higher order scatter event distribution were investigated in order to determine the best fit to true higher order scatter distribution. Each approximation was compared to higher order scatter event distributions created using the SIMIND Monte Carlo simulator. Sinograms containing only photons which had been scattered once and containing photons which had been scattered up to ten times were produced using the Monte Carlo simulator and a sinogram containing photons which had been scattered between two and ten times was generated by subtracting the first order scatter from the multiple order scatter sinogram. Simulations were performed for three realisations of the XCAT phantom (a standard male phantom, a standard female phantom and a male phantom with reduced contrast between the lung and soft tissue activities), in each simulation data were collected for six energy windows corresponding to the photopeak (126-154keV) and 5 scatter windows

with low energy cut-off between 60 and 100 keV and high energy cut off 126 keV. Estimated first order scatter sinograms were calculated for each phantom for each scatter window using the complete scatter model described by Equation 5.9. The estimated and simulated sinograms were generated for projections every 2^o over 360^o with 64^2 detector elements in each projection.

$$\boldsymbol{h} = w_h \left(\frac{\exp\left(-\frac{\boldsymbol{x}^2}{2\sigma_G^2}\right)}{2\pi\sigma_G^2} \otimes \boldsymbol{s}(\boldsymbol{\mu}) \right) \tag{8.3a}$$

$$\boldsymbol{h} = w_h \left(\frac{\exp\left(-\frac{\boldsymbol{x}^2}{2\sigma_G^2}\right)}{2\pi\sigma_G^2} \otimes \boldsymbol{s}(\boldsymbol{\mu}) \right) + w_s \tag{8.3b}$$

$$\boldsymbol{h} = w_h \left(\exp\left(-\sigma_E \boldsymbol{x}\right) \otimes \boldsymbol{s}(\boldsymbol{\mu}) \right) \tag{8.3c}$$

$$\boldsymbol{h} = w_h \left(\exp\left(-\sigma_E \boldsymbol{x}\right) \otimes \boldsymbol{s}(\boldsymbol{\mu}) \right) + w_s \tag{8.3d}$$

The MatLAB *fminsearch* function was used to find the parameters σ_G, σ_E, w_h and w_s that produced the lowest root mean square difference between the Monte Carlo simulation and the approximation in a given energy window for each of the three XCAT phantoms. The resulting RMS difference was used to determine the best approximation to the higher order scatter events.

The weighting factor w_p was determined by comparing the total number of counts in all projections for each phantom in the Monte Carlo simulated data to the estimated data for primary photons. The calculated weighting factors and blurring widths for the best approximation method were then used to estimate the complete sinogram measured in each energy window. The root mean square difference between the complete estimated sinograms and the complete Monte Carlo sinograms were compared for each energy window and each XCAT phantom realisation. The root mean square difference was used to assess the accuracy of the estimation for each energy window and hence to help select the most appropriate energy window to use in the SMLGA reconstruction algorithm. When selecting an appropriate energy window it is also important to consider the effect of noise since smaller energy windows will have a lower signal to noise ratio and will have an increased uncertainty when comparing the measured and estimated sinograms in the reconstruction algorithm.

The SMLGA-MLAA reconstruction algorithm assumes that both the higher order scatter distribution and primary photon contribution to the counts measured in the scatter energy window are independent of attenuation. The full scatter sinogram can, therefore, be substituted into the update equation derived in Chapter 6 to give Equation 8.4, where $\boldsymbol{s}^*(\boldsymbol{\mu})$ is given by 8.1 and $D'_{bd}(\boldsymbol{\mu}^i, k)$ is as given in Equation 6.5 (repeated here for clarity).

$$(\boldsymbol{\mu}^{i+1})_k = (\boldsymbol{\mu}^i)_k + \alpha_s \cdot \sum_d \left(- \sum_b D'_{bd}(\boldsymbol{\mu}^i, k) + (\boldsymbol{n}^s)_d \cdot \frac{\sum_b D'_{bd}(\boldsymbol{\mu}^i, k)}{(\boldsymbol{s}^*(\boldsymbol{\mu}))_d} \right) \tag{8.4}$$

$$\begin{aligned} D'_{bd}(\boldsymbol{\mu}^i, k) = \sum_{b \neq k} \Bigg[& (\boldsymbol{\phi})_b \omega_{bjk} \exp\left[- \int_b^k \boldsymbol{\mu}(x) \mathrm{d}x \right] c_{kj'd} \exp\left[- \int_k^d \boldsymbol{\mu}(x) \mathrm{d}x \right] N_{jj'} e^{-(\boldsymbol{\mu}^i)_k} \\ & - (\boldsymbol{\phi})_b \omega_{bjk} \exp\left[- \int_b^k \boldsymbol{\mu}(x) \mathrm{d}x \right] c_{kj'd} \exp\left[- \int_k^d \boldsymbol{\mu}(x) \mathrm{d}x \right] N_{jj'} (1 - e^{-(\boldsymbol{\mu}^i)_k}) \Bigg] \\ & + \sqrt[3]{\frac{3}{4\pi}} \frac{(\boldsymbol{\lambda})_{b=k}}{2} c_{kj'd} \exp\left[- \int_k^d \boldsymbol{\mu}(x) \mathrm{d}x \right] e^{-(\boldsymbol{\mu}^i)_{b=k} \sqrt[3]{\frac{3}{4\pi}}} \\ & - \frac{(\boldsymbol{\lambda})_{b=k}}{2} c_{kj'd} \exp\left[- \int_k^d \boldsymbol{\mu}(x) \mathrm{d}x \right] (1 - e^{-(\boldsymbol{\mu}^i)_{b=k} \sqrt[3]{\frac{3}{4\pi}}}) \end{aligned} \tag{8.5}$$

8.1.3 Scatter Correction of the Photopeak

The complete scatter model developed can also be used to estimate the contribution of scatter events to the photopeak and hence could be used to perform a scatter correction of the photopeak sinogram. The potential of this has been assessed by performing reconstructions of Monte Carlo simulations of photopeak projection data generated for the male XCAT phantom with perfect attenuation correction and scatter correction performed either using the exact scatter data or using scatter correction estimated by the scatter model developed in this work using the true attenuation map and the current reconstruction of the activity distribution.

As discussed in Section 2.5 a number of different methods of scatter correction have been developed. One of the simplest of these, and the most commonly used clinically, is the triple energy window (TEW) method. The triple energy window

scatter correction estimates the contribution of scatter to the photopeak using small energy windows positioned immediately above and below the photopeak window (King *et al.*. 1997, Ogawa *et al.*. 1991, Buvat *et al.*. 1995, Gustafsson *et al.*. 2000). The difference in counts between these two windows can be attributed to scatter in the lower energy window; alternatively all the counts in the lower window can be assumed to be scatter, removing the need for the upper energy window. A scaling factor is applied to the counts detected in the scatter window and the resulting number of counts is subtracted from the corresponding pixel in the photopeak measurements either prior to or during the reconstruction process.

A simplified TEW calculation, with a single energy window below the photopeak, has been investigated here as a possible method of scatter correction as it is much faster to calculate than the estimate of scatter using the scatter model. The scaling factor relating the number of counts in the scatter window to the scatter counts in the photopeak was assessed using Monte Carlo simulations of three realisations of the XCAT phantom with the SIMIND programme for five different scatter windows. Each scatter window had a maximum energy of 126keV while the lower energy cut off varied between 60 and 100 keV. In each case the scaling factor was calculated to be that required to match the mean number of counts in the scatter window (for all detector elements and all phantoms) to the mean number of scatter counts recorded in the photopeak window. In order to determine the optimum position of the window for the TEW correction the root mean square difference between the true photopeak scatter and that estimated using the appropriately scaled scatter measurement was calculated. This optimum TEW correction was then used as a third method of scatter correction during the reconstruction of the activity distribution with perfect attenuation correction.

8.1.4 Validation

The final SMLGA-MLAA algorithm to jointly estimate an activity distribution and attenuation map without the use of a transmission scan has been tested using Monte Carlo data generated for the XCAT phantom and a physical torso phantom. In each case reconstructions were performed using projections every 4^o over a 360^o rotation using the SMLGA-MLAA algorithm to estimate attenuation and the MLEM algorithm to estimate activity. The resulting activity distributions were compared to reconstruction of the same data using perfect attenuation

correction and without attenuation correction.

Each reconstruction was performed using 5 iterations with 10 subsets and alternated sub-iterations of the activity estimation with sub-iterations of the attenuation map estimation. Scatter correction was performed during the MLEM and MLAA parts of the reconstruction.

When considering scatter correction as part of the SMLGA-MLAA algorithm it is also possible that the scatter model could be used to estimate the contribution of scatter to the photopeak. However, the calculation of the scatter sinogram requires knowledge of both attenuation map and activity distribution and so is unlikely to provide an accurate scatter correction in the early iterations of the algorithm when the estimations of both the activity distribution and attenuation map contain significant errors. Hence, the TEW estimation of scatter was used to provide the scatter correction of the first full iteration (10 sub-iterations) of the algorithm before the scatter distribution was estimated using the scatter model. After each full iteration the contribution of scatter to the photopeak was estimated using the scatter model from the current estimates of the activity distribution and the attenuation map.

8.1.4.1 Monte Carlo Data

The SIMIND Monte Carlo simulator was used to generate projection data for the male XCAT phantom using three energy windows; 126-154keV (the photopeak), 90-126keV (the main scatter window) and 100-126keV (for TEW scatter correction). Each energy window accepted photons which had not been scattered and those which had been scattered up to 10 times. Data were simulated for 64 slices, each of width 0.625mm, centred on the myocardium. The attenuation map corresponding to the XCAT phantom extended beyond the field of view of the detector but the activity was restricted to within the field of view (i.e. scatter from outside the field of view of the camera was not considered). The use of a LEHR collimator was included in the Monte Carlo simulation to determine the resolution of the projection data; scatter within the collimator was also allowed.

Reconstructions were performed with perfect attenuation and scatter correction, without attenuation correction using TEW scatter correction and, with attenuation correction estimated using the SMLGA-MLAA algorithm and scatter correc-

tion estimated as described above. The accuracy of the use of the scatter model as a method of scatter correction at each point in the reconstruction was assessed by calculating the mean and root mean square difference between the estimated scatter and the true scatter distribution after each full iteration.

After each sub-iteration of the attenuation map estimation using the SMLGA-MLAA algorithm, constraints were applied to limit the attenuation in the abdominal region to be that of soft tissue inside the body outline and zero outside it and to fix the attenuation in regions of high activity (greater than 55% of the maximum counts per pixel) to be that of soft tissue.

8.1.4.2 Data Spectrum Phantom

Projection data were acquired for the Data Spectrum torso phantom using a GE Discovery 670 SPECT-CT system with LEHR collimators. Each compartment of the phantom was filled using ^{99m}Tc-pertechnetate such that the activity seen in the heart, body, lung and liver compartments were similar to those normally seen clinically. A matrix size of 64^2 was used for each projection giving a pixel size of 8.84mm for the acquired data. Three energy windows were used; 126-154keV for the photopeak, 100-126keV to provide data for a TEW scatter correction and 90-100keV which was combined with the TEW window to provide data for the scatter part of the attenuation map reconstruction. A fixed radius of rotation of 30cm was used and data were acquired with an average of 450kcounts per projection in the photopeak; typically clinical scans have an average of 200-300kcounts per projection.

The Data Spectrum phantom only recreates the torso and so only the top of the abdominal region is included. Therefore, it is not appropriate to fix the attenuation of the abdominal region to that of soft tissue in the reconstruction of the phantom data. Instead, the attenuation in slices beyond the extent of the phantom was fixed at zero.

When using real measurement data the exact contribution of scatter to the photopeak data is unknown. The 'gold-standard' reconstruction in this case, therefore, was assumed to be using the acquired CT data for attenuation correction with the scatter correction regime described above. This used a TEW estimate of scatter for the first full iteration of the reconstruction; in subsequent iterations

the contribution of scatter to the photopeak was estimated from the CT based attenuation map and the current estimate of the activity distribution using the scatter model. The results of this reconstruction were compared to that using the SMLGA-MLAA algorithm with scatter correction estimated using the TEW technique and the scatter model and, reconstruction without attenuation correction using TEW scatter correction throughout.

8.2 Results

8.2.1 Effect of Phantom on Reconstruction Accuracy

Figures 8.3 and 8.4 show the activity distributions and attenuation maps reconstructed for each version of the XCAT phantom using the SMLGA-MLAA algorithm; results from reconstructions performed using exact attenuation correction are also shown for comparison.

8.2.2 Estimation of Higher Order Scatter Events

Tables 8.2, 8.3 and 8.4 show the root mean square difference between each approximation to the higher order scatter events and the Monte Carlo simulation of the higher scatter event distribution for the male, female and low contrast phantoms respectively. These results show that in most cases the difference in the errors produced by each approximation is small. However, the approximation given in Equation 8.3b was found to produce the most accurate results more often than any of the other models. This model has therefore been selected to estimate the distribution of higher order scatter events that contribute to the measured scatter data.

The scaling factors and Gaussian blur widths found for the three different XCAT phantoms were averaged in order to find the overall factors to be used in the calculation of the full scatter sinogram. These values are shown in Table 8.5 for each of the energy windows tested. The selected approximation for higher order scatter event estimation has been substituted into Equation 8.1, with the appropriate scaling factors, and used to estimate the complete measured sinogram in each energy window. Since the scatter process is associated with a loss of energy

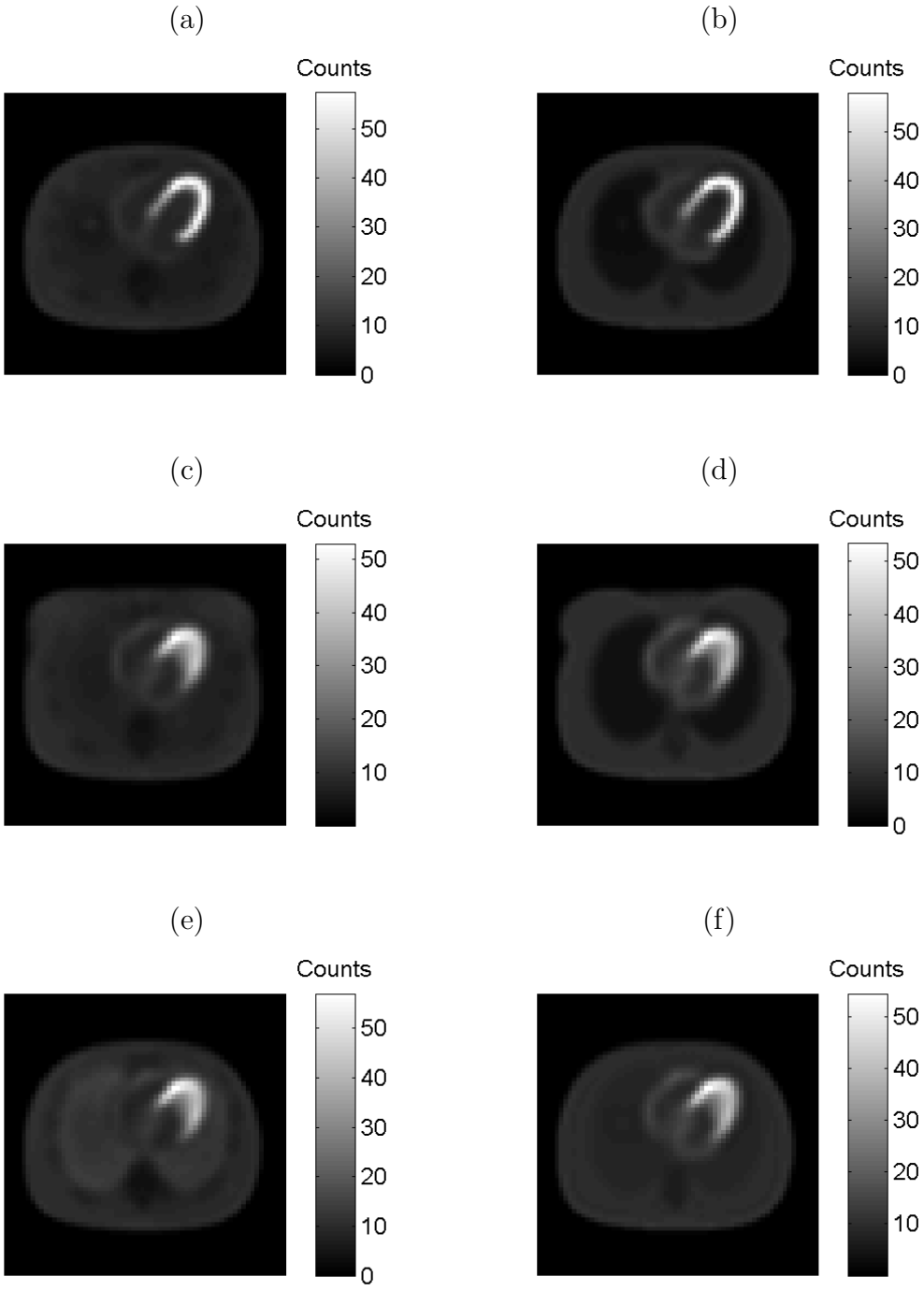

Figure 8.3: Activity distribution reconstructed for the male XCAT phantom using (a) SMLGA-MLAA algorithm and (b) exact attenuation correction, for the female XCAT phantom using (c) SMLGA-MLAA algorithm and (d) exact attenuation correction and, for the male XCAT phantom with increased lung activity using (e) SMLGA-MLAA algorithm and (f) exact attenuation correction

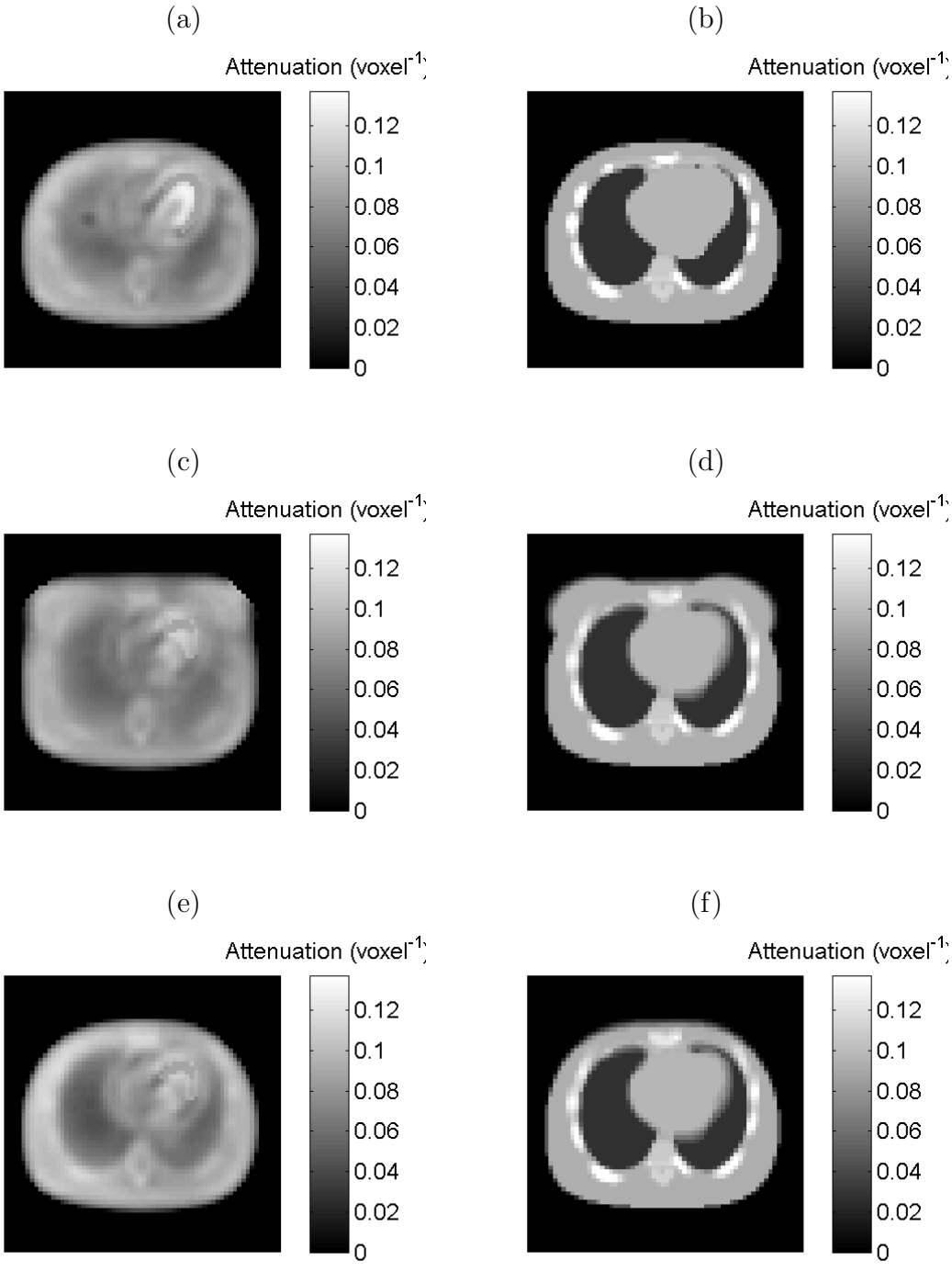

Figure 8.4: Attenuation maps reconstructed using the SMLGA-MLAA algorithm for (a) the male XCAT phantom, (c) the female XCAT phantom and, (e) for the male XCAT phantom with increased lung activity. The corresponding true attenuation maps are shown for (b) the male XCAT phantom, (d) the female XCAT phantom and, (f) for the male XCAT phantom with increased lung activity.

Energy window (keV)	Approximation			
	a	b	c	d
126-154	0.1093	0.1063	0.1093	0.1081
60-126	1.0383	1.0470	1.0383	1.0074
70-126	0.7967	0.7254	0.7967	0.8196
80-126	0.5812	0.5288	0.5812	0.5961
90-126	0.3967	0.3941	0.3967	0.4013
100-126	0.2433	0.2408	0.2433	0.2409

Table 8.2: RMS error in higher order scatter approximation compared to Monte Carlo data for the male XCAT phantom.

Energy window (keV)	Approximation			
	a	b	c	d
126-154	0.0964	0.0968	0.0964	0.0976
60-126	0.9849	0.9940	0.9849	1.0131
70-126	0.7545	0.7600	0.7545	0.7770
80-126	0.5487	0.5020	0.5487	0.5650
90-126	0.3737	0.3734	0.3737	0.3807
100-126	0.2286	0.2169	0.2286	0.2274

Table 8.3: RMS error in higher order scatter approximation compared to Monte Carlo data for the female XCAT phantom.

Energy window (keV)	Approximation			
	a	b	c	d
126-154	0.0964	0.0965	0.0964	0.0972
60-126	0.9590	0.9574	0.9590	0.9663
70-126	0.7342	0.7320	0.7342	0.7402
80-126	0.5350	0.5011	0.5350	0.5388
90-126	0.3661	0.3629	0.3661	0.3658
100-126	0.2263	0.2249	0.2263	0.2236

Table 8.4: RMS error in higher order scatter approximation compared to Monte Carlo data for the low lung contrast XCAT phantom.

it is expected that energy windows which accept lower energy photons will include more photons which have undergone multiple scatter events and hence will have a higher scaling factor w_h.

Generally the effect of increased numbers of higher order scatter photons in energy windows with a lower cut-off energy is that the error in the estimation of the complete sinogram is increased as shown by the root mean square differences between the estimated sinograms and the sinograms simulated using the SIMIND

Energy window (keV)	w_h	w_s	w_p	σ_G
126-154	8.05×10^{-4}	1.32×10^{-3}	1.04×10^{-2}	2.24
60-126	2.58×10^{-2}	7.03×10^{-4}	9.92×10^{-5}	1.45
70-126	1.60×10^{-2}	5.71×10^{-3}	9.92×10^{-5}	3.17
80-126	1.12×10^{-2}	5.25×10^{-3}	9.92×10^{-5}	6.01
90-126	1.07×10^{-2}	8.51×10^{-4}	9.92×10^{-5}	1.52
100-126	1.07×10^{-2}	8.51×10^{-4}	9.92×10^{-5}	2.67

Table 8.5: Scaling factors used in the calculation of the full scatter sinogram.

Energy	Root Mean Square Error				Average Count-rate
window (keV)	Male	Female	Low contrast	Mean	per detector
126-154	0.697	0.506	0.437	0.547	8.74
60-126	1.135	3.713	1.055	1.967	10.80
70-126	0.893	1.103	0.820	0.939	9.25
80-126	0.643	0.897	0.628	0.723	7.59
90-126	0.480	0.921	0.458	0.620	5.89
100-126	0.323	1.777	0.307	0.802	4.05

Table 8.6: Root mean square error between estimated and simulated complete sinograms for different energy windows.

Monte Carlo programme for each realisation of the XCAT phantom (Table 8.6). This would suggest that using a small energy window positioned close to the photopeak would offer the highest accuracy in the estimation of scatter. However, the use of the smallest energy window (100-126 keV) was found to have an increased root mean square error. This is likely to be due to the rejection of large numbers of single scatter photons as well as those which have been scattered multiple times and hence a higher level of noise in the Monte Carlo simulation. Increased noise would also be found in real measured data and so the energy window of 90-126keV was determined to be the most suitable for the estimation of the scatter sinogram.

8.2.3 Scatter Correction of the Photopeak

The scaling factor calculated to relate the total counts in each energy window to the scatter in the photopeak is shown in Table 8.7. The root mean square error of scatter estimated in the photopeak window using each lower energy window is also shown for the three phantoms tested. The results demonstrate that, as expected the most accurate estimate of the photopeak scatter is obtained by using a small

Energy window (keV)	Scaling Factor	Root Mean Square Error		
		Male	Female	Low contrast
60-126	0.2113	0.527	0.506	0.490
70-126	0.2467	0.511	0.492	0.477
80-126	0.3009	0.496	0.478	0.463
90-126	0.3873	0.480	0.463	0.449
100-126	0.5638	0.459	0.441	0.429

Table 8.7: Scaling factors used to relate low energy scatter window measurements to photopeak scatter and root mean square error between estimated and simulated peak scatter for different energy windows.

	Image		Region	
	Mean	RMSE	Mean	RMSE
Scatter model	0.0407	0.4939	0.0717	0.4024
TEW	0.1286	1.3711	0.4013	1.0847

Table 8.8: Mean error and root mean square error (RMSE) in reconstructions of the male XCAT phantom with perfect attenuation correction using different scatter correction techniques compared to reconstruction with exact scatter correction, for the whole image volume and for a region of interest centred over the heart.

energy window placed close to the photopeak. This is because a higher low energy cut-off excludes more photons which have been scattered through large angles or that have been scattered multiple times and which would be excluded from the photopeak window due to their reduced energy. The scaling factors estimated here for energy windows with lower energy cut-offs of 90 and 100keV show good agreement with the values reported by Buvat *et al.*. (1995) and Gustafsson *et al.*. (2000) of 0.55 and 0.43 respectively for a 92 to 125keV window

Figure 8.5 shows the central slice of the XCAT activity distribution calculated from Monte Carlo data with perfect attenuation correction using exact scatter correction compared to scatter correction estimated using the scatter model developed in this work and using a triple energy window technique. The difference between the results of the two estimation methods compared to that from exact scatter correction for this slice is illustrated in Figure 8.6. The activity distribution in the region of the heart is shown for each technique as polar plots in Figure 8.7 and the corresponding errors in Figure 8.8. The mean and root mean square errors in the whole reconstruction volume and in a region of interest centred over the heart are shown in Table 8.8.

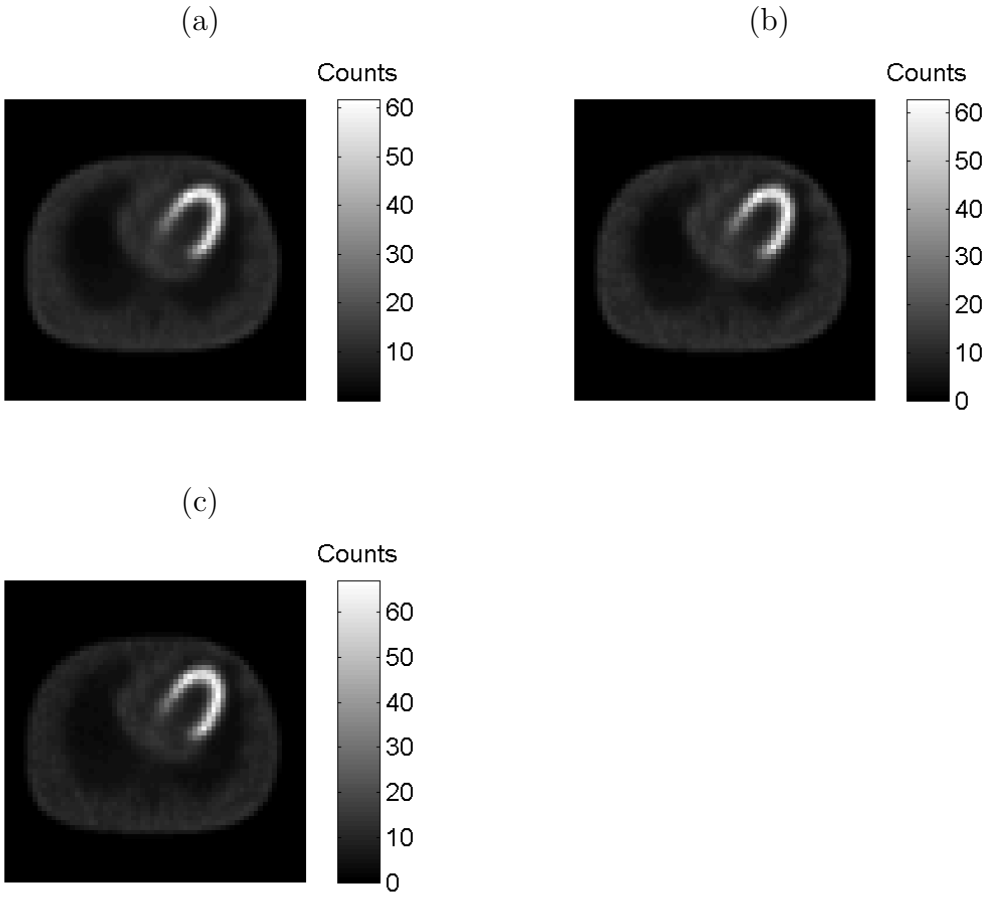

Figure 8.5: Activity distribution reconstructed for the male XCAT phantom from Monte Carlo data using perfect attenuation correction with (a) perfect scatter correction, (b) scatter correction estimated using the scatter model and, (c) with TEW scatter correction.

8.2.4 Validation

8.2.4.1 Monte Carlo Data

Figure 8.9 shows the activity distribution for the central slice of a reconstruction using Monte Carlo data using the SMLGA-MLAA algorithm to estimate an attenuation map and the scatter model to estimate the contribution of scatter to the photopeak. The activity distributions reconstructed when using perfect attenuation and scatter correction and, without attenuation correction using TEW scatter correction are also shown for comparison. The error in each reconstruction compared to the reconstruction with perfect attenuation correction is shown in Figure 8.10. The attenuation map that was reconstructed by the SMLGA-MLAA

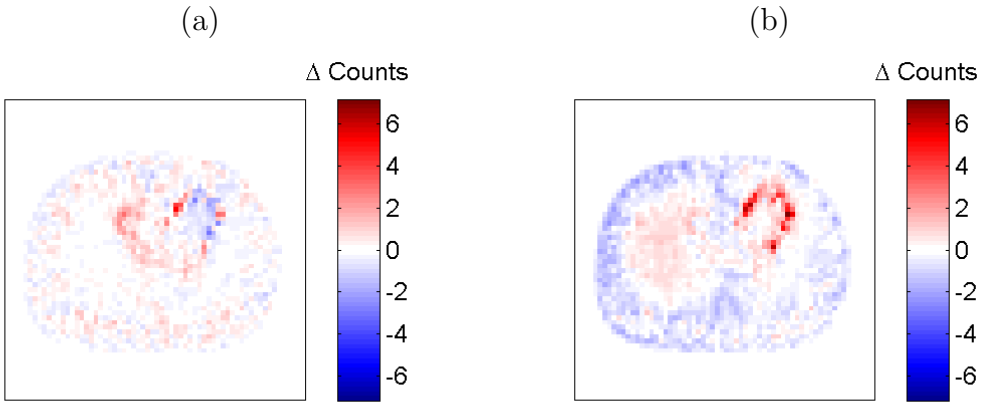

Figure 8.6: Error in reconstructed activity distribution reconstructed for the male XCAT phantom using perfect attenuation correction with (a) scatter correction estimated using the scatter model and (b) with TEW scatter correction, compared to reconstruction with exact scatter correction.

algorithm is shown in Figure 8.11. Polar plots of the activity distribution in the myocardium for each reconstruction are shown in Figure 8.12 and the corresponding differences compared to reconstruction with perfect attenuation correction in Figure 8.13.

The suitability of the use of the scatter model to estimate the contribution of scatter to the photopeak in the case where the true attenuation map is not known has been assessed by considering the mean and root mean square difference between the estimated scatter in the photopeak and the scatter distribution found from the Monte Carlo simulation. The errors after each iteration are shown in Table 8.9; the error in the TEW estimate compared to the exact scatter distribution is also shown.

8.2.4.2 Data Spectrum Phantom

Figure 8.14 shows the activity distribution for the central slice of a reconstruction of data acquired for the Data Spectrum torso phantom using the SMLGA-MLAA algorithm to estimate an attenuation map and the scatter model to estimate the contribution of scatter to the photopeak. The activity distributions reconstructed when using CT based attenuation correction and scatter correction estimated from the scatter model and, without attenuation correction using TEW scatter correction are also shown for comparison. The error in each reconstruction

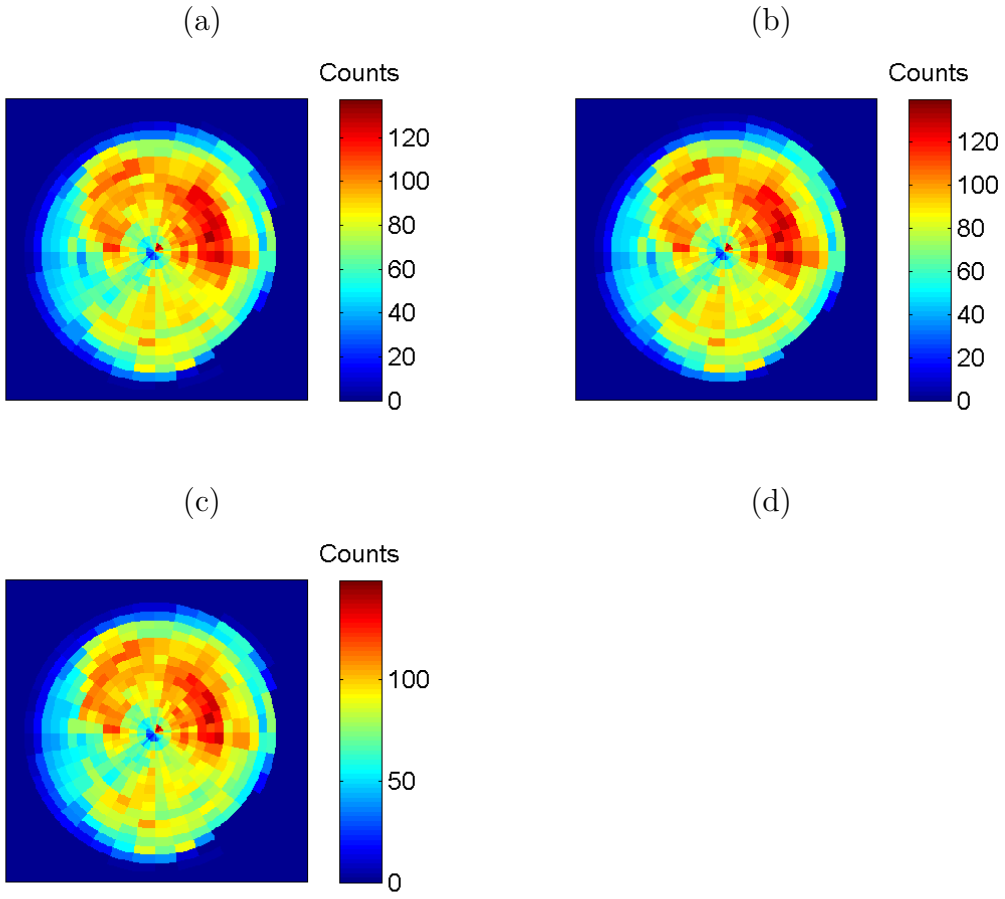

Figure 8.7: Polar plots of myocardial activity distribution reconstructed for the male XCAT phantom using perfect attenuation correction with (a) perfect scatter correction, (b) scatter correction estimated using the scatter model and (c) with TEW scatter correction.

Iteration	Mean	RMSE
1	0.053	0.2247
2	0.011	0.1793
3	0.033	0.1730
4	0.019	0.1695
5	0.024	0.1697
TEW estimate	0.002	0.4585

Table 8.9: Mean error and root mean square error (RMSE) in estimates of the contribution of scatter to the photopeak where the exact attenuation map is not known, for estimation using the scatter model with the estimation of activity distribution and attenuation map reconstructed after each iteration of the SMLGA-MLAA algorithm and for a TEW estimation.

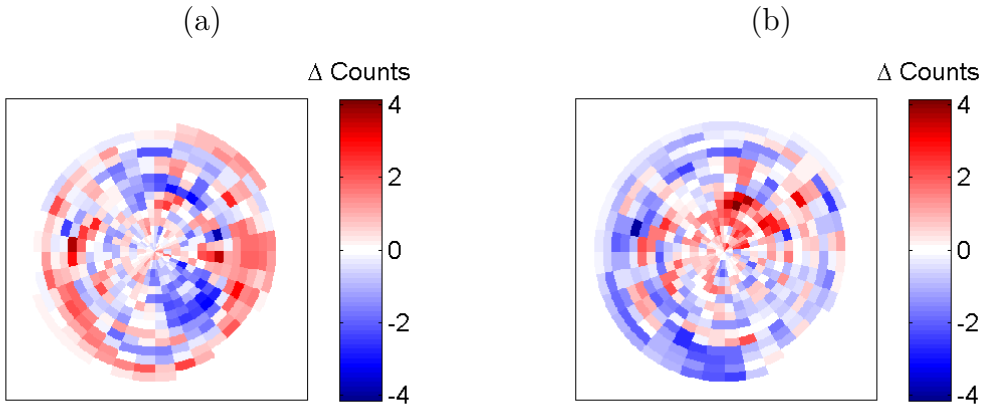

Figure 8.8: Polar plots of error in reconstructed activity distribution in the region of the heart reconstructed for the male XCAT phantom using perfect attenuation correction with (a) scatter correction estimated using the scatter model and (b) with TEW scatter correction, compared to reconstruction with exact scatter correction.

compared to the reconstruction with CT based attenuation correction is shown in Figure 8.15. The attenuation map that was reconstructed by the SMLGA-MLAA algorithm is shown in Figure 8.16. Polar plots of the activity distribution in the myocardium for each reconstruction are shown in Figure 8.17 and the corresponding differences compared to reconstruction with perfect attenuation correction in Figure 8.18.

8.3 Discussion

Tests performed using different variations of the XCAT phantom, with data created using the same model as used in the reconstruction algorithm, demonstrate that each region of the phantom attenuation map can be distinguished in all cases. However, the contrast between different tissue types is reduced, resulting in an overestimation of activity in regions of low attenuation and an underestimation in regions of high attenuation. The use of a female phantom presents the algorithm with a convex surface, between the breasts, which can be more difficult to recreate. The results presented here show that the concave region of the body outline is blurred but is partially recreated.

Other authors (Yamauchi *et al.*. 2014) who have attempted to recreate an at-

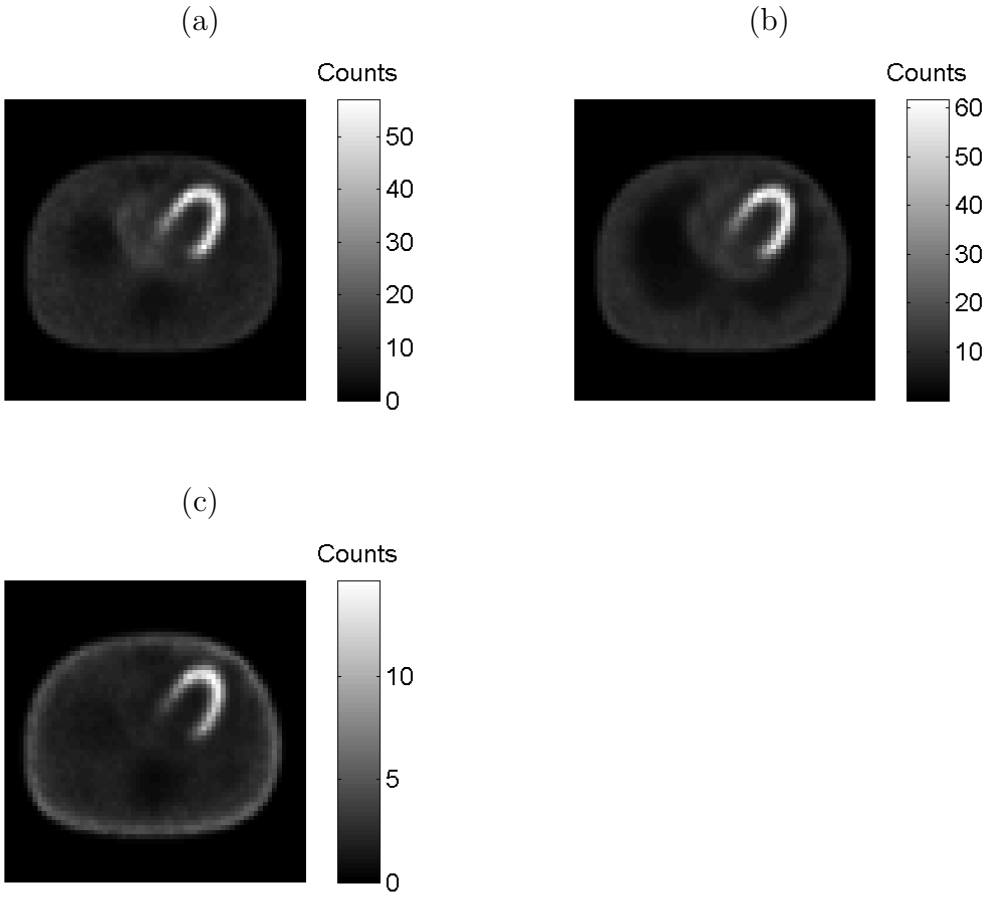

Figure 8.9: Activity distribution reconstructed for the male XCAT phantom using (a) SMLGA-MLAA algorithm to estimate attenuation, (b) exact attenuation correction and, (c) without attenuation correction.

tenuation map from scatter data have found that poor contrast in the activity distribution between soft tissue and lung prevented accurate assessment of the lung outline in the attenuation map. However, the results of the SMLGA-MLAA algorithm show the opposite effect and the contrast between lung and soft tissue in the attenuation map is more accurately recovered, with better delineation of the boundary, in the case where activity within the lung is increased.

The use of the scatter model developed in this work as a method of scatter correction of the photopeak has been shown to enable a more accurate reconstruction than the use of a triple energy window estimation of scatter. When comparing the activity distribution reconstructed using the exact attenuation map and the two scatter estimation methods with reconstruction using the exact attenuation and scatter correction the scatter model is shown to produce lower mean and

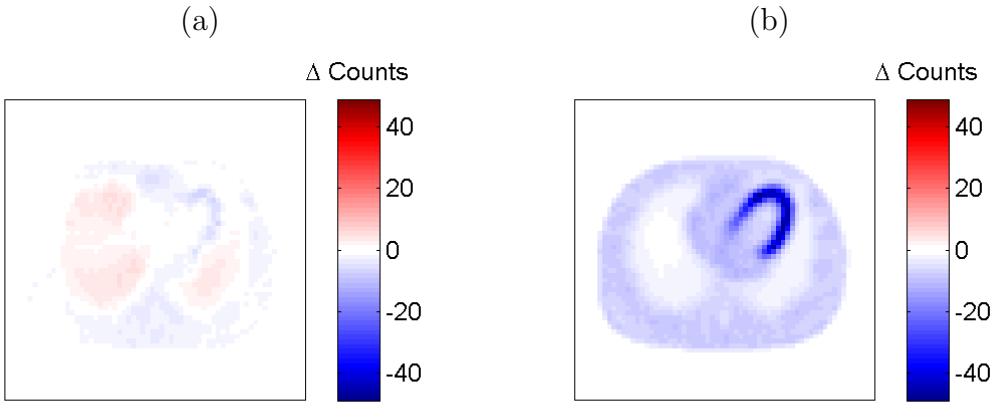

Figure 8.10: Error in reconstructed activity distribution reconstructed for the male XCAT phantom using (a) SMLGA-MLAA algorithm to estimate attenuation and, (b) without attenuation correction, compared to reconstruction with exact attenuation correction.

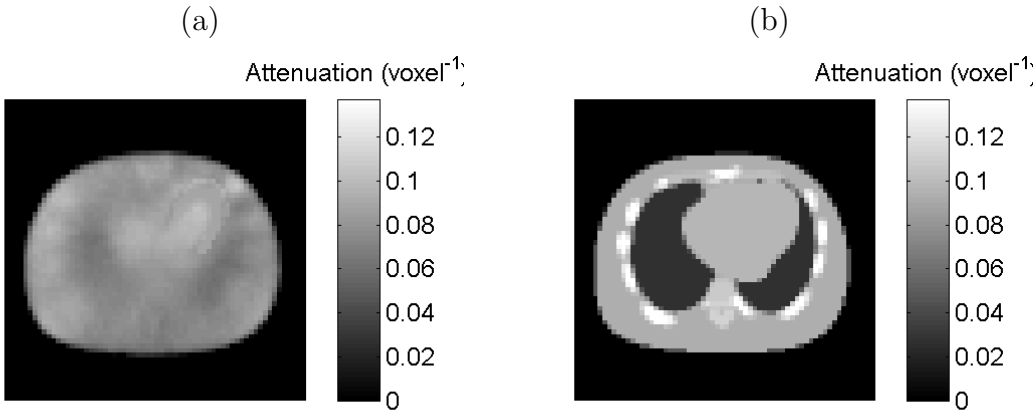

Figure 8.11: Attenuation map reconstructed for the male XCAT phantom using (a) SMLGA-MLAA algorithm to estimate attenuation and, (b) true attenuation map.

root mean square errors in the whole image and in a region of interest centred over the heart. This indicates that the bias in the reconstructed activity values is reduced and the precision is increased. The scatter model developed in this work can, therefore, be considered as a reasonable method of scatter correction where the attenuation map is known *a-priori*.

The final SMLGA-MLAA algorithm, with compensation for higher order scatter events and using the scatter model developed in this work as the basis of a scatter

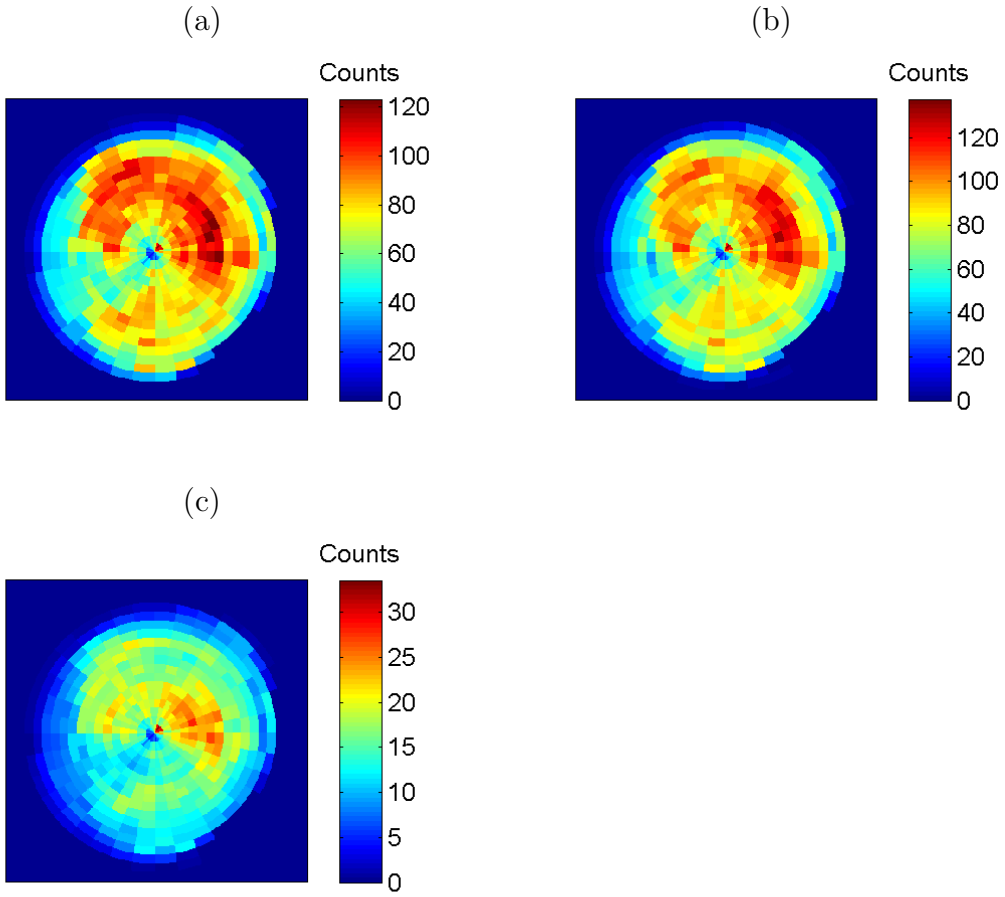

Figure 8.12: Polar plots of myocardial activity distribution reconstructed for the male XCAT phantom using (a) SMLGA-MLAA algorithm to estimate attenuation, (b) exact attenuation correction and, (c) without attenuation correction.

correction of the photopeak, was tested with Monte Carlo data simulated for the male XCAT phantom and using images acquired for the Data Spectrum torso phantom.

Reconstruction of projection data generated using Monte Carlo simulation demonstrate that the body outline can be recovered using the SMLGA-MLAA algorithm and that some contrast between lung and soft tissue is observed. There is also some increased attenuation in the region of the ribs on the right side of the body. However, the boundaries between the lung and soft tissue are not well defined and the true contrast between the lung as soft tissue is not recovered. The use of the estimated attenuation map reduces the global underestimation of counts found when reconstructing the activity distribution without attenuation correction and improves the uniformity of the reconstruction in the region of the myocardium.

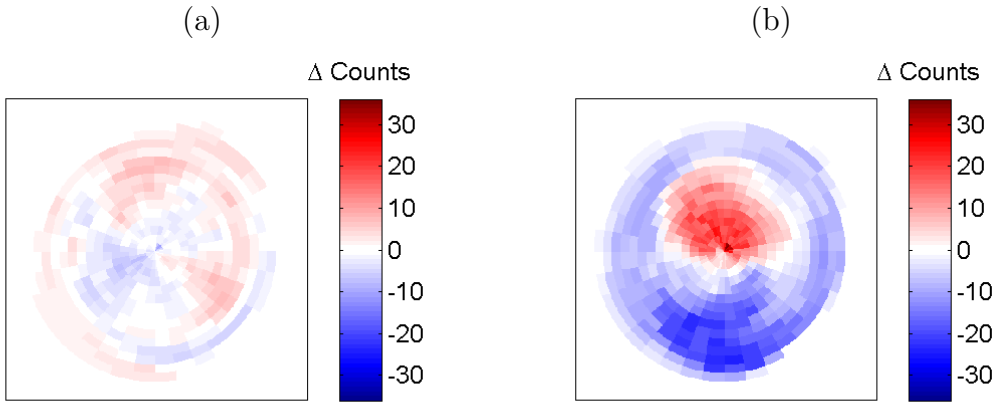

Figure 8.13: Polar plots of difference in myocardial activity distribution reconstructed for the male XCAT phantom using (a) SMLGA-MLAA algorithm to estimate attenuation and, (b) without attenuation correction, compared to reconstruction with exact attenuation correction.

When performing reconstruction without attenuation correction the scaled errors in the heart (shown in Figure 8.13) demonstrate an overestimation in the activity in the anterior wall and an underestimation in the inferior wall. This is because the anterior wall is closest to the chest wall and hence photons from this region are less likely to be attenuated that those originating more centrally in the body, such as the inferior wall of the heart.

The accuracy of the estimation of the contribution of scatter to the photopeak using the scatter model with an estimated activity distribution and attenuation map demonstrates increased bias compared to estimation using a TEW technique for all iterations. This is due to the overestimation of the attenuation in the lung causing an increase in the predicted scatter from these regions. However, the precision of the estimation is shown to be better than the TEW estimation for all iterations. This may be due to the reduced noise in the estimated scatter projections compared to the simulated TEW data.

When considering the results of the reconstruction of projection data acquired using the Data Spectrum phantom, the attenuation per voxel evaluated using SMLGA-MLAA broadly matches the CT based method except for two regions. Firstly, the estimated attenuation at the spine is significantly underestimated (estimated attenuation is close to 0). Here, the activity distribution is close to zero resulting in a very low estimated attenuation. A similar, but opposite

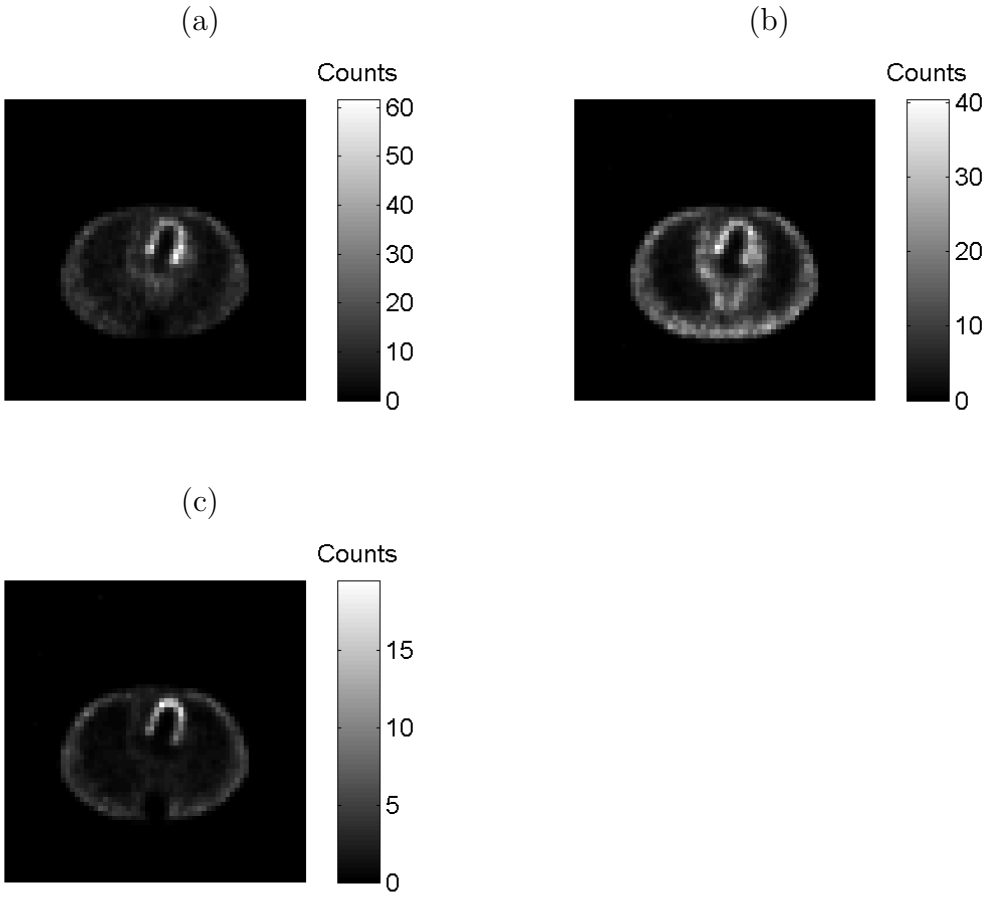

Figure 8.14: Activity distribution reconstructed for the Data Spectrum torso phantom using (a) SMLGA-MLAA algorithm to estimate attenuation, (b) CT based attenuation correction and, (c) without attenuation correction.

effect is observed in the region of the heart where the high activity results in a significant overestimation of the attenuation (by a factor of approximately 2). The region below the phantom (the patient bed) shows high levels of noise in the reconstruction due to the absence of activity in this region. This could be overcome by fixing the values of attenuation in the region of the patient bed to match the known attenuation and geometry of the bed.

Comparison of the distribution of errors in the reconstructed activity distribution for the myocardium is demonstrated using polar plots showing the difference between the SMLGA-MLAA reconstruction or reconstruction without attenuation correction compared to reconstruction using CT based attenuation correction. In each case the errors have been normalised to a mean of zero so that the variability within the myocardium is more clearly visualised. The reconstruction without at-

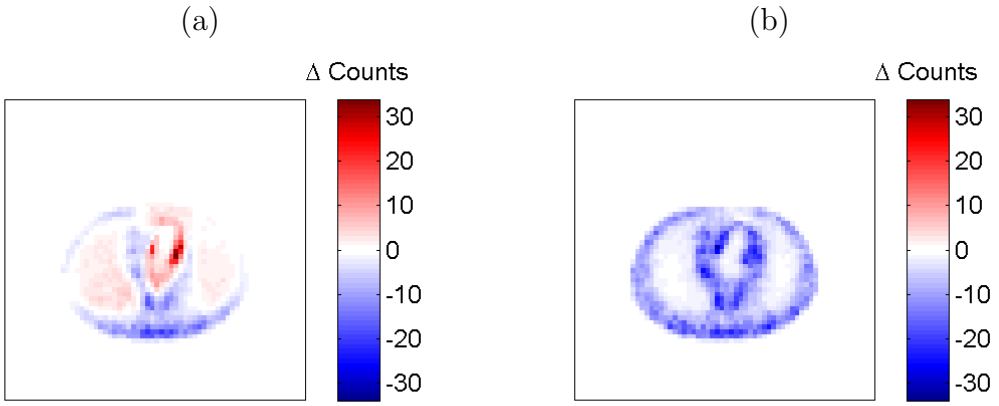

Figure 8.15: Error in reconstructed activity distribution reconstructed for the Data Spectrum phantom using (a) SMLGA-MLAA algorithm to estimate attenuation and, (b) without attenuation correction, compared to reconstruction with CT based attenuation correction.

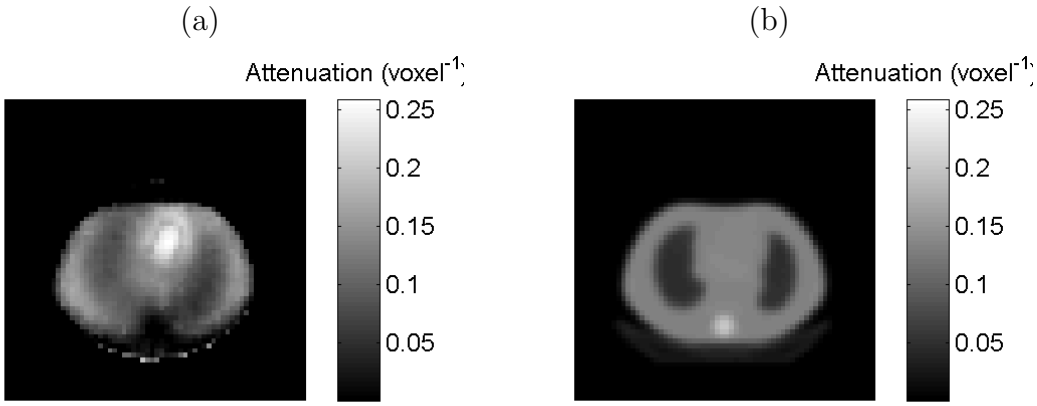

Figure 8.16: Attenuation map reconstructed for the Data Spectrum torso phantom using (a) SMLGA-MLAA algorithm to estimate attenuation and, (b) CT based attenuation map.

tenuation correction is shown to overestimate the activity at the apex of the heart (shown at the centre of the polar plot) and underestimate the activity towards the base of the heart (shown towards the outer rings of the polar plot). This effect is as expected since the apex of the heart lies closer to the chest wall and so photons from this region will experience less attenuation than those originating closer to the base of the heart. The use of the SMLGA-MLAA algorithm to estimate attenuation results in a reconstructed activity distribution with a smaller range of errors in the region of the myocardium and hence demonstrates that

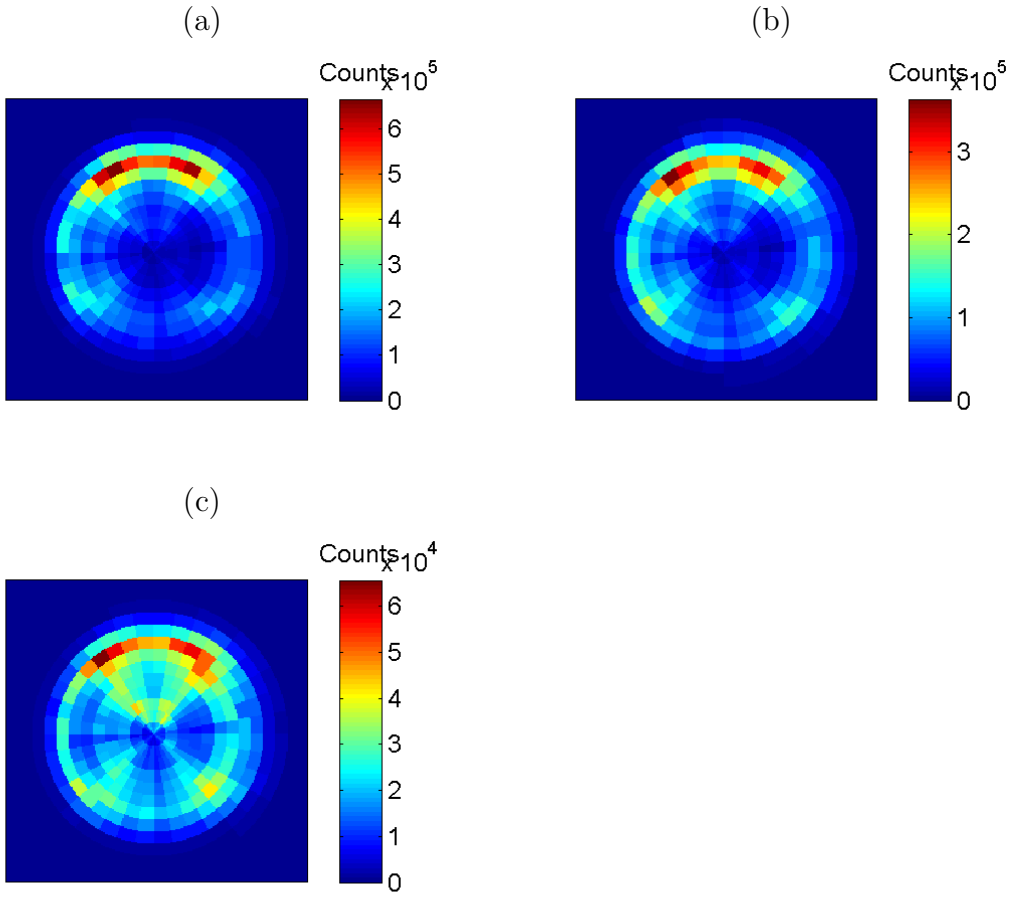

Figure 8.17: Polar plots of myocardial activity distribution reconstructed for the Data Spectrum torso phantom using (a) SMLGA-MLAA algorithm to estimate attenuation, (b) CT based attenuation correction and, (c) without attenuation correction.

this technique offers an improvement in reconstructed image quality compared to reconstruction without attenuation correction.

The results presented here also demonstrate that the use of scatter information in the joint reconstruction can improve the quality of the final images when compared to other joint estimation techniques presented in the literature. Sitek *et al.*. (2007) have also investigated the use of scatter data to improve the joint estimation of an activity and attenuation without transmission scanning. They also found that the use of scatter data can enable a reasonable reconstruction of the attenuation map for the Data Spectrum torso phantom with some recovery of the contrast between soft tissue and lung.

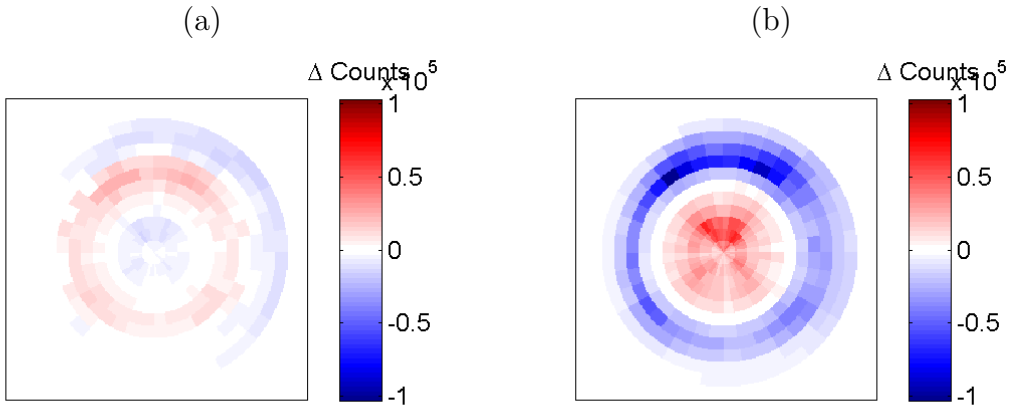

Figure 8.18: Polar plots of difference in myocardial activity distribution reconstructed for the Data Spectrum torso phantom using (a) SMLGA-MLAA algorithm to estimate attenuation and, (b) without attenuation correction, compared to reconstruction with CT based attenuation correction.

Other authors have developed techniques to jointly estimate attenuation and activity using a maximum likelihood optimisation technique (Nuyts *et al.*. 1999, Krol *et al.*. 2001). When tested with computer simulated, parallel beam, projection data these algorithms show significant cross-talk between the activity and attenuation reconstructions with regions of high activity appearing in the reconstructed attenuation map as regions of low attenuation. Similar cross-talk effects are seen in a number of alternative regularised non-linear optimisation techniques (Dicken 1999, Gourion *et al.*. 2002).

Bronnikov (2000) demonstrated that cross-talk between the activity and attenuation reconstruction could be avoided when using consistency conditions to recreate a simple mathematical torso phantom; however in 3 dimensions the attenuation towards the centre of the body was reduced compared to the true attenuation and the boundaries between regions were not accurately recovered in either 2 or 3 dimensions. Yan & Zeng (2009) also investigated the use of consistency conditions to recreate an attenuation map with regions of different attenuation. They demonstrated that an automatic segmentation can be performed for regions with sharp boundaries; however, the algorithm was found to fail in cases with high noise and blurred boundaries between regions.

Crepaldi & De Pierro (2007) presented a technique for reducing the effect of cross-talk in maximum likelihood based joint estimation by introducing an additional

iterative data refinement step. Tian *et al.*. (2006) also developed an algorithm which appears to be less susceptible to cross-talk using Kalman filtering to develop a linearised optimisation. Both the improved maximum likelihood algorithm and Kalman filtering technique demonstrated good reconstruction of phantoms using noise free computer simulated data with a parallel beam geometry; neither have been tested in the presence of noise or with realistic collimation.

The results of reconstruction using the SMLGA-MLAA algorithm developed in this work demonstrate the potential of the technique. However, further work is recommended to improve the quality of the attenuation map reconstructed using the SMLGA-MLAA algorithm. Possible areas for consideration include:

- improving the accuracy of the scatter model used as the basis of the algorithm, in particular the approximation of higher order scatter events could benefit from more accurate estimation,
- the use of an alternative optimisation strategy may to help avoid local minima in the likelihood of the reconstructed images and,
- additional constraints could be applied to further reduce the ill-posed nature of the problem.

8.4 Conclusion

The results presented in this chapter demonstrate that the SMLGA-MLAA algorithm can be used to reconstruct realistic data with improved accuracy compared to reconstruction without attenuation correction. The accuracy of the reconstruction does not appear to be significantly affected by the phantom shape and is improved in cases with more distributed activity distribution.

The use of the scatter model as a basis for scatter correction of photopeak data has been shown to improve precision compared to TEW scatter correction, even in the case where the attenuation map is not exact.

Further work is required to reduce the appearance of artefacts in the attenuation map reconstructed using the SMLGA-MLAA algorithm and to reduce the influence of the under-lying activity distribution on the attenuation map reconstruction.

9 Conclusion

9.1 Main Conclusions

In Chapter 3 an accurate 2-dimensional model for single order scatter was developed. The accuracy of the model was shown to be good for different phantoms and energy windows, including the effect of the energy resolution of the gamma camera, when compared to scatter distributions created using Monte Carlo simulation. This model was extended to 3 dimensions in Chapter 5. Improvements to the model were made by modelling the scattering of photons in voxels close to the point of emission using Monte Carlo simulation. The use of resolution modelling was also investigated and found to improve the accuracy of the estimation of both scattered and primary photons. However, it was found that including the effects of increased photon attenuation after the point of scatter and increased photon absorption in bone (as compared to soft tissue) did not offer any significant improvement in accuracy of the model compared to Monte Carlo simulation.

In Chapter 4 the use of scatter data, estimated using the model derived in Chapter 3, was shown to provide an accurate method of reconstructing an attenuation map, in 2 dimensions, without the use of a transmission scan. The results obtained using the SMLGA algorithm demonstrated improved reconstructions, compared to reconstruction without attenuation correction or using an attenuation map estimated using an MLAA technique, for data acquired using standard SPECT imaging geometries of 360^o or 180^o, or using a region-centric imaging geometry. The results were further improved, particularly close to the boundaries between different tissue types, by combining the SMLGA developed here with the MLAA algorithm.

The basic scatter model is developed in Chapter 5 to allow extension from 2 to 3 dimensions and to more accurately model the contribution of scatter from voxels close to the point of emission. This improved scatter model is then used as the basis of the 3-dimensional reconstruction and in Chapter 6 the use of the SMLGA-MLAA algorithm to estimate an attenuation map without measured transmission data was also shown to improve the quality of reconstruction of an activity distribution compared to reconstruction without attenuation correction in 3 dimensions. The use of ordered subsets in all parts of the reconstruction was shown to offer some saving in calculation time without adversely affecting the quality of the reconstructed images. The possibility of using a reduced matrix size of the calculation of the attenuation map was also considered as a method of reducing the total calculation. This was found to reduce the quality of the final reconstruction when used for all iterations, however, in the early iterations it provided a significant time saving without affecting image quality.

The use of a level sets technique to limit the attenuation map to be piecewise constant showed improved results in the region of the myocardium compared to estimation on a voxel by voxel basis in Chapter 7. The algorithm achieved the best results when limited to regions of soft tissue and lung, and in this case was able to accurately recover the value of attenuation in lung. However, a number of attenuation map and activity distribution combinations were found to have a similar likelihood and so the reconstruction produced by the gradient ascent algorithm was found to be highly dependent on the attenuation map used to initialise the algorithm. As an alternative to the use of level sets, the voxel by voxel calculation was modified to restrict the value of the attenuation map in some regions. This demonstrated that reducing the number of variables that must be found during the reconstruction process has the potential to greatly improve the quality of the final reconstructed images.

Validation of the final SMLGA-MLAA algorithm, including the contribution of photons that have been scattered multiple times, was performed using projection data generated using Monte Carlo simulation and using data acquired for a physical torso phantom. The results, presented in Chapter 8 demonstrated that the SMLGA-MLAA algorithm can be used to reconstruct realistic data with improved accuracy compared to reconstruction without attenuation correction. The accuracy of the reconstruction did not appear to be significantly affected by the phantom shape and was improved in cases with more uniform activity

distribution.

The use of the scatter model as a basis for scatter correction of photopeak data has been shown to improve precision compared to TEW scatter correction, even in the case where the attenuation map is not exact. However, inaccuracies in the estimated attenuation map, in particular the overestimation of the attenuation in the region of the lungs result in an increase in the bias of the estimation; in general the number of scattered photons is overestimated by the scatter model.

9.2 Summary of Contribution

The following points summarise the issues addressed and highlight the novel contributions presented in this thesis:

• A new model for single scatter has been developed and tested in 2 dimensions.

• The basic 2-dimensional scatter model has been extended to three dimensions and improved by more accurate modelling of the contribution of scatter from voxels close to the source voxel.

• A reconstruction algorithm (SMLGA) has been developed to estimate an attenuation map from measured scatter data.

• The SMLGA algorithm has been combined with a published method of estimating attenuation from photopeak data (MLAA) in order to improve the accuracy of the reconstruction compared to either technique alone.

• The use of the scatter model developed in this work for scatter correction of the photopeak has been investigated and shown to offer and improvement of TEW scatter estimation.

• The SMLGA-MLAA reconstruction algorithm has been validated using Monte Carlo simulation with the XCAT phantom and real measurements of a physical phantom and has been shown to enable recovery of the body outline and partial recovery of the lung regions.

9.3 Future Work

The maximum likelihood gradient ascent algorithm used to iteratively reconstruct an attenuation map from measured scatter data was found to be highly sensitive to the attenuation map used to initialise the algorithm when using a piecewise constant technique. This was shown to be due to the fact that a number of combinations of activity distribution and attenuation map were found to have very similar likelihood. Future work could be directed to investigate alternative algorithms which are more able to identify the global maximum in the likelihood than the gradient ascent technique used here. Algorithms such as simulated annealing, which sample the solution space more widely, may offer a potential alternative which is less sensitive to the starting conditions selected.

The scatter model developed in this work, and used as the basis of the SMLGA algorithm, does not attempt to calculate accurately the paths of photons which have been scattered more than once. This is because the calculation of all possible paths for photons which have been scattered more than once is practically impossible for any realistic matrix size and phantom. In this work the detection of photons which have been scattered multiple times has been approximated by a combination of the first order scatter sinogram, the primary scatter sinogram combined with a blurred versions of the scatter sinogram. The use of a Monte Carlo technique to simulate realistic scatter paths would be worthy of future investigation. A number of efficient Monte Carlo algorithms have been developed for scatter correction in SPECT imaging (Beekman *et al.*. 2002, Sohlberg *et al.*. 2008, de Wit *et al.*. 2004) which could potentially be further developed to allow their use within the reconstruction algorithm. This would enable a complete estimate of scatter in both the scatter and photopeak windows to be performed based on the current estimates of the activity distribution and attenuation map which could have the potential to improve the accuracy of the estimation and hence the reconstruction that can be achieved.

The version of the SMLGA-MLAA algorithm used here has been developed in MatLAB and takes several hours to run a complete reconstruction ($\sim$12 hours for 5 iterations with 10 subsets). Further work is required to improve the efficiency of the algorithm. A first step towards this may be achieved in MatLAB through the use of mex files to access C-code or using CUDA code to make more efficient use of available graphic processing units than is possible with just the MatLAB

parallel toolbox functions.

9.4 Papers arising from this work

The following publications have been submitted/published from the work presented in this thesis:

• Cade S. Bousse A. Arridge S. Evans M. & Hutton B. (2010). Estimating an attenuation map from measured scatter for 180o cardiac SPECT, *Journal of Nuclear Medicine* **51**(Supplement 2): 1357.

• Cade S. C. Arridge S. Evans M. J. & Hutton B. F. (2011). Attenuation map estimation without transmission scanning using measured scatter data, *Nuclear Science Symposium Conference Record*, pp. 2657-2663.

• Cade S. C. Arridge S. Evans M. J. & Hutton B. F. (2013). Use of measured scatter data for the attenuation correction of single photon emission tomography without transmission scanning, *Medical Physics* **40**(8).

• Cade S. C. Arridge S. Evans M. J. & Hutton B. F. Use of measured scatter data to reconstruct an attenuation map for attenuation and scatter correction, *Physics in Medicine and Biology, in preparation.*

References

Acton P. D., Pilowsky L. S., Kung H. F. & Ell P. J. (1999). Automatic segmentation of dynamic neuroreceptor single-photon emission tomography images using fuzzy clustering, *European Journal of Nuclear Medicine* **26**(6): 581–590.

Allender S., Scarborough P., Peto V., Rayner M., Leal J., Luengo-Fernandez R. & Gray A. (2008). *European Cardiovascular Disease Statistics 2008*, European Heart Network.

Bailey D. L. (1998). Transmission scanning in emission tomography, *European Journal of Nuclear Medicine* **25**(7): 774–787.

Bailey D. L., Schembri G. P., Harris B. E., Bailey E. A., Cooper R. A. & Roach P. J. (2008). Generation of planar images from lung ventilation/perfusion SPECT, *Annals of Nuclear Medicine* **22**: 437–445.

Beekman F. J., de Jong H. W. A. M. & van Geloven S. (2002). Efficient fully 3-D iterative SPECT reconstruction with Monte Carlo-based scatter compensation, *IEEE Transactions on Medical Imaging* **21**(8): 867–877.

Beekman F. J. & Kamphuis C. (2001). Ordered subset reconstruction for x-ray CT, *Physics in Medicine and Biology* **46**(7): 1835–1844.

Beekman F. J., Kamphuis C. & Frey E. C. (1997). Scatter compensation methods in 3D iterative SPECT reconstruction: A simulation study, *Physics in Medicine and Biology* **42**(8): 1619–1632.

Ben Younes R., Mas J. & Bidet R. (1988). A fully automated contour detection algorithm the preliminary step for scatter and attenuation compensation in spect, *European Journal of Nuclear Medicine and Molecular Imaging*

14: 586–589.

Berger M. (2001). A level set method for inverse problems, *Inverse Problems* **17**: 1327–1355.

Berger M. J., Hubbell J. H., Seltzer S. M., Chang J., Coursey J. S., Sukumar R., Zucker D. & Olsen K. (2010). XCOM: Photon cross section database, Online. Accessed 06/12/2011.
`http://physics.nist.gov/xcom`

Bettinardi V., Pagani E., Gilardi M. C., Landoni C., Riddell C., Rizzo G., Castiglioni I., Belluzzo D., Lucignani G., Schubert S. & Fazio F. (1999). An automatic classification technique for attenuation correction in positron emission tomography, *European Journal of Nuclear Medicine* **26**(5): 447–458.

Blankespoor S. C., Xu X., Kaiki K., Brown J. K., Tang H. R., Cann C. E. & Hasegawa B. H. (1996). Attenuation correction of SPECT using X-ray CT on an emission-transmission CT system: Myocardial perfusion assessment, *IEEE Transactions on Nuclear Science* **43**(4): 2263–2274.

Brix G., Doll J., Bellemann M. E., Trojan H., Haberkorn U., Schmidlin P. & Ostertag H. (1997). Use of scanner characteristics in iterative image reconstruction for high-resolution positron emission tomography studies of small animals, *European Journal of Nuclear Medicine* **24**(7): 779–786.

Bronnikov A. V. (1995). Approximate reconstruction of attenuation map in SPECT imaging, *IEEE Transactions on Nuclear Science* **42**(5): 1483–1488.

Bronnikov A. V. (1999). Numerical solution of the identification problem for the attenuated radon transform, *Inverse Problems* **15**(5): 1315–1324.

Bronnikov A. V. (2000). Reconstruction of attenuation map using discrete consistency conditions, *IEEE Transactions on Medical Imaging* **19**(5): 451–462.

Buvat I., Rodriguez-Villafuerte M., Todd-Pokropek A., Benali H. & Di Paola R. (1995). Comparative assessment of nine scatter correction methods based on spectral analysis using monte carlo simulations, *Journal of Nuclear Medicine* **36**(8): 1476–1488.

Censor Y., Gustafson D., Lent A. & Tuy H. (1979). New approach to the emission computerized tomography problem - simultaneous calculation of at-

tenuation and activity-coefficients, *IEEE Transactions on Nuclear Science* **26**(2): 2775–2779.

Chan T. F. & Tai X.-C. (2003). Level set and total variation regularization for elliptic inverse problems with discontinuous coefficients, *Journal of Computational Physics* **193**: 40–66.

Chang L.-T. (1978). A method for attenuation correction in radionuclide computed tomography, *IEEE Transactions on Nuclear Science* **NS-25**(1): 638–643.

Clinthorne N. H., Pan T. S., Chiao P. C., Rogers W. L. & Stamos J. A. (1993). Preconditioning methods for improved convergence-rates in iterative reconstructions, *IEEE Transactions on Medical Imaging* **12**(1): 78–83.

Crepaldi F. & De Pierro A. R. (2007). Activity and attenuation reconstruction for positron emission tomography using emission data only via maximum likelihood and iterative data refinement, *IEEE Transactions on Nuclear Science* **54**(1, Part 1): 100–106.

de Wit T. C., Xiao J. B., Bokulic T. & Beekman F. J. (2004). Monte-Carlo based statistical SPECT reconstruction: Influence of number of photon tracks, *IEEE Nuclear Science Symposium Conference Record*, IEEE, pp. 3018–3021.

Defrise M., Rezaei A. & Nuyts J. (2012). Time-of-flight PET data determine the attenuation sinogram up to a constant, *Physics in Medicine and Biology* **57**(4): 885–899.

Dicken V. (1999). A new approach towards simultaneous activity and attenuation reconstruction in emission tomography, *Inverse Problems* **15**(4): 931–960.

Dorn O. & Lesselier D. (2006). Level set methods for inverse scattering, *Inverse Problems* **22**: R67–R131.

Dorn O., Miller E. L. & Rappaport C. M. (2000). A shape reconstruction method for electromagnetic tomography using adjoint fields and level sets, *Inverse Problems* **16**: 1119–1156.

Erdogan H. & Fessler J. A. (1999). Ordered subsets algorithms for transmission tomography, *Physics in Medicine and Biology* **44**: 2835–2851.

Ficaro E. P., Fessler J. A., Rogers W. L. & Schwaiger M. (1994). Comparison of americium-241 and technetium-99m as transmission sources for attenuation correction of thallium-201 SPECT imaging of the heart, *Journal of Nuclear Medicine* **35**(4): 652–663.

Fokas A. S., Iserles A. & Marinakis V. (2006). Reconstruction algorithm for single photon emission computed tomography and its numerical implementation, *Journal of The Royal Society Interface* **3**(6): 45–54.

Frey E. C. & Tsui B. M. W. (1993). A practical method for incorporating scatter in a projector-backprojector for accurate scatter compensation in SPECT, *IEEE Transactions on Nuclear Science* **40**(4): 1107–1116.

Frey E. C. & Tsui B. M. W. (1996). A new method for modeling the spatially-variant, object-dependent scatter response function in SPECT, *IEEE Nuclear Science Symposium Conference Record*, Vol. 2, pp. 1082 –1086.

Garcia E. V., Van Train K., Maddahi J., Prigent F., Friedman J., Areeda J., Waxman A. & Berman D. S. (1985). Quantification of rotational thallium-201 myocardial tomography, *The Journal of Nuclear Medicine* **26**(1): 17–26.

Gilland D. R., Jaszczak R. J., Wang H., Turkington T. G., Greer K. L. & Coleman R. E. (1994). A 3d model of non-uniform attenuation and detector response for efficient iterative reconstruction in SPECT, *Physics in Medicine and Biology* **39**: 547–561.

Goetze S. & Wahl R. L. (2007). Prevalence of misregistration between SPECT and CT for attenuation-corrected myocardial perfusion SPECT, *Journal of Nuclear Cardiology* **14**(2): 200–206.

Gourion D., Noll D., Gantet P., Celler A. & Esquerre J. P. (2002). Attenuation correction using SPECT emission data only, *IEEE Transactions on Nuclear Science* **49**(5): 2172–2179.

Gustafsson A., Arlig A., Jacobsson L., Ljungberg M. & Wikkelso C. (2000). Dual-window scatter correction and energy window setting in cerebral blood flow SPECT: a monte carlo study, *Physics in Medicine and Biology* **45**: 3431–3440.

Han G. P., Liang Z. R. & You J. S. (1999). A fast ray-tracing technique for TCT and ECT studies, *IEEE Nuclear Science Symposium Conference Record*, Vol.

1-3, pp. 1515–1518.

Hansen C. L. & Siegel J. A. (1992). Attenuation correction of thallium SPECT using differential attenuation of thallium photons, *Journal of Nuclear Medicine* **33**(8): 1574–1577.

Health Curriculum (2012). Online. Accessed August 2012. `www.infomat.net/infomat/focus/health/health_curriculum/images/heart.gif`

Hebert T., Murphy P., Moore W., Dhekne R., Wendt R. & Blust M. (1993). Experimentally determining a parametric model for the point-source response of a gamma-camera, *IEEE Transactions on Nuclear Science* **40**(4, Part 1): 967–971.

Hubbell J. H. (1969). Photon cross sections, attenuation coefficients, and energy absorption coefficients from 10keV to 100GeV, *National Standard Reference Data System* **NBS-29**.

Hudson H. M. & Larkin R. S. (1994). Accelerated image reconstruction using ordered subsets of projection data, *IEEE Transactions on Medical Imaging* **13**(4): 601–609.

Hutton B. F., Buvat I. & Beekman F. J. (2011). Review and current status of spect scatter correction, *Physics in Medicine and Biology* **56**(14): R85.

Hutton B. F., Hudson H. M. & Beekman F. J. (1997). A clinical perspective of accelerated statistical reconstruction, *European Journal of Nuclear Medicine* **24**(7): 797–808.

Hutton B. F., Osiecki A. & Meikle S. R. (1996). Transmission-based scatter correction of 180 degrees myocardial single-photon emission tomographic studies, *European Journal of Nuclear Medicine* **23**(10): 1300–1308.

ICRP (ed.) (1983). *ICRP Publication 38: Radionuclide Transformations: Energy and Intensity of Emmissions.*, Annals of the ICRP.

Kaplan M. S. & Haynor D. R. (1999). Differential attenuation method for simultaneous estimation of activity and attenuation in multiemission single photon emission computed tomography, *Medical Physics* **26**(11): 2333–2340.

Kaplan M. S., Haynor D. R. & Vija H. (1999a). Comparison of the differential attenuation method for multi-emission SPECT with conventional methods of attenuation compensation, *IEEE Nuclear Science Symposium, Conference Record*, Vol. 1-3, pp. 879–883.

Kaplan M. S., Haynor D. R. & Vija H. (1999b). A differential attenuation method for simultaneous estimation of SPECT activity and attenuation distributions, *IEEE Transactions on Nuclear Science* **46**(3, Part 2): 535–541.

King M. A., de Vries D. J., Pan T. S., Pretorius P. H. & Case J. A. (1997). An investigation of the filtering of TEW scatter estimates used to compensate for scatter with ordered subset reconstructions, *IEEE Transactions on Nuclear Science* **44**(3, Part 2): 1140–1145.

Klein O. & Nishina Y. (1929). Uber die streuung von strahlung durch freie electronen nach der neuen relativistischen quantendynamik von dirac, *Z. Physik* **52**: 853–869.

Krol A., Bowsher J. E., Manglos S. H., Feiglin D. H., Tornai M. P. & Thomas E. D. (2001). An EM algorithm for estimating SPECT emission and transmission parameters from emission data only, *IEEE Transactions on Medical Imaging* **20**(3): 218–232.

Lange K., Bahn M. & Little R. (1987). A theoretical-study of some maximum-likelihood algorithms for emission and transmission tomography, *IEEE Transactions on Medical Imaging* **6**(2): 106–114.

Lange K. & Carson R. (1984). EM reconstruction algorithms for emission and transmission tomography, *Journal of Computer Assisted Tomography* **8**(2): 306–316.

Lautamaeki R., Brown T. L. Y., Merrill J. & Bengel F. M. (2008). CT-based attenuation correction in Rb-82-myocardial perfusion PET-CT: incidence of misalignment and effect on regional tracer distribution, *European Journal of Nuclear Medicine and Molecular Imaging* **35**(2): 305–310.

Lewitt R. M. & Matej S. (2003). Overview of methods for image reconstruction from projections in emission computed tomography, *Proceedings of the IEEE* **91**(10): 1588–1611.

Litman A., Lesselier D. & Santosa F. (1998). Reconstruction of a two-dimensional

binary obstacle by controlled evolution of a level-set, *Inverse Problems* **14**: 685–706.

Ljungberg M. & Strand S.-E. (1989). A Monte Carlo program for the simulation of scintillation camera characteristics, *Computer Methods and Programs in Biomedicine* **29**(4): 257 – 272.

Madsen M. T. & Lee J. R. (1999). Emission based attenuation correction of PET images of the thorax, *IEEE Nuclear Science Symposium Conference Record.*, Vol. 2, pp. 967 –971.

Martinez-Moeller A., Souvatzoglou M., Navab N., Schwaiger M. & Nekolla S. G. (2007). Artifacts from misaligned CT in cardiac perfusion PET/CT studies: Frequency, effects, and potential solutions, *Journal of Nuclear Medicine* **48**(2): 188–193.

Mayneord W. V. (1952). The radiography of the human body with radioactive isotopes, *British Journal of Radiology* **25**: 517–525.

McQuaid S. J. & Hutton B. F. (2008). Sources of attenuation-correction artefacts in cardiac PET/CT and SPECT/CT, *European Journal of Nuclear Medicine and Molecular Imaging* **35**(6): 1117–1123.

Meikle S. R., Dahlbom M. & Cherry S. R. (1993). Attenuation correction using count-limited transmission data in positron emission tomography, *Journal of Nuclear Medicine* **34**(1): 143–150.

Meikle S. R., Hutton B. F. & Bailey D. L. (1994). A transmission-dependent method for scatter correction in SPECT, *Journal of Nuclear Medicine* **35**(2): 360–367.

Miller M. I., Snyder D. L. & Miller T. R. (1985). Maximum-likelihood reconstruction for single-photon emission computed-tomography, *IEEE Transactions on Nuclear Science* **32**(1): 769–778.

Natterer F. (1993). Determination of tissue attenuation in emission tomography of optically dense media, *Inverse Problems* **9**(6): 731.

Núñez M., Prakash V., Vila R., Mut F., Alonso O. & Hutton B. F. (2009). Attenuation correction for lung SPECT: evidence of need and validation of

an attenuation map derived from the emission data, *European Journal of Nuclear Medicine* **36**: 1076–1089.

Nuyts J., Dupont P., Stroobants S., Benninck R., Mortelmans L. & Suetens P. (1999). Simultaneous maximum a posteriori reconstruction of attenuation and activity distributions from emission sinograms, *IEEE Transactions on Medical Imaging* **18**(5): 393–403.

Ogawa K., Harata Y., Ichihara T., Kubo A. & Hashimoto S. (1991). A practical method for position-dependent Compton-scatter correction in single photon-emission CT, *IEEE Transactions on Medical Imaging* **10**(3): 408–412.

Ollinger J. M. (1996). Model-based scatter correction for fully 3d pet, *Physics in Medicine and Biology* **41**(1): 153.
`http://stacks.iop.org/0031-9155/41/i=1/a=012`

Osher S. & Sethian J. A. (1988). Fronts propagating with curvature-dependent speed: Algorithms based on hamilton-jacobi formulations, *Journal of Computational Physics* **79**: 12–49.

Pan T. S., King M. A., Luo D. S., Dahlberg S. T. & Villegas B. J. (1997). Estimation of attenuation maps from scatter and photopeak window single photon-emission computed tomographic images of technetium 99m-labeled sestamibi, *Journal of Nuclear Cardiology* **4**(1, Part 1): 42–51.

Panin V. Y., Zeng G. L. & Gullberg G. T. (2001). A method of attenuation map and emission activity reconstruction from emission data, *IEEE Transactions on Nuclear Science* **48**(1, Part 1): 131–138.

Patton J. A. & Turkington T. G. (2008). SPECT/CT physical principles and attenuation correction, *Journal of Nuclear Medicine Technology* **36**(1): 1–10.

Popescu L. & Lewitt R. (2004). Ray tracing through a grid of blobs, *in* Seibert, JA (ed.), *2004 IEEE Nuclear Science Symposium Conference Record, Vols 1-7*, IEEE, pp. 3983–3986.

Ramlau R., Clackdoyle R., Noo F. & Bal G. (2000). Accurate attenuation correction in SPECT imaging using optimization of bilinear functions and assuming an unknown spatially-varying attenuation distribution, *Zeitschrift fur Angewandte Mathematik und Mechanik* **80**(9): 613–621.

Scheins J. J., Boschen F. & Herzog H. (2006). Analytical calculation of volumes-of-intersection for iterative, fully 3-D PET reconstruction, *IEEE Transactions on Medical Imaging* **25**(10): 1363–1369.

Schretter C. (2006). A fast tube of response ray-tracer, *Medical Physics* **33**(12): 4744–4748.

Segars W. P., Lalush D. S. & Tsui B. M. W. (1999). A realistic spline-based dynamic heart phantom, *IEEE Transactions on Nuclear Science* **46**(3): 503–506.

Serway R. A. (1982). *Physics for Scientists and Engineers*, fourth edn, Saunders College Publishing.

Shepp L. A. & Vardi Y. (1982). Maximum likelihood reconstruction for emission tomography, *IEEE Transactions on Medical Imaging* **MI-1**(2): 113–122.

Siddon R. L. (1985). Fast calculation of the exact radiological path for a 3-dimensional CT array, *Medical Physics* **12**(2): 252–255.

Sitek A., Moore S. C. & Kijewski M. F. (2007). Correction for photon attenuation without transmission measurements using compton scatter information in SPECT, *IEEE Nuclear Science Symposium Conference Record* pp. 4210–4212.

Sohlberg A., Watabe H. & Iida H. (2008). Acceleration of Monte Carlo-based scatter compensation for cardiac SPECT, *Physics in Medicine and Biology* **53**(14): N277–N285.

Sorensen J. A. & Phelps M. E. (1980). *Physics in Nuclear Medicine*, Grune and Stratton Inc., USA.

Tian Y., Liu H. & Shi P. (2006). Simultaneous reconstruction of tissue attenuation and radioactivity maps in SPECT, *Medical Image Computing and Computer-Assisted Intervetion* **4190**: 397–404. - MICCAI 2006, PT 1.

van den Doel K., Ascher U. M. & Leitao A. (2010). Multiple level sets for piecewise constant surface reconstruction in highly ill-posed problems, *Journal of Scientific Computing* **43**: 44–46.

Van Dyk J., Keane T. J. & Rider W. D. (1982). Lung density as measured

by computerized tomography: implications for radiotherapy, *International Journal of Radiation Oncology Biology Physics* **8**(8): 1363 – 1372.

Vese L. A. & Chan T. F. (2002). A multiphase level set framework for image segmentation using the mumford and shah model, *International Journal of Computer Vision* **50**(3): 271–293.

Walrand S. H. M., van Elmbt L. R. & Pauwels S. (1994). Quantitation in SPECT using an effective model of the scattering, *Physics in Medicine and Biology* **39**(4): 719–734.

Welch A., Gullberg G. T., Christian P. E., Datz F. L. & Morgan T. (1995). A transmission-map based scatter correction technique for SPECT in inhomogeneous-media, *Medical Physics* **22**(10): 1627–1635.

Xu M., Cutler P. D. & Luk W. K. (1996). Adaptive, segmented attenuation correction for whole-body PET imaging, *IEEE Transactions on Nuclear Science* **43**(1): 331 –336.

Yamauchi Y., Kanzaki Y., Otsuka K., Hayashi M., Okada M., Nogi S., Morita H., Komori T. & Ishizaka N. (2014). Novel attenuation correction of SPECT images using scatter photopeak winodw data for the detection of coronary artery disease, *Journal of Nuclear Cardiology* **21**(1): 109–117.

Yan Y. & Zeng G. L. (2009). Attenuation map estimation with SPECT emission data only, *International Journal of Imaging Systems and Technology* **19**(3): 271–276.

Zaidi H., Diaz-Gomez M., Boudraa A. & Slosman D. O. (2002). Fuzzy clustering-based segmented attenuation correction in whole-body PET imaging, *Physics in Medicine and Biology* **47**: 1143–1160.

Zaidi H. (ed.) (2006). *Quantitative Analysis in Nuclear Medicine Imaging*, Springer.

Zaidi H. & Hasegawa B. (2003). Determination of the attenuation map in emission tomography, *Journal of Nuclear Medicine* **44**(2): 291–315.

Zaidi H. & Koral K. F. (2004). Scatter modelling and compensation in emission tomography, *European Journal of Nuclear Medicine and Molecular Imaging* **31**(5): 761–782.

Zeng G. L. & GuIlberg G. T. (1992). Frequency domain implementation of the three-dimensional geometric point response correction in SPECT imaging, *IEEE Transactions on Nuclear Science* **39**(5): 1444–1453.

Zeng G. L., GuIlberg G. T., Bai C., Christian P. E., Trisjono F., Di Bella E. V. R., Tanner J. W. & Morgan H. T. (1998). Iterative reconstruction of fluorine-18 SPECT using geometric point response correction, *The Journal of Nuclear Medicine* **39**(1): 124–130.

Zeng G. L., GuIlberg G. T., Tsui B. M. W. & Terry J. A. (1991). Three-dimensional iterative reconstruction algorithms with attenuation and geometric point response correction, *IEEE Transactions on Nuclear Science* **38**(2): 693–702.

Appendix A Software Development

The software used in this work has been developed in MATLAB Version R2011a. Below is a list of the made programmes developed with a brief description of each; all the programmes listed were created by the author and made use of functions within MATLAB toolboxes where appropriate.

- CombinedUpdate: Calculate new attenuation map from individual updates calculated using Nuyts, scatter and Level set techniques with appropriate scaling factors.
- FuzzyCluster: Perform fuzzy cluster based segmentation of images using given cluster start values and iteration tolerance.
- KleinNish: Calculate scatter factors based on the Klein-Nishina formula (Klein & Nishina 1929) for a given photon energy window.
- LevelSet_UpdateVals: Calculate partial derivatives of existing level sets for use in 3D attenuation map estimation.
- ReconParam: Create parameters required for repeated use in forward projection and reconstruction of scatter data; includes scatter factors and paths and collimator response blurring functions.
- RotateMAPAttn and RotateMPAAttn_3D: Perform MAP iterative image reconstruction of attenuation map using Nuyts method (Nuyts *et al.*. 1999) with rotation based projectors for a parallel beam geometry (in 2 or 3 dimensions respectively).
- RotateMAPAttn_3DBlur_SC: Perform MAP iterative image reconstruction

of attenuation map using Nuyts method (Nuyts *et al.*. 1999) with rotation based projectors including the effects of collimator blurring. Scatter correction can performed during the reconstruction process.

- RotateOSEM and RotateOSEM_3D: Perform OSEM iterative image reconstruction of given sinogram using given attenuation data using rotation based projectors for a parallel beam geometry (in 2 or 3 dimensions respectively).

- RotateOSEM_3DBlurSC: Perform OSEM iterative image reconstruction of given sinogram using given attenuation data using rotation based projectors including the effects of collimator blurring. Scatter correction can performed during the reconstruction process.

- RotateScatterSino and RotateScatterSino3D: Calculation of scatter sinogram using Klein-Nishina formula with a rotation based projector (in 2 or 3 dimensions respectively).

- RotateScatterSino3D_P2: Calculation of scatter sinogram using data obtained from simulations to give scatter angles and solid angle effects for nearest neighbours with a rotation based forward projector.

- RotateScatterSino3D_BlurP: Calculation of scatter sinogram using data obtained from simulations to give scatter angles and solid angle effects for nearest neighbours. Distance dependant resolution effects are included in this version which uses a rotation based forward projector and operates in 3D.

- RotateScatterSino3D_Energy and RotateScatterSino3D_EnergyC: Modification of the calculation of scatter sinogram to include the effect of increased attenuation after the point of scatter with and without the effect of reduced scatter fraction in bone respectively.

- RotateScatterUpdate: Iterative update of attenuation map in 2 dimensions using measured and estimated scatter sinograms. Scatter is modelled using Klein-Nishina data; the forward and backprojections are rotation based.

- RotateSino and RotateSino3D: Create attenuated sinogram using a rotation based projector with parallel beam geometry (in 2 or 3 dimensions respectively).

- RotateSino_3DBlur: Create attenuated sinogram using a rotation based projector including the effects of collimator blurring.
- ScattRecon_3DBlur: Iterative update of attenuation map using measured and estimated scatter sinograms using first order scatter only. Scatter is modelled using data obtained from simulations to give scatter angles and solid angle effects for nearest neighbours. Distance dependant resolution effects are included in this version which uses a rotation based forward projector and operates in 3D. This reconstruction is uses the same scatter estimation method as RotateScatterSino3D_BlurP.
- ScattRecon_3DBlur_Full: This is a modification of ScattRecon_3DBlur to include the effect of photons which have been scattered multiple times and of photons that have not been scattered and which are included in the measured scatter sinogram.
- SiddonPoints: Use Siddon method (Siddon 1985) to create paths between a source voxel and each target voxel.